LBL-11203 c.2
SAC-31
UC-70

SWEDISH-AMERICAN COOPERATIVE PROGRAM ON RADIOACTIVE WASTE STORAGE IN MINED CAVERNS IN CRYSTALLINE ROCK

RECEIVED
LAWRENCE
BERKELEY LABORATORY
AUG 31 1981
LIBRARY AND
DOCUMENTS SECTION

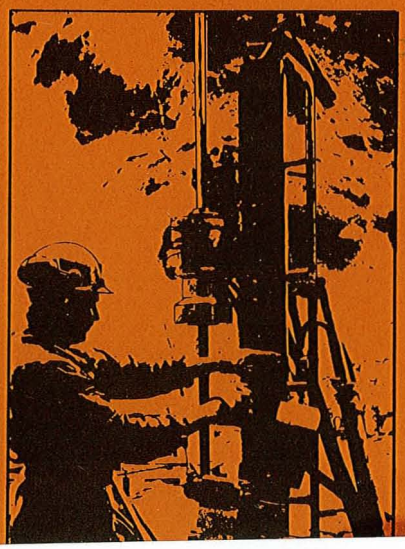

Technical Information Report No. 31

STRENGTH AND PERMEABILITY TESTS ON ULTRA-LARGE STRIPA GRANITE CORE

R. Thorpe, D. J. Watkins, W. E. Ralph,
R. Hsu, and S. Flexser

Lawrence Berkeley Laboratory
University of California
Berkeley, CA 94720

September 1980

TWO-WEEK LOAN COPY

This is a Library Circulating Copy which may be borrowed for two weeks. For a personal retention copy, call Tech. Info. Division, Ext. 6782

A Joint Project of

Swedish Nuclear Fuel Supply Co.
Fack 10240 Stockholm, Sweden

Operated for the Swedish
Nuclear Power Utility Industry

Lawrence Berkeley Laboratory
Earth Sciences Division
University of California
Berkeley, California 94720, USA

Operated for the U.S. Department of
Energy under Contract W-7405-ENG-48

LBL-11203 c.2

LBL-11203
SAC-31
UC-70

STRENGTH AND PERMEABILITY TESTS ON ULTRA-LARGE STRIPA GRANITE CORE

R. Thorpe, D.J. Watkins, W.E. Ralph, R. Hsu, and S. Flexser

Lawrence Berkeley Laboratory
University of California
Berkeley, CA 94720

September, 1980

This work was supported by the Assistant Secretary for Nuclear Energy, Office of Waste Isolation of the U.S. Department of Energy under contract W-7405-ENG-48. Funding for this project is administered by the Office of Nuclear Waste Isolation at Battelle Memorial Institute.

PREFACE

This report is one of a series documenting the results of the Swedish-American cooperative research program in which the cooperating scientists explore the geological, geophysical, hydrological, geochemical, and structural effects anticipated from the use of a large crystalline rock mass as a geologic repository for nuclear waste. This program has been sponsored by the Swedish Nuclear Power Utilities through the Swedish Nuclear Fuel Supply Company (SKBF), and the U.S. Department of Energy (DOE) through the Lawrence Berkeley Laboratory.

The principal investigators are L.B. Nilsson and O. Degerman for SKBF, and N.G.W. Cook, P.A. Witherspoon, and J.E. Gale for LBL. Other participants will appear as authors of the individual reports.

Previous technical reports in this series are listed below.

1. Swedish-American Cooperative Program on Radioactive Waste Storage in Mined Caverns by P.A. Witherspoon and O. Degerman. (LBL-7049, SAC-01).

2. Large Scale Permeability Test of the Granite in the Stripa Mine and Thermal Conductivity Test by Lars Lundstrom and Haken Stille. (LBL-7052, SAC-02).

3. The Mechanical Properties of the Stripa Granite by Graham Swan (LBL-7074, SAC-03).

4. Stress Measurements in the Stripa Granite by Hans Carlsson (LBL-7078, SAC-04).

5. Borehole Drilling and Related Activities at the Stripa Mine by P.J. Kurfurst, T. Hugo-Persson, and G. Rudolph (LBL-7080, SAC-05).

6. A Pilot Heater Test in the Stripa Granite by Hans Carlsson (LBL-7086, SAC-06).

7. An Analysis of Measured Values for the State of Stress in the Earth's Crust by Dennis B. Jamison and Neville G.W. Cook (LBL-7071, SAC-07).

8. Mining Methods Used in the Underground Tunnels and Test Rooms at Stripa by B. Andersson and P.A. Halén (LBL-7081, SAC-08).

9. Theoretical Temperature Fields for the Stripa Heater Project by T. Chan, Neville G.W. Cook, and C.F. Tsang (LBL-7082, SAC-09).

10. Mechanical and Thermal Design Considerations for Radioactive Waste Repositories in Hard Rock. Part I: An Appraisal of Hard Rock for Potential Underground Repositories of Radioactive Waste by N.G.W. Cook; Part II: In Situ Heating Experiments in Hard Rock: Their Objectives and Design by N.G.W. Cook and P.A. Witherspoon (LBL-7073, SAC-10).

11. Full-Scale and Time-Scale Heating Experiments at Stripa: Preliminary Results by N.G.W. Cook and M. Hood (LBL-7072; SAC-11).

12. Geochemistry and Isotope Hydrology of Groundwaters in the Stripa Granite: Results and Preliminary Interpretation by P. Fritz, J.F. Barker, and J.E. Gale (LBL-8285, SAC-12).

13. Electrical Heaters for Thermo-Mechanical Tests at the Stripa Mine by R.H. Burleigh, E.P. Binnall, A.O. DuBois, D.O. Norgren, and A.R. Ortiz (LBL-7063, SAC-13).

14. Data Acquisition, Handling, and Display for the Heater Experiments at Stripa by Maurice B. McEvoy (LBL-7062, SAC-14).

15. An Approach to the Fracture Hydrology at Stripa: Preliminary Results by J.E. Gale and P.A. Witherspoon (LBL-7079, SAC-15).

16. Preliminary Report on Geophysical and Mechanical Borehole Measurements at Stripa by P. Nelson, B. Paulsson, R. Rachiele, L. Andersson, T. Schrauf, W. Hustrulid, O. Duran, and K.A. Magnussen (LBL-8280, SAC-16).

17. Observations of a Potential Size-Effect in Experimental Determination of the Hydraulic Properties of Fractures by P.A. Witherspoon, C.H. Amick, J.E. Gale, and K. Iwai (LBL-8571, SAC-17).

18. Rock Mass Characterization for Storage in Nuclear Waste in Granite by P.A. Witherspoon, P. Nelson, T. Doe, R. Thorpe, B. Paulsson, J.E. Gale, and C. Forster (LBL-8570, SAC-18).

19. Fracture Detection in Crystalline Rock Using Ultrasonic Shear Waves by K.H. Waters, S.P. Palmer, and W.F. Farrell (LBL-7051, SAC-19).

20. Characterization of Discontinuities in the Stripa Granite--Time Scale Heater Experiment by R. Thorpe (LBL-7083, SAC-20).

21. Geology and Fracture System at Stripa by A. Olkiewicz, J.E. Gale, R. Thorpe, and B. Paulsson (LBL-8907, SAC-21).

22. Calculated Thermally Induced Displacements and Stresses for Heater Experiments at Stripa by T. Chan and N.G.W. Cook (LBL-7061, SAC-22).

23. Validity of Cubic Law for Fluid Flow in a Deformable Rock Fracture by P.A. Witherspoon, J. Wang, K. Iwai and J.E. Gale (LBL-9557, SAC-23).

24. Determination of In-Situ Thermal Properties of Stripa Granite from Temperature Measurements in the Full-Scale Heater Experiments: Methods and Primary Results by J. Jeffry, T. Chan, N.G.W. Cook and P.A. Witherspoon (LBL-8424, SAC-24).

25. Instrumentation Evaluation, Calibration, and Installation for Heater Tests Simulating Nuclear Waste In Crystalline Rock, Sweden by T. Schrauf, H. Pratt, E. Simonson, W. Hustrulid, P. Nelson, A. DuBois, E. Binnall, and R. Haught (LBL-8313, SAC-25).

26. Part I: Some Results from a Field Investigation of Thermo-Mechanical Loading of a Rock Mass When Heater Canisters are Emplaced in the Rock by M. Hood. Part II: The Application of Field Data from Heater Experiments Conducted at Stripa, Sweden for Repository Design by M. Hood, H. Carlsson, and P.H. Nelson (LBL-9392, SAC-26).

27. Progress with Field Investigations at Stripa by P.A. Witherspoon, N.G.W. Cook, and J.E. Gale (LBL-10559, SAC-27).

28. A Laboratory Assessment of the Use of Borehole Pressure Transients to Measure the Permeability of Fractured Rock Masses by C. Forster and J.E. Gale (LBL-8674, SAC-28).

29. Thermal and Thermomechanical Data for In Situ Heater Experiments at Stripa, Sweden by T. Chan, E. Binnall, P. Nelson, O. Wan, C. Weaver, K. Ang, J. Braley, and M. McEvoy (LBL-11477, SAC-29).

30. The Effect of Radon Transport in Groundwater Upon Gamma Ray Borehole Logs by P.H. Nelson, R. Rachiele, and A. Smith (LBL-11180, SAC-30).

TABLE OF CONTENTS

	Page
PREFACE	iii
LIST OF FIGURES	ix
LIST OF TABLES	xiii
NOMENCLATURE	xv
ABSTRACT	xix
1. INTRODUCTION	1
2. DESCRIPTION OF SAMPLE	4
3. TESTS ON SMALL DIAMETER CORES	10
4. PRELIMINARY FALLING-HEAD PERMEABILITY TESTS	12
5. EXPERIMENTAL PROCEDURES AND APPARATUS	19
5.1 Large Triaxial Testing Machine	19
5.2 Experiment Design	19
5.3 Hydraulic and Load Control Systems	26
5.4 Core Instrumentation	26
5.5 Data Acquisition	31
5.6 Data Reduction	32
6. TEST RESULTS AND INTERPRETATION	33
6.1 Mechanical Behavior	33
6.1.1 Macroscopic Load-Deformation Behavior	33
6.1.2 Decomposition of Load-Deformation Response	41
6.1.2.1 Fractures Perpendicular to the Core Axis	42
6.1.2.2 Fractures Inclined to the Core Axis	49
6.1.2.3 Parameters for Mechanical Closure of Fractures	53
6.1.3 Strain Gauge Data	56
6.1.4 Time-Dependent Mechanical Behavior	59
6.1.4.1 Macroscopic Time-Dependent Deformation	59
6.1.4.2 Time-Dependent Behavior of Individual Fractures	61
6.2 Coupled Hydraulic-Mechanical Behavior	64
6.2.1 Applicability of Darcy's Law	64
6.2.2 Macroscopic Stress-Flow Relationship	67
6.2.3 Relationship Between Flow and Fracture Deformations	72
7. CONCLUSIONS AND RECOMMENDATIONS	76
7.1 Mechanical Behavior	76
7.2 Coupled Hydraulic-Mechanical Behavior	78
ACKNOWLEDGMENTS	80
REFERENCES	81

			Page
APPENDIX	I:	Sample Preparation	84
APPENDIX	II:	Fracture Mapping and Characterization	94
APPENDIX	III:	Petrography of Ultra-Large Core	99
APPENDIX	IV:	Tests on 5.2 cm Diameter Cores	121
APPENDIX	V:	Falling-Head Tests	135
APPENDIX	VI:	Control, Instrumentation and Data Acquisition Equipment	149
APPENDIX	VII:	Test Data on Engineering Units	165

LIST OF FIGURES

		Page
1.1	Ultra-large Stripa core	3
2.1	Location of core hole	5
2.2	In-situ sample orientation	5
2.3	Fractures in core	6
2.4	Surface of fracture B	8
2.5	Surface map - fracture B	8
4.1	Schematic of falling-head permeability test	13
4.2	Borehole fracture log, injection intervals and falling-head test results	14
4.3	External seepage from central borehole	15
5.1	Large triaxial testing machine	20
5.2	Schematic of test arrangement	21
5.3	Axial stress-history applied to sample	24
5.4	Data gathering and control schematic	27
5.5	Instrument locations - Stripa core	29
5.6	Instrumented Stripa core	30
6.1	Macroscopic stress-strain record, with calculated strain at center of core	34
6.2	Post-failure fracture map	36
6.3	Plot of downward normal vector to plane of sample top	37
6.4	Macroscopic axial and circumferential stress-strain data	40
6.5	Calculated overall displacements at 80°, 90°, and 130°	43
6.6	Fracture C displacements (E = 60 GPa)	43
6.7	Fracture B displacements (E = 60 GPa)	45
6.8	Fracture A displacements (E = 60 GPa)	45
6.9	Calculated macroscopic and fracture displacements at 310° orientation (E = 60 GPa)	46

Page

6.10 Calculated macroscopic and fracture displacements at 190° orientation (E = 60 GPa) 46

6.11 Calculated macroscopic and fracture displacements at 80° orientation (E = 60 GPa) 47

6.12 Plots of downward normal vectors to fracture displacement planes 48

6.13 Vertical displacements on fractures E and F (E = 60 GPa) . . . 50

6.14 Vertical and horizontal displacements on fracture D (E = 60 GPa) 52

6.15 Calculated normal displacement versus shear stress for fracture D 54

6.16 Calculated normal displacement versus normal stress for fracture D 54

6.17 Stress-strain data from strain gauges opposite inclined fractures 57

6.18 Stress-strain data from strain gauges near inclined fractures . 57

6.19 Axial stress versus time since start of load ramps 60

6.20 Macroscopic axial strain versus time 60

6.21 Circumferential strain versus time 60

6.22 Calculated center displacement versus time for fracture A (E = 60 GPa) 62

6.23 Calculated center displacement versus time for fracture B (E = 60 GPa) 62

6.24 Calculated center displacement versus time for fracture C (E = 60 GPa) 62

6.25 Calculated shear displacement versus time for fracture D (E = 60 GPa) 63

6.26 Calculated normal displacement versus time for fracture D (E = 60 GPa) 63

6.27 Measured overall flow rate versus differential pressure head . 66

Page

6.28 Calculated single-fracture hydraulic conductivity versus axial stress, compared with previously published data 71

6.29 Measured and calculated overall flows-per-unit-head versus axial stress 74

A1.1 Core as recovered from rib of entry 85

A1.2 Dimensions of core before capping 87

A1.3 Top cap reinforcement 89

A1.4 Bottom cap reinforcement 90

A1.5 Dimensions of capped core 93

A2.1 Stereograph of major fracture poles in Stripa core 98

A3.1 Chlorite-filled fracture from top surface of ultra-large core . 111

A3.2 Fractures associated with fracture B of ultra-large core . . . 113

A3.3 Veinlets of sericite, with lesser chlorite, forming in perithitic microcline grain; near dominant fracture B of ultra-large core 115

A3.4 Pervasive fracturing and alteration of matrix minerals to sericite and chlorite 116

A3.5 Fault gouge 118

A4.1 Typical uniaxial compression test record for intact Stripa granite 124

A4.2 Mohr diagram for intact Stripa granite 127

A4.3 Mohr diagram for healed fractures in Stripa granite 127

A4.4 Key to figures A4.5 - A4.11 132

A4.5 Map of Sample S1 133

A4.6 Map of Sample S2 133

A4.7 Map of Sample S3 133

A4.8 Map of Sample S4 133

A4.9 Map of Sample T1 134

Page

A4.10 Map of Sample T2 134

A4.11 Map of Sample S5 134

A5.1 Borehole packer unit for falling-head tests 136

A5.2 Results of falling-head tests Nos. 1 and 7 139

A5.3 Results of falling-head tests Nos. 2 and 9 139

A5.4 Results of falling-head tests Nos. 3, 10 and 11 140

A5.5 Results of falling-head tests Nos. 4 and 8 140

A5.6 Results of falling-head tests Nos. 5 and 6 141

A5.7 Results of falling-head tests Nos. 12 and 13 142

A5.8 Results of falling-head tests Nos. 3, 14, and 16 142

A6.1 Mounted LVDT 155

A6.2 Exploded view of LVDT unit 156

A6.3 Assembled LVDT unit 157

A6.4 LVDT orientation references 157

A6.5 LVDT for measuring axial deformation 159

A6.6 Girth gauge 161

A6.7 LVDT damaged by corrosion 163

LIST OF TABLES

		Page
3.1	Uniaxial and triaxial test data for naturally fractured and intact 5.2 cm diameter cores of Stripa granite	11
4.1	Inferred flow-paths from various sections of the center borehole	16
5.1	Axial-stress levels and differential pressures for permeability tests	24
6.1	Psuedo-elastic properties computed from overall stress-strain record of Fig. 6.5	40
6.2	Parameters for mechanical closure of fractures	55
6.3	Results and computed overall hydraulic parameters from stress-flow tests on ultra-large Stripa core	65
6.4	Computation of overall flow parameters based on parallel-plate models of fractures B and D	70
A1.1	Concrete for Stripa core end caps	91
A2.1	Ultra-large Stripa core - axial borehole log	96
A3.1	Electron microprobe analysis of chlorite grains from sample of Stripa granite from 4.60 m level in borehole N1 in time-scale drift	100
A3.2	Excerpts of chemical analyses of some representative biotites from granitic rocks	100
A3.3	X-ray fluorescence major element analysis of relatively fracture-free sample from ~0.4 m level in core OH1 BH E7 in full-scale drift	102
A3.4	X-ray diffraction peaks of whole fracture filling from fracture C, ultra-large core	103
A3.5	X-ray diffraction peaks of chlorite-enriched separate from fracture forming top surface of ultra-large core	104
A3.6	Errors in d-spacing read from diffraction films	106
A4.1	Description of 5.2 cm diameter sample	122
A4.2	Results of indirect tension tests on small core sections	124
A4.3	Summary of previous laboratory strength data for intact Stripa granite	128

Page

A5.1 Flow parameters computed from falling-head test results 145

A5.2 Approximate matrix permeabilities 148

A6.1 Principal instrumentation and control equipment 150

A6.2 Strain gauge mounting procedure 153

A6.3 LVDT locations and orientations 158

A6.4 Data channel assignments 164

NOMENCLATURE

A	Angle between fracture and horizontal
A	Constant (fracture closure parameter)
A	Cross-sectional area of flow
A	Cross-sectional area of core
A	Distance between LVDT anchors
A_m	Initial head (extrapolated)
A_s	Area of standpipe
B	Angle between fracture plane and LVDT axis
c	Cohesion intercept (Mohr envelope)
d	d-spacing (x-ray diffraction)
E	Young's modulus
g	Acceleration due to gravity
h_l	Head-loss
h_m	Hydraulic head
h_o	Initial head
h_z	Corrected head
I_s	Point-load strength index
k	Coefficient of permeability
k_f	Fracture permeability
k_m	Permeability of unstressed rock matrix
k_{rm}	Equivalent rock mass permeability of sample
L	Length of flow
L	Length of interval between packers
P	Axial load
Q	Flow rate

$Q/\Delta h$	Flow-per-unit-head
Re	Reynolds number
r_1	Radius of borehole
r_2	Radius of core
s	Length between packers
t	Time
t	Constant (fracture closure parameter)
t_m	Time
u	Approximate shear displacement
V_{mc}	Maximum aperture closure
x	Angle between fracture plane and core axis
β	Angular coordinate (anti-clockwise from orientation line)
Δd	Error in reading of d-spacing
Δh	Differential hydraulic head
Δv	Change in aperture
Φ	LVDT displacement
ε_θ	Circumferential strain
ε_z	Vertical (axial) strain
Θ	Angular coordinate (clockwise from orientation line)
μ	Dynamic viscosity
ν	Poisson's ratio
ξ	Initial stress
ρ	Fluid density
σ	Stress
σ_1	Axial stress
σ_3	Confining pressure

σ_n	Axial or normal stress
τ	Shear stress
ϕ	Angle of internal friction
ψ	Angle between fracture plane and core axis
2b	Absolute fracture aperture
2θ	Location of x-ray diffraction peak

ABSTRACT

This report presents the results of laboratory tests on a 1 meter diameter by 2 meters high sample of granitic (quartz monzonite) rock from the Stripa mine in Sweden. The tests were designed to study the mechanical and hydraulic properties of the rock. Injection and withdrawal permeability tests were performed at several levels of axial stress using a borehole through the long axis of the core. The sample was pervasively fractured and its behavior under uniaxial compressive stress was very complicated. Its stress-strain behavior at low stresses was generally similar to that of small cores containing single healed fractures. However, this large core failed at a peak stress of 7.55 MPa, much less than the typical strength measured in small cores. The complex failure mechanism included a significant creep component. The sample was highly permeable, with flows-per-unit head ranging from 0.11 to 1.55 cm^2/sec. Initial application of axial load caused a decrease in permeability, but this was followed by rapid increase in conductivity coincident with the failure of the core. The hydraulic regime in the fracture system was too intricate to be satisfactorily modeled by simple analogs based on the observed closure of the principal fractures. The test results contribute to the data base being compiled for the rock mass at the Stripa site, but their proper application will require synthesis of results from several laboratory and in situ test programs.

1. INTRODUCTION

An inactive iron ore mine at Stripa, Sweden is the site of a group of experiments designed to evaluate the suitability of deep granitic rock as repositories for nuclear waste. The work is sponsored by the Swedish-American Cooperative Project on Radioactive Waste Storage in Mined Caverns in Crystalline Rock (Witherspoon and Degerman, 1978). The program has two principal elements: investigation of subsurface hydrology (Gale and Witherspoon, 1979) and study of the thermomechanical response of the rock to heat sources emplaced in the floor of mine entries (Cook and Witherspoon, 1978).

Analysis and interpretation of the data gathered from the large-scale in situ experiments require knowledge of the mechanical and hydraulic properties of the rock mass. Fracture systems in rock play a dominant role in its behavior and, often, as with the mine at Stripa, evaluation of its properties requires the synthesis of data from many different in situ and laboratory techniques. Traditionally, laboratory tests have been performed on samples of rock with dimensions of several centimeters. However, there is convincing evidence that the mechanical properties of rock are size dependent (Jaeger, 1966; Pratt et al., 1972), and the potential for a similar "size effect" in experimental determination of the hydraulic properties of fractures has been observed (Witherspoon et al., 1979). Thus, it is important to obtain measurements on rock samples with dimensions much closer to those of practical concern, namely meters rather than centimeters.

Laboratory tests to investigate the mechanical properties of the Stripa rock (Swan, 1978) and to study flow in fractures (Witherspoon, Wang et al., 1979) have been performed on standard-sized samples, and further investigations

are in progress (Witherspoon, Watkins, et al., 1979). This report presents the results of laboratory tests on a large cylindrical sample of rock from the Stripa mine. Figure 1.1 shows the approximately 1 meter diameter by 2 meters high core after preparation for testing and placement of reinforced concrete end caps.

The objectives of the test program were: 1) to investigate the strength and mechanical behavior of the sample under uniaxial compression, and 2) to study the hydraulic properties (permeability) of the sample, including the coupled relationship between the hydraulic properties and the applied axial stress. Because the sample was highly fractured, both its hydraulic and mechanical properties were complex. It was possible to quantify its general macroscopic properties, but detailed analysis, particularly of the hydraulic properties of the fracture system, was generally restricted to qualitative and semi-quantitative procedures. However, the tests generated a large volume of data that should serve as a valuable resource for further research on the behavior of fractured rock masses.

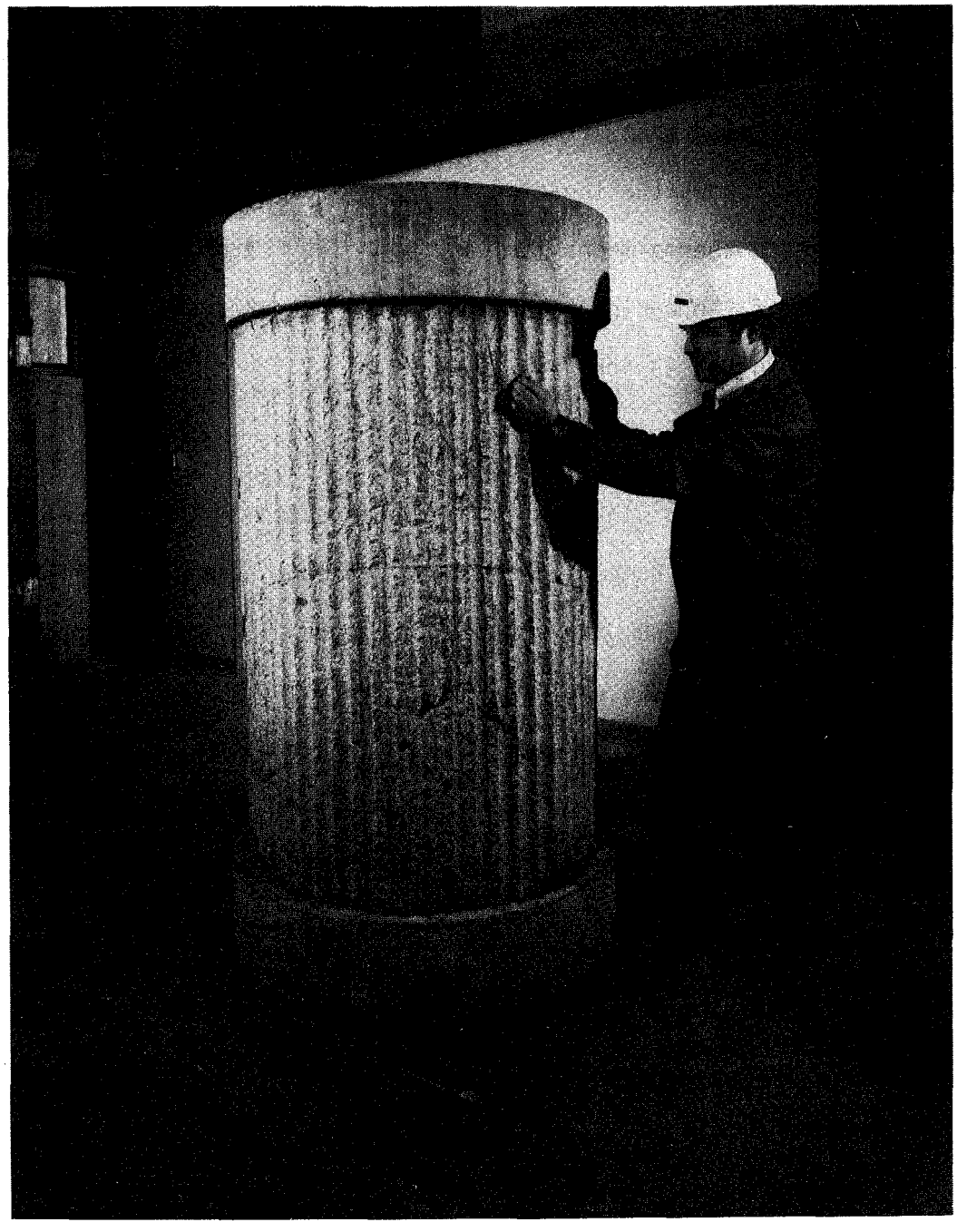

CBB 796-8236

Fig. 1.1 Ultra-large Stripa core.

2. DESCRIPTION OF SAMPLE

The sample was recovered from the granitic formation in the Hagconsult drift at the 360 m level. The core was cut from the rib of the entry by a slot drilling technique such that its long axis was oriented approximately horizontal. Figure 2.1 shows the location of the sampling site relative to the sites of the in-situ thermo-mechanical and hydrology experiments on the 335 m level. Details of the coring technique and of preparation of the sample for testing are given in Appendix I.

The granitic rock in the Stripa mine is pervasively fractured (Thorpe, 1979; Olkiewicz et al., 1979). The sample was intersected by two principal sets of fractures and a large number of secondary discontinuities with lengths and spacings ranging from the scale of the core to the microscopic. Fractures observable by the naked eye were mapped by using a plastic overlay and by logging a 7.62 cm diameter hole drilled through the long axis of the core. These procedures and a detailed description of the fracture geometry and characteristics are given in Appendix II. Figure 2.3 shows the fractures traced on a development of the surfaces of the sample together with the log of the core drilled along the axis of the sample.

There were two dominant fracture sets in the core. One, consisting of the fractures designated A, B and C in Fig. 2.3, formed essentially continuous surfaces oriented approximately normal to the core axis; members of the other, designated D, E and F in Fig. 2.3, were generally discontinuous and were oriented at 25° to 30° to the long axis of the core. Figure 2.2 shows the approximate in situ orientation of the core and dominant fracture sets. The bearing of the core axis was S 14° W and it plunged downward at 15°.

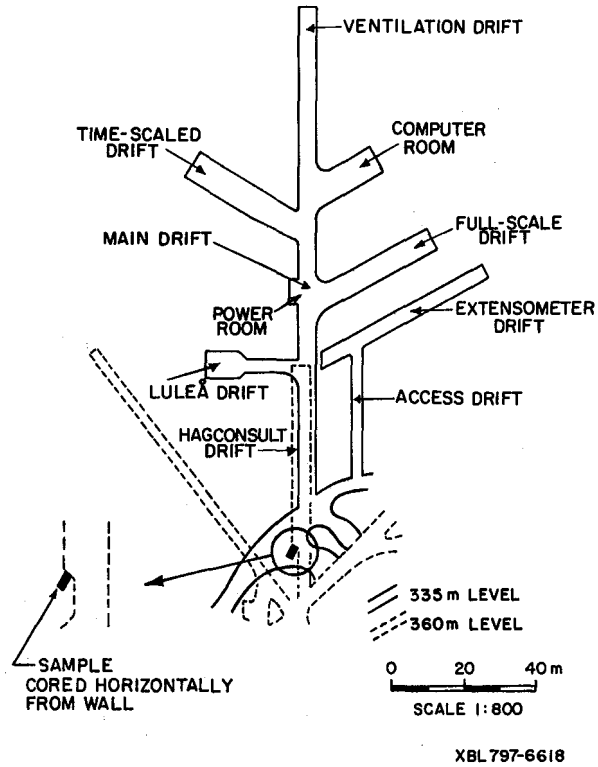

Fig. 2.1 Location of core hole.

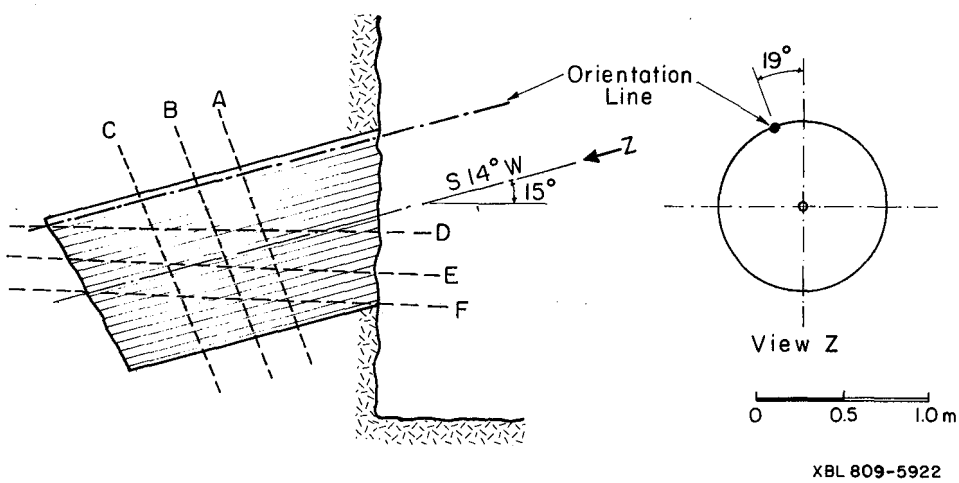

Fig. 2.2 In-situ sample orientation.

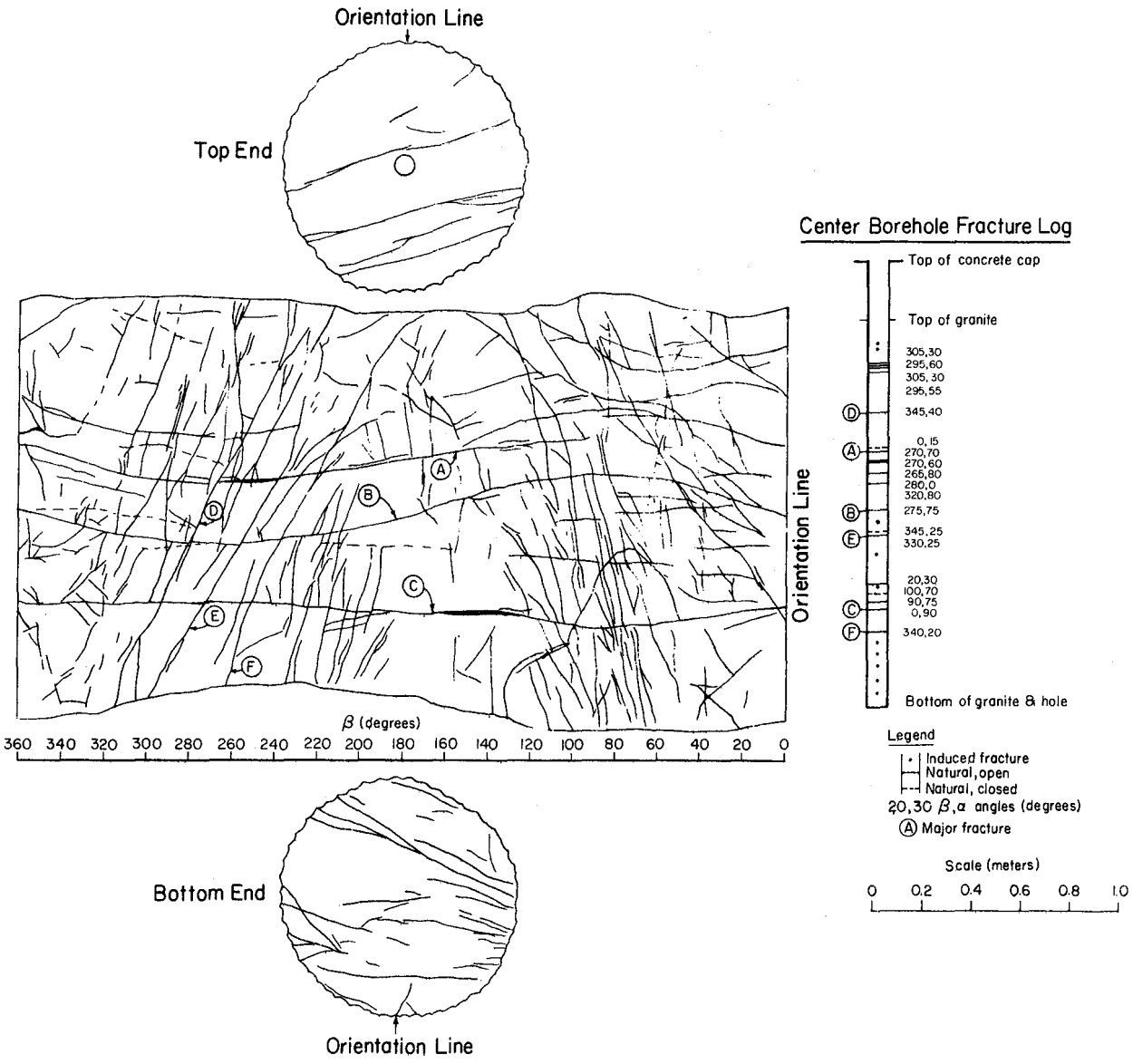

Fig. 2.3 Fractures in core.

An orientation line on the surface of the core was located 341° clockwise (19° anticlockwise) from the top when looking down the core hole. All geometrical relationships in the core were defined relative to its axis and this orientation line.

During preparation, the core was inadvertently separated at fracture B (see Fig. 2.4). The two halves were successfully re-seated so that, to the naked eye, the sample was in the same condition as before the separation. However, significant changes in the hydraulic properties of fracture B must have occurred. While the core was separated, the fracture surface was inspected and mapped. This surface was uniformly coated with a loose brownish dust, which is thought to have been transported into the voids by drilling fluid. There was no depositional pattern in the dust that might suggest localized flow paths through the fracture. Because the dust was considered foreign matter that might have prevented accurate re-seating, it was carefully removed with a vacuum cleaner. This process did not disturb the thin layer of hardened dark green chlorite mineralization adhering to the surfaces of the fracture.

As shown in Fig. 2.5, the surface of fracture B was intersected by traces of the major inclined fractures designated D, E and F in Fig. 2.3. These intersecting fractures formed en-echelon scarps with relief of 1 to 2 cm along one edge of the core (foreground in Fig. 2.4). The height of these scarps diminished across the core and, in the case of fractures E and F, no clear traces were visible on the opposite side (background in Fig. 2.4). This observation is consistent with the external fracture map (Fig. 2.3) that shows these fractures to be discontinuous across the diameter of the core.

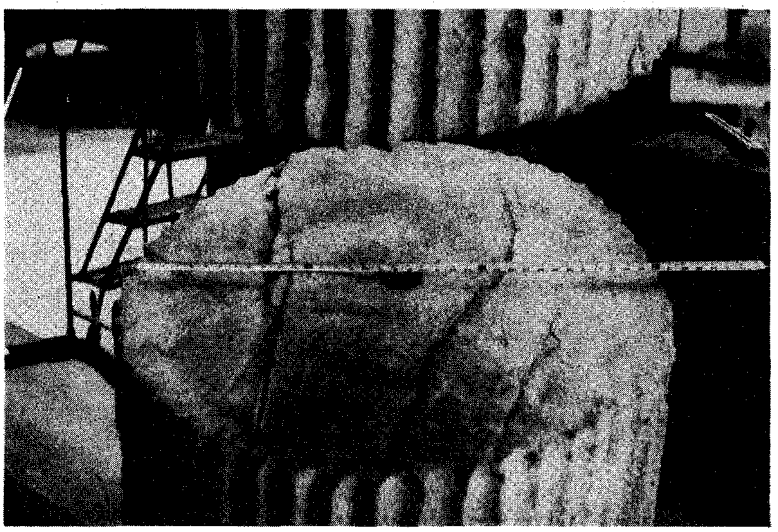

CBB 797-8795

Fig. 2.4 Surface of fracture B.

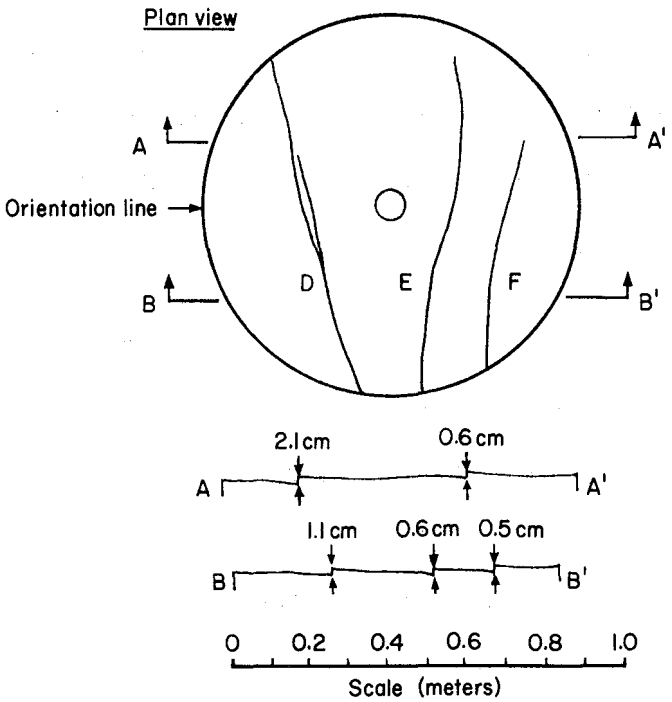

XBL 796-10419

Fig. 2.5 Surface map - fracture B.

The geology of the Stripa mine has been described by Olkiewicz et al. (1979). According to these authors, the sampling site shown in Fig. 2.1 is about 20 m horizontally from where the granite contacts the synclinal leptite formation that contains the ore body. The rock in which the thermo-mechanical and hydrology experiments are located was found to be principally composed of massive granites and monzogranites. As part of the work described in this report, a petrographic study was conducted on the ultra-large core to determine its specific mineral composition. The results are reported in Appendix III. The major minerals of the rock matrix were found to be quartz, plagioclase and microcline. Their relative abundance (73.8% silica) indicated that the sample was formed of quartz monzonite rather than a true granite. The specific gravity of the rock matrix was 2.65. The fracture-filling minerals were predominately chlorite and sericite. The two principal fracture sets were not generally distinguishable on the basis of these minerals. However, in some portions of the inclined fractures (D, E, and F) where a significant thickening of the filling material occurred, calcite was prominent.

3. TESTS ON SMALL DIAMETER CORES

To provide a basis for design of the test program for the ultra-large core and to assess the range and sensitivity requirements of the instrumentation, a series of strength tests was performed on 5.2 cm diameter cores of Stripa granite. These small diameter samples were obtained from boreholes drilled in the mine as part of the general research activities at Stripa (Kurfurst et al., 1978). Because they were sampled from several different locations in the mine, they were not specifically representative of the rock from which the core was extracted, but they were considered sufficiently similar for the purpose of this study. A series of compressive and tensile tests was performed on intact specimens and samples containing fractures at various orientations to the long axis of the sample. The principal results are summarized in Table 3.1. Test procedures are described in Appendix IV, which also compares these data with results of tests performed by others on small intact samples of Stripa granite. As a linear approximation, the lower-bound Mohr's envelope for the intact rock was found to have a cohesion intercept $c = 2.50$ MPa and an angle of friction, ϕ, of 60°. For samples containing well-filled, healed fractures, these parameters were typically $c = 7.3$ MPa and $\phi = 55°$. The average elastic modulus measured in compression tests was about 55 GPa for intact samples, and similar results were obtained for samples containing well-healed fractures.

Table 3.1. Uniaxial and triaxial test data for naturally fractured and intact Stripa granite (52 mm diam. core).

Specimen number	Type of test	Confining pressure, σ_3 MPa	Failure stress, σ_1 (MPa)	Tangent modulus (GPa)	Total strain at failure (%)	Initial nonlinear strain (%)
Fractured specimens						
S1	Triaxial comp.	6.90	247.8	58.81	0.50	0.06
S2	Triaxial comp.	3.45	210.5	56.48	0.47	0.10
S3	Triaxial comp.	0	82.2	53.16	0.30	0.07
S4	Uniaxial comp.	0	156.6	74.61	0.42	0.14
S5	Triaxial comp.	6.90	151.2	46.06	0.41	0.08
T1	Direct tension	--	2.6	--	--	--
T2	Direct tension	--	4.1	--	--	--
Intact specimens						
S6	Direct tension	--	9.7	--	--	--
S7	Direct tension	--	7.1	--	--	--
S8	Triaxial comp.	6.90	329.4	48.04	0.72	0.04
S9	Triaxial comp.	3.45	264.2	52.86	0.63	0.12
S10	Uniaxial comp.	0	208.2	52.81	0.49	0.06
S11	Uniaxial comp.	0	178.3	54.54	0.48	0.12

4. PRELIMINARY FALLING HEAD PERMEABILITY TESTS

Because of the pervasive fractures in the ultra-large Stripa core, a series of preliminary tests were performed to assess the general magnitude of flow rates that would be encountered in the final test configuration. In addition, it was important to identify the primary flow paths through the rock and to estimate the relative permeabilities of the different fracture zones in the core. For these purposes a simple falling-head test, shown schematically in Fig. 4.1, was used. Data for computing injection head and flow rate were taken directly from observations of water-level change in the standpipe. Several tests were performed with the rubber packers located over different lengths and different sections of the borehole. The principal results are summarized in Figs. 4.2 and 4.3 and Table 4.1. Details of the test procedure, data analysis, and a more extensive discussion of the results are presented in Appendix V.

Figure 4.2 presents the results of the falling-head tests in the normalized form $Q/\Delta h$ (flow-per-unit-head) where Q is flow rate and Δh is the head loss between the injection interval and the periphery of the sample. The figure also shows the relationship between the test intervals and the major fractures logged in the center borehole. The test intervals were overlapped to determine the relative flow contributions of each major fracture. Values of flow-per-unit head range from 2×10^{-7} cm^2/sec in test interval No. 1, where the rock is free of significant fractures, to approximately 1.0 cm^2/sec in interval No. 2, which includes fracture B. During each falling-head test, observations were made of the pattern of seepage on the surface of the core. Fig. 4.3 was developed by superposition of the observations for each test; thus, it is an approximate representation of the pattern that would

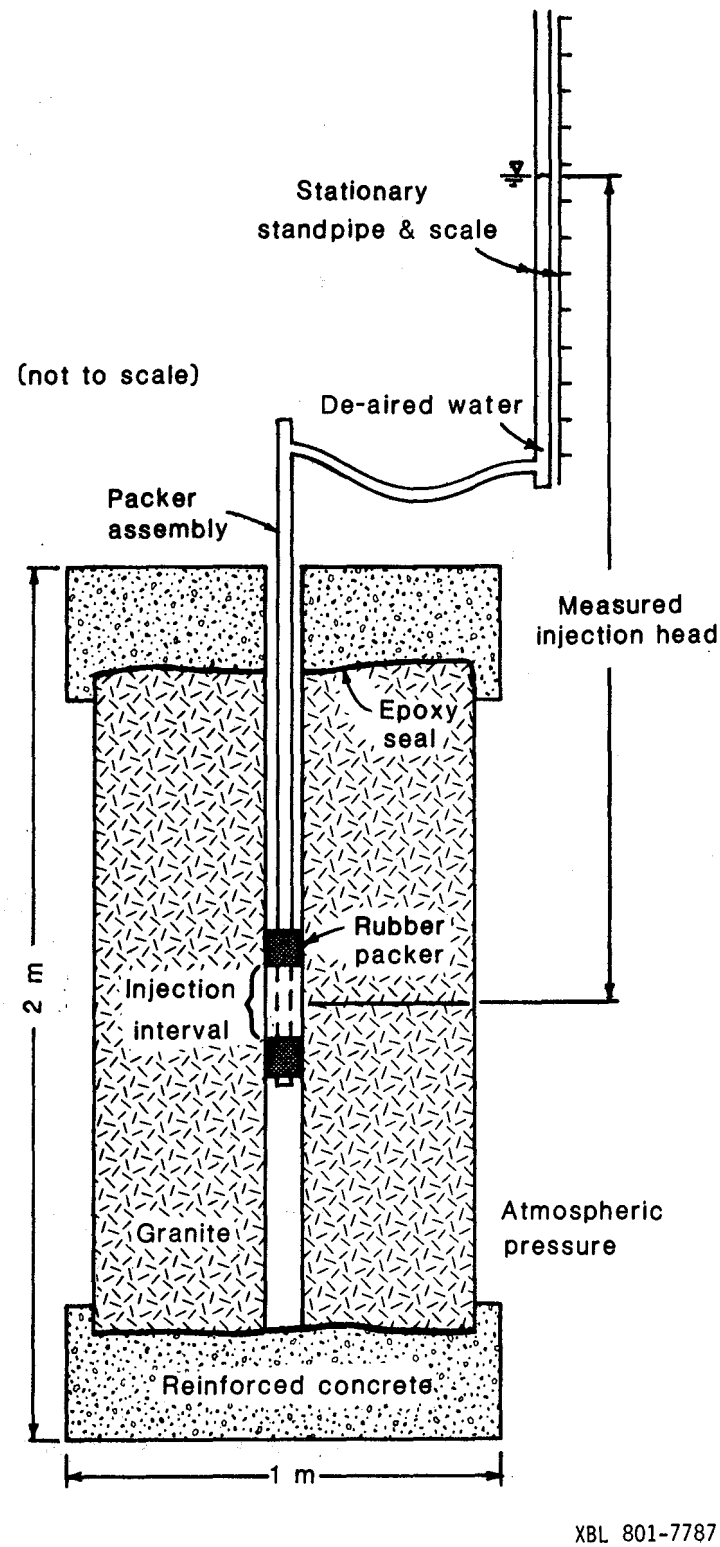

Fig. 4.1 Schematic of falling-head permeability test.

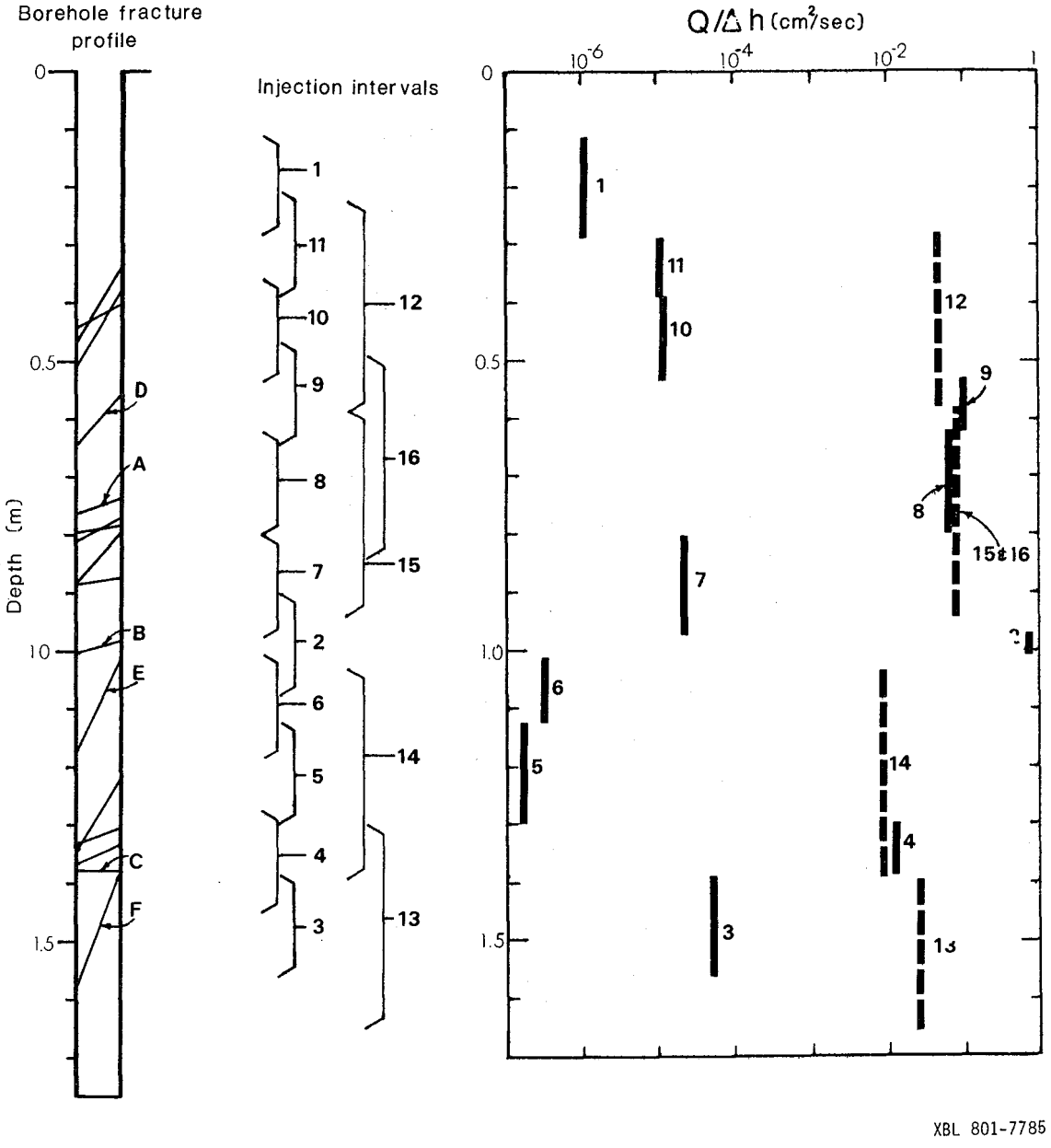

Fig. 4.2 Borehole fracture log, injection intervals and falling-head test results. Long-interval tests are shown by broken line.

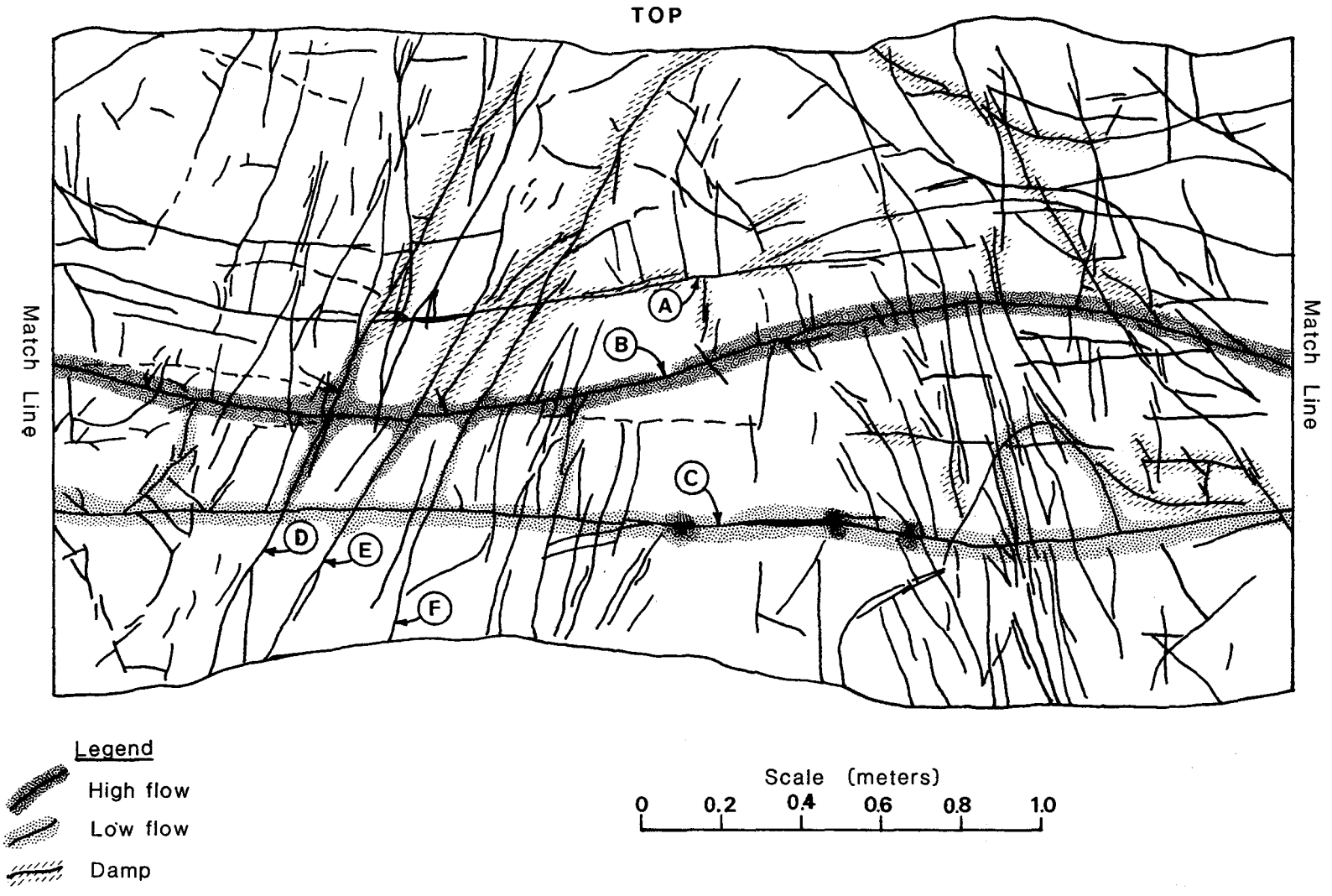

Fig. 4.3 Seepage at surface of core from injection into center borehole.

Table 4.1. Inferred flowpaths from various sections of the center borehole.

Test No.	Borehole interval (m)	Fracture flowpaths*
1	0.114 - 0.286	(D7)-D-B
2	0.904 - 1.076	B
3	1.390 - 1.562	(F)-C-E(F)-B
4	1.278 - 1.450	C-EF-B
5	1.124 - 1.300	(E')-B
6	1.010 - 1.186	(E)-B
7	0.800 - 0.976	(E')?-A
8	0.624 - 0.800	(A)-D-B-DE-C
9	0.470 - 0.646	D-B-DE-C
10	0.360 - 0.536	(D')-(D)-B-(D)(E)-C
11	0.214 - 0.390	(D')-(D)-(B)-(D)(E)-C
12	0.229 - 0.581	(D)-B-F
13	1.304 - 1.656	C-D(E)(F)-B
14	1.043 - 1.395	CC'-(E)-B
15	0.590 - 0.942	D-B-DEF-C
16	0.492 - 0.844	(A)-FE-B-DEF-C

*Explanation:

X - flow on major fracture "X," as delineated by Fig. 4.3.

X' - minor fracture parallel to major fracture "X," but not necessarily visible on exterior of core; may also indicate seepage through intact rock onto fracture "X."

(X) - inferred path - flow does not exit on fracture "X."

XY - flow on parallel fractures "X" & "Y," with majority of flow on "X."

occur during flow into the entire length of the borehole. Individual flowpaths from discrete sections of the borehole can be inferred from these results and are presented in Table 4.1.

Analysis of the results indicated that fracture B, opened during sample preparation, was the dominant flowpath influencing the hydraulic regime in the core, and that the fractures were hydraulically interconnected in a complex manner. In addition, there is evidence that flowpaths within a specific fracture do not have simple geometries. It is reasonable to assume that the fracture-filling materials form impermeable contact zones over some portions of the fracture surfaces and that flowpaths are influenced by the presence of the linear scarp-like features (Fig. 2.4) formed where one fracture is offset by a member of another fracture set. These effects were seen where water exited from the core in a jet-like fashion, such as at the isolated high-flow zones on fracture C shown in Fig. 4.3.

Analysis of the falling-head test data provided estimates of the coefficient of permeability of the unstressed rock matrix (k_m). In this context the term "matrix" means an interval in the borehole that was not intersected by a fracture that could be identified as a major flow conduit. It is not intended to imply that these portions of the sample were totally free of discontinuities. Estimated values of k_m ranged from 10^{-5} to 10^{-7} cm/sec. Because of uncertainties regarding boundary conditions in the falling-head tests and the simplifying assumptions made in the analyses, the test results are primarily qualitative. Also, the falling-head tests were performed under zero applied load. Changes in the relative conductivity of the flowpaths were anticipated when the core was later subjected to axial

stress. In general terms, fractures oriented normal to the axis of a core close under axial load, while steeply inclined fractures exhibit shear dilatancy. However, the falling-head tests provide useful data regarding the general hydraulic characteristics of the core, the probable geometries of the principal flowpaths, and at least a first-order estimate of fracture conductivities and matrix permeability.

5. EXPERIMENTAL PROCEDURES AND APPARATUS

5.1 Large Triaxial Testing Machine

The Stripa core was tested at the University of California's Rockfill Testing Facility in Richmond, California. Figure 5.1 shows the large triaxial vessel being positioned over the core. The equipment in the lower left was used to control water pressure during permeability testing. The triaxial vessel was originally designed for testing rockfill materials (Becker, et al., 1972). The vessel can accommodate cylindrical samples up to approximately 1 meter diameter by 2.5 meters high. Maximum working pressure in the vessel is 5.2 MPa. Axial (deviatoric) loads are applied to the sample through a 45.7 cm diameter piston driven by a servo-controlled hydraulic actuator with a 106.7 cm internal diameter. Maximum axial load capacity is 17.8 MN.

5.2 Experiment Design

The test procedure was designed to study both the load-deformation behavior on the sample and its hydraulic characteristics. The test arrangement is shown schematically in Fig. 5.2.

The permeability of the sample was studied in two modes: (1) divergent, steady-state flow outward from the center borehole through the rock into the triaxial vessel (injection tests) and (2) convergent, steady-state flow from the triaxial vessel into the central borehole (withdrawal tests). To maintain uniform hydraulic boundary conditions around the sample and to eliminate air trapped in the flowpaths through the sample, the tests were performed with the triaxial vessel filled with pressurized water.

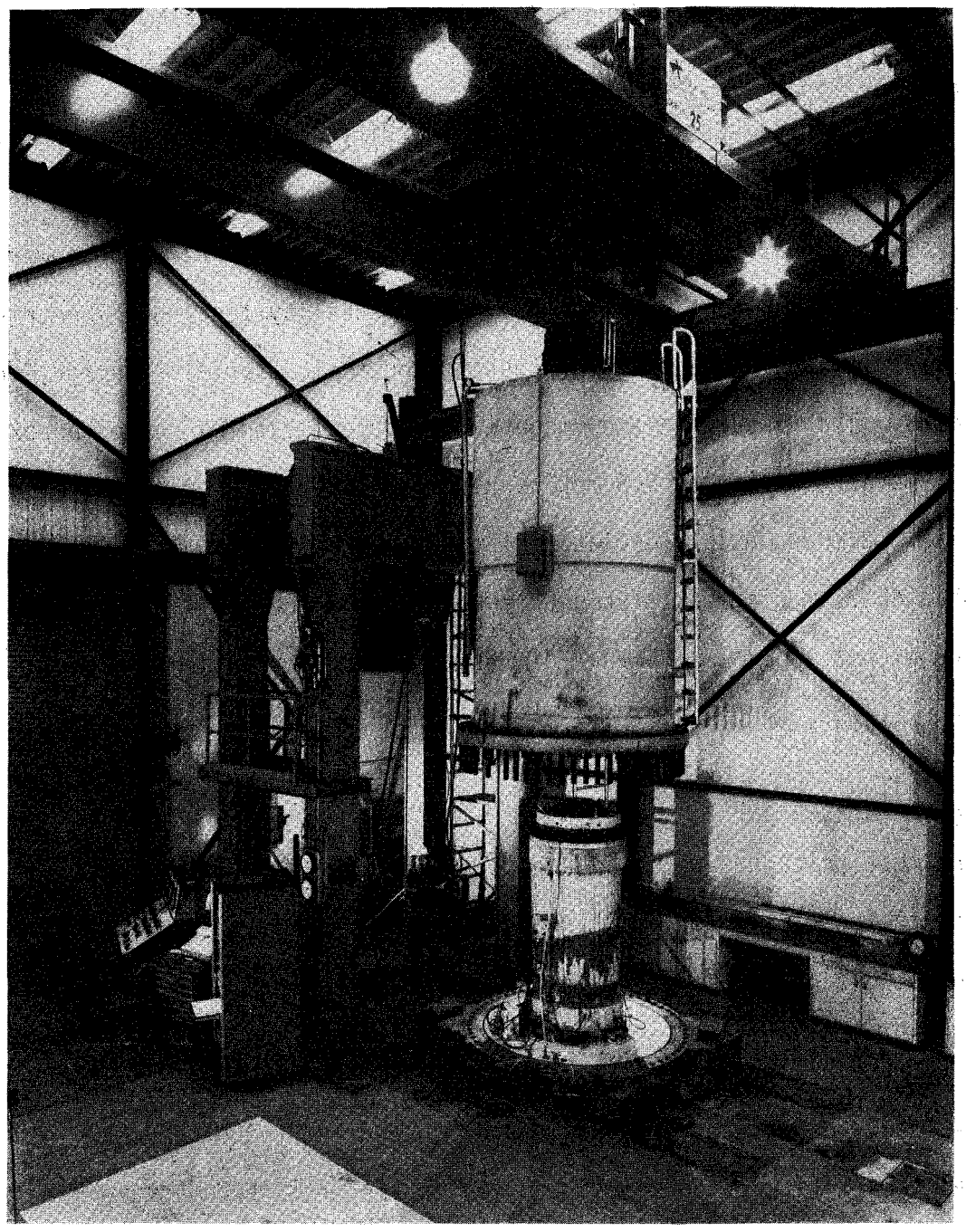

CBB 802-2028

Fig. 5.1 Large triaxial testing machine.

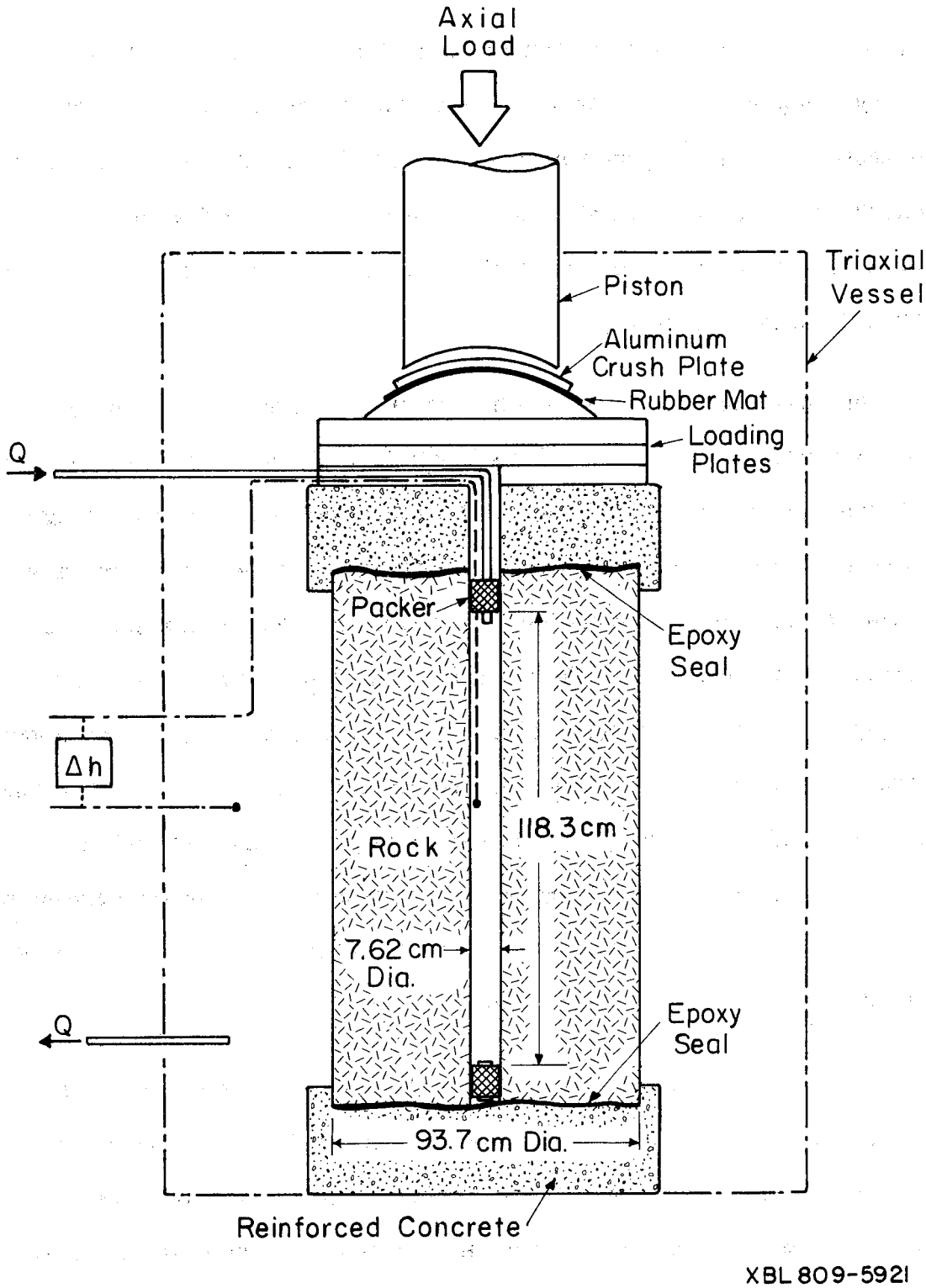

Fig. 5.2 Schematic of test arrangement.

The vessel was initially filled from the local domestic supply and de-aired by applying a vacuum to the top of the vessel for a period of several hours. To keep any remaining air in solution, the vessel was then pressurized to approximately 1400 kPa. To saturate the sample, this pressure was maintained for 24 hours before testing started and held close to 1400 kPa throughout the test program.

For the injection tests, de-aired water was pumped through a pipe passing through the triaxial vessel wall and into the borehole. As shown in Fig. 5.2, the top and bottom of the borehole were sealed by rubber packers. Water flowing through the rock into the vessel was carried away through a second pipe equipped with a back-pressure regulator set to maintain a constant pressure in the vessel. Steady-state conditions were achieved by regulating the injection pressure so as to maintain a constant, predetermined differential head, Δh, between the pressure in the borehole and that in the vessel. This head difference was measured between two small-diameter, no-flow monitoring tubes. One tube was carried through the upper packer in the borehole, terminating at the mid-height of the sample, and the other was connected directly to the inside of the vessel.

At the start of each series of divergent tests, de-aired water was injected into the sample under a very low differential head between the borehole and the triaxial vessel. The differential pressure was then increased to the desired test value and the equipment adjusted to establish steady-state flow conditions. Values of differential head, flow rate, and axial load recorded under these conditions were used to analyze the permeability characteristics of the sample. Subsequent divergent permeability

tests in a series were then performed in a similar manner at the same axial stress level after adjusting the differential head to a new, pre-selected value. After completing a series of divergent tests, the flow through the sample was carefully reduced to zero before reversing the direction of flow and initiating convergent permeability tests, which were conducted similarly to the divergent tests. As discussed in Appendix VI, because of the high permeability of the Stripa core and the characteristics of the fluid control equipment, considerable difficulty was experienced in achieving controlled steady-state conditions for differential heads in excess of approximately 40 kPa. This limited the number of permeability tests performed at each axial stress level to those listed in Table 5.1. As shown in Fig. 5.3, the time required to perform a series of permeability tests at a given stress level varied between 1.5 and 3 hours so that the total duration of testing exceeded 10 hours. For convergent flow conditions, a similar procedure was used, with water being injected into the triaxial vessel and withdrawn from the top of the borehole.

The mechanical properties of fractured rock and the hydraulic properties of fractures are sensitive to effective stress history (Jaeger and Cook, 1976; Witherspoon, Amick, et al., 1979). It was, therefore, necessary to design the tests so that water pressures induced in the void spaces within the core during permeability tests were small relative to the total axial stress applied to the sample. Based on practical considerations related to the resolution of the pressure control and flow measuring equipment, a limit of 350 kPa was set for the differential pressure applied between the center borehole and the exterior of the core. During the performance of the tests, the maximum differential pressure actually applied was 41.3 kPa. Thus

Table 5.1. Axial-stress levels and differential pressures for permeability tests.

Test No.	Axial Stress Level* (MPa)	Test Mode	Nominal Differential Pressure** (kPa)
1	0	Divergent	3.4
	0	Divergent	3.4
2	0.85	Divergent	10.3
	0.85	Convergent	-17.2
	2.89	Divergent	15.9
	2.89	Divergent	27.6
3	2.89	Divergent	17.9
	2.89	Convergent	-10.3
	5.56	Divergent	41.3
	5.56	Divergent	20.7
4	5.56	Convergent	-20.7
	5.56	Convergent	-41.3
5	7.40	Divergent	10.3

*Assumes cross-sectional area of 6940 cm^2.

**Actual (measured) values varied--see Table 6.3.

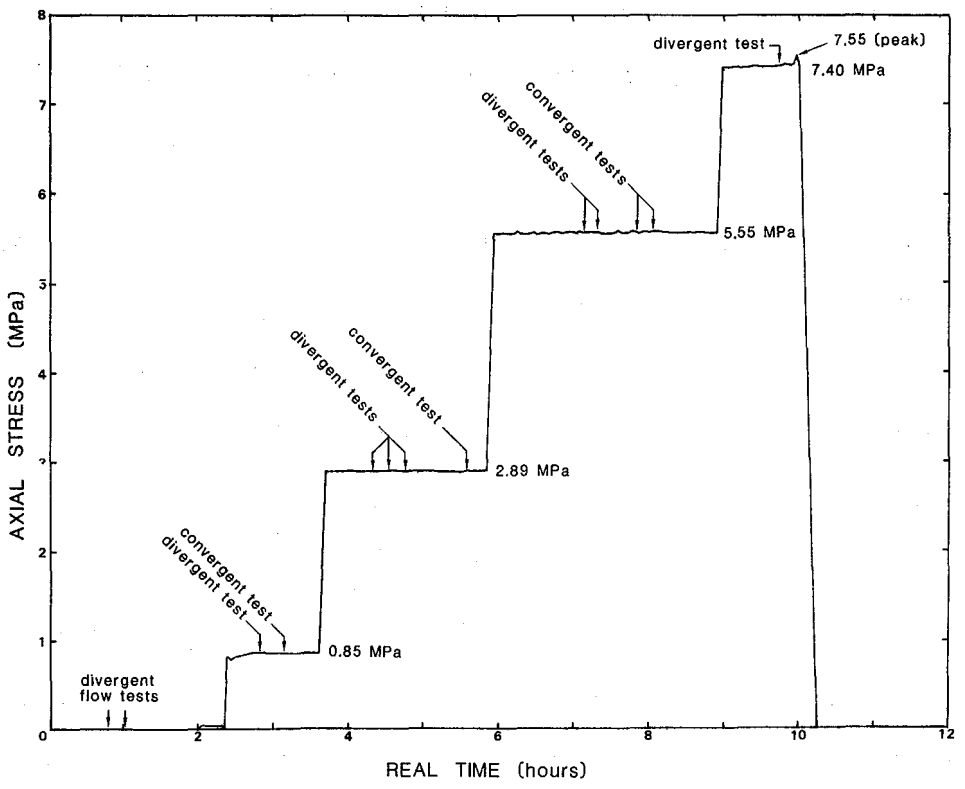

Fig. 5.3 Axial stress history applied to sample.

changes in effective stress induced during the permeability tests were judged to have had minimal influence on the experimental results.

Using the above procedures, the test program took the form of a modified unconfined compressive strength test in which the continuous monotonic increase in axial loading was interrupted while the load was held constant and permeability tests performed. In this way it was possible to study both the stress-strain characteristics of the sample and the relationship between axial stress and permeability (stress-flow characteristics).

This procedure is similar to that followed by previous investigators such as Bernaix (1969), Witherspoon et al. (1977), Iwai (1976), and Gale (1975). The axial-stress history applied to the sample is shown in Fig. 5.3. The rate of loading of approximately 0.5 MPa/min was chosen in general accordance with the guidelines of the International Society for Rock Mechanics (ISRM) for triaxial strength-testing of rock specimens (ISRM, 1978). Selection of the axial stress amplitudes at which the load was held constant for permeability tests was based on the anticipated form of the stress-permeability relationship and the estimated strength of the core. Because the sample was tested in unconfined compression, it was anticipated that the presence of the steeply inclined fractures D, E, and F would result in the sample being considerably weaker than indicated by strength tests on small-diameter samples of intact rock. For these reasons, permeability tests were conducted at several relatively modest axial stress levels to ensure that adequate permeability data were obtained. The nominal stress-levels at which these tests were conducted are listed in Table 5.1. Permeability tests at higher axial stresses and during repeated cycles of loading and

unloading were originally planned but were precluded by gross shear failure of the sample, which occurred at a peak axial stress of 7.55 MPa (Fig. 5.3).

5.3 Hydraulic and Load Control Systems

Figure 5.4 shows a schematic representation of the data gathering and control equipment used for the test program. De-aired water for the permeability tests was provided by an air-actuated reciprocating pump. The differential pressure across the sample was maintained by a pressure regulator controlled by electronic feedback from a differential pressure transducer. The pressure in the triaxial vessel was similarly controlled by feedback from an absolute pressure transducer. The capability to reverse the direction of flow through the sample, for conversion from divergent to convergent permeability tests, was provided by a manually operated four-way valve. Flow rates were measured by an impeller-type flow meter supplemented by a flow totalizer. Auxiliary measurements of water temperature and absolute borehole pressure were also made.

Axial load was applied to the sample by the 45.7 cm diameter loading piston driven by the servo-controlled hydraulic actuator. As shown in Fig. 5.2, loads were transferred from the piston to the sample through a series of crush plates and loading platens designed to minimize eccentric and non-uniform loading. Axial loads were measured by a load-cell mounted in the end of the loading piston. Details of the load and fluid control equipment are given in Appendix VI.

5.4 Core Instrumentation

The core was instrumented to measure its gross axial and radial deformation under uniaxial loading and to monitor the change in aperture of the

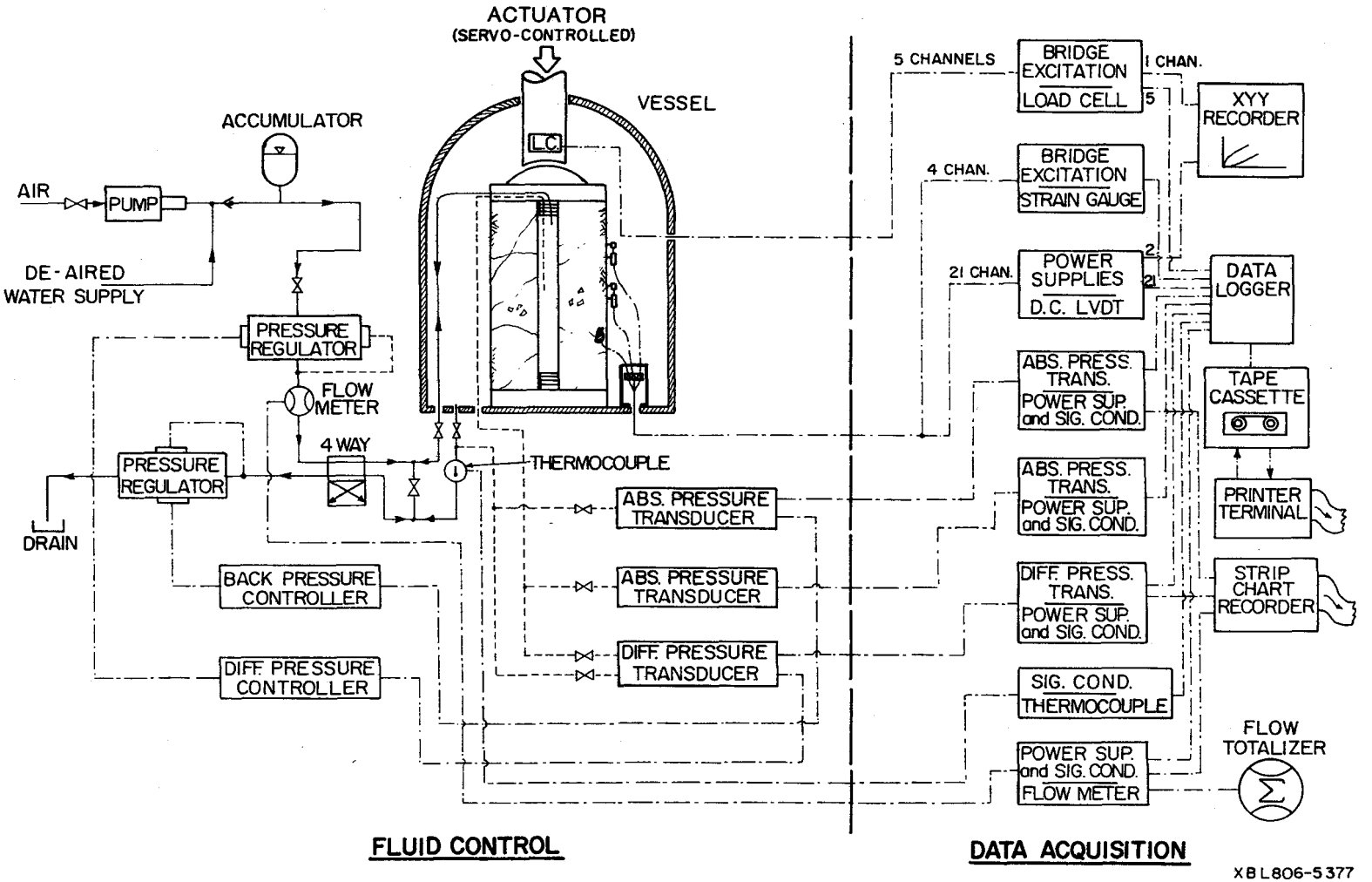

Fig. 5.4 Data gathering and control schematic.

principal fractures during the progress of the test. Linear variable differential transformers (LVDT's) mounted between anchor points drilled into the rock were used to measure these deformations. Because limited space was available for pressure feed-throughs to carry signal conductors thorugh the base of the triaxial vessel, it was not possible to fully instrument all the major fractures in the sample, and only 27 instruments were mounted. Figure 5.5 shows the instrument locations relative to the major surface fractures, and each instrument's identification number. Figure 5.6 is a photograph of the instrumented core. Details of the instrument construction, mounting techniques, and their precise orientations are presented in Appendix VI.

Overall axial deformation was measured by LVDT Nos. 19, 20, and 21 mounted between anchors near the top and bottom of the sample. These anchor locations were selected so as to detect tilting of the top of the sample due to shear deformation on the steeply inclined fractures and to minimize localized effects of fractures near the anchor points. Radial deformation was measured at the mid-height of the sample by LVDT No. 18, which was attached to a girth gauge mounted around the circumference of the core. Displacements across fractures were monitored by LVDT's No. 1 through 17. Their locations were selected according to the anticipated mode of sample deformation, based on the preliminary falling head tests, and on the relative contribution of the major fractures to the permeability of the core. On major fractures, where shear deformation was judged to be probable, orthogonal pairs of LVDT's were mounted to allow resolution of deformations into directions normal and parallel to the fracture plane. Single LVDT's were oriented normal to the fracture plane where significant shear motion was not anticipated or only a first-order check on fracture deformation was required.

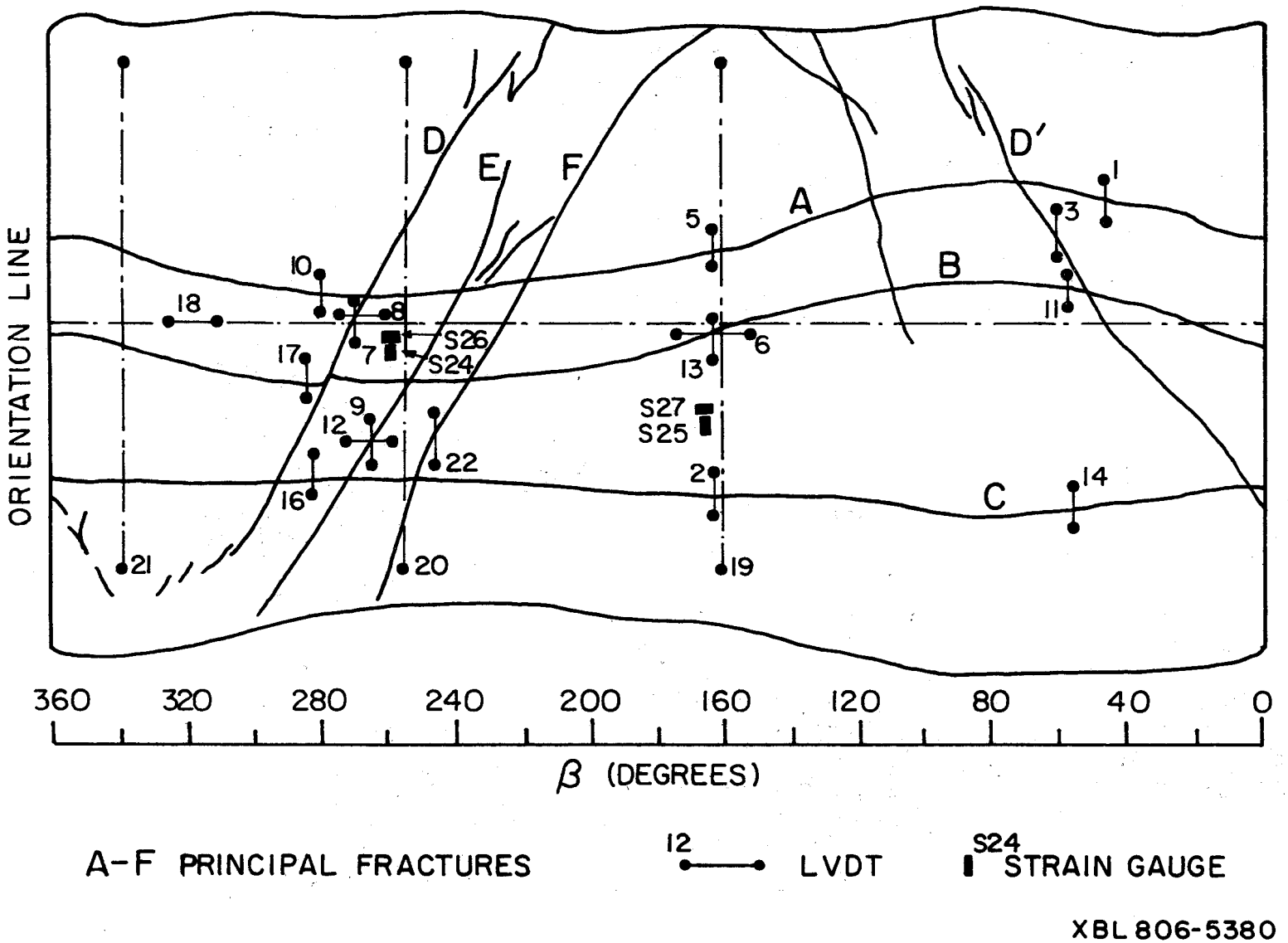

Fig. 5.5 Instrument locations - Stripa core.

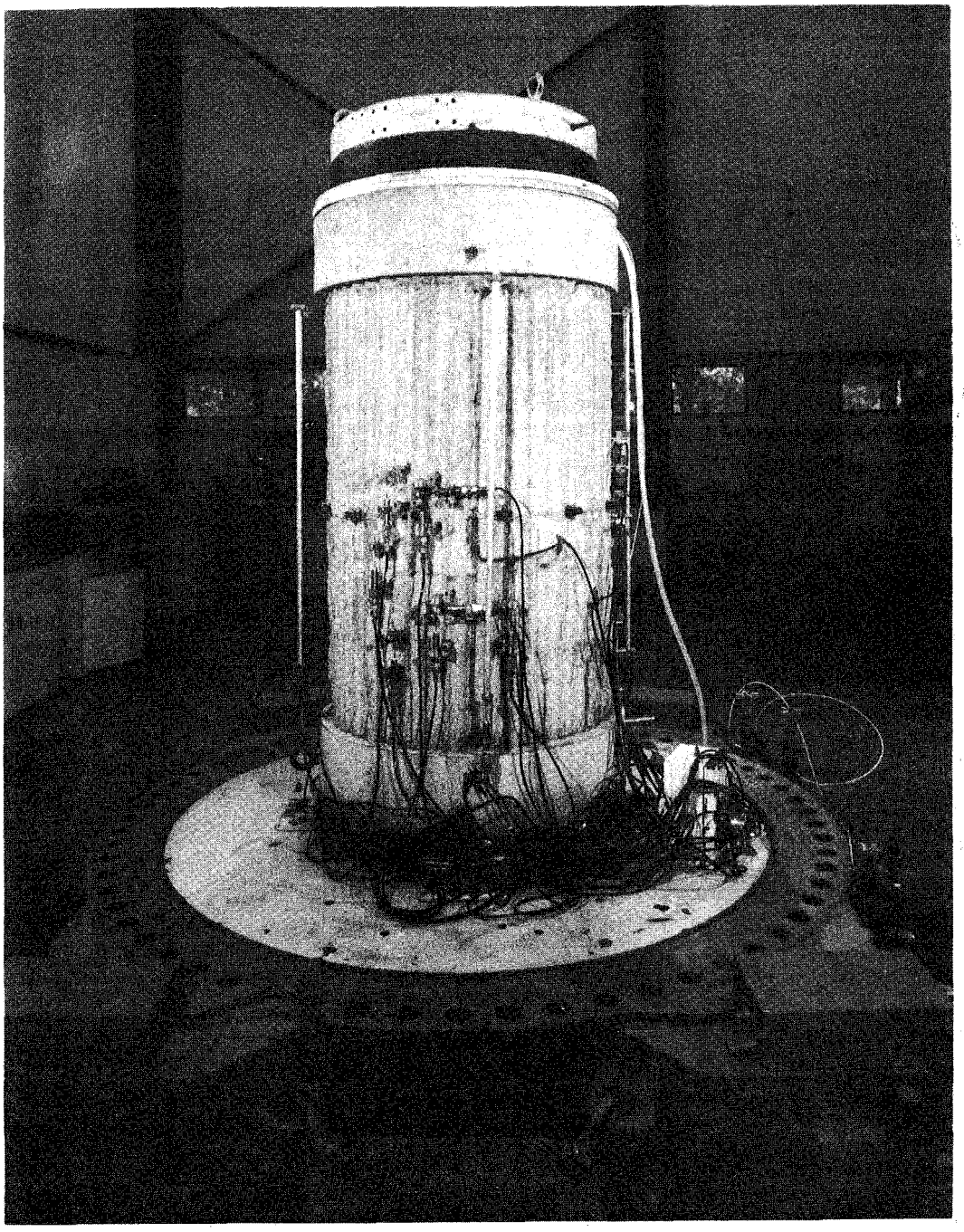

CBB 802-2032

Fig. 5.6 Instrumented core.

Because the sample was so pervasively fractured, there were few places where strain gauges could be suitably mounted to measure localized strains in the rock matrix. Four such gauges, nevertheless, were cemented, at two locations, to the rock. Two (Nos. 25 and 27 in Fig. 5.5) were set where perturbations of the stress field from major fractures were anticipated to be small, while two others, Nos. 24 and 26, were mounted on a spot surrounded by major fractures, so as to provide a general indication of the influence of fractures on the strain field. Axial strain was measured by the vertically oriented gauge in each pair, and circumferential strain by the horizontally oriented gauges.

5.5 Data Acquisition

The data acquisition system used for the test program is shown schematically in Fig. 5.4 and details of the system components are given in Appendix VI. A total of 34 signal channels were scanned using a programmable data logger, and the data was stored in digital form on a magnetic tape cassette. Hardcopy of the data was obtained from a printing terminal that also served as a control console. To provide a direct indication of sample behavior during testing, gross sample deformation was plotted as a function of axial load in real-time analog form on an XYY recorder. Outputs from the flow meter, absolute borehole pressure, and differential pressure transducers were also plotted in analog form on a strip chart recorder. These records were used to obtain mean values of flow rate and differential head for analysis of the permeability tests. Data obtained from the flow meter was supplemented by data recorded manually using a stop watch and the flow totalizer.

Data from the test instrumentation were recorded throughout the test. The maximum scan rate capabilty of the data acquisition system was one complete scan of all 34 data channels in 30 seconds. This scan rate was maintained throughout, except during periods when the axial load was held constant. During these periods, the scan rate was reduced to a maximum of one sweep per minute to limit the data to a manageable quantity.

5.6 Data Reduction

The data gathered during the test program in raw digital voltage form were reduced to engineering units using instrument calibrations obtained from tests performed immediately before the triaxial vessel was closed over the core. These computations were performed using a Tektronix 4051 mini-computer, and the results were stored on magnetic tape in a format suitable for computer-aided data analysis. Copies of this tape have been retained as a source of data for future study. A hardcopy record of the data in the form of engineering units is provided in Appendix VII.

6. TEST RESULTS AND INTERPRETATION

The core's pervasive fracturing made both its mechanical and hydraulic behavior extremely complex. While its general macroscopic behavior could be interpreted by standard analytic procedures, a complete quantitative analysis of the contribution of individual fractures to the overall behavior, and of the relationship between stress-induced changes in fracture geometry and changes in hydraulic conductivity, was not possible. By making certain simplifying assumptions, however, reasonable qualitative and semi-quantitative interpretations of sample behavior could be made. It is important to remember that the core was tested in unconfined, uniaxial compression and that the stress, displacement, and hydraulic boundary conditions of such a test are not generally representative of the boundary conditions in an in situ rock mass. Despite these limitations, the test results provide valuable insights into the behavior, under controlled laboratory conditions, of naturally fractured ultra-large rock samples of much greater complexity than previously attempted. The test results may also be used as a source of empirical data for evaluation and testing of numerical and other analytic models.

6.1 Mechanical Behavior

6.1.1 Macroscopic Load-Deformation Behavior

The macroscopic load-displacement response of the core is illustrated by Fig. 6.1, which plots compressional strain, measured by the axial LVDT units that spanned the height of the core, against the applied axial stress. Assuming plane sections through the core remain planar, the displacement at the center of the core can be calculated by using data from these three LVDTs to define the plane of displacements. This is shown by the solid

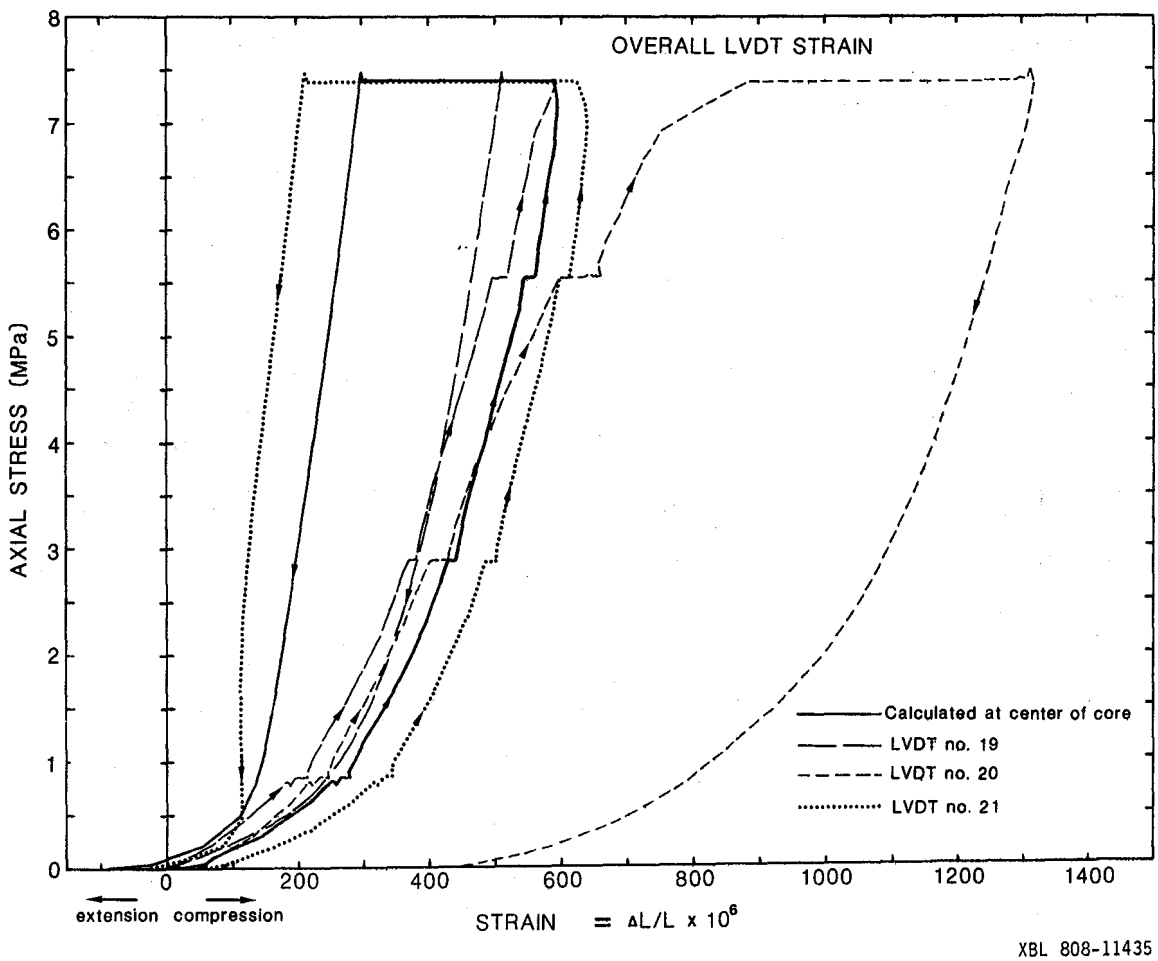

Fig. 6.1 Macroscopic stress-strain record, with calculated strain at center of core.

curve in Fig. 6.1. Strain along the central axis of the sample has been calculated by dividing the displacement by 1.30 meters, the distance between the anchor points for these instruments. According to the figure, the uniaxial strength of the sample was 7.4 MPa and the strain at failure was about 0.06%. Based on this data alone, the pre-failure tangent modulus for the sample as a whole would be 52.3 GPa. Because of the known heterogeneity of the core, however, and the effects of sampling disturbance, these parameters may be low relative to the rock mass behavior in situ.

To better understand the failure mode and the complete load-deformation response, a map of the post-failure fracturing on the surface of the core was prepared (Fig. 6.2). Much of the induced fracturing followed the major pre-existing joints, most notably along inclined fracture D. Near LVDT No. 20, fracture D strongly controlled the fracturing, which is intuitively consistent with the continuity and transmissivity observed in the falling-head tests (see Section 4). On the other side of the core, where the trace of fracture D becomes poorly defined, the induced fracture pattern is less continuous. Thus, it appears that the observed overall failure mode was a combination of shearing failure in the Mohr-Coulomb sense and brittle fracturing typical of uniaxial failure of intact rock specimens. Determination of which mechanism predominated is difficult due to lack of displacement data from the "brittle" zone of the core opposite LVDT No. 20. Based strictly on the three axial LVDT displacements, however, it appears likely that slip along D caused appreciable tilting of the sample. An indication of this is given in Fig 6.3, which plots the horizontal-direction cosines, of the downward normal vector to the plane formed by the top of the sample. Assuming the plane defined by the three LVDTs was perfectly horizontal prior

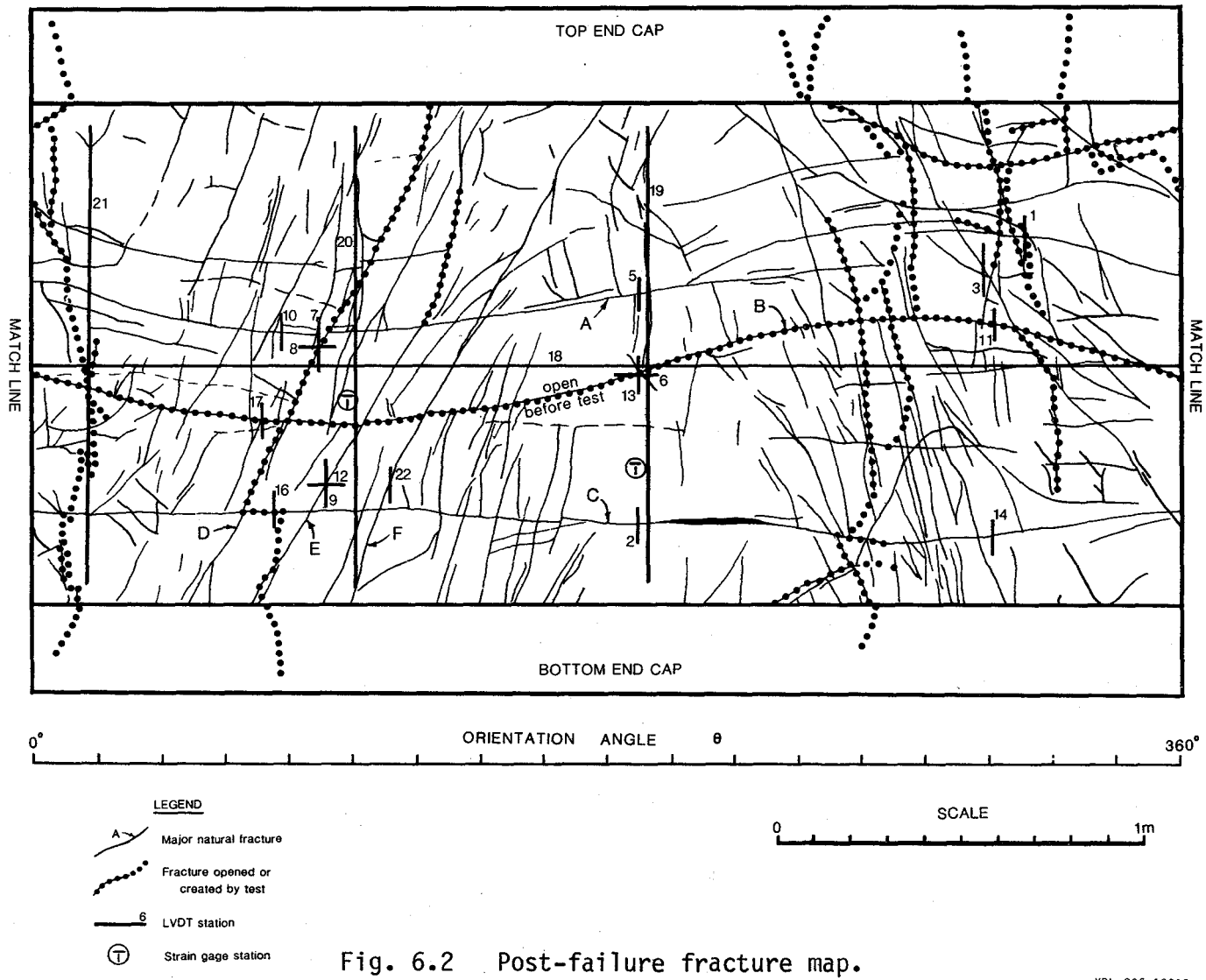

Fig. 6.2 Post-failure fracture map.

XBL 806-10319

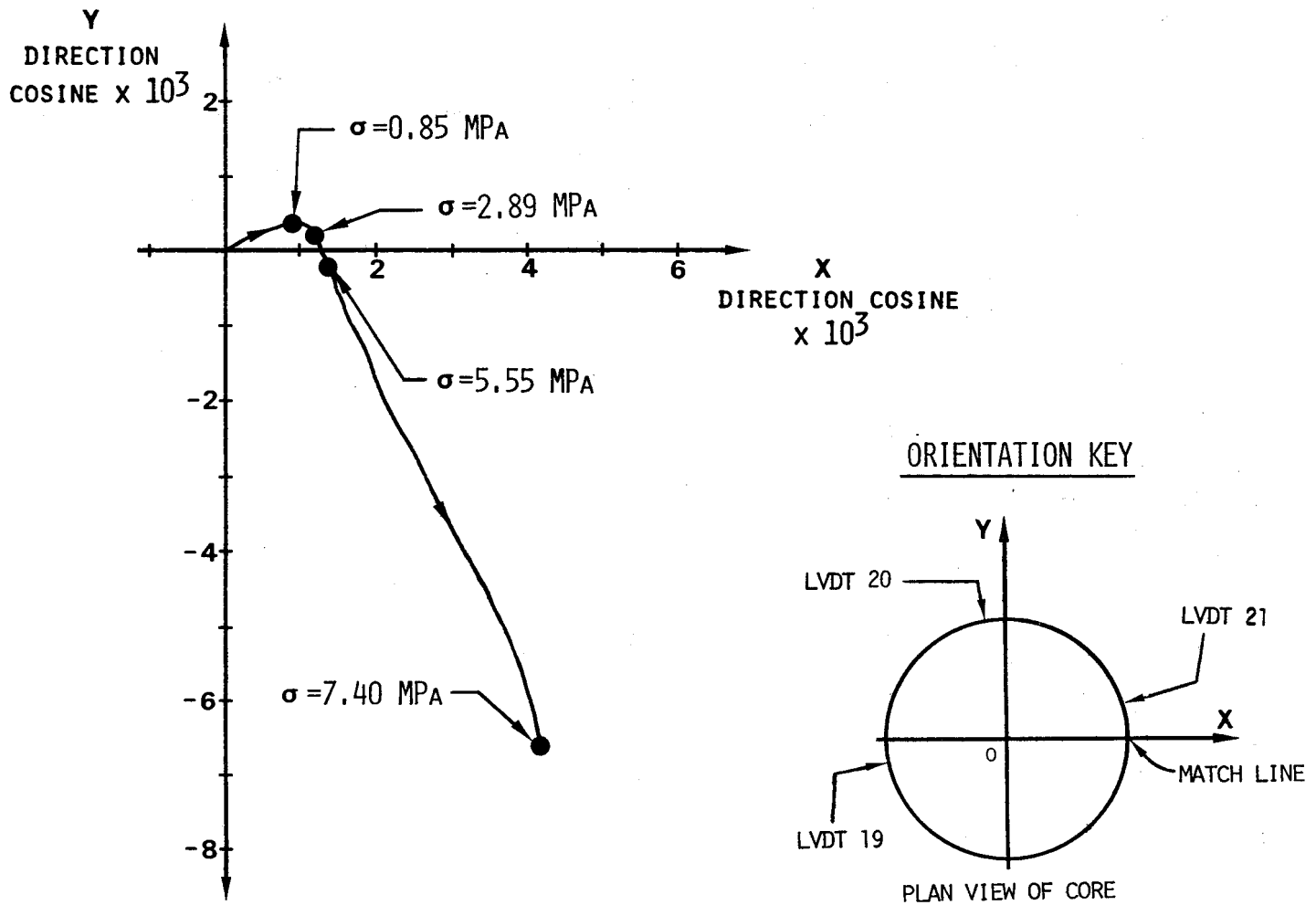

XBL 808-11475

Fig. 6.3 Plot of downward normal vector to the plane of the top of the sample. X and Y axes are horizontal direction cosines.

to load application, the figure shows that gradual tilting occurred in the direction of LVDT No. 19 during loading to 2.89 MPa. At higher loads, tilting shifted toward LVDT No. 20, which measured vertical displacement over a portion of the core intersected by the major inclined fractures. The pronounced tilting in this direction prior to failure was most probably due to shearing along fracture D. Load eccentricity computations, based on data from the load cell instrumentation, showed that the position of the load vector during the test was slightly off-center and within the quadrant between LVDT Nos. 19 and 20. This is generally consistent with the tilting of the normal vector in Fig. 6.3.

The effect of measurement scale on the observed stiffness and strength of rock has been discussed by a number of investigators, most recently by Heuzé (1980). Test results from the large Stripa core provide additional evidence of the importance of the "size effect," but on a scale rarely attempted in laboratory testing of naturally jointed rock samples. The unconfined uniaxial strength of the core was only about 5% of the average strength obtained from tests on small samples reported in Appendix IV. Similarly, the axial strain at failure was only 10% to 20% of the average failure strain for small samples (see Table 3.1). To attribute these differences solely to a "size effect" may be misleading because the effects of sampling disturbance, among other factors, can have a substantial effect on the measured properties of rock. The ultra-large core was recovered from the rock mass using techniques specifically designed to avoid disturbance of the fractures. The small samples were recovered from boreholes and suffered rougher handling. It is probable that only the sections of core containing the strongest fractures survived intact and this is reflected in the results

of the strength tests on the small cores.

Strains in the small fractured samples, computed as the change in length divided by the total length, were generally linear with axial stress up to the point of failure; therefore, single tangent moduli could be estimated from the loading curves. The average of these values (see Table A4.3, Appendix IV) was 57.8 GPa. The calculated stress-strain curve for the central axis of the large core, as shown in Fig. 6.1, is distinctly non-linear. However, tangent moduli can be estimated at points along the curve near each point at which stress was held constant during the test. These are listed in Table 6.1. The highest is 52.3 GPa, within the low range of values found for the small fractured samples. The initial stress-strain behavior of the small cores were also nonlinear with low tangent moduli. These comparisons suggest that the pre-failure properties of the large core were similar in general character to the properties of the small fractured samples. Development of the more linear portion of the stress-strain curve was pre-empted in the large core by failure along the adversely oriented inclined fractures.

Figure 6.4 shows a plot of the circumferential, or girth, strain (ε_θ) computed from LVDT No. 18 and the overall axial strain from Fig. 6.1. Poisson's ratios for different stress levels were estimated by dividing the tangent slope of the girth curve by that of the axial curve. Several such ratios are shown in Table 6.1. The zero reading at σ_1 = 0.85 MPa is believed to result from initial sticking of the girth gauge wire. The other values, particularly the ratio 1.28 computed for the 5.55 MPa stress-level, are much greater than would be expected from assumptions of elastic behavior.

Table 6.1. Pseudo-elastic properties computed from overall stress-strain record, Fig. 6.1.

Axial stress (MPa)	Tangent modulus (GPa)	Slope of girth strain curve (GPa)	Poisson's ratio, ν
0.85	7.1	∞ *	0 *
2.89	23.0	-47.1	0.49
5.55	45.2	-35.4	1.28
7.55	52.3 **	∞ *	0 *

* Anomalous reading due to LVDT sticking.

**From unload curve.

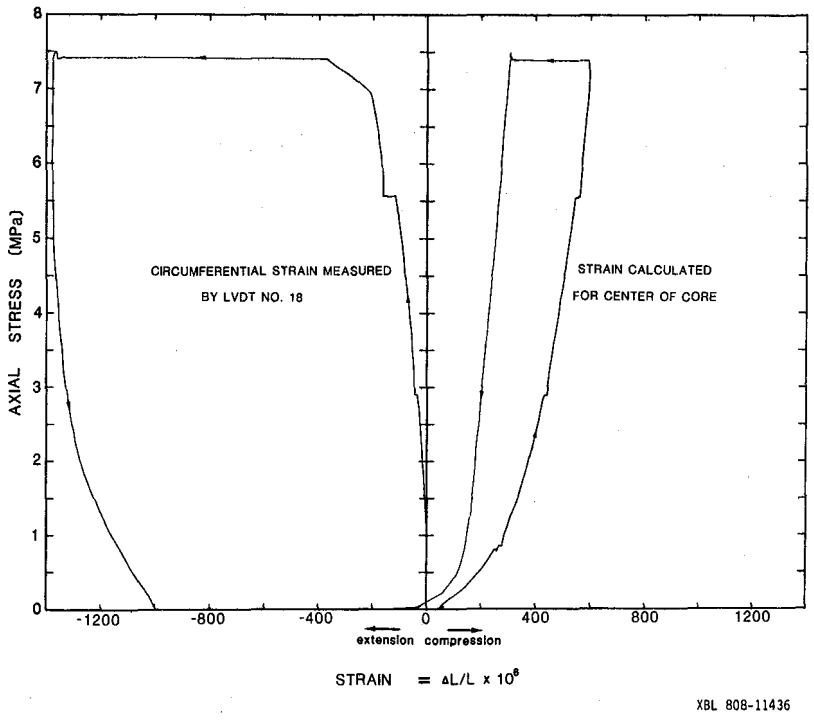

Fig. 6.4 Macroscopic axial and circumferential stress-strain data.

As will be discussed later, these anomalous values can be attributed to the shear behavior associated with the inclined fractures.

6.1.2 Decomposition of Mechanical Response

The large Stripa core was instrumented in such a way that its gross deformation could be approximately decomposed into the separate contributions of major discontinuities and the intact rock matrix. This decomposition aids understanding of the macroscopic behavior of the rock mass and is necessary for analysis of flow through a system of discrete fractures. Due to the complexity of the fracture system, evaluation of fracture deformations was limited to the major fractures labeled A through F in Fig. 6.2.

As originally installed, LVDTs were provided to measure deformation at three points, spaced 120° apart, for each of the fractures A, B, and C. However, several LVDT's malfunctioned due to the pressure-sealing problems described in Appendix VI. This left fractures B and C with only two points of measurement each. In order to "replace" the missing data and make a reasonable estimate of the fracture deformations, the overall axial displacement and tilt plane computations discussed in Section 6.1.1 were used. Assuming that, prior to failure, plane sections remained planar, the overall displacement at any location around the circumference of the core could be calculated from the equation of the tilt plane. Overall displacements were thus calculated for the $\theta = 80°$ and $\theta = 130°$ locations. As shown in Fig. 6.2, these locations approximately coincide with the positions of vertical LVDTs mounted across the principal fractures. Data for the $\theta = 190°$ locations were obtained directly from LVDT No. 19. The total overall deformations were reduced by an amount equal to the estimated strain in the rock

between the principal fractures. This gave the deformation due to the fractures alone. The resulting curves are shown in Fig. 6.5. Estimate of strains in the rock matrix were based on an assumed modulus of 60 GPa, close to the average of values obtained from the small core tests. The presence of a large number of secondary fractures in the rock separating the major fractures in the large core suggests that this assumed modulus may be somewhat high. However, any resulting error is small because a 15% decrease in the assumed modulus only affects the values plotted on Fig. 6.5 by about 5%. The calculated curve for the $\theta = 130°$ location indicates upward movement of that section of the core relative to the center. This behavior is judged to be real from consideration of the failure kinetics of the core. Failure involved tilting by the upper part of the core.

6.1.2.1 Fractures Perpendicular to Core Axis. From the curves on Fig. 6.5, displacements at the location of LVDT No. 14, which malfunctioned on fracture C, could be estimated. As shown in Fig. 6.9, this was done by subtracting the reading from LVDTs No. 1, 3, and 11 from the $\theta = 130°$ fracture deformation curve on Fig. 6.5. Displacements obtained from functioning LVDTs were adjusted for intact rock strain between the anchor points. A malfunction of LVDT No. 11 prevented the extension of the calculated curves beyond an axial stress of 5.56 MPa. Taking the measured and calculated displacements at the $\theta = 80°$, 190° and 310° peripheral locations, the closure at the center of fracture C (average closure) could be calculated. These results are plotted on Fig. 6.6. The shape of the center displacement curve suggests that after initial closure the normal displacement across the fracture reversed. Because this implies release of load, it does not accurately represent the actual deformation that occurred but may be con-

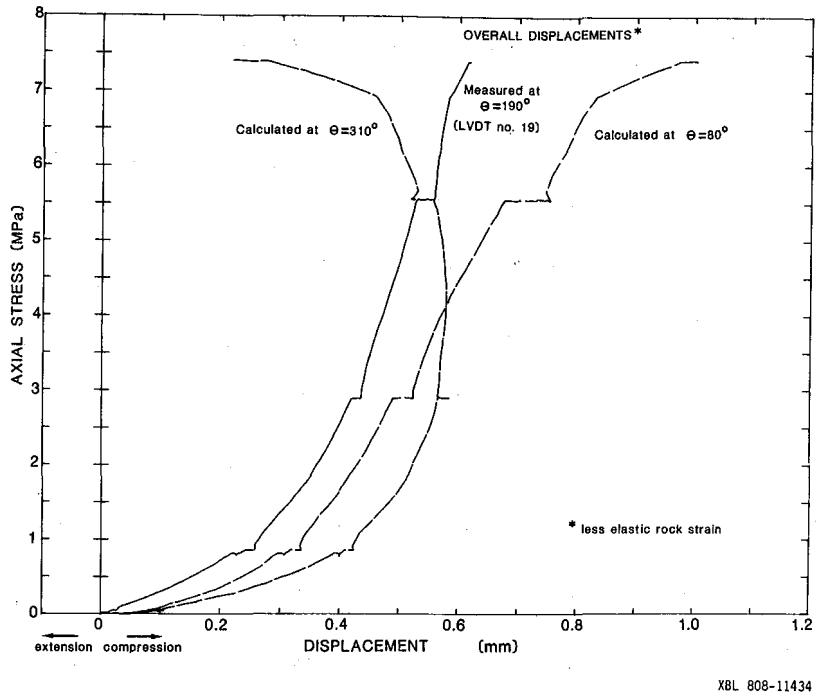

Fig. 6.5 Calculated overall displacements at 80°, 190°, and 310°. Orientation angles measured counterclockwise from the match line. Linear elastic rock strain (E = 60 GPa) has been subtracted to yield "fracture" deformations.

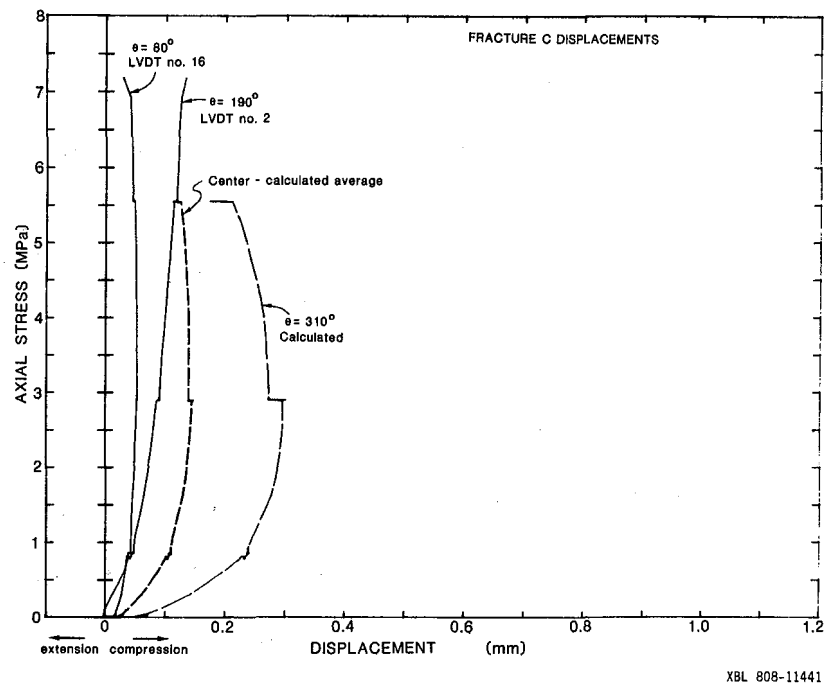

Fig. 6.6 Fracture C displacements (E=60 GPa).

sidered a lower bound to the closure of fracture C.

A similar approach was used to estimate the average closure of fracture B. This involved reconstructing displacements at the location of LVDT No. 13, which failed at the start of the test. This was done by subtracting the adjusted readings of LVDT Nos. 2 and 5 from the calculated overall displacement on Fig. 6.5 for the $\theta = 190°$ location (LVDT No. 19). This decomposition is shown in Fig. 6.10. The resulting stress-displacement curves for fracture B are shown on Fig. 6.7. In this case the estimated center closures are more accurate as there was less uncertainty in reconstructing data for "missing" LVDTs. Extension of the curve above the 5.56 MPa stress level was not possible, due to the malfunctioning of LVDT No. 11. Also in Fig. 6.7 are data from LVDT No. 6 that recorded significant fracture displacement (up to 0.08 mm) approximately in the plane of fracture B. This is an indication of shearing along the fracture and emphasizes the complex response of the core to uniaxial loading.

All three LVDTs mounted across fracture A apparently functioned properly. The pertinent stress displacement curves are shown on Fig. 6.8.

No decompositon of the overall displacement was necessary at the $\theta = 80°$ location because LVDT Nos. 7, 9, 10, 16, and 17 all performed well. However, when the measured displacements across fractures A, D, B, E, and C were added as shown in Fig. 6.11, their sum was about 20% larger than the calculated overall fracture compression. Fracture F does not enter the computation, and deformation of fracture A has been included with that of fracture D via LVDT No. 7. All fracture measurements were adjusted for strains in the intact rock between the anchor points; and as previously discussed, the

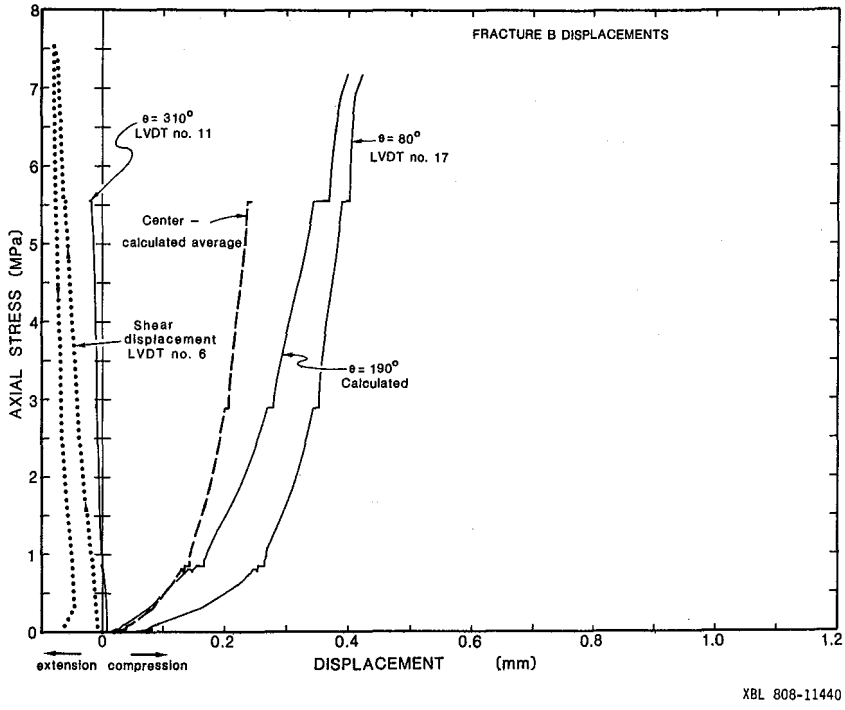

Fig. 6.7 Fracture B displacements (E=60 GPa).

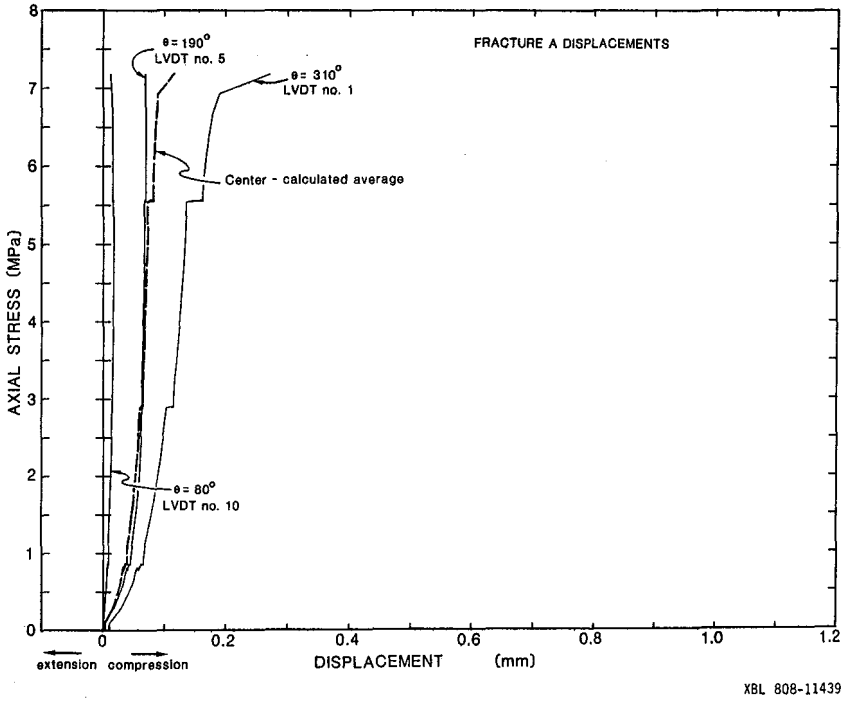

Fig. 6.8 Fracture A displacements (E=60 GPa).

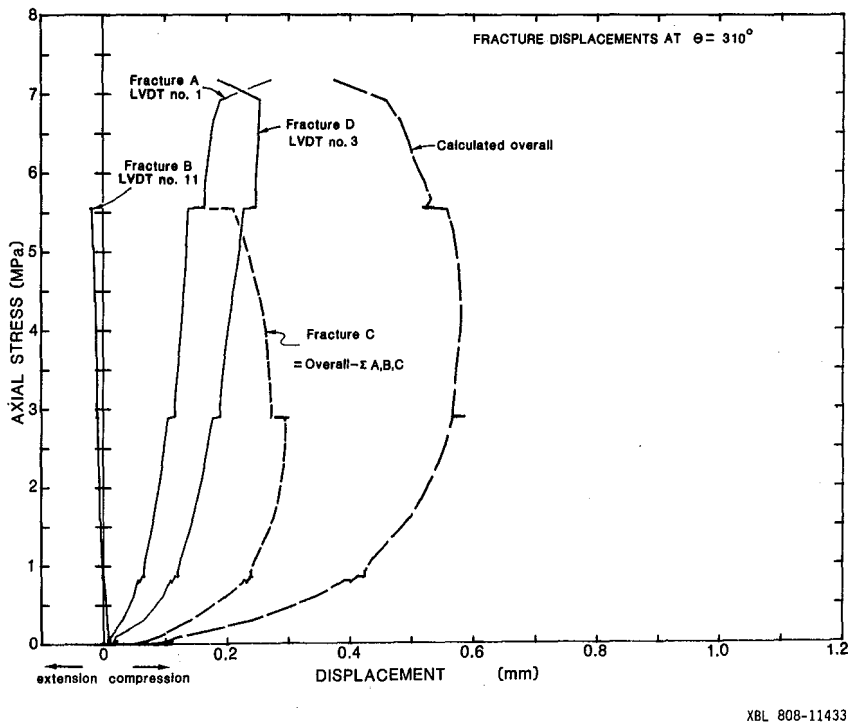

Fig. 6.9 Calculated macroscopic and fracture displacements at 310° orientation (E=60 GPa).

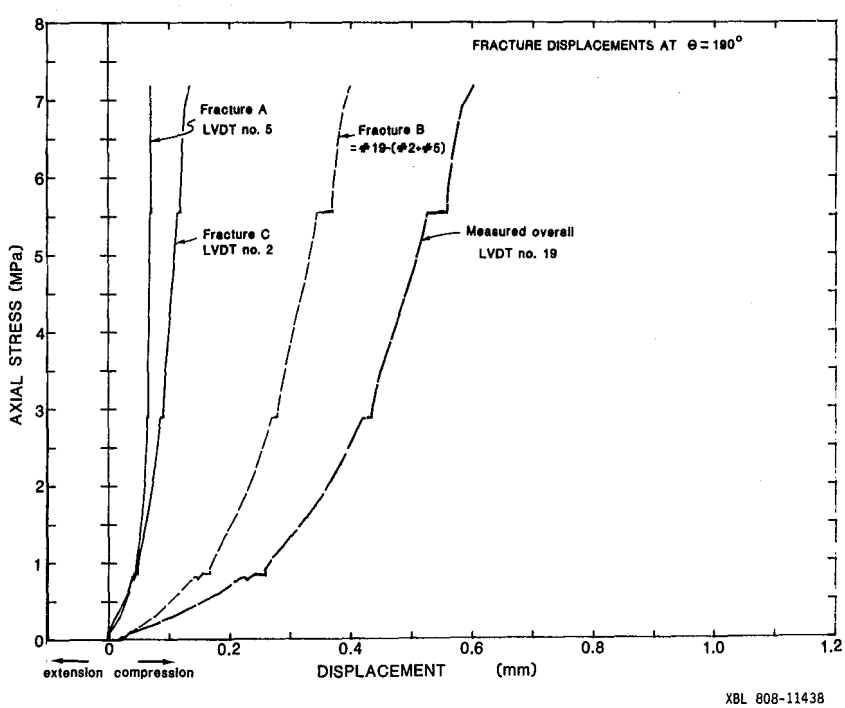

Fig. 6.10 Calculated macroscopic and fracture displacements at 190° orientation.

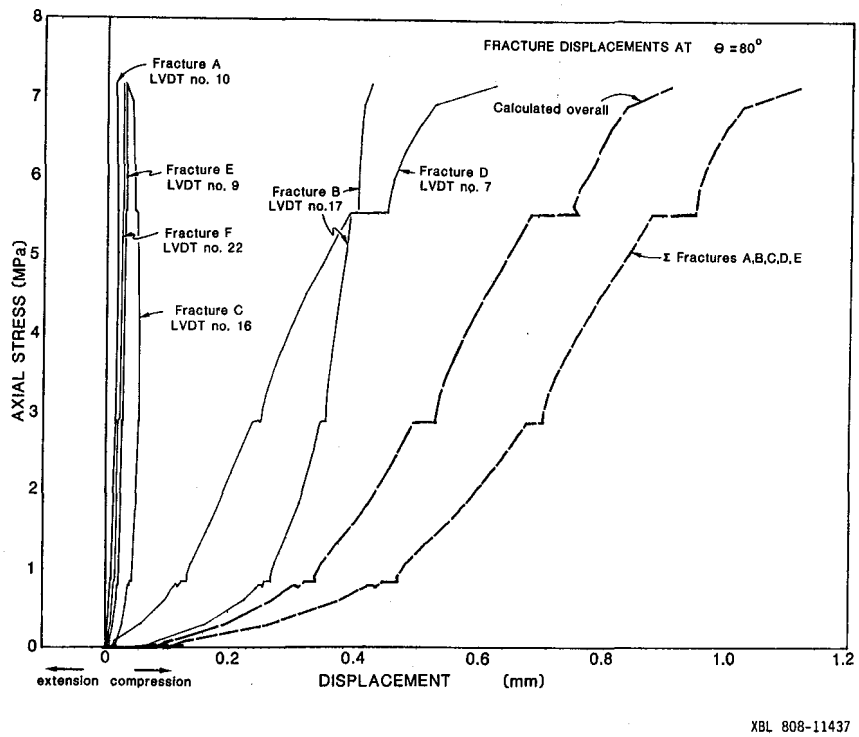

Fig. 6.11 Calculated macroscopic and fracture displacements at 80° orientation (E=60 GPa). Fracture F displacement also shown.

choice of modulus can account for a 20% underestimation on the overall fracture deformation.

There are two possible explanations for the discrepancy. First, a systematic error in the LVDT instrumentation could have produced a cumulative discrepancy when the several fracture readings are added and compared to the single overall value. No such systematic error has been found in the instrumentation system. The second and more plausible explanation involves the assumption of uniform planar deformation of individual fractures and the core as a whole. Due to such features as the intersection of fractures D and B at $\theta = 80°$ (see Fig. 6.2), local deformation fields may be discontinuous. For example, due to nonplanar deformation, the closure of fracture B at the location of LVDT No. 20 may have been less than or greater than that measured at LVDT No. 17, which was about 25 cm on the other side of fracture D. As

discussed later, measurements from strain gauges in the vicinity of LVDT No. 20 and the B-D fracture intersection seem to support this explanation.

Figure 6.12 is a plot of the horizontal components (direction cosines) of the downward normals to planes defined by the fracture displacements in Figs. 6.6, 6.7, and 6.8. For uniform tilting of the core, these diagrams should be similar to Fig. 6.3, which plots the orientation of the overall tilting. In this case all fracture planes perpendicular to the core would initially be expected to tilt toward LVDT No. 19, and thereafter in the direction of LVDT No. 20. The projection of the downward normals should correspondingly move in the opposite direction. As indicated by Fig. 6.12, this trend is generally apparent for the fracture data; however, the downward normal for fracture A moves back in the direction of LVDT No. 19 at

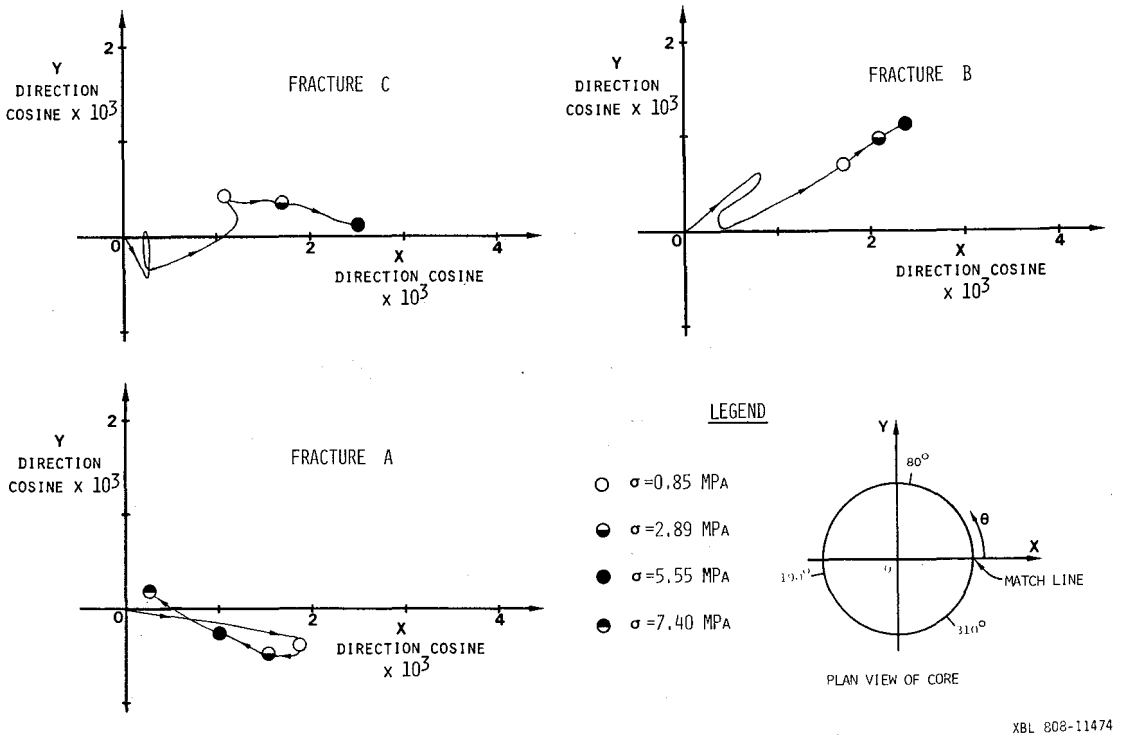

Fig. 6.12 Plots of downward normal vectors to fracture displacement planes.

the higher loads. Since this is contrary to the movement of the overall vector in Fig. 6.3, it appears that the closure of fracture A was nonuniform. The motions of the normals to fractures B and C are more consistent with the motion indicated on Fig. 6.3 and therefore the displacements on these fractures probably more closely approximated the assumption of uniform planar deformation.

6.1.2.2 Fractures Inclined to the Core Axis. As indicated by data obtained from the girth gauge (LVDT No. 18), significant lateral expansion of the sample occurred as a result of shear displacement on the inclined fractures. Fractures B and D were primarily responsible, as is evident from the post-failure fracture map (Fig. 6.2). No post-failure opening of either fracture E or F was visible, but they did compress nonlinearly in the vertical direction, as shown on Fig. 6.13. Both curves in the figure represent fracture deformations only, each curve having been corrected for intact rock strain between the LVDT anchor points. The nearly vertical portions of the curves indicate that after some initial movement these fractures stabilized and had no significant influence on the deformation behavior of the sample at higher stresses. However, at low stresses, particularly below 2 MPa, the fractures introduced considerable nonlinear and inelastic behavior. Nonrecoverable displacements of about 0.10 and 0.05 mm were measured for fractures E and F, respectively. Since no systematic errors are believed to be involved, Fig. 6.13 illustrates that even apparently well-healed fractures can cause deviations in the linear elastic behavior of a rock mass.

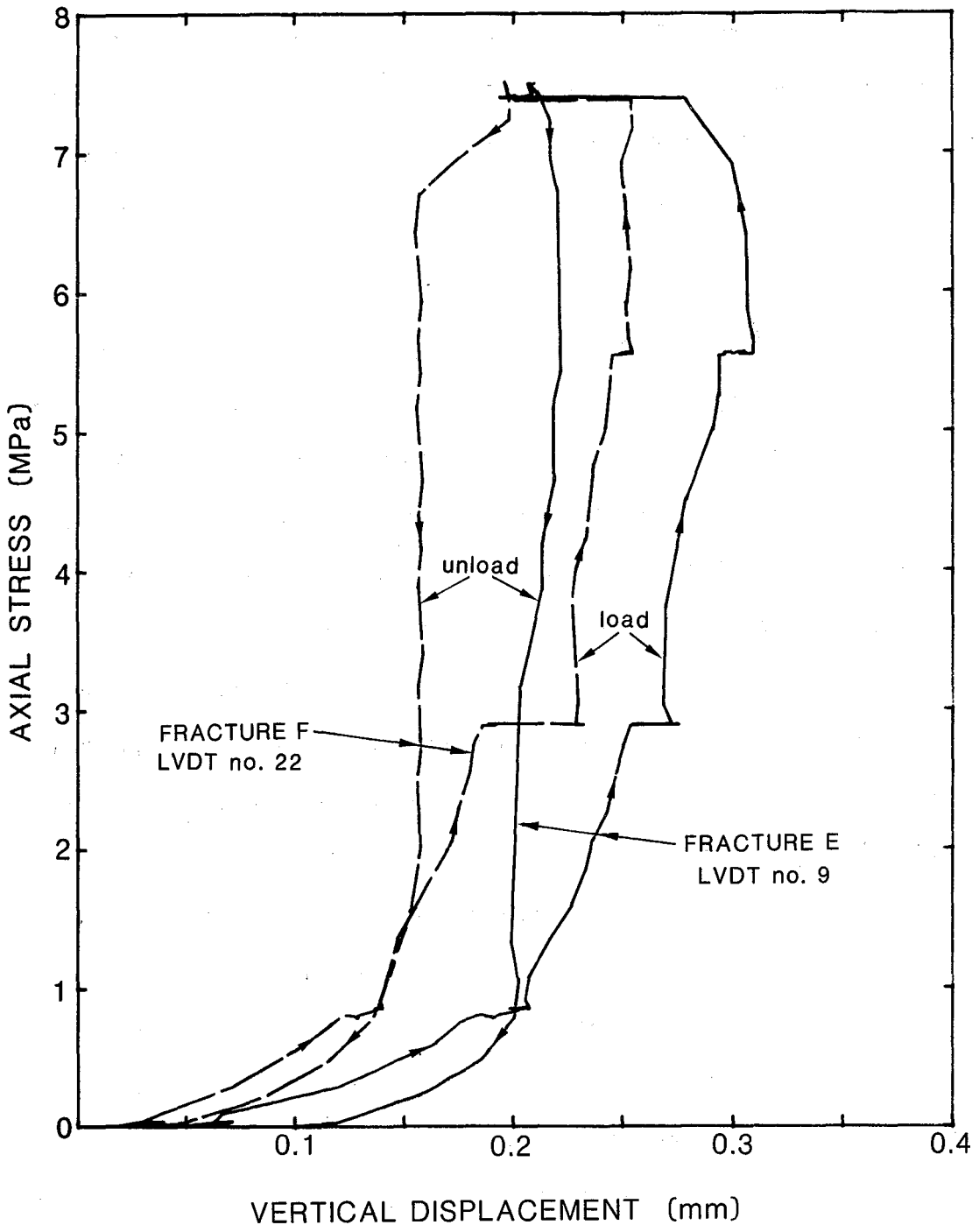

XBL 808-11473

Fig. 6.13 Vertical displacments on fracture E and F (E=60 GPa).

Figure 6.14 is a plot of the horizontal and vertical displacements across fracture D, together with the horizontal, or approximate shear displacements, on fracture B. It was noted earlier that the girth gauge (LVDT No. 18) apparently gave anomalous readings in the early stages of loading. The non-zero responses of LVDT Nos. 6 and 8 were not compatible with the overall measurement from LVDT No. 18, which showed no displacement below 1 MPa axial stress. After LVDT No. 18 began to move, however, it displaced rapidly relative to the fracture gauges. This suggests that the initial sticking was recovered as loading progressed. Another explanation for the discrepancy between the fracture data and the girth displacement is that a rotational component of shearing was active on the inclined fractures. This is difficult to substantiate, however, due to lack of sufficient LVDTs to measure the lateral movements of all fractures.

All the curves in Fig. 6.14 for fracture D are nonlinear and clearly indicate slip along the fracture. The nature of fracturing around LVDT No. 3 (see Fig. 6.2) suggests that the failure mode was more complex than simple shear. Displacements measured by LVDT No. 7 showed that a major portion of the deformation due to axial loading was recovered on unloading. This apparent behavior may have been influenced by the reinforced concrete end cap. The cap bridged across fracture D and remained attached to portions of the sample that remained intact after the shear failure. Neglecting any possible rotational components, approximate shear and normal displacements, u and Δv, can be calculated for fracture D from:

$$u = 1/2\ (\delta_7 \cdot \cos 25° + \delta_3 \cdot \cos 35°) - \delta_8 \cdot \cos 65° \qquad (6.1)$$

$$\Delta v = 1/2\ (\delta_7 \cdot \sin 25° + \delta_3 \cdot \sin 35°) + \delta_8 \cdot \sin 65° \qquad (6.2)$$

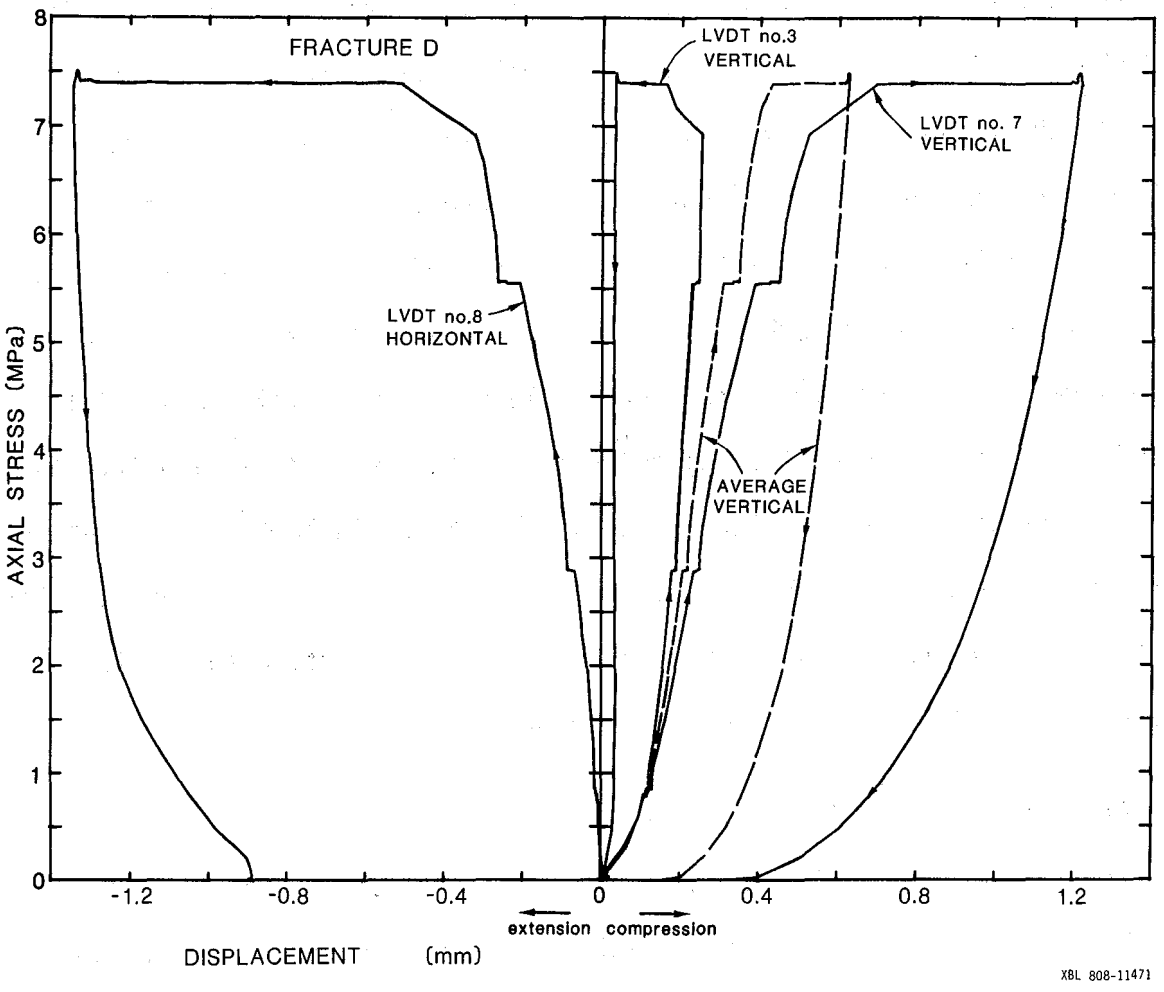

Fig. 6.14 Vertical and horizontal displacements on fracture D.

where ϕ_n is reading from LVDT No. n, corrected for rock strain between anchor points, and the angles are the acute angles between the fracture and the LVDT's (see Appendix VI). Shear and normal stresses on the fracture, τ and σ_n, can be estimated as

$$\tau = (P/A) \cdot \cos 30° \tag{6.3}$$

and $$\sigma_n = (P/A) \cdot \sin 30°, \tag{6.4}$$

where P is the axial load, A is the cross-sectional area of the core, and 30° is the approximate angle between fracture D and the core axis. Resulting stress-displacement relationships for the fracture are shown in Figs. 6.15 and 6.16. The negative (extension) normal displacements shown on Fig. 6.16 indicate shear dilatency. Because of the uncertain boundary conditions in regard to shear stiffness and the fact that the normal stress was not constant, an estimation of shear stiffness and peak shear strength was unwarranted. When considering the hydraulic conductivity of fracture D, however, Fig. 6.16 is useful in that it relates the apparent fracture aperture to the applied stress.

6.1.2.3 Parameters for the Mechanical Closure of Fractures. Goodman (1976) used the following equation to describe the normal deformation of a discontinuity:

$$\frac{\sigma_n - \xi}{\xi} = A\left(\frac{\Delta v}{V_{mc} - \Delta v}\right)^t \quad , \quad (\Delta v < V_{mc}) \tag{6.5}$$

where ξ is the initial (seating) stress, Δv is the measured change in aperture from the initial condition, V_{mc} is the maximum possible closure of the fracture, and A and t are constants. Estimates of V_{mc} obtained from Figs. 6.6, 6.7, 6.8 and 6.16 are listed in Table 6.2. These data provide only

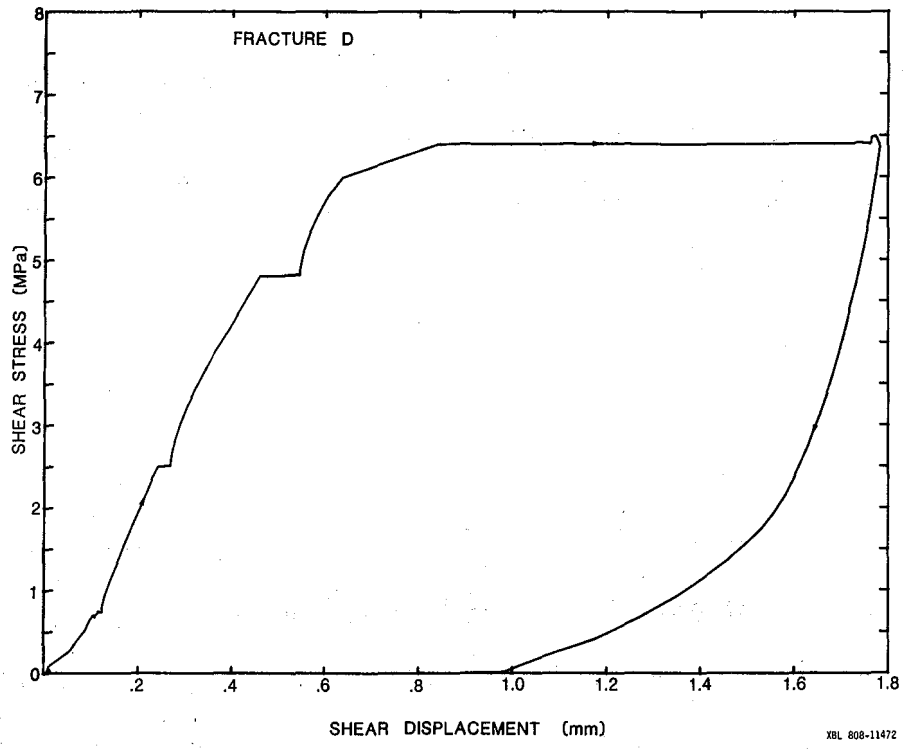

Fig. 6.15 Calculated shear stress versus shear displacement for fracture D.

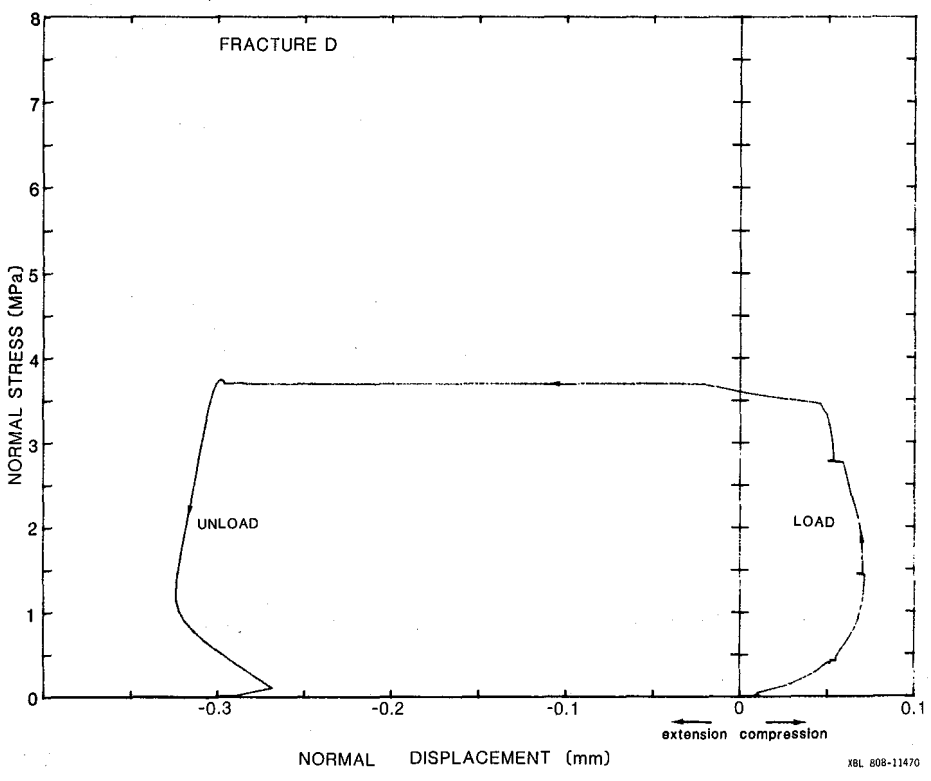

Fig. 6.16 Calculated normal displacement versus normal stress for fracture D.

Table 6.2. Parameters for mechanical closure of fractures [derived by Eq. (6.5)].

Fracture	V_{mc}(mm)*	ξ (MPa)**	A	t
A	0.08	0.02	6.9	1.8
B	0.30	0.03	3.9	1.6
C	0.15	0.04	1.2	1.1
D	~0.1	0.03	1.0	1.0

*Estimate of stress-displacement curves.

**Approximate weight of rock above fracture divided by cross-sectional area of core.

rough approximations and should be regarded as accurate to only within 10 to 30%. Logarithmic plotting of the fracture closure data in the form of Eq. (6.5) was used to obtain the constants A and t, which are also listed in Table 6.2.

6.1.3 Strain Gauge Data

As described in Section 5.4, two pairs of strain gauges were affixed to the core at the locations shown on Fig. 6.2. As is common practice for uniaxial testing, the gauges were mounted axially and circumferentially, with the assumption that these are the principal strain directions. Because of the prominent discontinuities, this assumption was questionable for the Stripa core. It would have been preferable to use three gauges at each location so that the magnitude and direction of the principal strains, and thus stresses, could be calculated. This was not possible due to the limited number of available electrical feedthroughs into the triaxial vessel. Strain gauges No. 24 and 26 were mounted near the intersections of the principal fracture sets and No. 25 and 27 were located opposite this position on a relatively unfractured portion of the sample.

By assuming that the stress field at the gauge locations corresponded to uniformly uniaxial loading, the two sets of strain-gauge data were plotted in the form of stress-strain curves on Figs. 6.17 and 6.18. The strains plotted on these figures are half the apparent strains calculated from the output voltages gathered during the test. The reason for this discrepancy is that strains based on the raw outputs would imply that the modulus of the rock matrix in the sample was very much less than that measured in our tests (Appendix IV), or obtained by others, for Stripa granite. If a reasonable

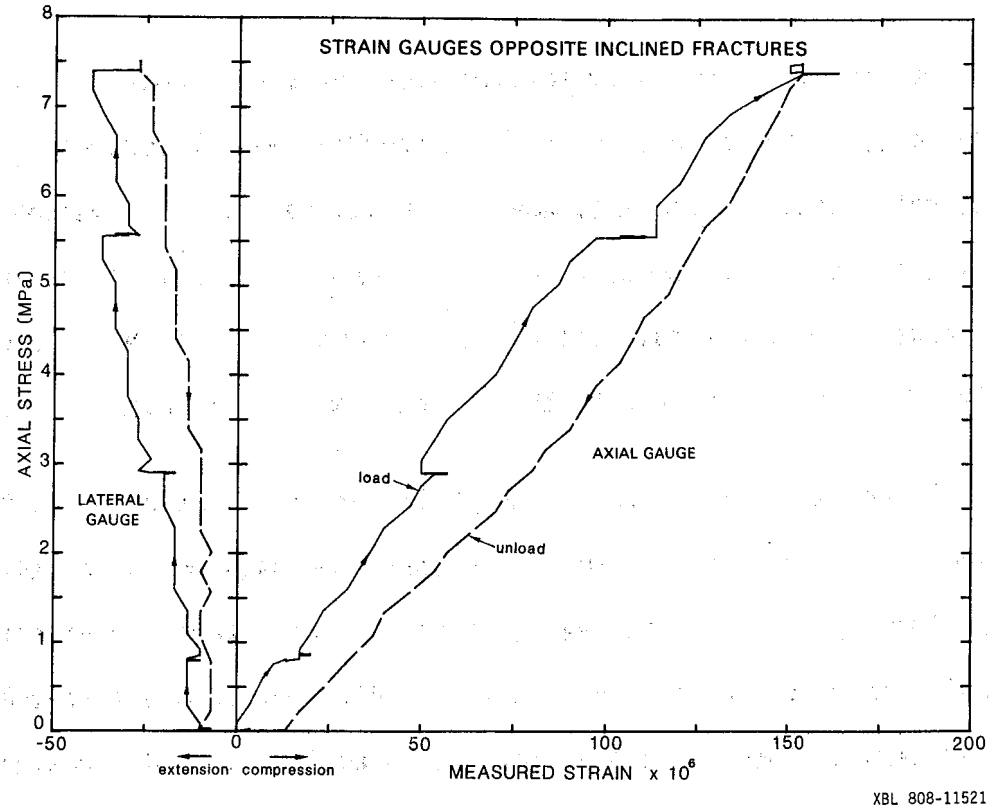

Fig. 6.17 Stress-strain data from strain gauges opposite inclined fractures (Gauge Nos. 25 and 27).

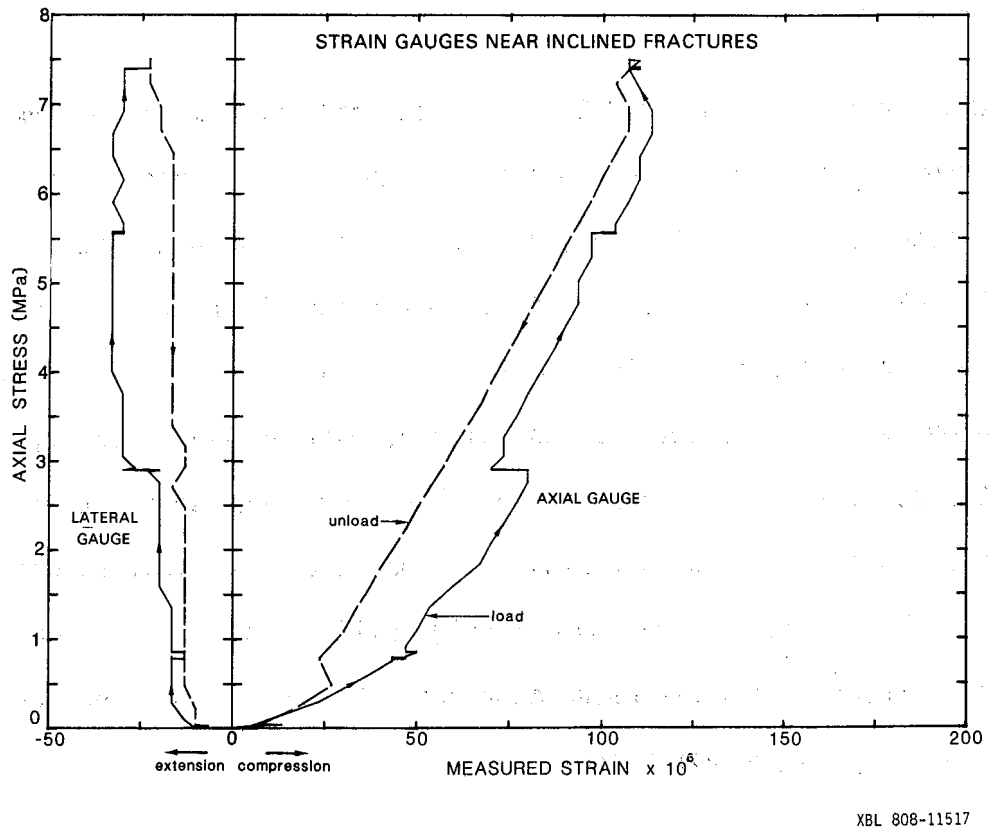

Fig. 6.18 Stress-strain data from strain gauges near inclined fractures (Gauge Nos. 24 and 26).

value is assumed for the modulus, axial stresses inferred from the raw data are almost exactly twice those computed from the known axial loading. Although a careful check of the instrumentation did not find any systematic error, it is suspected that such an error was present. We have therefore elected to present the strain-gauge data in the form shown in the figures. The unmodified data are preserved in the records compiled in Appendix VII.

The axial stress-strain curve on Fig. 6.17 for the location opposite the fractured section of the core is linear over each load segment with a slope (E) of approximately 57 GPa. The average slope of the lateral strain data is -225 GPa, which indicates a Poisson's ratio, ν, of 0.25. Since these values of E and ν agree with those obtained from small samples, it indicates that the stresses in the mid-section of the core, away from the major discontinuities, are uniaxial. This agrees with an intuitive judgment based on the core and fracture geometries.

However, near fractures D and E, the stress field was more complex, as is evident from the nonlinear and nonelastic form of the curves in Fig. 6.18. Calculated tangent stiffnesses from the various loading segments vary from about 30 GPa at the start of loading to over 100 GPa near failure. Also, the apparent Poisson's ratio from these two gauges is less than 0.11. These anomalous values indicate that the discontinuities significantly perturbed the local state of stress at this location. The apparent artificially high calculated modulus suggests that the actual vertical stress at this point was lower than that assumed in Fig. 6.18. This could be due either to nonuniform stress distribution across this portion of the core or reorientation of the principal stress directions.

As discussed in Section 6.1.2.1, the strain gauge data support the inference that fracture B did not close uniformly, particularly near its intersection with fracture D. Data from the vertical strain gauge near this location indicate that the axial stress here was lower than the mean applied uniaxial stress. This suggests that fracture B closed less at a point near LVDT No. 20 than at LVDT No. 17, which is on the other side of the D-B fracture intersection.

6.1.4 Time-Dependent Mechanical Behavior

From the stress-strain curves presented in the previous sections, it can be seen that during the period when the axial load was held constant, there were noticeable time-dependent deformations at all scales of measurement.

Figure 6.19 is a modified version of Fig. 5.3 in which the zero point of the abscissa represents the time at which any loading or unloading ramp was started. The figure provides a useful reference for the following discussion.

6.1.4.1 Macroscopic Time-Dependent Deformation. Figures 6.20 and 6.21 display the creep behavior of the macroscopic axial and circumferential deformations. The dashed portions of the curves represent strain during loading or unloading, and the solid portions are the creep strain during periods of constant load. Immediately after a load level is reached, deformation continues, but the rate gradually decreases and resembles transient or primary creep. Following the primary creep phase (for the first three load levels), the deformation approaches a steady-state rate of increase which resembles secondary creep, although the rates are very low. The strain rate for the first load level, 14×10^{-6}/hr (0.0182 mm/hr), is higher

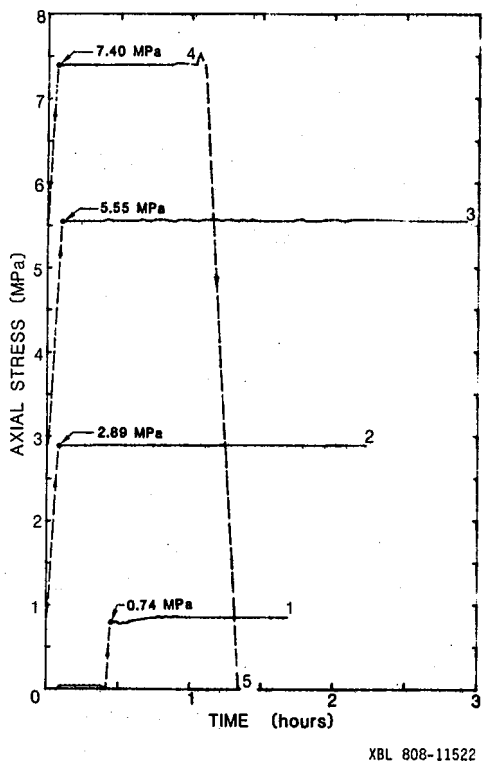

Fig. 6.19 Axial stress versus time since start of load ramps.

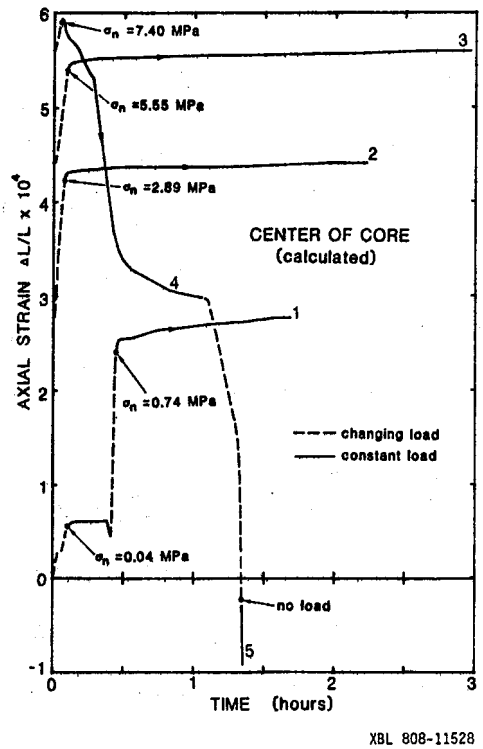

Fig. 6.20 Macroscopic axial strain versus time.

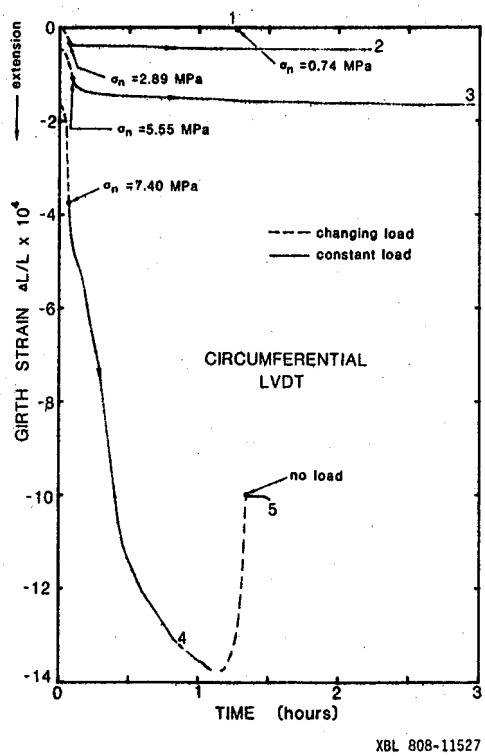

Fig. 6.21 Circumferential strain versus time.

than that for the second and third levels, 3.3 x 10^{-6}/hr (0.0040 mm/hr). Close examination of the first three curves indicates that the strain rate approached zero near the ends of the periods when loads were held constant. This means that the sample stabilized under the smaller loads, although the time required to reach stability increased as the load was raised.

Curve 4 in Figs. 6.20 and 6.21 represents creep during failure. The irregularities in the curve immediately following the peak strain are probably due to portions of the core being unloaded during a progressive failure process. However, curve 5 of Fig. 6.20 extends beyond the original (zero) strain. This is misleading because it suggests the average core height increased after failure. An explanation for this anomaly lies in a probable lack of uniformity in the absolute post-failure displacement readings. Figure 6.21 shows that the overall girth displacements were similar to those measured axially, except that a large amount of permanent set is shown in the record. This was due to the non-recoverable shear and normal deformations on the major fractures.

6.1.4.2 Time-dependent behavior of individual fractures. The transient deformations calculated for the fractures perpendicular to the axis are shown in Figs. 6.22, 6.23, and 6.24. Curves 4 and 5, describing failure and post-loading creep, are missing from Figs. 6.23 and 6.24 because LVDT No. 11 malfunctioned. These data are generally similar to the curves in Fig. 6.20, except that fracture A does not show the erratic failure and unloading response.

Figures 6.25 and 6.26 are the time-dependent shear and normal deformation for the inclined fracture D. Both show predominantly primary-creep

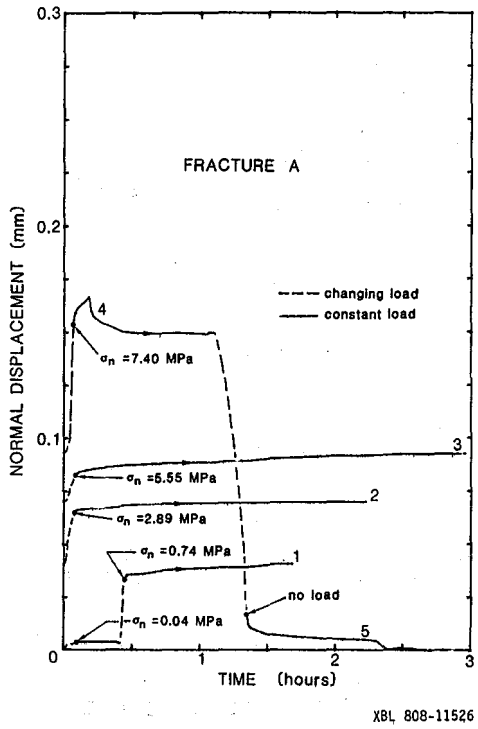

Fig. 6.22 Calculated center displacement versus time for fracture A (E=60 GPa).

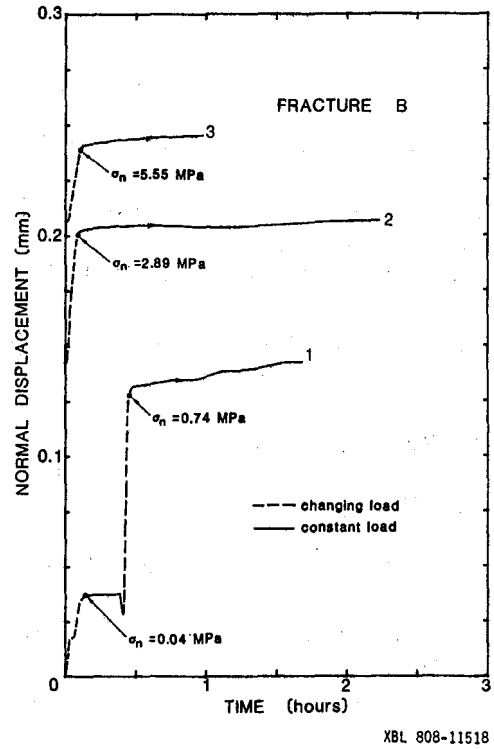

Fig. 6.23 Calculated center displacement versus time for fracture B (E=60 GPa).

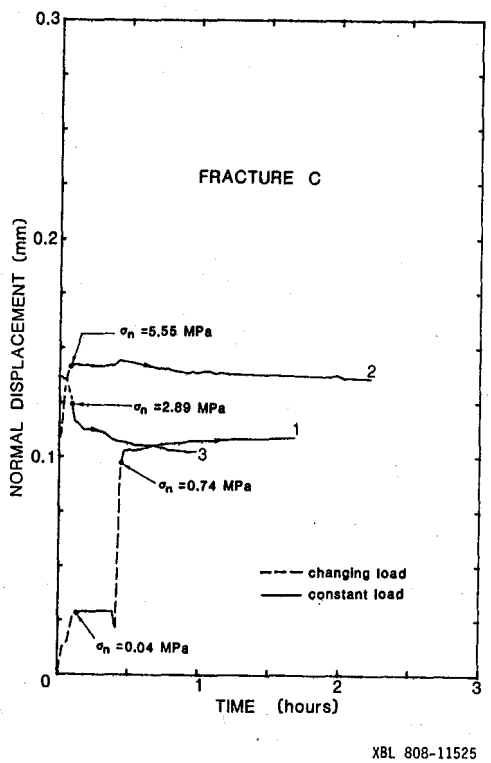

Fig. 6.24 Calculated center displacement versus time for fracture C (E=60 GPa).

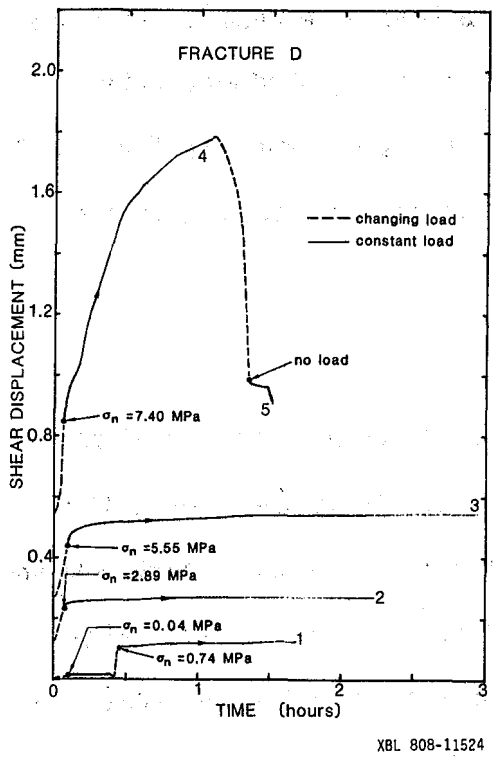

Fig. 6.25 Calculated shear displacement versus time for fracture D (E=60 GPa).

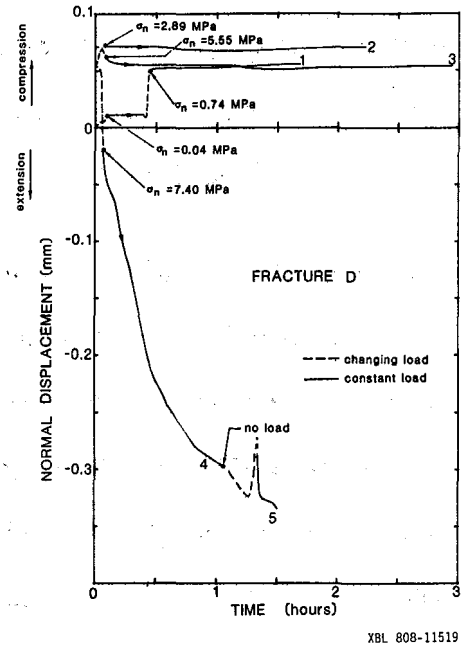

Fig. 6.26 Calculated normal displacement versus time for fracture D (E=60 GPa).

behavior until the load level corresponding to curve 4, where shearing and opening of the fracture accelerated. The creep rate gradually decreased and the sample was apprently tending toward a stable condition under the constant maximum applied load. This may be due to the post-failure residual strength of the sample. Unloading had little effect, since shearing displacements were essentially non-recoverable. A relatively large permanent set of nearly 0.9 mm was recorded for the shear displacement on this fracture, and that in the normal direction was about -0.3 mm (opening).

6.2 Coupled Hydraulic-Mechanical Behavior

The results of the divergent and convergent flow tests performed at the several stress levels are summarized in Table 6.3. The number of tests it was possible to conduct in practice was less than optimal, but the data base is sufficient for study of the general characteristics of the coupled hydraulic-mechanical properties of the sample. Questions of interest are (a) the general applicability of Darcy's law, (b) the relationship between macroscopic flow parameters and axial stess, and (c) the relationship between measured fracture deformations and changes in the flow parameters.

6.2.1 Applicability of Darcy's Law

In order to check the applicability of Darcy's law in this instance, it suffices to show that there is a linear relationship between the steady isothermal flow and the pressure head. For this purpose, Fig. 6.27 plots the measured flow rate Q against the applied pressure differential Δh for each of the flow tests. Although the data are too sparse to draw firm conclusions, the deviation from the linear assumption appears to be small. The slight divergence from linearity that is present could be due to turbulent effects

Table 6.3. Results and computed overall hydraulic parameters from stress-flow tests on ultra-large Stripa core.

Flow Test No.	Axial Stress (MPa)	Test Mode	Differential Head, Δh (cm H_2O)	Steady-State Flow Parameters					
				Flowrate (l/min)	$Q/\Delta h$ cm^2/sec)	k_{rm} * (10-3 cm/sec)	2b ** (cm)	k_f † (cm/sec)	Re †† (x 10^4)
1	0	DIV	28.1	2.61	1.548	5.25	0.027	14.64	2.17
		DIV	28.1	2.61	1.548	5.25	0.027	14.64	2.17
2	0.85	DIV	96.4	2.92	0.505	1.71	0.018	6.93	2.43
		CONV	-186.4	-3.94	0.352	1.19	0.016	5.44	3.28
3	2.89	DIV	156.2	1.93	0.206	0.70	0.014	3.81	1.61
		DIV	273.6	2.99	0.182	0.62	0.013	3.53	2.49
		DIV	152.6	1.82	0.199	0.68	0.013	3.72	1.52
		CONV	-109.7	-1.06	0.166	0.56	0.012	3.30	0.88
4	5.56	DIV	422.7	3.48	0.137	0.46	0.012	2.93	2.90
		DIV	211.7	1.95	0.154	0.52	0.012	3.16	1.62
		CONV	-216.6	-1.52	0.117	0.40	0.011	2.60	1.26
		CONV	-427.7	-2.73	0.106	0.36	0.011	2.46	2.27
5	7.40	DIV	103.4	3.64	0.587	1.99	0.019	7.67	3.03

*From Eq. (6.6)
**From Eq. (6.9)
†From Eq. (6.10)
††From Eq. (6.13)

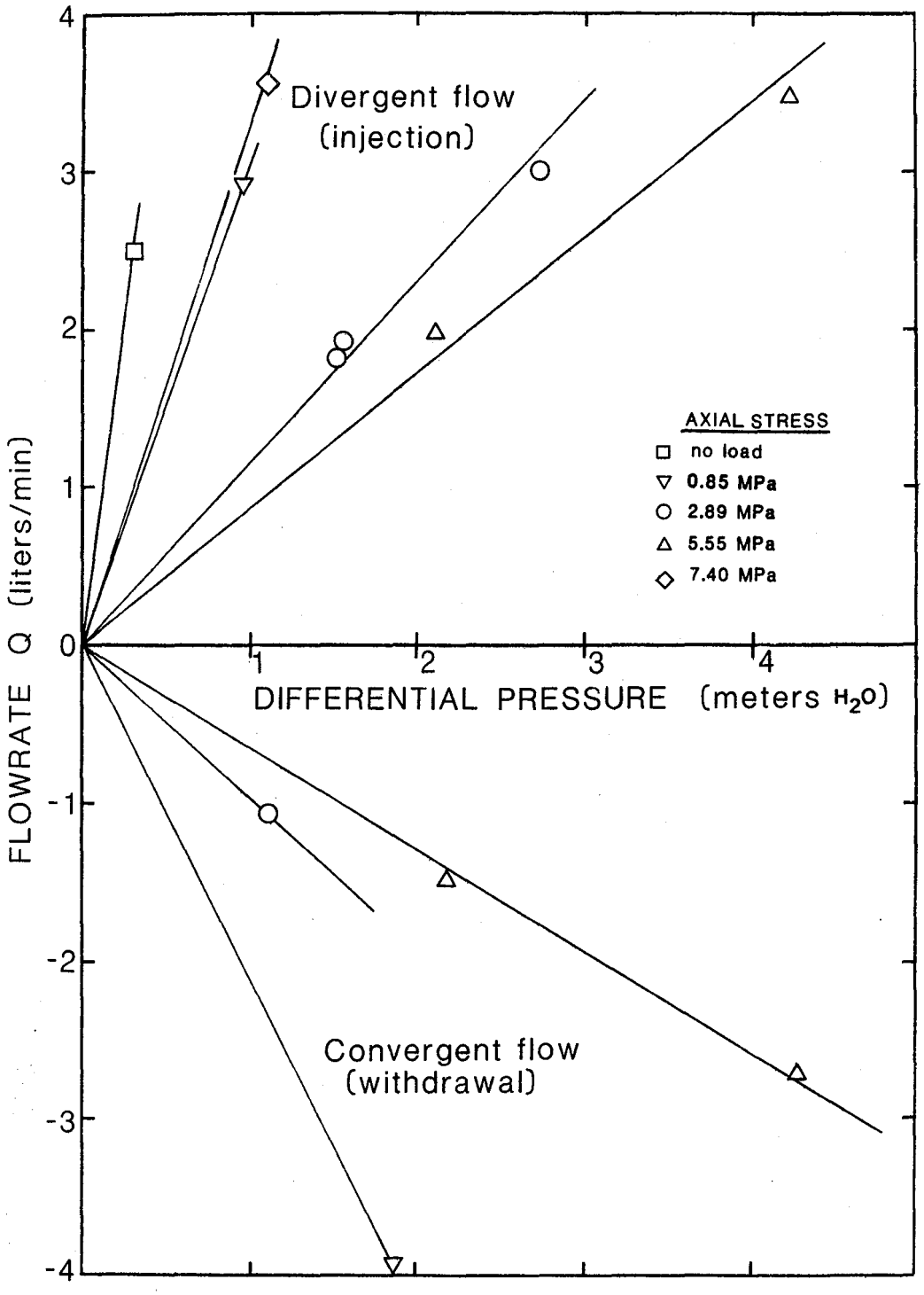

XBL 808-11523

Fig. 6.27 Measured overall flowrate versus differential pressure head.

at the fracture boundaries. Using a single-fracture model the upper-bound Reynolds numbers were calculated and are given in Table 6.3. Louis (1969) has suggested that turbulent flow can be present in natural fractures at such high Reynolds numbers.

The apparent differences between divergent and convergent flow shown by Fig. 6.27 are further indications of the complexity of the hydraulic properties of the core. The absolute slopes of the divergent data are generally higher than those for the convergent, as shown by the $Q/\Delta h$ values in Table 6.3. Such behavior is probably due to the opening of fractures by internal pressure and their closure upon external pressurization. Bernaix (1969) has proposed a similar test as an index measurement of degree of rock fissuring, but his recommended pressure gradients are much greater than those employed here. In the present context, the inclined set of fractures are most likely responsible for the divergent flow being higher than the convergent, since they would tend to have been opened preferentially by the tangential tension generated by outward flow from the borehole.

6.2.2 Macroscopic Stress-Flow Relationship

Assuming Darcy's law is applicable, the equivalent rock mass permeability of the core is

$$k_{rm} = \frac{(Q/\Delta h)\left(\ln r_2/r_1\right)}{4\pi s} , \qquad (6.6)$$

where Q is the flow rate through the core, Δh is differential pressure head between the borehole and outside the core, r_2 is 47 cm, the outside radius of the core, r_1 is 3.8 cm, the radius of the borehole, and s is 118 cm, the spacing between packers in the borehole. Computed values of k_{rm} are listed

in Table 6.3. Equation (6.6) assumes the flow through the fractured sample could be equated with radial flow through an equivalent porous medium over a core length of 118 cm. That is, porosity is assumed to be uniformly distributed throughout the rock. It would also model the permeability of a rock mass with an impermeable matrix but with fractures oriented normal to the borehole and spaced at 118 cm.

Results of the falling-head tests reported in Section 4 indicate that fracture B accounts for over 90% of the flow through the core. It is therefore reasonable, at least for conditions of low axial stress, to adopt the "fractured rock" model described by Eq. (6.6) in the present context. The fracture permeability, k_f, for such a single-fracture model has been derived by a number of authors (see, for example, Snow, 1965; Louis, 1969; Noorishad et al., 1971; and Witherspoon et al., 1977) as:

$$k_f = \frac{\rho_f}{12\mu} \; g\,(2b)^2 \quad , \tag{6.7}$$

where 2b is the apparent (absolute) aperture of the fracture, ρ_f is the fluid density, μ is the dynamic viscosity, and g is the acceleration due to gravity. In the case of radial fracture flow,

$$k_f = \frac{(Q/\Delta h)\left(\ln {}^{r}2/r_1\right)}{4\pi b} \quad . \tag{6.8}$$

Combining (6.7) and (6.8) yields

$$2b = \left[\frac{\left(\frac{12\mu}{\rho_f\, g}\right)(Q/\Delta h)\left(\ln {}^{r}2/r_1\right)}{2\pi}\right]^{1/3} \tag{6.9}$$

Substituting (6.9) into (6.8) gives the equation relating k_f to direct laboratory data:

$$k_f = \left[\frac{(Q/\Delta h)^2 \left(\ln {}^{r}2/r_1 \right)^2}{\left(\frac{12\mu}{\rho_f g} \right) (2\pi)^2} \right]^{1/3} \tag{6.10}$$

Equations (6.6) and (6.8) indicate that the relationship between k_f and k_{rm} is:

$$k_{rm} = \left(\frac{2b}{s} \right) k_f, \tag{6.11}$$

or

$$k_{rm} = \frac{1}{s} \left[\left(\frac{12\mu}{\rho_{fg}} \right) k_f^{\,3} \right]^{1/2} \tag{6.12}$$

Values of 2b and k_f calculated from the test data are listed in Table 6.4. In this connection, the packer spacing s is analogous to the spacing between parallel fractures with apertures of 2b in the equivalent rock mass.

The Reynolds numbers given in Table 6.3 were calculated by the equation

$$Re = \frac{\rho Q}{\pi \mu \, r_1}, \tag{6.13}$$

which was derived by Baker (1955) and used by Witherspoon et al. (1977) to give maximum values for flow into a fracture at the borehole wall.

Figure 6.28 compares the values of k_f from Table 6.4 with previous stress-flow results obtained by Iwai (1976), Pratt, Swolfs, et al. (1977), and Witherspoon et al. (1977). Pre-failure data for the ultra-large core are two orders of magnitude higher than the referenced data, although the rate of decrease in k_f with stress is similar to that found by Pratt et al. These differences can be attributed to differences in the mechanical properties, weathering, filling materials and other characteristics of the fractures tested in the various programs.

Table 6.4 Computation of overall flow parameters based on parallel-plate models of fractures B and D.

Flow Test No.	Axial Stress (MPa)	Changes in aperture* Δv (cm)		Results using initial apertures from flow data††					Results using initial apertures from displacement data†††				
				Fracture B		Fracture D		Overall	Fracture B		Fracture D		Overall
		B**	D†	Aperture (cm)	$(Q/\Delta h)_B$ (cm/sec)	Aperture (cm)	$(Q/\Delta h)_D$ (cm/sec)	$(Q/\Delta h)_{B+D}$ cm/sec	Aperture (cm)	$(Q/\Delta h)_B$ cm/sec	Aperture (cm)	$(Q/\Delta h)_D$ cm/sec	$(Q/\Delta h)_{B+D}$ cm/sec
1	0	0	0	0.022	0.900	0.011	0.100	0.984	0.03	2.219	0.01	0.082	2.301
2	0.85	0.85	0.0052	0.008	0.042	0.006	0.018	0.060	0.016	0.337	0.0048	0.009	0.346
3	2.89	0.020	0.007	0.002	0.001	0.004	0.005	0.006	0.01	0.082	0.003	0.002	0.084
4	5.56	0.024	0.0055	0	0	0.005	0.010	0.010	0.006	0.018	0.0045	0.007	0.025
5	7.40	~0.026	-0.202	0	0	0.213	794	794	0.004	0.005	0.0302	2.263	2.268

*Average values for center of fracture; closure is positive.

**From Fig. 6.7.

†From Fig. 6.16.

††From preliminary flow test results; Fig. 4.2.

†††From Figs. 6.7 and 6.16 for B and D, respectively.

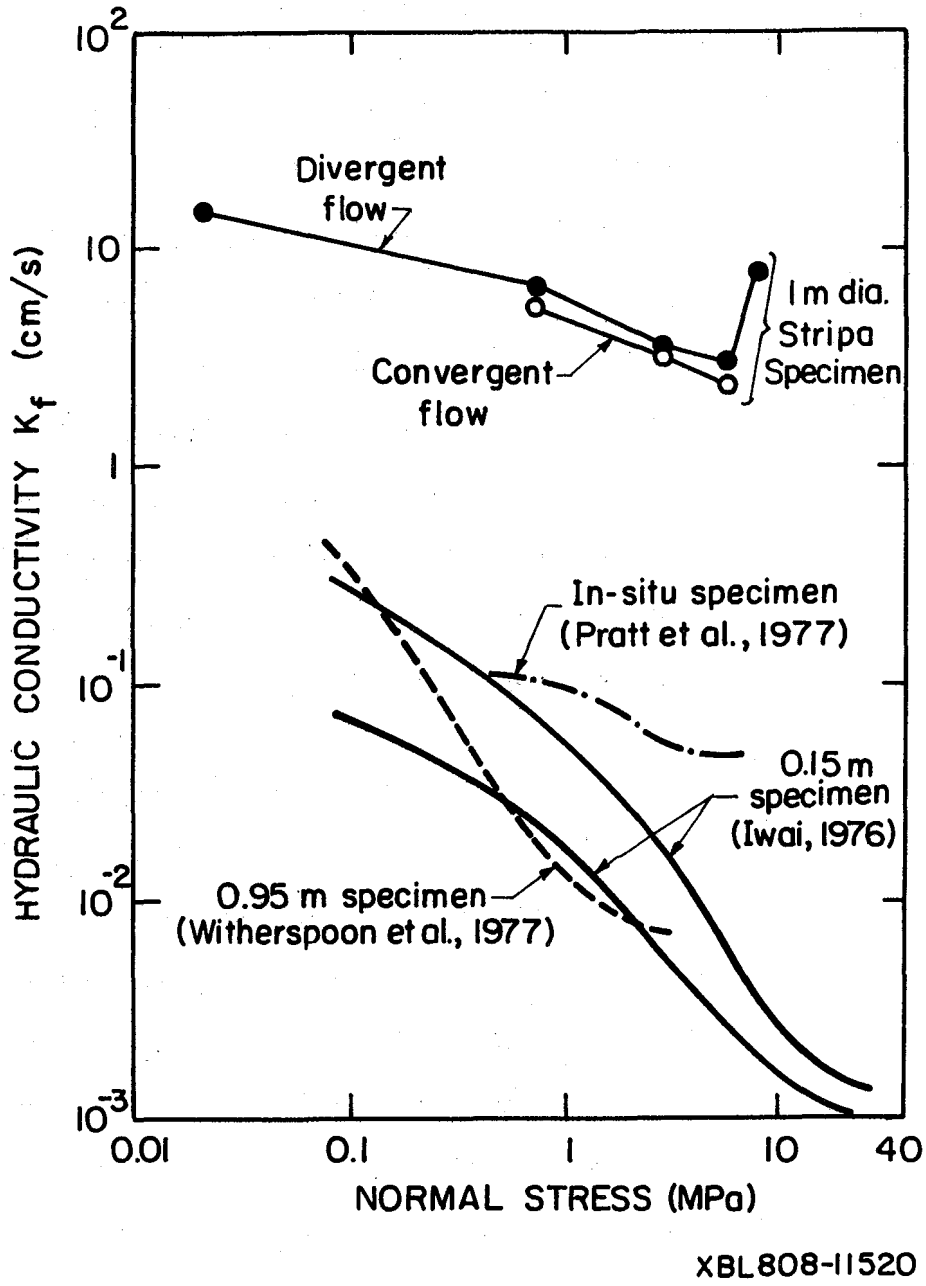

Fig. 6.28 Calculated single-fracture hydraulic conductivity versus axial stress, compared with previously published data.

6.2.3 Relationship Between Flow and Fracture Deformations

A definite linkage between the overall flowrate and measured fracture deformations would be difficult to establish for the Stripa core due to the complicated flowpaths illustrated in Fig. 4.3 and Table 4.1. However, if it is assumed that fracture B remained the dominant flowpath even at higher stresses, then a simplified analysis can be made. According to results of the preliminary flow testing, the inclined fracture D was the second most conductive. The flow-per-unit-head, $Q/\Delta h$, for this fracture was approximately 10% of that for fracture B. Fracture C followed this by nearly another order of magnitude decrease. Therefore, in the following discussion only fractures B and D are considered. The approach is to estimate values of the overall flow per unit head based on fracture deformation measurements, then to compare these with the measured values of $Q/\Delta h$.

A correct numerical simulation of the core and its discontinuities would necessarily be three-dimensional; however, for present purposes the flow system can be grossly simplified by assuming that fractures D and B are hydraulically independent and that each can be analytically modeled as parallel-plate conduits. While this assumption ignores the intersection of these fractures, it is legitimate from the standpoint of their relative hydraulic conductivities. In other words, errors introduced in the characterization of fracture D are at least an order of magnitude less than those for fracture B. Although flow on fracture D may not have been truly radial, this further simplification is made and we assume that the distance over which the pressure head is dissipated is equal to the radius of the core. Given these assumptions, the connection between the mechanical fracture data and hydraulic behavior is then given by Eq. (6.9). By rearranging (6.9) and assuming

a linear $Q/\Delta h$ relationship, the total flow parameter is the sum of contributions from n parallel fractures:

$$(Q/\Delta h)_{total} = \frac{-2\pi \quad \rho fg}{12\mu \left(\log_e \quad r_2/r_1\right)} \sum^{n} (2b)_i^{\,3} \quad . \tag{6.14}$$

Because of the cubic relationship, the crucial factor in applying Eq. (6.14) is the magnitude of the fracture aperture, 2b. With the changes in apertures given by Figs. 6.7 and 6.15, the absolute apertures of the two fractures were estimated in two ways. First, estimated asymptotes to the curves in Figs. 6.6 and 6.15, V_{mc}, were taken as the initial (no load) fracture apertures. According to Table 6.3, these were estimated to be 0.3 mm and 0.1 mm for B and D, respectively. Subtracting the respective values of Δv from these numbers then gave the absolute apertures listed in Table 6.4.

In the second method, apertures were estimated through the use of the preliminary flow test data presented in Fig. 4.2, Section 4. Values of $Q/\Delta h$ for fractures B and D were about 0.9 and 0.1 cm^2/sec, and by Eq. (6.9) these correspond to apertures of 0.22 and 0.11 mm, respectively. Absolute apertures were then computed as described above, and these estimates are also listed in Table 6.4.

Using Eq. (6.14) for a single fracture, flows-per-unit-head were calculated from the absolute apertures and listed in Table 6.4 for fractures B and D. For each level of axial stress these flows were then summed according to Eq. (6.14) to give estimates of the overall $Q/\Delta h$. Figure 6.29 compares these with the average measured $Q/\Delta h$ values listed in Table 6.3. Both the calculated zero-stress values of $Q/\Delta h$ are near the measured values.

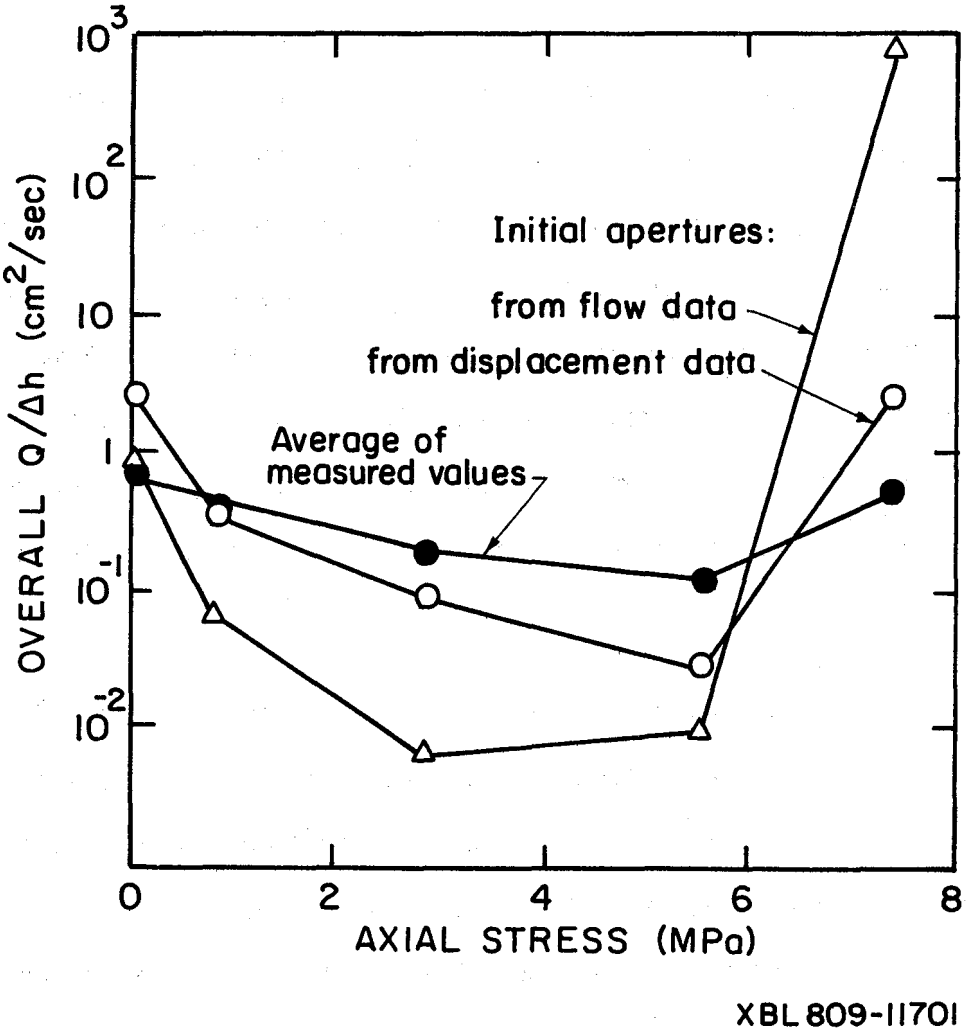

Fig. 6.29 Measured and calculated overall flows-per-unit-head versus axial stress. Simple two-fracture model assumed.

However, the changes in $Q/\Delta h$ calculated from the LVDT data diverge significantly from the measured data. This is probably due to the inadequacy of the simplified model to represent the complexity of the flow regime.

The simplified model, that considered flow only through two separated fractures, could not account for the full complexity of the actual hydraulic regime. It is also probable that the flow on fracture B was not uniformly radial. There was evidence of shear deformation on fracture B, which may have affected its hydraulic properties in ways that could not be accounted for by a simple one-dimensional closure of parallel plates.

7. CONCLUSIONS AND RECOMMENDATIONS

The tests conducted on the sample of granitic Stripa rock demonstrated the feasibility of retrieving, preparing, and testing ultra-large core specimens of naturally fractured rock. The pervasively fractured nature of the core complicated its mechanical and hydraulic behavior. For this reason, the test data does not lend itself easily to quantitative study of the basic phenomena controlling the mechanical and hydraulic behavior of discrete fractures. However, the sample was representative of a highly fractured rock mass and thus was typical of the complex material frequently encountered in the practical engineering design of underground facilities.

7.1 Mechanical Behavior

The macroscopic stress-strain response of the core was markedly nonlinear, but the tangent modulus of deformation measured prior to failure was 52.3 GPa, which is within the range obtained from small diameter samples of Stripa granite. The peak unconfined compressive strength of the core was 7.55 MPa, and failure occurred at 0.06% strain. These values are much less than those obtained from tests on small diameter cores of the type typically used in laboratory tests. At low stress levels, however, the deformation response of small samples was also nonlinear, and for conditions prior to failure the macroscopic axial stress-strain response of the large core was approximately similar at comparable levels of stress and strain. The weakness of the large core was clearly related to the adverse orientation of major fractures relative to the direction of loading. The shear strength of such fractures increases markedly with confining pressure. The unconfined conditions in the test arrangement reported here are not generally representative of the stress field in the rock mass around underground openings.

It is therefore misleading to attribute the relative weakness of the large core solely to a "size effect." To fully describe the properties of such a fractured rock mass, it is necessary to perform a complete series of experiments that include tests over the appropriate range of confining pressures. In evaluating test results it is also necessary to consider other factors that influence sample strength, such as sample disturbance, heterogeneity, anisotropy, fracture orientation, and stress history.

The test program provided the opportunity to study the relationship between the macroscopic deformation behavior of the core and the localized displacements occurring on fractures and within the intact rock. It was found that, at locations on the core remote from major discontinuities, the assumption of a simple uniaxial stress field is reasonably accurate. However, there was evidence of significant perturbation of the stress field close to fractures and their intersections, particularly near discontinuities under shear loading. The near-field state of stress has a controlling effect on fracture behavior and consequently on the macroscopic behavior of a rock mass. In tests where measured parameters are sensitive to the deformation behavior of fractures, it is recommended that sufficient instrumentation be provided to define the state of stress in close proximity to the fractures. This is particularly important to the study of the coupling between the hydraulic and mechanical properties of fractured rock.

The number of instruments mounted on the core was large compared to that used in conventional tests. Even so, they were insufficient to provide a detailed description of its complex behavior under load. Several instruments failed in service and this further limited the available data. Im-

proved instrument designs (particularly for LVDTs) are required if they are to operate reliably when immersed under water in the triaxial vessel. The number of feed-throughs for instrument signal conductors also needs to be increased. However, there is a practical limit to the number of instruments that can be used and this should always be considered in sample selection and experiment design.

7.2 Coupled Hydraulic-Mechanical Behavior

Compared to results from previous studies of the permeability of fractured rock, the permeability of the large Stripa core was more than two orders of magnitude greater. This observation must be considered in its proper context if inferences are to be drawn about the hydraulic properties of the rock mass in the Stripa mine. The boundary conditions applied to a sample in uniaxial compressive tests are not, in general, similar to those acting on an element of rock located at some arbitrary point around an underground opening. Fully defining the coupling between stress and fluid flow would require performing many additional tests to model the complete range of conditions prevailing in the rock mass. Such tests would consider the relationship between fracture orientations and the direction of principal stresses. Only in rare instances is such comprehensive testing possible. For practical design, rock mass properties are estimated by synthesis of data from different laboratory and in situ testing techniques. Applied in this way, the permeability data obtained from the ultra-large core tests could provide a basis for estimating the hydraulic properties of rock close to the ribs of the underground entries at Stripa.

The large core was by necessity sampled from the rock immediately adjacent to an underground opening. These zones suffer disturbance due to

blasting and stress changes resulting from the excavation. Rock further away from the opening is less influenced by these effects and its in situ permeability may be less than that of our sample. One of the principal fractures in the core was separated during preparation. Other disturbances must have occurred during coring, shipping and handling. All these effects can be expected to have altered the hydraulic properties of the core and probably increased its permeability relative to its in situ condition. Because fracture conductivity is a function of the cube of the aperture, it can be assumed that sample disturbance has a major influence on the measured hydraulic properties of fractured rock. Little, if any work, has been done to investigate these effects. There is need for research to investigate the magnitude of error introduced by sample disturbance and to develeop techniques by which its effects may be minimized or accounted for.

The hydraulic regime within the test sample was modeled through a simplified parallel plate analogy. This required gross simplifying assumptions to be made with respect to: flow paths in the core; the geometry of the fracture system, and of flow within specific fractures; absolute fracture apertures; and the hydraulic boundary conditions. Flows-per-unit-head ($Q/\Delta h$) calculated from this model, using fracture apertures estimated from measurements of fracture closure, were at least an order of magnitude lower than measured values of $Q/\Delta h$. This result suggests that flow through natural fracture systems as complex as those in the large Stripa core is not amenable to quantitative analysis by simplified analogs. However, the test program has nevertheless yielded a data base that should be valuable to the development and verification of more advanced models, including computer-aided numerical techniques.

ACKNOWLEDGMENTS

The Rockfill Testing Facility in Richmond, California is the property of the California Department of Water Resources (DWR) and is operated under lease by LBL. Mr. William D. Hammond is the DWR's technical representative. His enthusiastic cooperation materially assisted the research program. Professor John Gale of the University of Waterloo provided major guidance in experiment design and Mr. Clarence Chan of the University of California freely contributed experienced advice in the area of test procedure and equipment design. Many individual members of the staff of LBL and the University of California contributed to the project effort, notably J.B. Greer, W.E. Canaday, and R. Hall (electronics and instrumentation), M.C. Moebus, I.W. Lee and R.W. Davies (mechanical equipment), G.C. Pelatowski (illustration), and L.L. Egenberger, B. Jones and L.T. Armetta (report preparation). This project was sponsored by the U.S. Department of Energy through the Office of Nuclear Waste Isolation, Battelle Memorial Institute, under Contract W-7405-ENG-48. M.R. Wigley acted as project manager for the Office of Nuclear Waste Isolation. His support for the work is gratefully acknowledged.

REFERENCES

American Concrete Institute (ACI). 1977. "Recommended Practice for Selecting Proportions for Normal and Heavyweight Concrete." (ACI 211.1-77).

Andersson, B. and P.A. Halén. 1978. Mining Methods Used in the Underground Tunnels and Test Rooms at Stripa. Lawrence Berkeley Laboratory Report LBL-7081, SAC-08, Berkeley, California.

Anamet Laboratories, Inc. 1980. Chemical Analysis and Compound Identification of Deposits. Lab No. 380.439. Berkeley, California.

Baker, W.J. 1955. "Flow in Fissured Formations." Proceedings Fourth Petroleum Congress, Rome, Vol. II, pp. 379-393.

Becker, E., C.K. Chan and H.B. Seed. 1972. Strength and Deformation Characteristics of Rockfill Materials in Plane Strain and Triaxial Compression Tests, Geotechnical Engineering Report No. 72-3, University of California, Berkeley.

Bernaix, J. 1969. "New Laboratory Methods of Studying the Mechanical Properties of Rocks." Intl. J. Rock Mech. Min. Sci., 6, p. 43.

Bouwer, H. 1978. Groundwater Hydrology. McGraw-Hill, Inc. pp. 113-117.

Broch, E. and J.A. Franklin. 1972. "The Point Load Test." Int. J. Rock Mech. Min. Sci., 9, pp. 669-697.

Cook, N.G.W., and P.A. Witherspoon. 1978. Mechanical and Thermal Design Considerations for Radioactive Waste Repositories in Hard Rock. Part II: In Situ Heating Experiments in Hard Rock: Their Objectives and Design. LBL-7073, SAC-10, UC-70. Berkeley, California.

Deer, W.A., R.A. Howie, and J. Zussman. 1962. Rock Forming Minerals. Longmans, Green & Co., Ltd., London.

Gale, J.E. 1975. A Numerical, Field and Laboratory Study of Flow in Rocks With Deformable Fractures. Ph.D. Thesis, Department of Civil Engineering, University of California, Berkeley, California.

Gale, J.E. and P.A. Witherspoon. 1979. An Approach to the Fracture Hydrology at Stripa: Preliminary Results. LBL-7979, SAC-15. Berkeley, California.

Goodman, R.E. 1976. Methods of Geological Engineering in Discontinuous Rock. West Publishing Co., St. Paul, Minn.

Hebert, A.J. and K. Street, Jr. 1973. A Nondispersive Soft X-ray Fluorescence Spectrometer for Quantitative Analysis of the Major Elements in Rock and Minerals. Lawrence Berkeley Laboratory Report LBL-1616, Berkeley, California.

Heuzé, F.E. 1980. "Scale Effects in the Determination of Rock Mass Strength and Deformability." Rock Mechanics, 12, pp. 167-192.

Hsu, R. and D.J. Watkins. 1979. Calibration of Load Cell-Rockfill Test Facility. University of California, Richmond, California.

International Society for Rock Mechanics (ISRM). 1978. Suggested Methods For Determining the Strength of Rock Materials in Triaxial Compression. Pergamon Press, London, England.

Iwai, K. 1976. Fundamental Studies of Fluid Flow Through a Single Fracture. Ph.D. Thesis, Department of Civil Engineering, University of California, Berkeley, California.

Jaeger, J.C. 1966. "The Brittle Fracture of Rocks." Proceedings of the Eighth Rock Mechanics Symposium. American Institute of Mining Engineers, University of Minnesota, Minneapolis, Minnesota.

Jaeger, J.C. and N.G.W. Cook. 1976. Fundamentals of Rock Mechanics, 2nd edition. Chapman and Hall, London.

Kurfurst, P.J., T. Hugo-Persson and G. Rudolph. 1978. Borehole Drilling and Related Activities at the Stripa Mine. LBL-7080, SAC-05. Berkeley, California.

Lambe, T.W. 1951. Soil Testing for Engineers. John Wiley and Sons, New York, pp. 52-60.

Louis, C. 1969. A Study of Groundwater Flow in Jointed Rock and its Influence on the Stability of Rock Masses. Imperial College Rock Mechanics Research Report No. 10. London, England.

Noorishad, J., P.A. Witherspoon, and T.L. Breke. 1971. A Method for Coupled Stress and Flow Analysis of Fractured Rock Masses. Geotechnical Engineering Report No. 71-6, University of California, Berkeley.

Olkiewicz, A., J.E. Gale, R. Thorpe, and B. Paulsson. 1979. Geology and Fracture System at Stripa. LBL-8907, SAC-21, UC-70. Berkeley, California.

Pratt, H.R., A.D. Black, W.S. Brown, and W.F. Brace. 1972. "The Effect of Specimen Size on the Mechanical Properties of Unjointed Diorite." Intl. J. Rock Mech. Min. Sci., 9, pp. 513-529.

Pratt, H., T.A. Schrauf, and L. Bills. 1977. Summary Report - Thermal and Mechanical Properties of Granite - Stripa, Sweden. Terra Tek Report no. TR 77-92. Salt Lake City, Utah.

Pratt, H.R., H.S. Swolfs, W.F. Brace, A.D. Black and J.W. Handin. 1977. "Elastic and Transport Properties of In Situ Jointed Granite." Intl. J. Rock Mech. Min. Sci. Geomech. Abstr. 14: 35-45.

Snow, D.T. 1965. A Parallel Plate Model of Fractured Permeable Media. Ph.D. Thesis, Department of Civil Engineering, University of California, Berkeley, California.

Swan, G. 1978. The Mechanical Properties of Stripa Granite. LBL-7074, SAC-03. Berkeley, California.

Thorpe, R. 1979. Characterization of Discontinuities in the Stripa Granite --Time Scaled Heater Experiment. Lawrence Berkeley Laboratory Report LBL-7083, SAC-20. Berkeley, California.

Witherspoon, P., C. Amick, J. Gale. 1977. Stress-Flow Behavior of a Fault Zone with Fluid Injection and Withdrawal. Report to U.S. Geological Survey. Department of Mining Engineering, University of California, Berkeley.

Witherspoon, P.A., C.H. Amick, J.E. Gale, and K. Iwai. 1979. Observations of a Potential Size-Effect in Experimental Determination of the Hydraulic Properties of Fractures. LBL-8571, SAC-17. Berkeley, California.

Witherspoon, P.A., and O. Degerman. 1978. Swedish-American Cooperative Program on Radioactive Waste Storage in Mined Caverns Program Summary. LBL-7049, SAC-01. Berkeley, California.

Witherspoon, P.A., J.S.Y. Wang, K. Iwai, and J.E. Gale. 1979. Validity of Cubic Law for Fluid Flow in a Deformable Rock Fracture. LBL-9557, SAC-23. Berkeley, California.

Witherspoon, P.A., D.J. Watkins, N.G.W. Cook, M. Hood, and J.E. Gale. 1979. "Laboratory Investigations on the Hydraulic and Thermomechanical Properties of Crystalline Rock." Proceedings, National Waste Terminal Storage Program Information Meeting. October 30 - November 1, 1979. Office of Nuclear Waste Isolation, Columbus, Ohio, pp. 19-25.

APPENDIX I

SAMPLE PREPARATION

A1.1 SAMPLING AND TRANSPORT

The cylindrical core (94 cm diameter by 166 cm long) was recovered by a slot drilling technique that has been described by Andersson and Halén (1978). A 64 mm diameter pilot hole was first drilled to a depth of 25 cm into the rib of the entry. This hole was then extended to 160 cm depth with a 35 mm bit, such that an anchor bolt could be installed through the long axis of the core. A pretensioning load of 100 kgm was applied to the bolt to hold the core in compression. Coring of the sample was done by percussion drilling a series of 52 peripheral holes, to form a slot, cylindrically around the pilot hole. Each hole was made with a 51 mm diameter drill, held in place by a guide which followed the previously drilled hole. The first peripheral hole ("first hole") was used to define an orienting base line for the geometry of the core and its fracture system. With the slot completed, the core broke along a pre-existing fracture at the bottom of the hole and was pulled from the rib, as shown in Fig. A1.1. After removal from the core hole, the sample was protected by a cage of steel reinforcing bars, packed in rubber and timber padding, and crated for shipment to the U.S. (gross shipping weight 4000 kg.).

A1.2 CORE DIMENSIONS BEFORE PREPARATION

The gross dimensions of the core were approximately 94 cm diameter and 166 cm mean length. The slot drilling technique gave the core a fluted appearance (see Fig. 1.1). The flutes had a typical cord length of 50 mm and a depth of 18 mm. The dimensions of the core deviated somewhat from a right cylindrical prism. At any point along the axis the section deviated from a

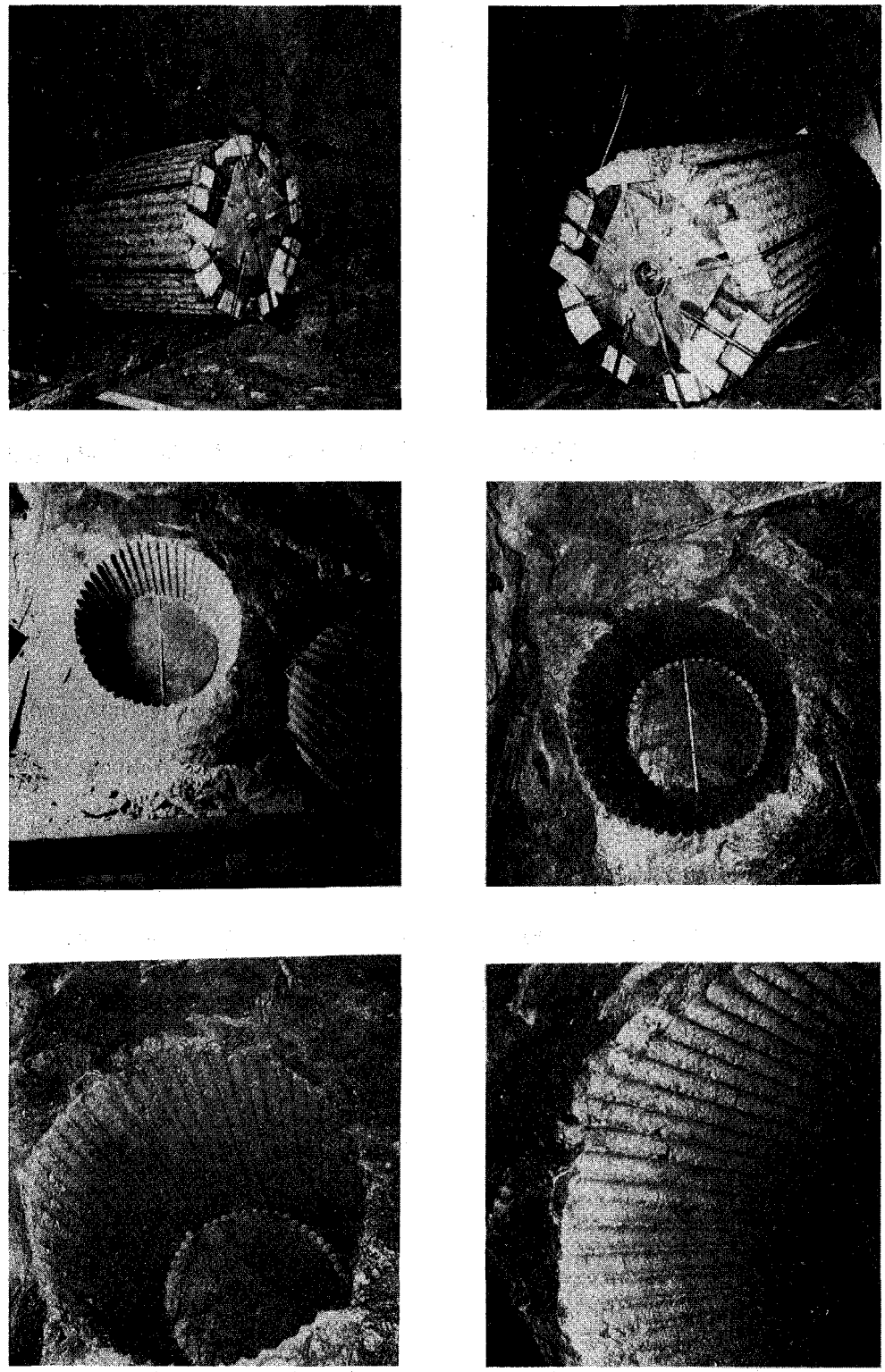

XBB-788-10480

Fig. A1.1 Core as recovered from rib of entry.

circular form by about ± 2 cm across a chord through the center, and the mean diameter at the top of the core was some 2 cm greater than the diameter at the bottom. For present purposes, however, it may be assumed that the core is a right cylindrical prism of 93.7 cm mean diameter measured inside the flutes. The top of the core formed by the rib of the underground entry had an irregular surface approximately normal to the long axis. The bottom of the core was formed by a natural fracture oriented at about 15° to the normal of the axis. The 35 mm diameter hole through the center of the core deviated from this axis by approximately 2°. The principal core dimensions are shown in Fig. A1.2.

A1.3 PREPARATION FOR TESTING

As delivered to the test facility, the core was crated in a horizontal orientation supported by a timber cradle designed to prevent rolling. After removal of the reinforcing bar cage, the core was firmly strapped to the cradle using cargo banding and wire ropes padded by 2.5 cm by 2.5 cm wood battens. All lifting loads during core preparation were applied to the wooden cradle so that no significant tensile or bending stresses were applied to the core.

Before standing upright, the bottom of the core was sandblasted to remove a thin layer of fracture filling material adhering to the surface. The core was rotated into the vertical, bottom up, orientation using a five-ton monorail crane and wire rope rigging. To avoid damage to the unprotected top of the core, the sample was lowered into a sandbox containing 30 cm deep sand. The support cradle and cargo banding were then removed from the core. To avoid undesirable stress concentrations and minimize the

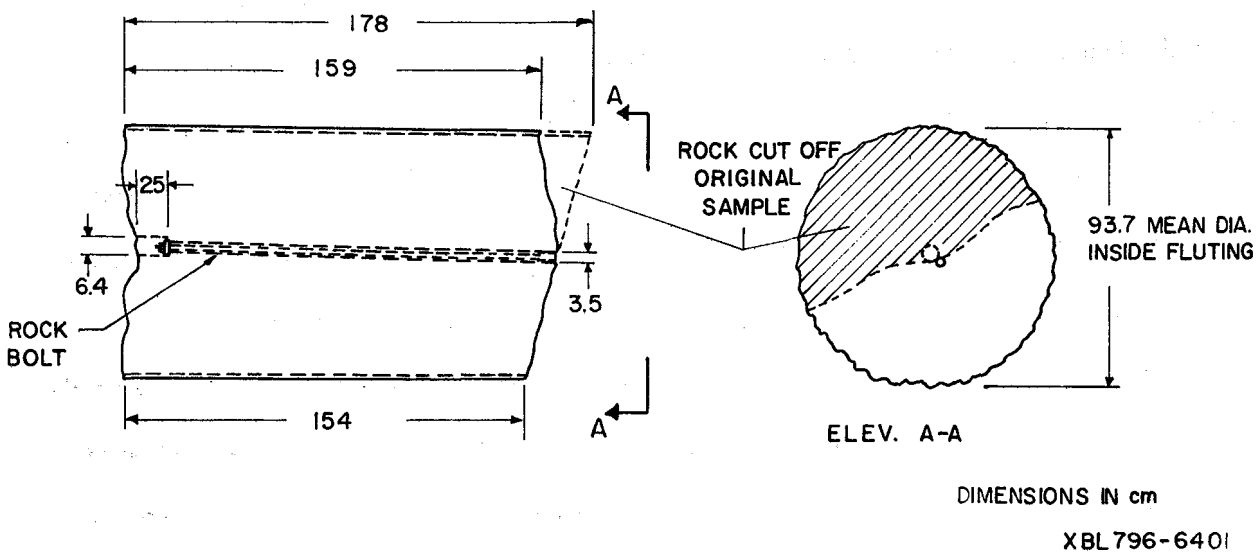

Fig. A1.2 Dimensions of core before capping.

thickness of the end cap, a portion of the bottom of the core was cut away as shown in Fig. A1.2. This portion of the rock was removed by drilling 2.2 cm diameter holes at 15 cm centers horizontally into the core and driving in feather wedges to split off the rock. Considerable difficulty was experienced during this procedure due to the fractures in the core. The feather wedges split away rock only as far as the nearest discontinuity so that many successive cycles of hole drilling and wedging were required. The inclined fracture surfaces tended to force the bit off line. This resulted in excessive damage to the bits. A rotary hammer and carbide-tipped masonry bits were used initially. These bits gave rapid hole penetration, but the carbide tips tended to fracture easily. Diamond core bits had longer life but were also subject to excessive wear. Typical diamond bit life was 1.5 meters of hole.

To test the core under uniaxial loading it was necessary to construct flat and parallel caps at each end of the core. These were constructed from reinforced concrete. They were designed as simple slabs requiring only nominal reinforcement in concrete designed for a 28-day strength of 41.4 MN/m^2. The arrangement of the reinforcement for both caps is shown in Figs. A1.3 and A1.4. To provide a safe means of handling the core the bottom cap was also provided with a system of lifting eyes. The compression steel was anchored by epoxy cement into 2.2 cm diameter holes drilled a minimum of 10 cm into the core. The concrete mix was designed in accordance with ACI standard 211.1-77 (ACI, 1977). The mix proportions and the 28-day strength are given in Table A1.1.

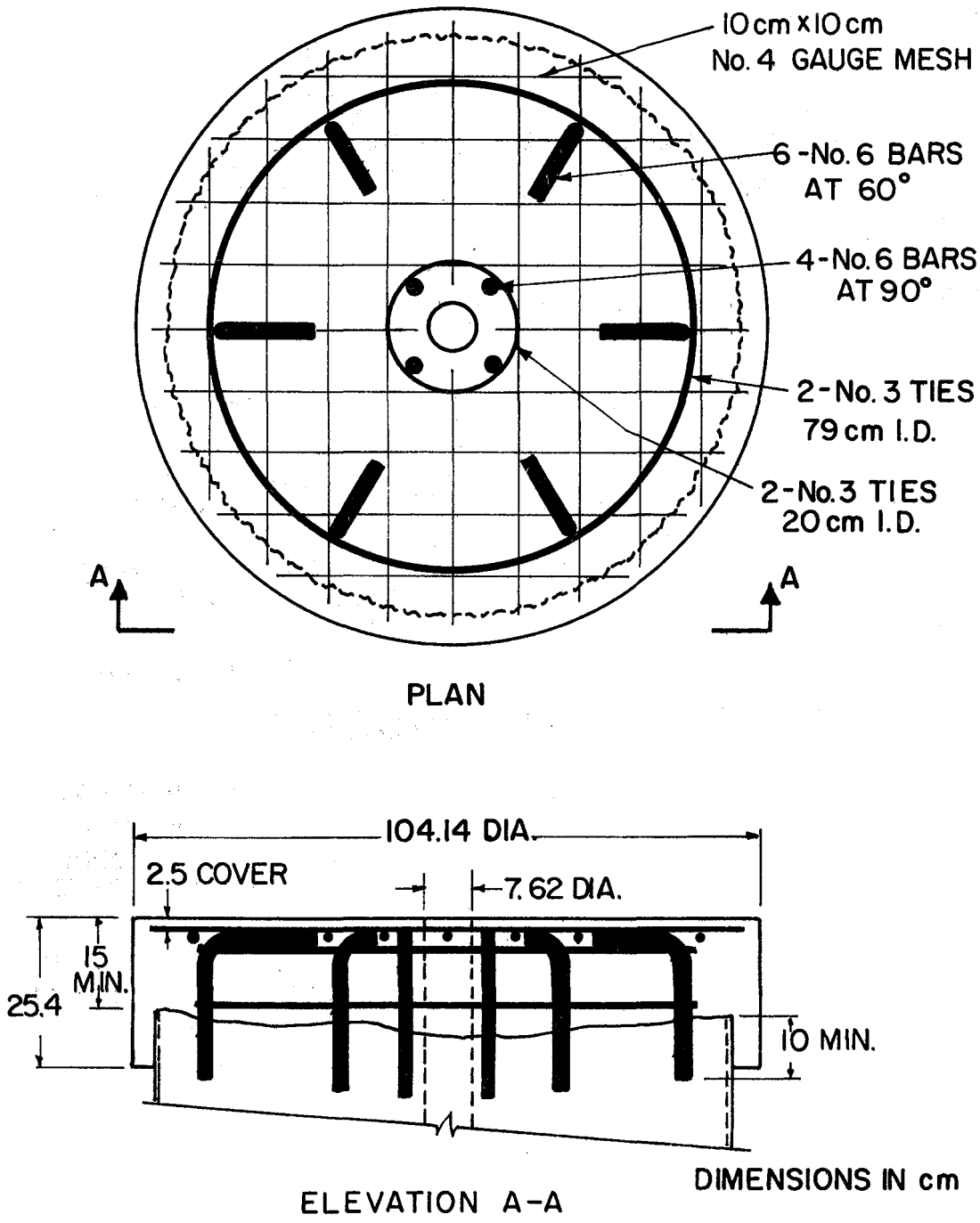

NOTES:

BARS - GRADE 60 DEFORMED

MESH - GRADE 40 PLAIN

XBL 796-6404

Fig. A1.3 Top cap reinforcement.

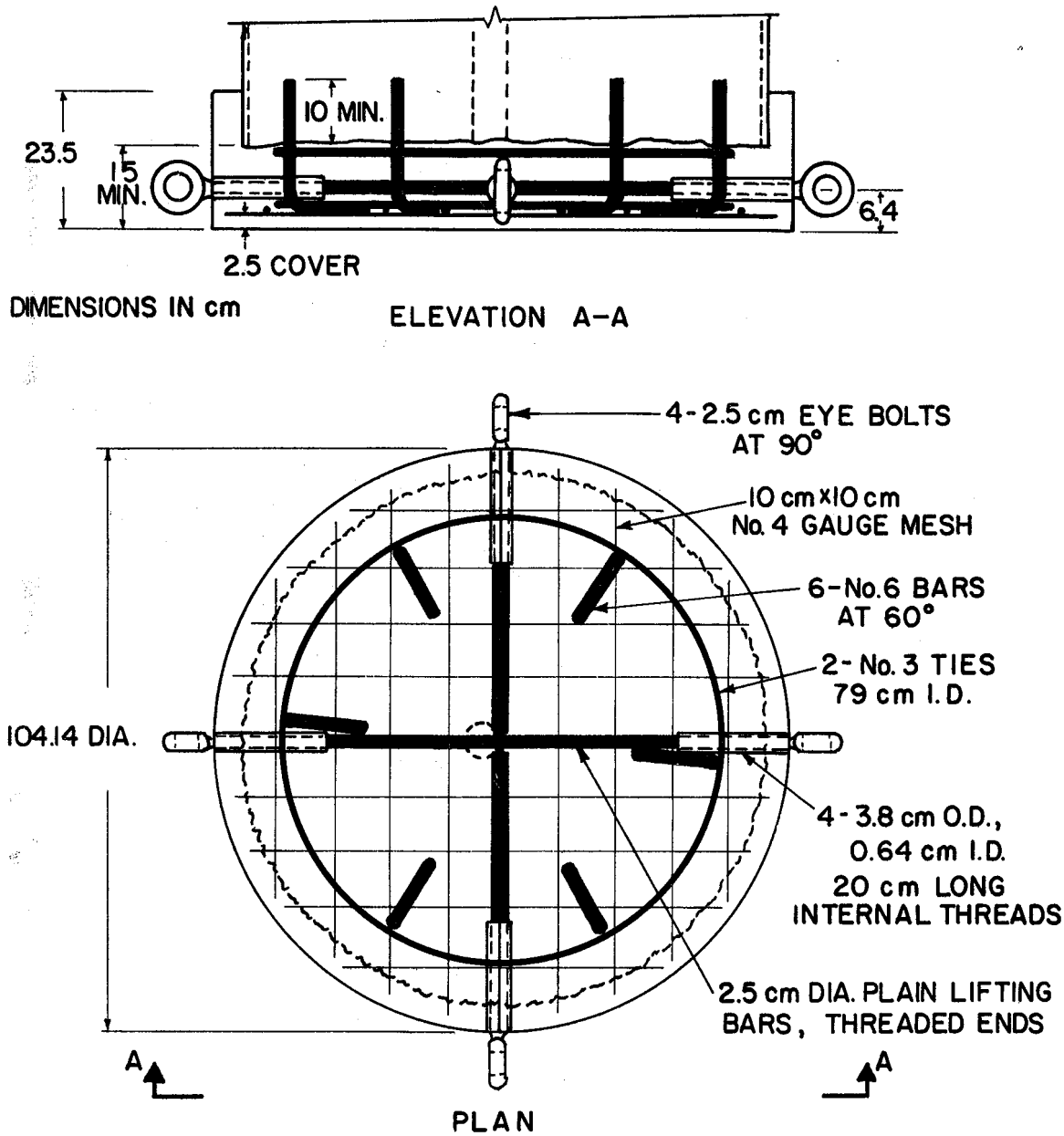

NOTES:

BARS - GRADE 60 DEFORMED

MESH - GRADE 40 PLAIN

XBL796-6403

Fig. A1.4 Bottom cap reinforcement.

Table A1.1. Concrete for Stripa core end caps.

Materials	
Sand:	Olympia Grade Zero
Coarse aggregate:	1.27 cm to No. 4 Sieve
Cement:	Type I & II
Air entrainment:	None
Nominal slump:	7.5 - 10.0 cm
Proportions per cubic meter	
Water (net)	216.55 Kg.
Cement	528.61 Kg.
Coarse agg. (dry)	944.92 Kg.
Sand (dry)	643.70 Kg.
28-Day strength	
40.88 MN/m^2*	
Elastic modulus	
1.55×10^4 MN/m^2* (for axial stress less than 20 MN/m^2)	

*Mean of three tests using 7.62 cm dia. by 15.24 cm cylinders.

Because the core was not a perfect right cylinder, the long axis was arbitrarily assumed to be parallel to the axis of the first peripheral hole drilled during core recovery. This "first hole" was then used as a reference datum for measurements. To ensure that the surface of the end cap was normal to the axis, a 60 cm x 60 cm x 2.5 cm thick aluminum plate, supported at three points by stiff modeling clay, was set on the end of the core with its surface carefully oriented normal to the axis of the "first hole." The plywood cap mold was constructed using this plate as a reference surface.

To ensure a good bond between the cap concrete and the rock, the surface of the core was treated with a custom-designed epoxy cement.* Subsequent coring through the concrete/rock joint showed that a good bond was achieved.

The bottom cap was allowed to cure under damp cloth covers for a period of seven days before the mold was removed. The surface of the cap was then lapped flat using a commercial terrazo grinder. Using the cradle and rigging system, the core was then upended into a top-up orientation and the top cap cast in a manner similar to the bottom cap; care being taken to ensure that the surfaces of both caps were flat and parallel.

For permeability testing, a 7.62 cm diam hole was required through the axis of the core. This hole was drilled using a 7.62 cm diam diamond coring bit mounted in a drill press. Because the original 35 mm rock bolt hole through the core deviated from the axial direction by about 2°, it was not possible to drill the 7.62 cm diam hole normal to the end caps, but directional drilling reduced the deviation from the axial direction to 1.3°.

*Sinmast AS15-epoxy for bonding wet concrete to rock supplied by Sinmast of California, Inc., 350 West Cutting Blvd., Richmond, CA 94802.

To avoid damage to the core during handling, an axial compression of approximately 48 KN/m^2 was applied to the core through a 19.1 mm diam. anchor bolt set in the axial borehole. Despite these precautions, the sample was separated across fracture B as the result of a rigging accident. See Section 2 and Figs. 2.3, 2.4 and 2.5.

The final configuration of the capped core is shown in Figs. 1.1 and A1.5. The net weight of the prepared core was determined to be 3628.7 kg using a 22,700 kg hydraulic dynamometer.

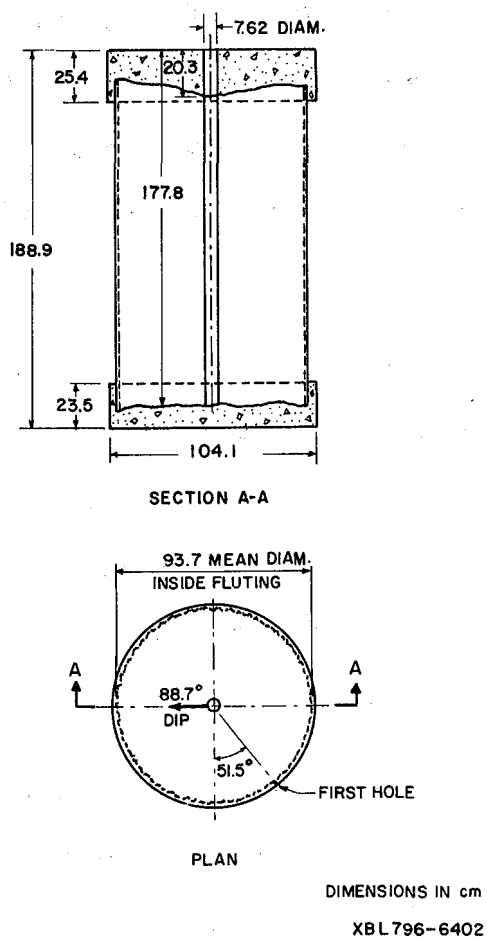

Fig. A1.5 Dimensions of capped core.

APPENDIX II

FRACTURE MAPPING AND CHARACTERIZATION

A2.1 SURFICIAL FRACTURE MAPPING

The surface expression of the fractures in the ultra-large core were mapped by wrapping the core in a sheet of clear plastic, upon which the fractures were traced. The ends of the core were mapped on separate overlays. Since the bottom surface was actually a chlorite-coated fracture, it was sandblasted before mapping in order to expose fracture traces. The resulting one-to-one maps were then photographically reduced and traced to produce the fracture layouts shown in Fig. 2.3. In general, fractures appeared to be about a millimeter or less wide. The major fractures are designated A through F in Fig. 2.3. Several apparently open zones could be observed in the major fractures.

Determination of fracture mineralization during mapping was limited to simple observation. The dominant fracture mineralization appeared to be chlorite judging from the appearance of exposed fractures on the ends of the sample. Discontinuous bands of mica with thickness of about a centimeter were present, and two lenses of light green mineralization (possibly altered muscovite) were exposed on fractures A and C.

For testing purposes, the orientations of discontinuities relative to the core axis were of primary importance. These orientations can be determined from Fig. 2.3 by use of the local coordinate system shown. Two parameters define the orientation of a planar surface in a cylindrical core: (1) The apparent dip direction relative to a known reference line, and

(2) the minimum angle between the apparent dip vector in the fracture plane and the core axis. The former is given by the clockwise angle (looking down the hole) between the lower lip of the plane and the reference line (first slot hole). This angle can be scaled from the β axis in the figure. The angle α between the plane and the core axis can be measured directly at the inflection point of the sinusoidal fracture trace, i.e., the acute angle between the tangent at this point and the vertical axis is the α angle.

A2.2 FRACTURE CHARACTERIZATION FROM AXIAL BOREHOLE

The core obtained from drilling the 7.62 cm diameter hole through the center of the sample was logged to gain additional fracture characterization data. The log is given in Table A2.1, and a schematic profile of the borehole fractures is shown in Fig. 2.3. Fractures are described according to the following:

(1) Depth of center of fracture relative to top of concrete cap.

(2) Type: Natural or induced, open or closed.

(3) Orientation-angles α and β relative to orientation line on exterior of sample.

(4) Infilling material; type of mineral, thickness, color, and surface characteristics.

Only the more prominent of the numerous hairline fractures were logged. In general, the logged fractures were naturally occurring and open upon retrieval.

An attempt was made to correlate, on an observational basis, the major fractures mapped on the exterior of the sample with features in the center core and to delineate potential flow paths. It was possible to geometrical-

Table A2.1. Ultra-large Stripa core - axial borehole log core diameter 70 mm.

Depth m	Fracture type					β°	α°	Infilling		Color	Surface* Roughness	Slickensiding	Remarks
	Natural	Induced	Open	Closed	Other			Type	Thickness mm				
0.23													Depth Ref. to Top of Concrete Cap.
0.32													Top of Granite
0.34													Bottom of Original 64 mm Hole
0.40	x		x			305	30	K,C	1	LT. GR.	2	-	Truncated by Another Fracture
0.41	x		x			295	60	K,C	<1	LT. GR.	3	-	Lower Half Lost; Curved
0.42	x		x			305	30	K,C	1	LT. GR.	2	-	Truncated by Another Fracture
0.44	x		x			295	55	K,C	1	LT. GR.	1	-	Only Thru. Half Core
0.60	x		x			345	40	K	1	DK. GR.	1	?	Planar (Fracture D)
0.74				x		0	15	C?	1	W.			Incipient
0.75	x		x			270	70	K,C	<1	LT. GR.	5	-	Curved (Fracture A)
0.79	x		x			270	60	K,C	<1	LT. GR.	1	-	Only Thru. Half Core
0.79	x		x			265	80	K,C	<1	LT. GR.	1	-	
0.84	x		x			~280	40	C	<1	W, LT. GR.	1	Slight	Vertical
0.88	x		x			320	80	C	<1	W.	2	-	
0.99	x		x			275	75	K,C	1	W, DK. GR.	2	β≈290	Drill Mud: Faint Slickenside (Fracture B)
1.03		x											
1.07				x		345	~25	C?	<1	W, LT. GR.	2-4	-	Offset 1/2 cm?
1.09	x		x			330	~25	K,C	<1	BL, W.	2-4	-	Offset 2 cm; Part Open (Fracture E)
1.16		x											
1.28	x		x			20	30	K,C	1	BL, W.	2	-	Part Open
1.28		x											
1.32	x		x			~100	~70	?	<1	?	1	-	4 parallel Fractures 1.31 - 1.33
1.35	x		x			~ 90	75	C,K	<1	LT. GR. W.	1	-	
1.38	x		x			-	90						(Fracture C)
1.47	x		x			340	20	K,C	1	BL, W.	5	?	(Fracture F)
-		x											Several Ind. Fracs. 1.51 to 1.77
1.77					x								Bottom of Granite; Sand blasted

Key:
K - Chlorite, C - Calcite, Lt. Gr. - Light Green, Dk. Gr. - Dark Green, W. - White, Bl. - Blue,
*Numbers are subjective estimates of relative roughness.

ly correlate six of these, labelled A through F in Fig. 2.3 and Table A2.1. Fractures A, B and C were continuous through the sample, and therefore easy to locate in the center borehole. Fractures D, E, and F, although apparently discontinuous, were correlated with features in the center core. However, the connection remains somewhat uncertain from the observational standpoint.

As discussed in Section 2, fracture B was accidentally opened during sample preparation. This provided the opportunity to map its surface features. The results were given in Figs. 2.4 and 2.5.

A2.3 INTERPRETATION

The dominant fractures in the core had two basic orientations. One set of principal fractures was approximately normal to the core axis (A, B and C in Fig. 2.3) and formed three essentially continuous surfaces with α angles between 75° and 90°. A fourth member of this set of fractures formed the bottom surface of the core before it was cut away during sample preparation. This surface exhibited slight traces of slickensiding.

The second dominant fracture set (D, E and F) was steeply inclined with α = 25° to 30°. These fractures were ususally discontinuous and had a wide distribution of trace lengths. Where their surfaces were exposed, no slickensiding could be detected but, as discussed in Section 2, they produced offsets of 1-2 cm on fracture B. It is not clear whether they were originally created by shearing or were extension fractures subjected to subsequent shear displacement. It is also uncertain whether the deformation occurred rapidly while the rock was plastic or resulted from long-term creep.

From the relative orientations of the fractures given in Fig. 2.3, their absolute orientations can be determined if the hole direction is known. Figure A2.1 is a stereographic projection showing the poles of fractures B, C, D, and the bottom surface of the core. The Z' vector designates the downward axis of the core hole. The fractures normal to the core axis, such as A in Fig. 2.3, correspond to the pervasive set of steeply dipping fractures in the Stripa mine reported by Olkiewicz et al. (1979) and Thorpe (1979). The fractures inclined to the axis, such as D in Fig. 2.3, correlate with the extension fracturing that is roughly perpendicular to the tabular granite body and to the direction of in situ principal stress (Thorpe, 1979).

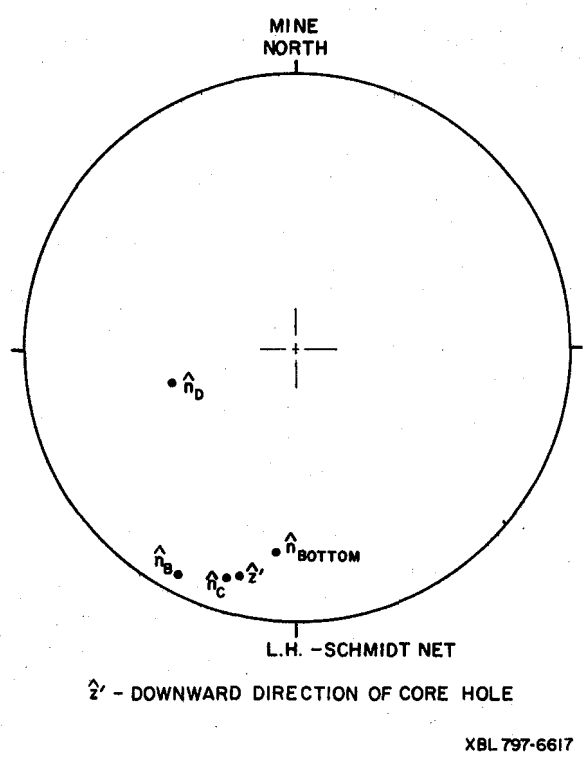

Fig. A2.1 Stereograph of major fracture poles in Stripa core.

APPENDIX III

PETROGRAPHY OF ULTRA-LARGE CORE

To study the petrography of the ultra-large Stripa core, six thin sections were prepared from material sampled from the core, and two samples of fracture fillings and the mineral separates thereof were studied using x-ray diffraction photographs and diffractograms. These were supplemented by five thin sections from rock gathered in the full-scale and time-scale heater experiment drifts (see Fig. 2.1), five x-ray diffraction patterns of samples from the full-scale drift, an electron microprobe analysis of various minerals in a sample from the full-scale drift, and a soft x-ray flourescence chemical analysis of another sample from the full-scale drift. The specific gravity of the rock forming the large core was determined from a 1040 gm sample cut from the bottom of the core. This was done by weighing the sample in air and in water. The specific gravity was 2.65 and the unit weight 2648.84 kg/m^3.

A3.1 ANALYTIC RESULTS

A3.1.1 Electron Microprobe

The abundance of the four major oxides in chlorite were obtained from a sample from the time-scale drift, using an electron microprobe. Other elements analyzed were Na, Ca, Zr, and U; their oxides were generally present only in trace amounts (<0.1 wt.%). The results are given in Table A3.1. The total percentage by weight of analyzed oxides was ~85.5%. Added to the 10-13% H_2O by weight commonly reported in chlorites, the total is 95-98%. These results can be compared with representative analyses of biotites from granite rocks compiled by Deer et al. (1962) given in Table A3.2.

Table A3.1 Electron microprobe analysis of chlorite grains in sample of Stripa granite from 4.60 m level of borehole N1 in time-scale drift.

Data averaged over 30 points

Element	Weight %	Std. Deviation
*FeO	34.24	1.02
MgO	6.25	0.33
SiO_2	24.99	0.95
Al_2O_3	19.09	0.65

*Total iron expressed as FeO. Oxidation state of iron unknown.

Table A3.2. Excerpts of chemical analyses of representative biotites from granitic rocks (Deer et al., 1962).

		1.	2.	3.	4.
Total Fe as	FeO	22.84	30.23	33.66	23.82
	MgO	8.23	4.23	0.95	7.96
	SiO_2	34.64	37.17	35.40	38.30
	Al_2O_3	16.30	14.60	11.82	13.99

1. Anal. 9, quartz monzonite, Scotland
2. Anal. 11, granite, S. California
3. Anal. 12, granite, Ireland
4. Anal. 7, granodiorite, S. California

A3.1.2 Chemical Analysis

A whole rock chemical analysis was obtained for a sample from the full-scale drift using a multiple anode soft x-ray fluorescence spectrometer (Hebert and Street, 1973). The sample was first ground to a fine powder, then fused with a $LiBO_2$ flux and poured to form a glass disc.

The analysis in Table A3.3 is an average of two analyses of this sample. Errors are computed as 2% of reported values for relatively abundant oxides, except for Na_2O for which a 5% error is used. This corresponds roughly to one standard deviation. For oxides of very low abundance, values are more approximate, as noted, and in these cases the errors signify only the variation between the two analyses.

A3.1.3 X-ray Diffraction

Tables A3.4 and A3.5 give the results of x-ray diffraction analyses of samples from fracture C and the top surface of the core, respectively. Patterns were made with a Debye-Scherrer powder camera, CuKα radiation, and Ni filter. Peaks are designated strong (s), medium (m), or weak (w), as qualitative estimates of line densities in the x-ray photographs. The weakest peaks are not listed.

In order to index these patterns to prominent d-spacings of specific minerals, separates enriched in various of the fracture-filling minerals were analyzed first. These included separates enriched in quartz, feldspars, and muscovite (i.e. chorite separated out), and a separate enriched in epidote, from fractures in cores in the full-scale drift. Prior diffraction analysis of these separates was necessary because variations in d-spacings and relative peak strengths occur in response to variations in chemical composition

Table A3.3. X-ray fluorescence major element analysis of relatively fracture-free sample from ~4.0 m level in core OH1 BH E7 in full-scale drift.

Element	Weight %
Na_2O	4.14 ± 2.1
MgO	~0.2 ± 0.7
Al_2O_2	14.24 ± 0.28
SiO_2	73.83 ± 1.48
K_2O	4.65 ± 0.09
CaO	0.85 ± 0.02
TiO_2	~0.3 ± 0.2
Cr_2O_3	<0.05
MnO	~0.03 ± 0.01
FeO	0.96 ± 0.02
Total	98.90

Table A3.4. X-ray diffraction peaks of whole fracture filling from fracture C, ultra-large core. Dominant minerals are quartz, muscovite (sericite), plagioclase, and fluorite. Some chlorite also present. (Composite of 2 readings.)

Strength*	2θ (degrees)	d(Å)	d-spacings of minerals (Å)
m-s	8.87- 8.90	9.94 -9.98	Muscovite 9.95
m-s	12.50-12.53	7.07 -7.08	Chlorite 7.05-7.08
w	19.75-19.85	4.473-4.495	Muscovite 4.47-4.48
m-s	20.83-20.90	4.250-4.264	Quartz 4.26
w	22.10-22.13	4.018-4.022	Plagioclase 4.03
s	26.63-26.70	3.339-3.347	Quartz 3.343
w-m	27.75-27.80	3.209-3.215	Plagioclase 3.20 or Muscovite 3.20
w-m	28.08	3.178	Plagioclase 3.18
w	28.30-28.35	3.148-3.153	Fluorite 3.153 or Plagioclase 3.15
w-m	34.90-34.95	2.567-2.571	Muscovite 2.56-2.57
m	36.53-36.58	2.456-2.460	Quartz 2.458
m	39.53	2.280	Quartz 2.282
m	42.43-42.48	2.128-2.130	Quartz 2.128
m-s	47.00-47.05	1.930-1.933	Fluorite 1.931
m-s	50.15-50.18	1.818-1.819	Quartz 1.817
w-m	54.90	1.672	Quartz 1.672
w-m	55.78-55.80	1.647-1.648	Fluorite 1.647
m-s	59.95-60.00	1.542-1.543	Quartz 1.541
m	67.70-67.78	1.383-1.384	Quartz 1.382
m	68.18-68.20	1.375	Quartz 1.375

* s = strong; m = medium; w = weak.

Table A3.5. X-ray diffraction peaks of chlorite-enriched separate from fracture forming top surface of ultra-large core. (Composite of 2 readings.)

Strength*	2Θ (degrees)	d(Å)	d-spacings of chloritest(Å)
m-s	6.33- 6.40	13.8-13.9	a) 14.1 b) 14.0
s	12.50-12.53	7.06-7.09	a) 7.05 b) 7.08
w	18.93-18.95	4.683-4.688	a) 4.67 b) 4.681
s	25.33-25.35	3.513-3.516	a) 3.52 b) 3.523
m	34.30-34.38	2.609-2.614	a) 2.601 b) 2.619
m	34.88-34.98	2.565-2.572	a) 2.554 b) 2.574
m	36.48-36.53	2.460-2.463	a) 2.454 b) 2.469
m	37.43-37.53	2.397-2.403	a) 2.392 b) 2.405
m	39.58-39.63	2.274-2.277	a) 2.266 b) 2.279
m-s	45.00-45.05	2.012-2.014	a) 2.009 b) 2.014
w	48.10-48.15	1.890-1.892	a) 1.882 b) 1.893
s	59.23-59.28	1.559-1.560	a) 1.551 b) 1.560
w	60.83	1.523	a) 1.513 b) 1.523

* s = strong; m = medium; w = weak

†Two varieties of chlorite have d-spacings closest to those of Stripa chlorite: a) thuringite, with somewhat lower d-spacings; and b) bavalite, with somewhat higher d-spacings. Both are somewhat richer in Fe, and poorer in Mg, than the Stripa chlorite as given in Table A3.1.

in several of these minerals, particularly in the chlorites, but also, to a lesser degree, in the feldspars and muscovite. (In addition to these, a nearly pure separate of pyrite was prepared from a fracture in the full-scale drift, and the identification of pyrite was confirmed by diffraction.)

Samples were prepared for diffraction by grinding, washing, and then sieving for the 230-320 mesh (62 μm - 44 μm) fraction. Mineral separates were then obtained by heavy liquid separation in bromoform and/or by use of the Frantz isodynamic magnetic separator.

The error in reading of diffraction films ($\Delta 2\Theta$) was less than 0.1°. This corresponds to decreasing errors in d-spacing (Δd) with increasing 2Θ (or decreasing d), shown in Table A3.6.

A3.2 MINERALOGY OF THE UNFRACTURED GRANITIC MATRIX

The term "matrix" is used here to refer to the primary minerals which crystallized from a granitic melt. The major constituents of the matrix were quartz, plagioclase, and microcline, in order of abundance. Together these comprised 90-95% of the unfractured rock. The remainder included two phases of mica, muscovite and biotite, the latter completely altered to chlorite. Garnet was also present in trace amounts, as were tiny grains, probably zircon, within the chloritized biotite.

A3.2.1 Quartz and Feldspars

Quartz and both feldspars commonly occurred in grain sizes up to 2-3 mm, but also occurred in finely intergrown aggregates. Quartz was unaltered, but the feldspars were commonly partially or completely altered.

Table A3.6. Errors in d-spacing read from diffraction films.

d	Δd*
14.0 Å	0.22 Å
10.0	0.11
7.0	0.05
3.0	0.01
1.5	0.002

* Corresponding to 0.1° Δ2θ.

Plagioclase, the Na-rich feldspar, generally contained small grains or patches of sericite alteration (a textural variety of muscovite), and occasionally small patches of calcite alteration. Where not obviously altered, plagioclase still had a dusty appearance in thin section, probably due to the growths of minute alteration products. Oligoclase (70-90 mol. % Na; 10-30 mol. % Ca) was the probable variety of plagioclase present, judging from occurrences in chemically similar granitic rocks, and from x-ray diffraction evidence.

Microcline, the K-rich feldspar, generally occurred with the crosshatch twinning characteristic of this mineral. It was perthitic to microperthitic (terms relating to the intergrowth of thin bands of the Na-rich feldspar) within the microcline host due to the slow cooling of the granitic pluton. The degree of coarseness of these intergrowths is a rough indicator of the size (and hence the rate of cooling) of the pluton; here it suggests a pluton of small to medium dimension (Deer et al., 1962). The microcline often included sericitic alteration along cleavage planes and in patches. It was less abundant but similar to the alteration in plagioclase. Also, the dusty appearance ubiquitous in the plagioclase grains was absent in the microcline, which, like quartz, was clear.

A3.2.2 Micas

The mica minerals were distributed in the matrix as isolated grains generally 0.1 to 1.0 mm in size, or more commonly in somewhat larger intergrowths of both micas. The white mica, muscovite, was clear and unaltered, or was progressively altered to chlorite or (rarely) epidote along cleavage planes. The dark mica originally crystallized as biotite, but was subse-

quently thoroughly replaced by dark green chlorite. An occasional paler brown grain, or part of a grain, was the only direct evidence that this mica was originally biotite. However, chlorite is not recognized to crystallize from a melt, whereas it is a common pseudomorphous hydrothermal alteration product of biotite in granitic rocks, where its composition is often related to that of the original biotite (Deer et al., 1962).

The percentage by weight of FeO and MgO obtained from chemical analysis may be used as indices for biotite from granitic rocks. As shown by Tables A3.1 and A3.2, these values are roughly comparable in the Stripa chlorite and the granitic biotites. (Biotites in other types of rocks generally have far lower FeO and higher MgO values). This chemical correlation provides more direct evidence for the growth of chlorite at Stripa directly from biotite of the original granitic matrix, probably with little chemical change.

A3.2.3 Trace Minerals

The trace minerals of the matrix included garnet and probably zircon. Garnet occurred as isolated anhedral grains 0.5 to 1.0 mm in size which were not quite isotopic. They were probably spessartine-almandine (Mn-Fe) garnets. Grains of zircon occurred in the chloritized biotite, commonly surrounded by strong pleochroic haloes due to inclusion in the zircon of elements of U or Th decay series. The identification of zircon is somewhat uncertain optically, as the grains are very small and often altered (possibly metamict from radiation damage). However, zircon is a common trace mineral in granitic biotite, and several grains analyzed on the microprobe (from the same sample as that analyzed in Table A3.1) gave high counts of zirconium.

A3.2.4 Chemical Composition

The chemical composition of the granitic matrix is difficult to ascertain as it is cut almost everywhere by networks of fine fractures. However, a suitable, nearly fracture-free sample was located in a core from the full-scale drift. The silica content of 73.8%, obtained by soft x-ray fluorescence (Table A3.3), shows the rock to be a quartz monzonite, rather than a granite in the strict sense. (Strictly speaking, "granite" refers to the most siliceous member of the granitic family, while quartz monzonite is one step less siliceous. In the loose sense, however, "granite" is an appropriate term for any granitic rock, and for simplicity is so used here.) This designation is also consistent with the relative abundances, of quartz and feldspars in the rock matrix. These relative abundances, however, show some variation in different samples, so that the single analysis in Table A3.3 should be taken as an approximation.

A3.3 MINERALOGY OF FRACTURE FILLINGS

An outstanding characteristic of the Stripa granite is the degree to which it is fractured. It would be difficult to draw a line greater than a few millimeters long anywhere in the rock which does not cross a fracture of some sort, and in many places the original matrix minerals are thoroughly riddled with fractures down to the finest scale.

Thin sections from the ultra-large core were examined, as well as core sections from the time-scale and full-scale drifts, where thicker fractures are more abundant. Considering the rock mass around the experiment sites as a whole, several types of fractures could be distinguished microscopically on the basis of their predominant mineralogy. Most commonly these

fracture-filling materials were found intergrown, particularly on thicker fractures, so that the distinctions between fracture types was somewhat artificial. However, in some fine fractures in the ultra-large core, the mineralogy was sufficiently distinct to make a preliminary classification.

The most common type of fracture was filled mainly with chlorite. They occurred in tiny veinlets 0.1 mm or less in width, and in fractures up to several centimeters. All but the finest of these were megascopically black or nearly so. On first inspection, they appeared to be uniformly dark chlorite. However, this was seldom the case; the chlorite in these fractures was nearly always complexly intergrown with an assortment of other minerals. Chief among these was quartz, which was almost as abundant as chlorite in these fractures and which occurred as tiny grains of about the same size as the chlorite grains (generally <<0.1 mm). Plagioclase grains of similar size occurred less commonly. Both these and the quartz grains appeared to have grown in place in the smaller chloritic fractures (up to 1 or 2 mm, roughly), although in wider chloritic fractures there was clearly much material from the original matrix which had been broken and included with the chlorite. Also, pyrite was intergrown in these chlorite fractures, either disseminated or along veinlets of its own, and there were occasional patches of calcite and fluorite (Fig. A3.1).

A second common type of fracture occurred, generally as very thin yellow-green veins. These were predominantly sericite (fine-grained muscovite) in a distinctive growth habit of fine sheath-like aggregates. Usually, these fractures were no wider than 0.3 mm; apparently wider fractures tended to be dominated by chlorite. Intergrown with the sericite, but of much

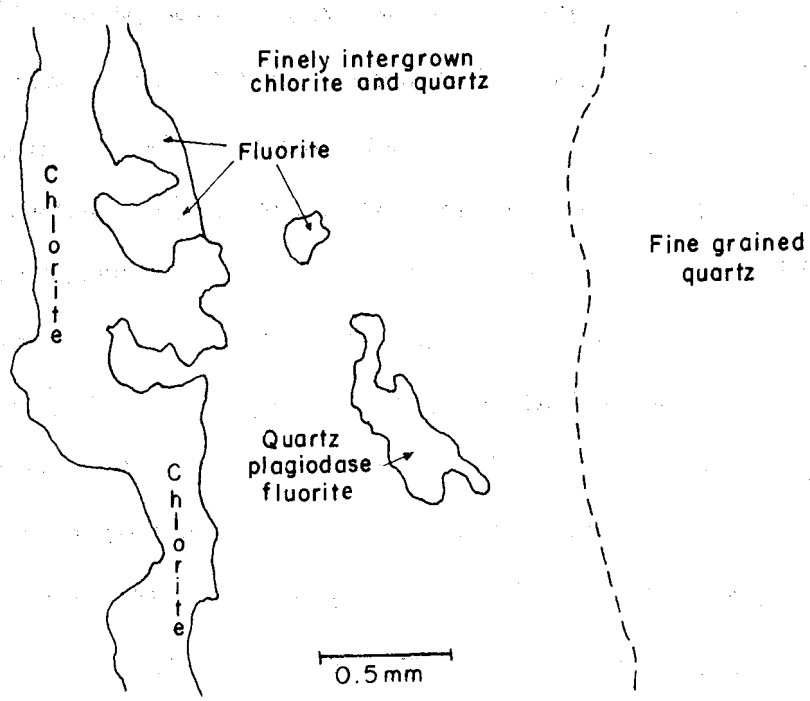

XBB 791-14877

Fig. A3.1 Chlorite-filled fracture from top surface of ultra-large core. Chlorite occurs with and without finely-intergrown quartz. Accessory minerals are fluorite and plagioclase. Plane polarized light. 40X magnification.

lesser abundance, were disseminated grains of pyrite, and prisms of epidote which were somewhat altered, probably to a clay mineral (Fig. A3.2). Also intergrown, though less abundantly still, were fluorite and calcite.

Finally, a third type of fracture filling was that dominated by epidote. Epidote was found only in one sample from the full-scale drift, and not in the ultra-large core. Nevertheless, epidote may well be present in the core. The reason for this ambiguity is that unless seen in the microscope these epidote fractures are difficult to identify. Their light green color is shared in some cases by chlorite-dominated fractures that may have an abundance of sericite or clay and very fine fault gouge material, and probably by other types of fracture fillings as well (one example from the ultra-large core is discussed below). Thus, fractures predominantly filled with epidote, though they may be fairly abundant, were not as common as would be expected from hand specimens alone. Even microscopically, epidote proved difficult to identify. This was due in part to a general clay alteration that often obscured the small prisms (<0.1 mm). Also, the epidote itself is unusual optically, with very low birefrigence and anomalous extinction. These properties may indicate an Fe-poor species of epidote, but this would be unusual since it co-exists with Fe-rich chlorite. The only reason it can be called epidote with certainty is that an x-ray diffraction pattern was obtained on the above-mentioned fracture sample, enriched in light green grains, from the full-scale drift. The peaks remaining after the quartz and feldspar peaks were deleted identify the mineral as epidote.

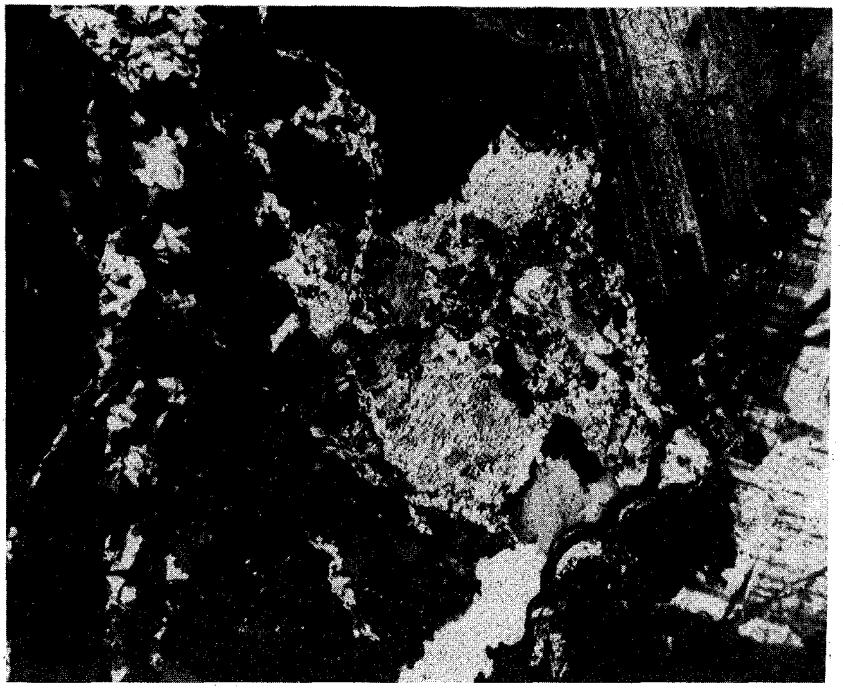

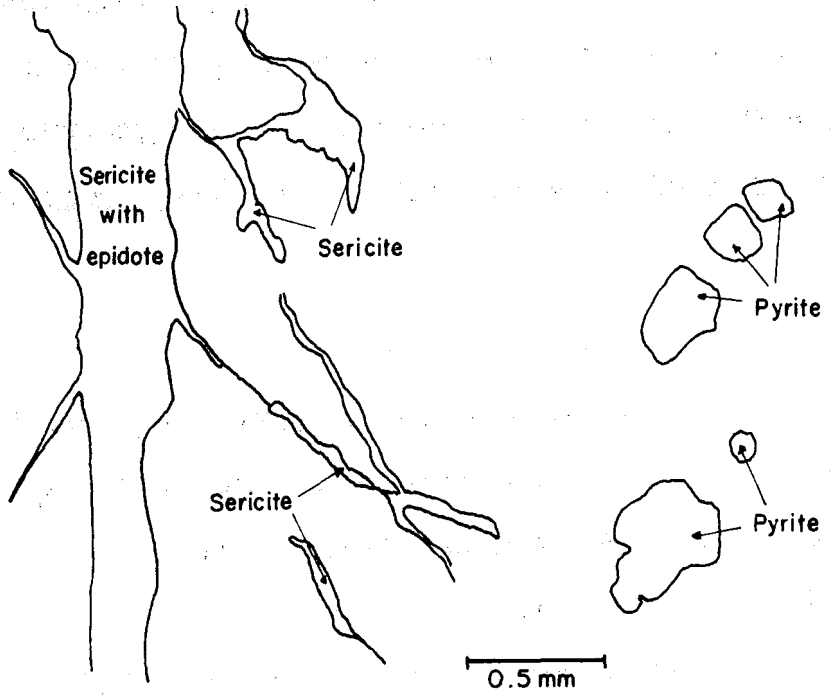

XBB 7910-14878

Fig. A3.2 Fractures associated with fracture B of ultra-large core. Prominent fracture (left) is filled with sericite and lesser epidote; sericite-filled veinlets branch off from it. Pyrite-filled fracture (right) merges with sericite-filled fracture below photo. Cross-polarized light. 40X magnification.

A3.4 INTERPRETATION OF FRACTURE MINERALOGY AND TEXTURES

The common occurrence of chlorite and sericite in the Stripa granite as both fracture fillings and as alteration products of the matrix minerals suggests that fracture formation may be related to that alteration. This relationship was in fact borne out by textural relations in thin section. For instance, the sericitic alteration of feldspars along edges or along internal cleavage planes very commonly became through-going and graded imperceptibly into sericite veins (Fig. A3.3). This fine veining in turn graded into more pervasive fracturing, so that fractures became continuous across several grains. (Often such fractures terminated in patches of coarse micas of the granitic matrix.) This was common around sericite fractures, where small continuous veinlets merged to fill a more continuous, wider fracture. In the vicinity of thicker fracturing this could be even more pervasive, until the matrix material was so riddled and shattered into a chaotic network of fractures that the orignal grains were no longer recognizable (Fig. A3.4).

Another line of evidence of the close genetic relationship of fracture formation and matrix alteration came from observation of chlorite growth. Muscovite in the matrix was often altered on edges and along cleavage planes to chlorite, and in more fractured areas was thoroughly altered. This parallels the more complete conversion of the original biotite to chlorite. Similarly within fractures, intergrowths of chlorite and sericite were more common than growths of one or the other alone. In many cases it is apparent that chlorite replaced sericite (hence the artificiality of the distinction between these two "types" of fractures). In the alteration of feldspar, chlorite could be seen replacing the sericite that formed as the initial

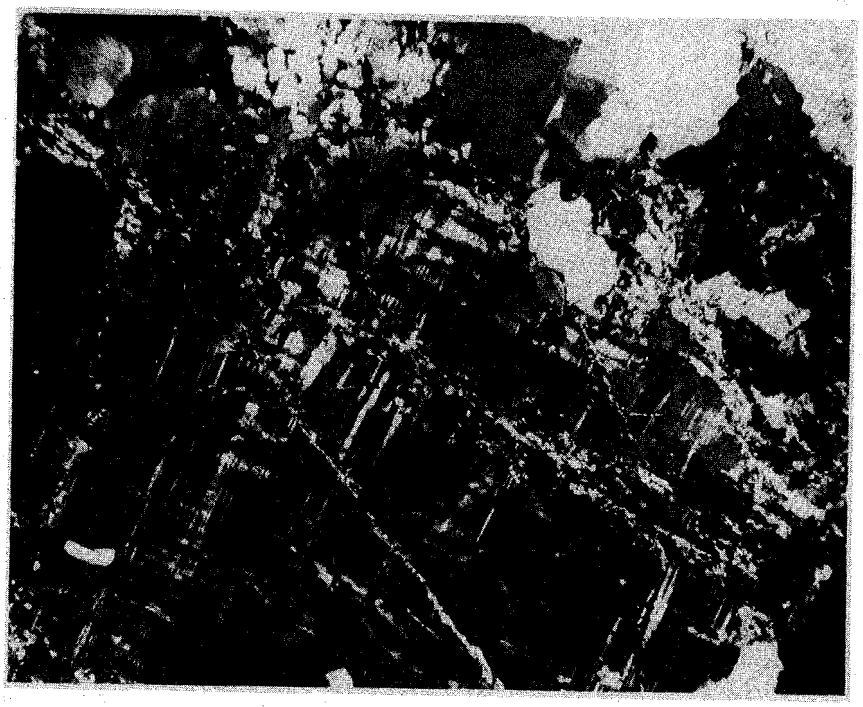

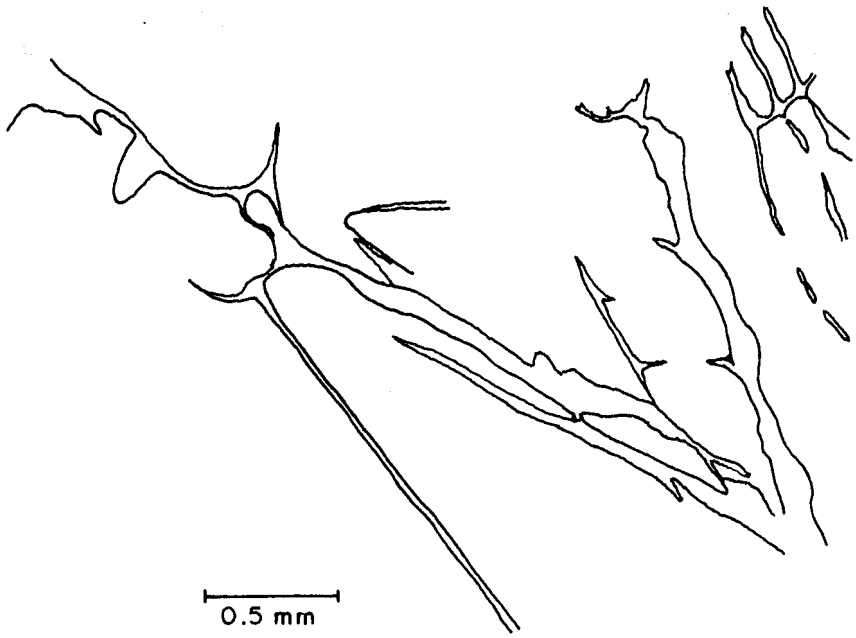

XBB 7910-14879

Fig. A3.3 Veinlets of sericite with lesser chlorite, forming in perthitic microcline grain; near dominant fracture B of ultra-large core. Cross-polarized light. 40X magnification.

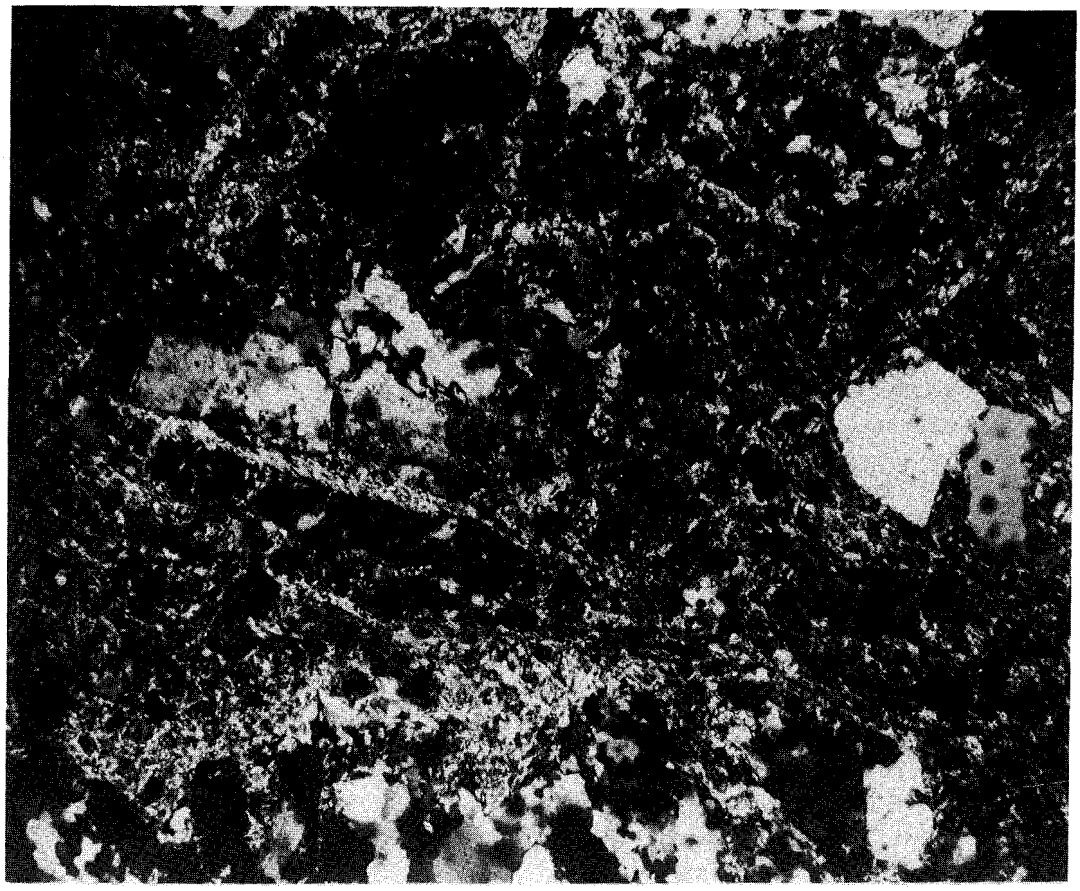

XBB 7910-14880

Fig. A3.4 Pervasive fracturing and alteration of matrix minerals to sericite and chlorite. From a several-cm-wide fracture zone, 8.35 m level in core OH1 BHE16 in full-scale drift. Cross-polarized light. 40X magnification.

feldspar alteration product (a complication not included in the earlier discussion of matrix mineralogy). In all these contexts, sericite alteration and subsequent formation of sericite fractures was followed or accompanied by replacement to chlorite. Also, both epidote and calcite occurred as alteration products as well as in fractures: epidote on occasion as tiny grains along muscovite cleavages, and calcite as patches within plagioclase.

There was also a connection found in the larger fractures in the time-scale and full-scale drifts with movement along the fracture surfaces. Thin sections of several fractures 1-2 cm or more in width from the full-scale and time-scale drifts showed unmistakable signs of fault gouge. In one sample a black chloritic fracture contained abundant broken quartz and feldspar crystals, and thin bands of highly comminuted, or mylonitized debris. In another sample (see Fig. A3.5), a lighter green fracture was composed of lenses of rounded quartz and feldspars, in a mass of comminuted debris, sericite, chlorite, and brown clay.

A3.5 CORRELATION OF FRACTURE TYPES WITH THE DOMINANT FRACTURES OF THE ULTRA-LARGE CORE

The major fractures in the ultra-large core are mapped on Fig. 2.3. Six thin sections from the core were examined. Five were from rock drilled from the borehole through the center. One included fracture C, three included or were adjacent to fracture B, and one included a major inclined fracture. Diffraction measurements on two samples were obtained from the surface of the core: one from a light green lens in fracture C, the other from the chloritic fracture surface forming the top of the core.

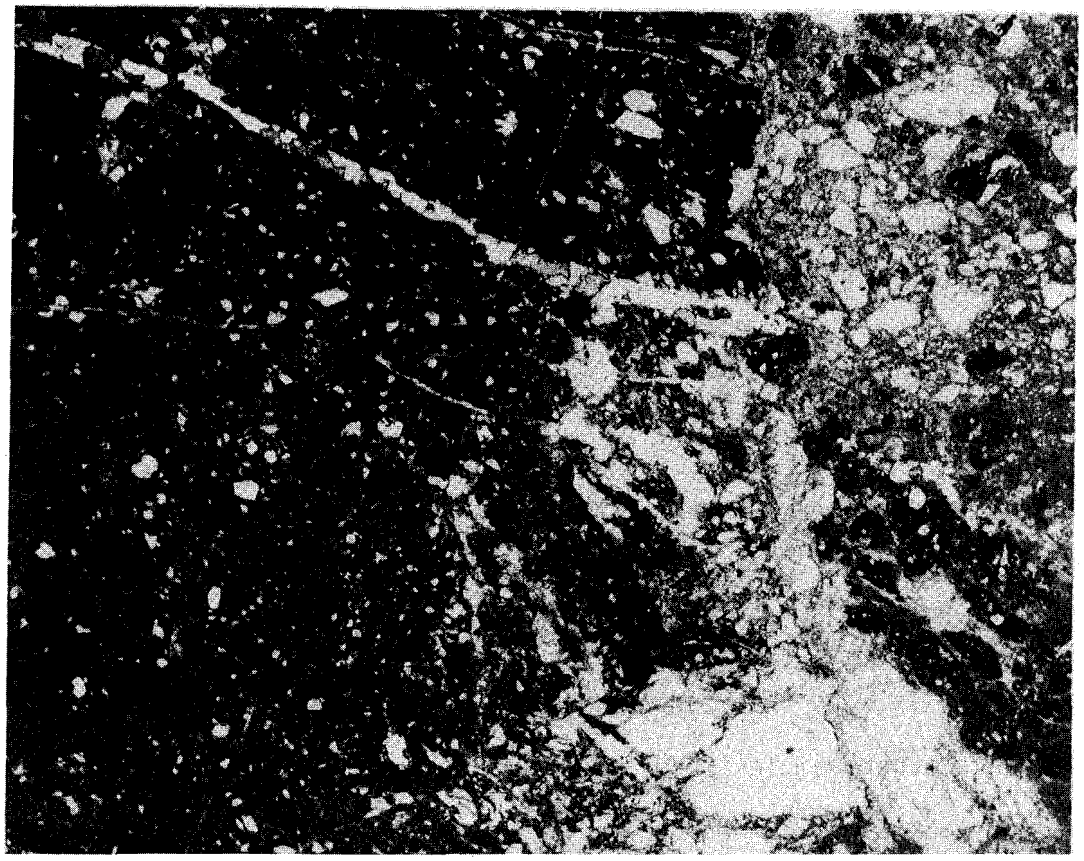

XBB 7910-14881

Fig. A3.5 Fault gouge consisting of broken grains of quartz and feldspars included in finely ground material, brown clay, chlorite, and sericite. Darker areas are richer in clay, while lighter areas contain coarser grains and are richer in chlorite and sericite. Fine fracture (upper portion of photo) is filled with quartz, chlorite, and sericite. From 1-2 cm-wide light-green fracture, 8.97 m level in core OV2BHE3 in time-scale drift. Plane polarized light. 20X magnification.

The first set of fractures (A through C), although continuous through the core, was typically very fine when seen in thin sections. The mineralogy was either sericite- or chlorite-dominated, and in places is a mixture of both. The lowest of these, fracture C, contained a band 3-5 cm in width containing numerous semi-continuous light green fractures or lenses up to 1 or 2 mm wide, within a darker chloritic fracture. These were originally thought to be epidote. One such lens was sampled; its diffraction pattern showed the major constituents to be quartz, sericite, feldspar, and fluorite, with a lesser amount of chlorite (Table A3.4). As mentioned above, fractures that appear to be filled with epidote can be deceptive. These lenses were too inaccessible to make thin sections, so epidote may or may not be abundant elsewhere along fracture C, and it may not even be a lesser component of this particular lens. (Most minerals must be major constituents of a diffraction sample in order to show up clearly on the resulting pattern.) A second diffraction pattern, from the thicker chloritic fracture that formed the top of the core, is presented in Table A3.5. Here chlorite was concentrated in the sample, and the resulting pattern is composed nearly entirely of chlorite peaks.

The inclined fractures (D through F), although discontinuous, were in places considerably thicker than the first set. They also showed some displacement, up to 1 or 2 cm, of the horizontal fractures that intersect them. Mineralogically, these fractures were for the most part similar to the other set, as they were filled with chlorite, with some thin light green sericite portions as well. But where they were thicker, up to several millimeters in places, they were filled with distinct calcite lenses within chlorite borders, and often with parallel growths of a light green filling

(sericite or epidote). Unfortunately, as with the lenses in fracture C, it was not possible to chisel coherent pieces of these thicker fractures for thin sections.

APPENDIX IV

TESTS ON 5.2 CM DIAMETER CORES

A4.1 SELECTION AND PREPARATION OF SPECIMENS

Seven fractured and six unfractured core specimens were tested. All were 52 mm diameter, but their lengths varied from 13 to 15 cm (2.5 to 3.0 length/diameter ratio). Samples were selected from core from various boreholes drilled to install extensometers for the full-scale heater experiment. They were selected on the basis of their suitability for the type of test, i.e., either the core section was unfractured or it contained a principal fracture oriented perpendicular to the core axis for the direct tension test or an inclined fracture for the compression test. The range of fracture inclination for the compression tests was 20° to 35° relative to the long axis of the core. The specimens used are described in Table A4.1.

Specimens were taken from longer sections of intact core by point-load tension tests applied several centimeters beyond the desired end of the specimen. The core sections were then cut with a diamond saw to the approximate final sample size, and the ends of the specimens were milled to within 0.05 mm of parallel (0.001 mm/mm diameter).

The surface of the fractured samples were mapped before and after testing. These maps are given in Figures A4.4 through A4.11. All samples were tested in an air-dried, unsaturated state, and tests were done at room temperature.

Table A4.1. Description of 5.2 cm diameter samples.

Specimen number	Location borehole number	Location depth (m)	Type of test	Length (cm)	Diameter (cm)	Natural fracture orientation (° from axis)
S1	E20	9.17	Triaxial comp.	15.14	5.17	34
S2	E14	2.82	Triaxial comp.	15.24	5.17	31
S3	E13	3.52	Uniaxial comp.	15.33	5.18	18
S4	E12	9.53	Uniaxial comp.	15.23	5.20	22
S5	E12	9.90	Triaxial comp.	15.23	5.20	30
T1	E12	5.05	Direct tension	15.35	5.20	80
T2	E12	5.48	Direct tension	15.22	5.18	85
S6	E13	1.41	Direct tension	15.24	5.18	Intact
S7	E13	1.57	Direct tension	15.24	5.18	Intact
S8	E13	1.74	Triaxial comp.	15.26	5.18	Intact
S9	E10	1.26	Triaxial comp.	15.04	5.21	Intact
S10	E10	1.50	Uniaxial comp.	15.06	5.20	Intact
S11	E10	1.65	Uniaxial comp.	14.80	5.21	Intact

A4.2 TEST PROCEDURES AND RESULTS

A4.2.1 Indirect "Point Load" Tension Test

This test provides an index of rock strength. The method consists of loading in a section of rock core across its diameter by means of a pair of spherical-headed platens. The apparatus and procedure used were similar to those described by Broch and Franklin (1972). The point load strength index, I_s, is computed as $I_s = P/D^2$, where P is the failure load and D is the distance between the loading platens (diameter of the core in this case). I_s is not the true tensile strength, since a large compressional stress component is involved in the loading. However, it does provide a useful comparison of the tensile strength of intact rock samples with those containing healed fractures. Results of the point load tests are given in Table A4.2. Although the number of tests was not large, these data indicate that the fractures substantially reduced the strength of the rock.

A.4.2.2. Uniaxial compression tests

Uniaxial compression tests were performed on two fractured samples and two intact samples. No confinement was applied, except for several rubber bands which helped hold the specimens together after failure. A 7414 kN (160,000 lb) Riehle test machine was used for loading, and its lack of stiffness generally prevented following sample response past the peak load. Loading platens were made of smooth steel, with no special friction reducers. Overall deformation of a sample was measured with an LVDT. The basic test data consisted of a load-deformation curve, a typical example of which is shown on Fig. A4.1. The modulus of elasticity was computed from the slope of the best linear fit through the higher load portions of the curve.

Table A4.2. Results of indirect tension tests on small core sections (52 mm diam).

Borehole number	Depth (m)	Point-load strength index I_s (MPa)
Intact granite (ave. = 11.31 MPa)		
E20	9.28	13.68
E14	2.91	11.43
E14	2.72	9.35
E13	3.67	9.18
E12	9.64	11.26
E12	10.00	11.61
E12	9.81	11.09
E12	6.62	12.84
Naturally fractured granite (ave. = 4.68 MPa)		
E12	5.12	5.37
E12	4.97	2.42
E12	5.57	6.24

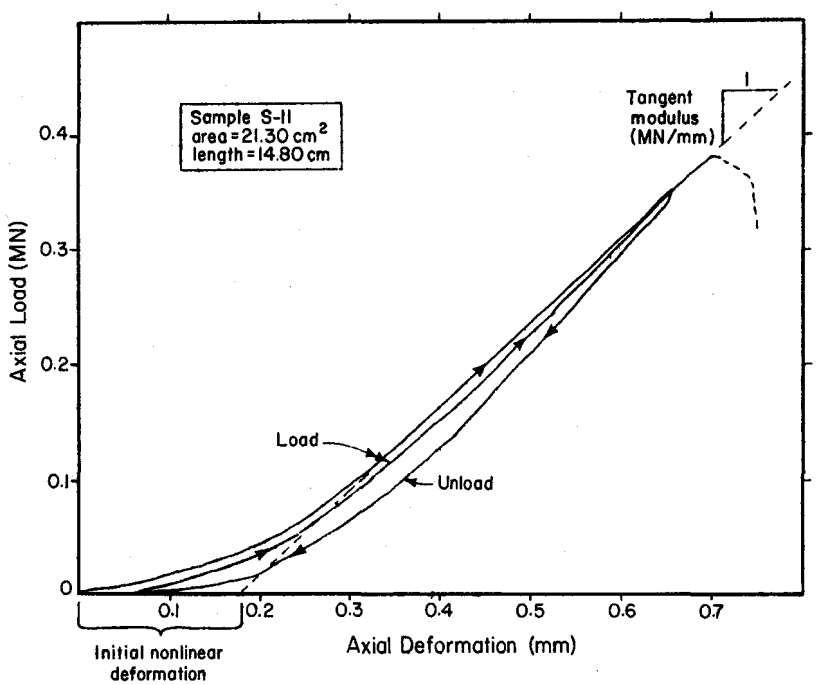

Fig. A4.1 Typical uniaxial compression test record for intact Stripa granite.

Results of the uniaxial compression tests have been summarized in Table 3.1. The failure mode of the intact granite was typical of low-ductility rock: exterior spalling preceded failure, as evidenced by many longitudinal fractures. These fractures intersected the ends of the 13 cm specimen (S-11), but failed to do so in the longer 15 cm specimen (S-10). As expected, failures of the samples containing healed fractures were generally confined to the inclined fracture surfaces. Sample S-3 broke wholely along its fracture, while sample S-4 developed longitudinal fracturing in addition to failure along its pre-existing healed fracture.

A4.2.3 Triaxial Compression Tests

Two intact and three naturally fractured specimens were tested in triaxial compression. The test machine was the same as described above, and the triaxial cell was of a standard single-piston design without spherical bearing plates for the axial load. Confining pressures were 3.45 and 6.90 MPa. Axial displacement was measured by an LVDT mounted outside the triaxial cell and a correction made for strain in the piston. Results of the triaxial tests were presented in Table 3.1. For the samples with healed fractures, S-1, S-2, and S-5, failure predictably occurred along the inclined pre-existing weaknesses. In most cases, incipient, axially oriented fractures were also seen in the failed cores. Only in sample S-2 did a failure surface extend through intact rock and intersect the end of the sample.

A4.2.4 Direct Tension Tests

Two specimens each of intact and naturally fractured rock were tested in direct tension. The load was applied with the Riehle test machine through a pair of moment-reducing eyebolts connected to each end of the sample. The

linkage at an end of the sample was made through a threaded aluminum cylinder glued with epoxy to the rock. Axial alignment was maintained during gluing by clamping the sample and the end pieces onto a metal channel section. Because of the number of linkages in the loading apparatus, the sample deformation could not be accurately measured, hence no tensile moduli were computed. The two naturally fractured specimens contained fractures oriented roughly perpendicular to the applied load, and in each case failure occurred on these planes. Both intact samples failed at the epoxy end connections; the true rock strengths, therefore, are higher than those measured by the tests. The results have been listed in Table 3.1.

A4.3 INTERPRETATION OF RESULTS

A4.3.1 Ultimate Strength

The relative strengths of the intact and fractured granite are represented by Mohr diagrams in Figs. A4.2 and A4.3, which contain all the data from Table 3.1. Figure A4.2 also includes data from previous tests on Stripa granite reported by Pratt et al. (1977) and Swan (1978), which are listed in Table A4.3. The intact rock strength curve is constructed as the tangent envelope to the Mohr circles. According to the Mohr-Coulomb strength criterion, the curve is expressed linearly as

$$\tau = c + \sigma \tan\phi, \qquad \text{(A4.1)}$$

where c is the cohesion intercept, ϕ is the angle of internal friction, τ is the shear stress, and σ is the compressive stress. Over the low stress range in Fig. A4.2, c and ϕ are approximately 25 MPa and 65°, respectively. For conservatism, the average tensile strength circle has been used in this construction.

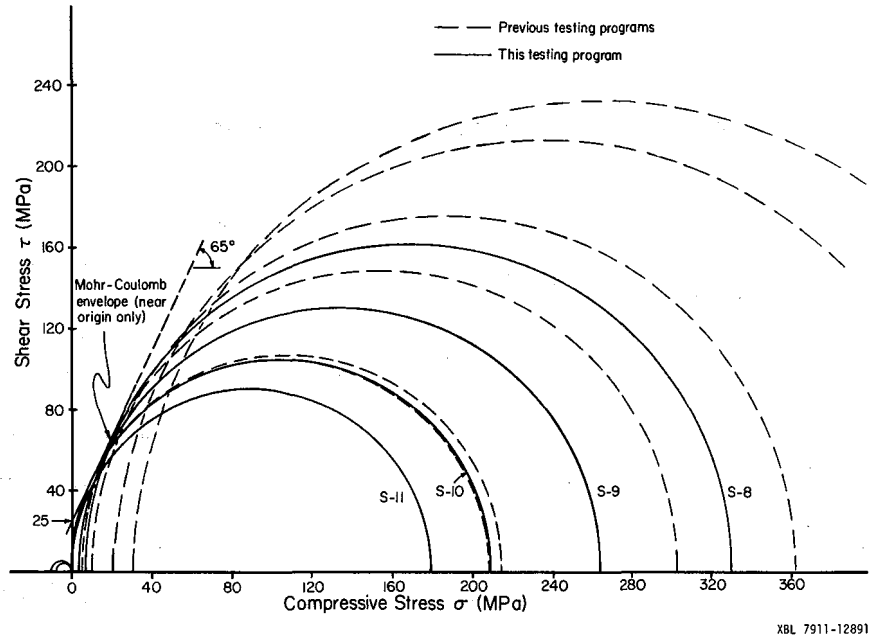

Fig. A4.2 Mohr diagram for intact Stripa granite.

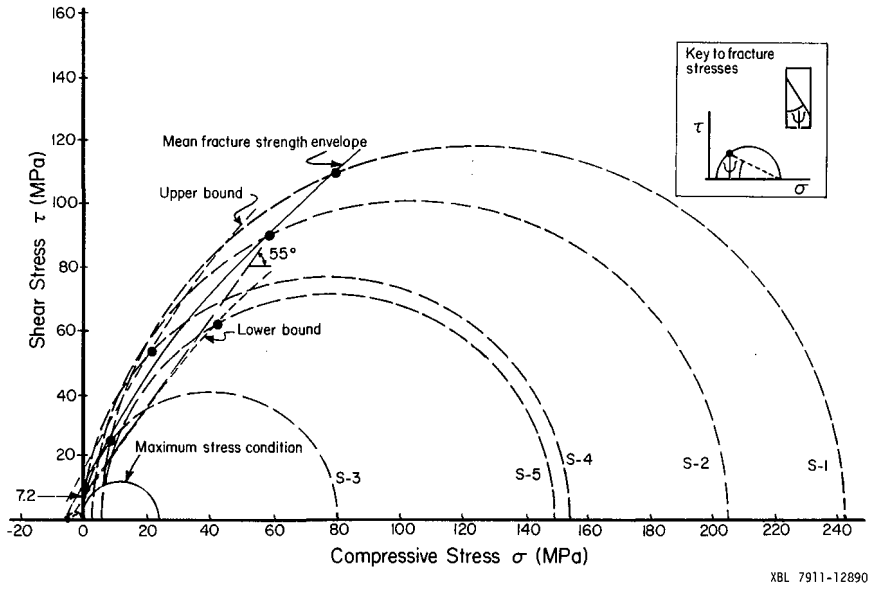

Fig. A4.3 Mohr diagram for healed fractures in Stripa granite.

Table A4.3. Summary of previous laboratory strength data for intact Stripa granite.

Type of test	σ_3 (MPa)	$\sigma_{failure}$ (MPa)	Young's modulus (GPa)	Reported by
Uniaxial compression	0	214 ±24	52.3±6.5	Pratt et al. (1977)
Uniaxial compression	0	207.6±31.4	69.4±6.6	Swan (1978)
Triaxial compression	5	308.5± 9.8	75.4±1.8	Swan (1978)
Triaxial compression	10	372 ±25.6	77.2±0.9	Swan (1978)
Triaxial compression	20	470 ± 6.3	82.2±2.2	Swan (1978)
Triaxial compression	30	530.3±14.0	83.2±0.6	Swan (1978)
Brazilian tensile strength	0	13.3±1.4	--	Pratt et al. (1977)
Brazilian tensile strength	0	15.0±1.8	--	Swan (1978)

The mean fracture strength curve (dashed line) shown in Fig. A4.3 is also roughly parabolic, having been drawn as a best fit through points of stress determined according to the inset in the figure. Upper- and lower-bound fracture strengh envelopes have also been constructed. Comparison of Figs. A4.2 and A4.3 indicates that the presence of fractures decreased the strength of the rock. The point-load test data showed a comparable reduction in tensile strength.

The results obtained from the tests on the small diameter cores were used to make an estimate of the unconfined, uniaxial compressive strength of the ultra-large core. To calculate failure stresses, the fracture-strength envelope for the small cores can be approximated by the Mohr-Coulomb criterion with c equal to 7.3 MPa and ϕ equal to about 55°. For uniaxial compression, the theoretical stresses on a plane inclined at ψ degress to the core axis are:

$$\sigma = \sigma_1 \sin\psi^2 = \frac{\sigma_1}{2} (1 - \cos 2\psi) \qquad \text{(A4.2)}$$

and

$$\tau = \sigma_1 \sin\psi\cos\psi = \frac{\sigma_1}{2} \sin 2\psi \quad . \qquad \text{(A4.3)}$$

Substituting (A4.2) and (A4.3) into (A4.1) gives the maximum axial stress

$$\sigma_1 = \frac{2c}{[\sin 2\psi - \tan\phi(1 - \cos 2\psi)]} \quad . \qquad \text{(A4.4)}$$

The three most prominent inclined fractures in the large core were oriented at $\psi = 28°$. Substituting this value, along with the above c and ϕ values, into (A4.4) gives $\sigma_1 = 73.2$ MPa. Because other fractures in the large core, although less continuous, were inclined from 10° to 30° to its long axis, it was conservative to assume that the plane of weakness was oriented at $\psi = 45 - \phi/2 = 17.5°$. Substituting this into (A4.4) gives $\sigma_1 = 46.3$ MPa.

As reported in Section 6.1.1, the actual uniaxial strength of the large core was only 7.4 MPa. This large discrepancy illustrates the difficulty of predicting the strength of large blocks of rock from tests performed on small core samples.

A4.3.2 Deformation

As in the prediction of strength, estimation of the large core's deformation characteristics was dependent upon its similarity to the small jointed samples. The tangent moduli in Table 3.1 showed little difference between fractured and intact rock. This suggests that these natural fractures were effectively closed and did not influence the elastic modulus. Similar observations from tests on other rock have been discussed by Jaeger and Cook (1976). Therefore, if it were assumed that the deformation behavior of the small samples was similar to that of the large sample, the elastic modulus of the large core should have been about 55 GPa, which is the average of values listed in Table 3. This compares with a tangent modulus of 52.3 GPa computed for the large core just prior to failure.

Nonlinearity can be introduced in the initial portion of a stress-strain curve by microfissure closure (Jaeger and Cook, 1976). Because deformation measurements were not made directly on the samples, the test data from the small cores were affected by the end conditions and the loading platens. The magnitude of these errors was estimated from a test using a machined aluminum specimen. Based on these tests, the initial measured strains due to microfracture closure in the small samples were reduced by 0.06%, to correct for testing errors.

The amount of closure of the fractures normal to the long axis of the large core was difficult to predict from the small core test and was complicated by the accidental opening of fracture B. However, as proposed by Goodman (1976), an upper bound estimate could be made from the thickness of filling material in the joints. There were three main perpendicular fractures in the large core, and their filling thicknesses add up to about 4 mm. Initial closure of these fractures was expected to be highly nonlinear and nonelastic, generating a hyperbolic load-displacement function (Goodman, 1976).

Based on the above assumptions, the estimated total axial deformation of the large core under an axial stress of 24 MPa was then the summation of:

Closure of major perpendicular fractures	~ 4 mm
Microfissure closure ~ $6 \times 10^{-4} \times 1524$ mm	~ 0.9 mm
Elastic displacement ~ (24MPa/55GPa) x 1524 mm	~ 0.7 mm
Total for large core	~ 5.6 mm

This represents an overall strain of 0.36%.

As described in Section 6.1.1, the actual failure strain of the large core was only 0.06%, due to failure at low stress along the steeply inclined fractures. By simple linear interpolation, data from tests on the small cores would have predicted a strain of some 0.11% in the large core at a failure stress of 7.55 MPa.

KEY TO FIGURES

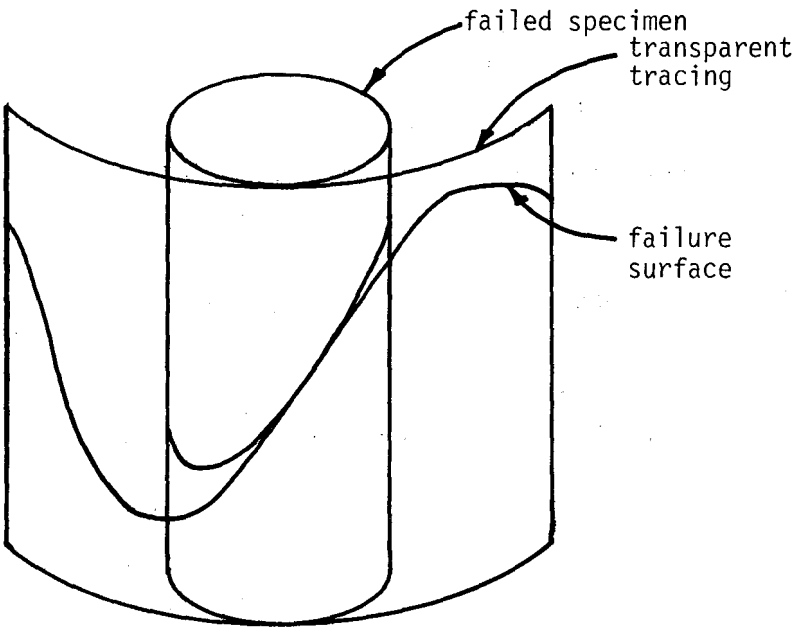

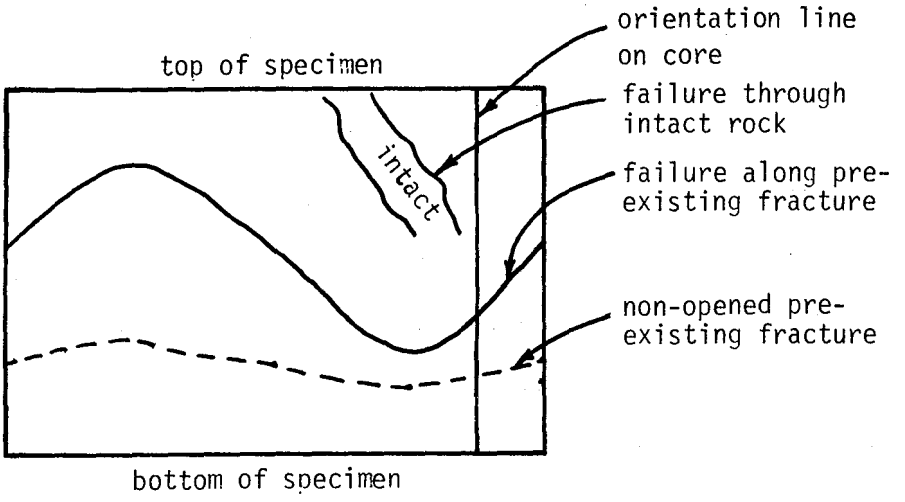

XBL 7911-12892

Fig. A4.4 Key to Figures A4.5 to A4.11.

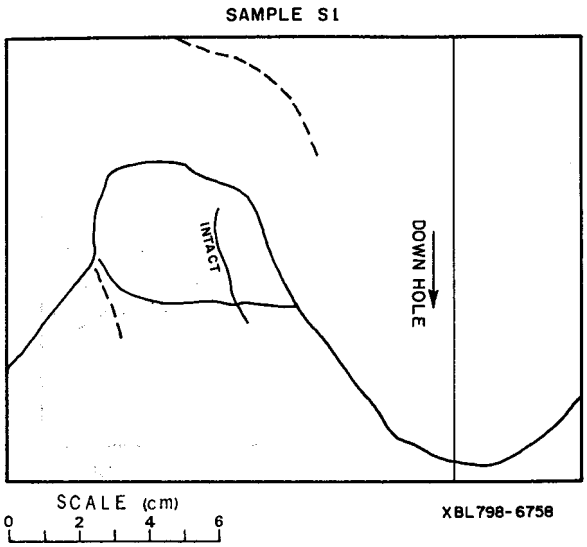

Fig. A4.5 Map of sample S1.

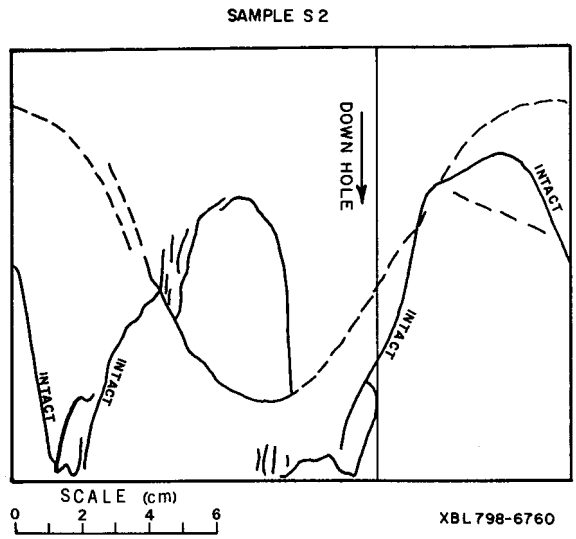

Fig. A4.6 Map of sample S2.

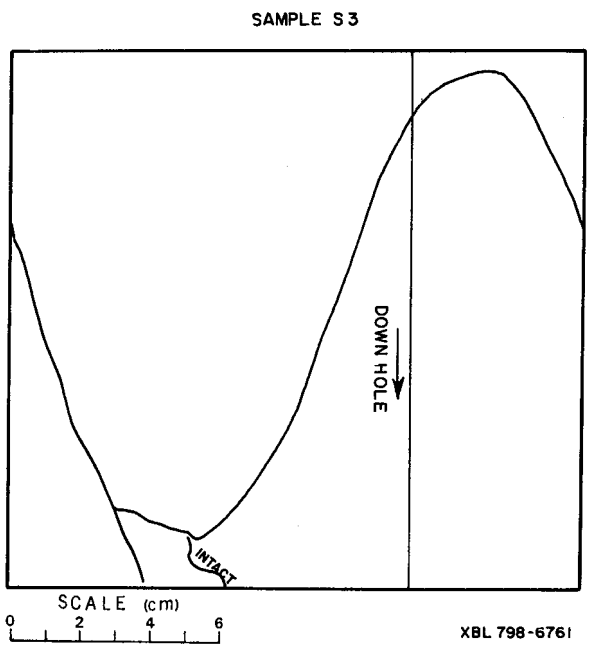

Fig. A4.7 Map of sample S3.

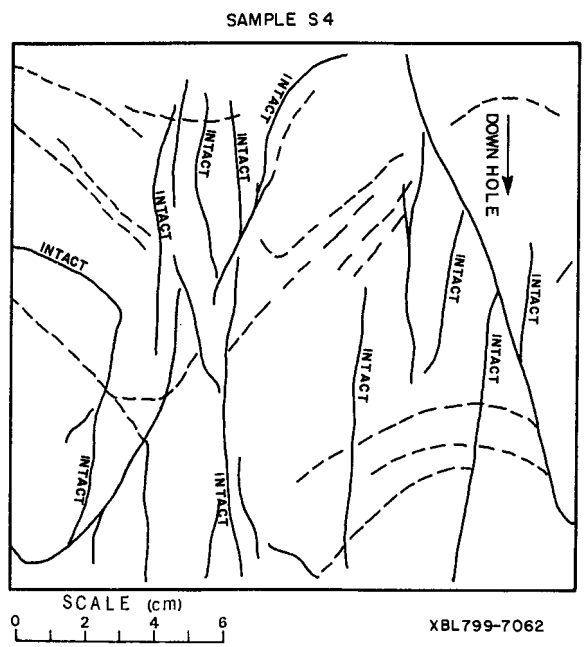

Fig. A4.8 Map of sample S4.

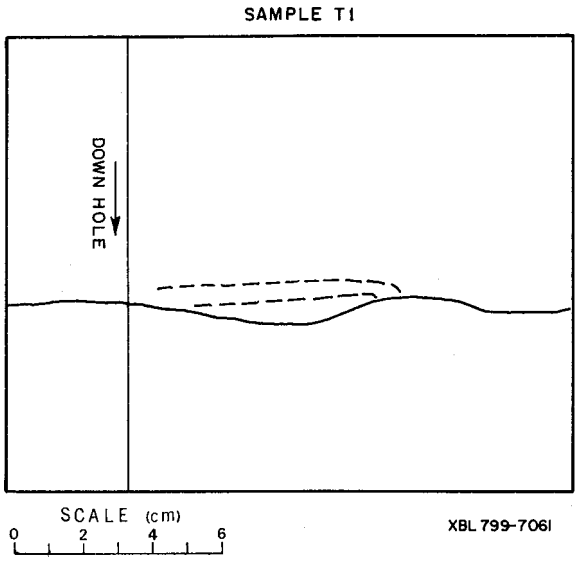

Fig. A4.9 Map of sample T1.

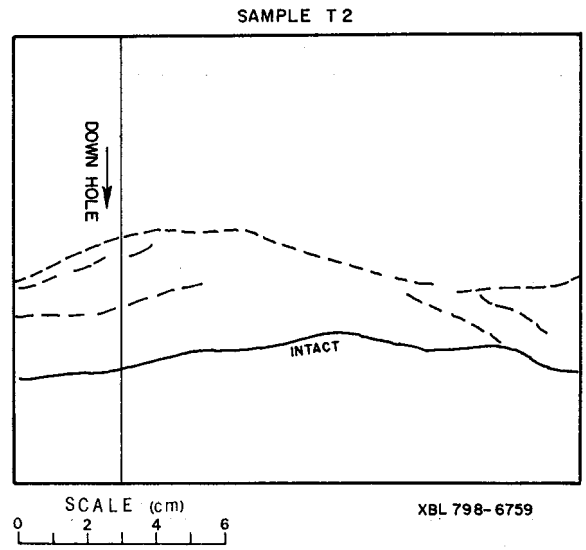

Fig. A4.10 Map of sample T2.

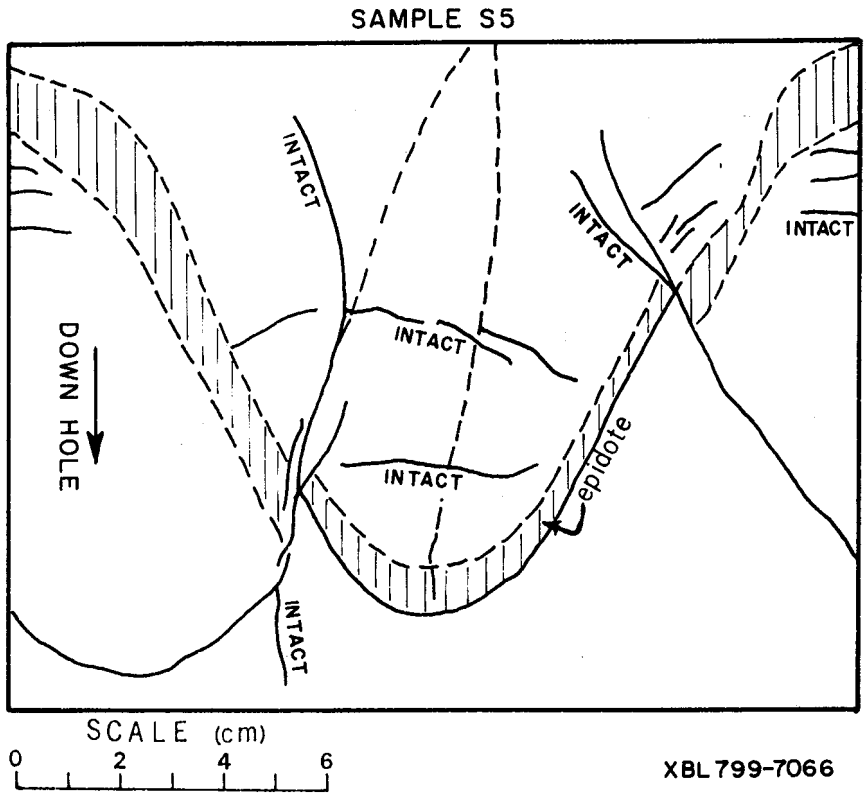

Fig. A4.11 Map of sample S5.

APPENDIX V

FALLING-HEAD TESTS

The purposes, experimental procedures, and principal results of the falling-head tests were summarized in Section 4. Additional details and analysis are given in this appendix.

A5.1 PACKER DESIGN

A simple packer system was designed for the falling-head tests. The assembled unit is shown in Fig. A5.1 Each packer consisted of six 7.62 cm diameter by 1.27 cm thick rubber rings threaded over a mandrel. The packers were sealed against the borehole walls by radial expansion from axial compression applied through a nut on the mandrel. Compression was transmitted from the upper to lower packer through a perforated pipe slid over the mandrel. The interval between the packers could be adjusted by changing the length of the perforated pipe.

The packers were tested under air pressure in a 7.6 cm diameter clear plastic pipe. When installed by compressing the packers with a 30 Nm torque a complete seal was formed under 200 kPa air pressure. To allow for the roughness of the walls, this torque was doubled when the packers were installed in the borehole. As a further check on packer performance, the system was tested in a 2.6 cm diameter borehole in a block of Sierra white granite. In this test, it was also possible to directly observe any leakage past the packers. None was visible under injection pressures up to 250 kPa. Water flow into the interval was about 3×10^{-4} liters/min, which corresponds to a rock permeability of 10^{-6} cm/sec. These tests demonstrated the reliability of the packer design. The same basic design was used for the perme-

CBB 798-11027

Fig. A5.1 Borehole packer unit for falling-head tests.

ability tests in the triaxial vessel. In those tests the upper and lower packers were installed independently and a nylon tube was passed through the upper packer to measure water pressure in the interval.

A5.2 TEST PROCEDURE

The test arrangement is shown schematically in Fig. 4.1. After setting the packers at a predetermined location in the borehole, de-aired water was injected into the interval from an elevated standpipe connected to the packer system by a flexible hose. The flow rate was calculated from the rate of fall in head and the area of the standpipe. Three clear plastic standpipes of nominal diameters 6.4, 19 and 44 mm were used so that suitable flowrates could be selected as appropriate for the changing conductivities of the different borehole intervals.

The true pressure in the interval was found by correcting the total head in the standpipe for losses upstream from the interval. The relationship between head loss, h_l, and flowrate, Q, was determined empirically and found to be:

$$h_l = 0.557Q^{1.472} \quad . \qquad \text{(A5.1)}$$

This calibration gave only approximate losses, and at flowrates greater than several liters per minute the true injection pressure was uncertain. The maximum flow the system could supply was about 3 liters/min, which was less than the "take" of the whole sample. Because this high conductivity prevented the borehole from remaining full of water during the installation of the packer, it was necessary to purge the interval of air via a tube passing through the top packer.

Two packer spacings of 0.172 m and 0.352 m were used. The short intervals were chosen relative to the major fractures so as to limit flow to only one or possibly two fractures. Tests with the longer intervals included more fractures in relation to the major fractures logged in the center borehole. By overlapping the intervals, the relative flow contributions of major fractures could be determined.

A5.3 TEST RESULTS AND ANALYSIS

Each of the injection intervals in Fig. 4.2 correspond to the chronological test numbers shown. Test results are plotted in semilog form of head against time in Figs. A5.2 to A5.8. Several injection cycles were made for each test and the curves in the figures are from the final cycles of the tests. This selection was somewhat subjective, but because the degree of saturation of the core probably increased as successive subtests were run, it can be assumed that constant saturation conditions were approached. The core was not immersed in water, and full saturation was probably not reached. However, based on the usual interpretation of similar tests on soils (Lambe, 1951), a linear logarithmic rate of falling head was taken to indicate a constant degree of saturation. The curves shown on Figs. A5.2 to A5.8 are generally quite linear, and the results are therefore considered sufficiently accurate for comparing the hydraulic properties of the different borehole intervals.

To make these comparisons, the analysis assumed that Darcy's law applied. In modified form this can be stated as:

$$Q/\Delta h = k\ (A/L) \quad , \qquad \text{(A5.2)}$$

where k is the coefficient of permeability, Q is the flow rate, Δh is the

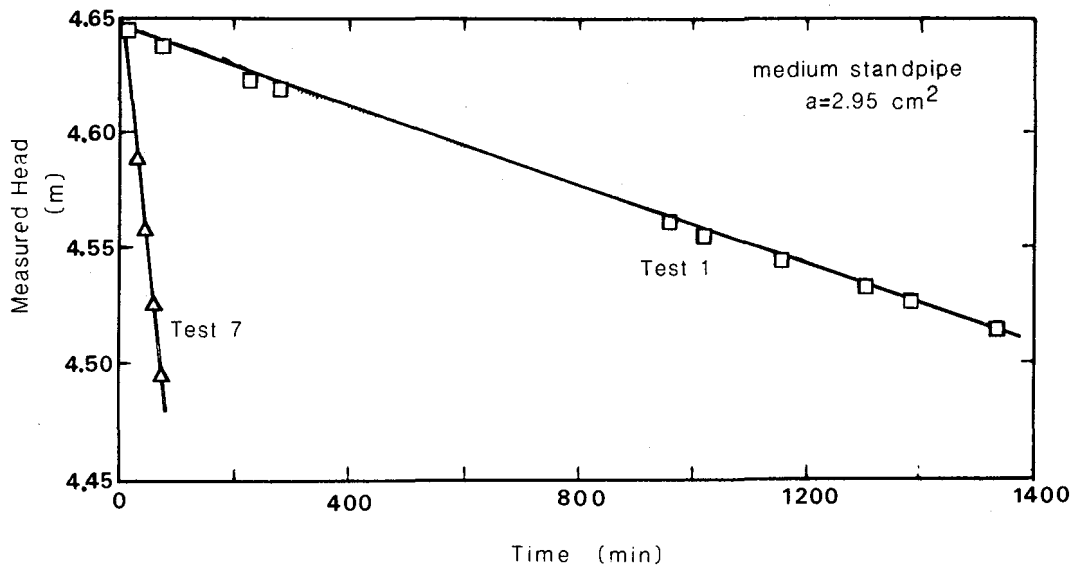

XBL 801-7774

Fig. A5.2 Results of falling-head tests Nos. 1 and 7.

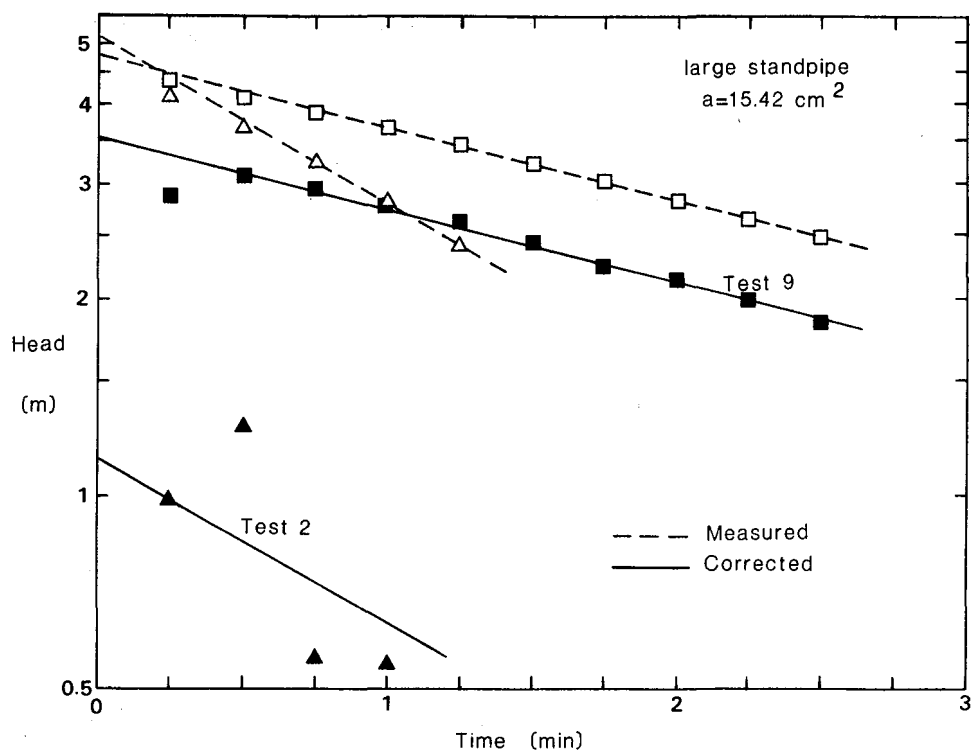

XBL 801-7781

Fig. A5.3 Results of falling-head tests Nos. 2 and 9.

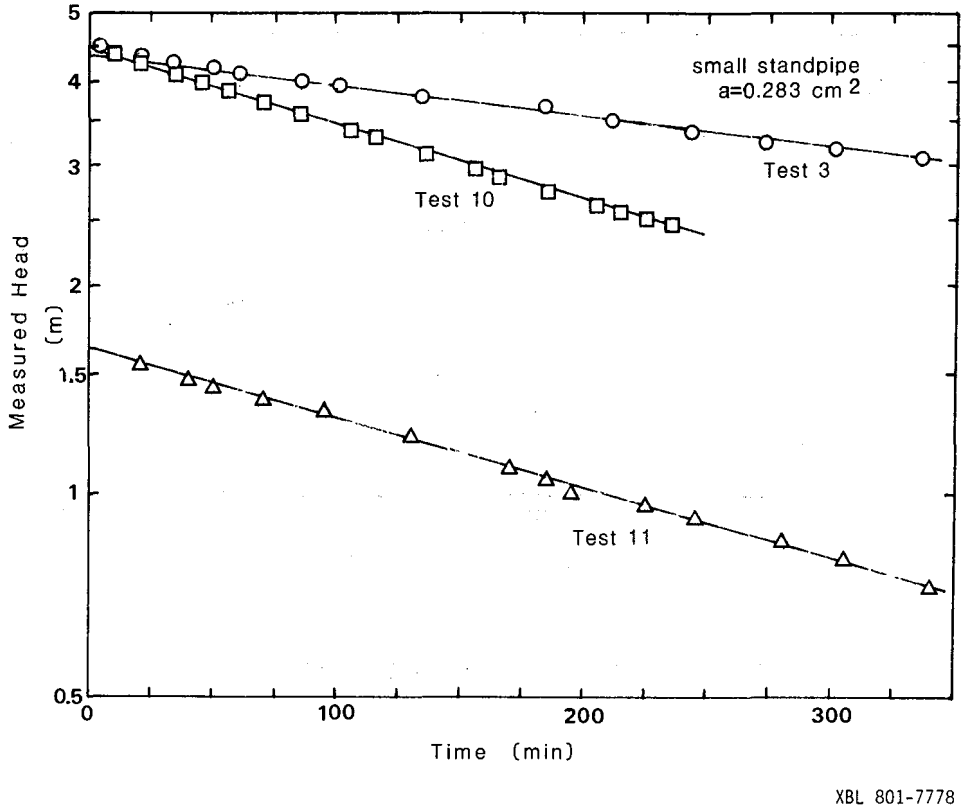

Fig. A5.4 Results of falling-head tests Nos. 3, 10 and 11.

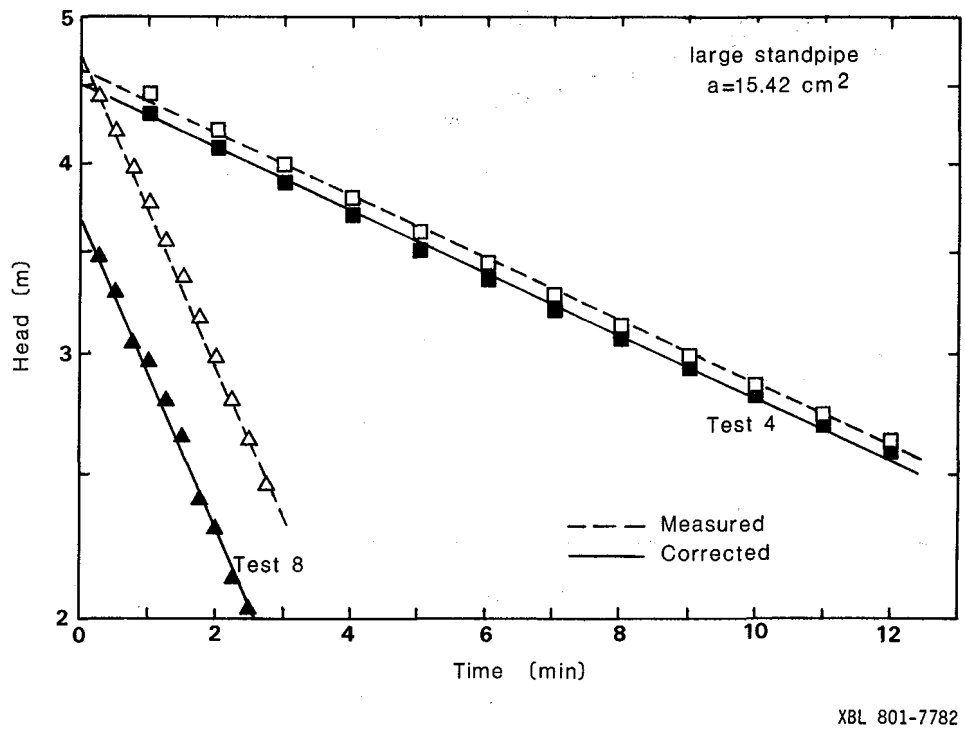

Fig. A5.5 Results of falling-head tests Nos. 4 and 8.

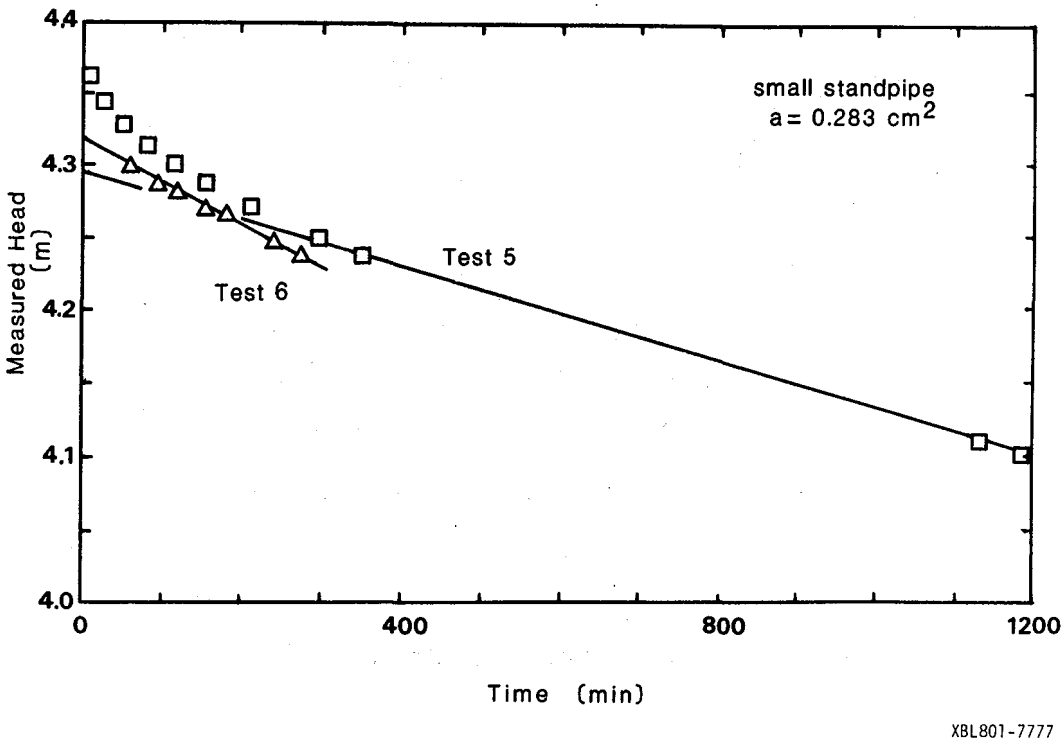

Fig. A5.6 Results of falling-head tests Nos. 5 and 6.

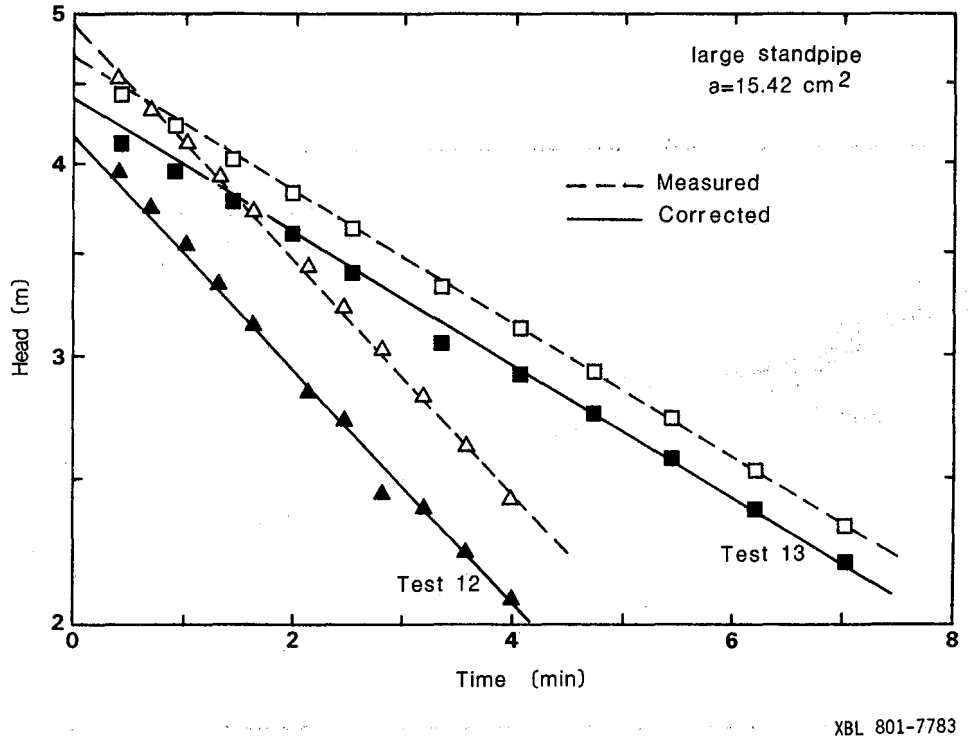

Fig. A5.7 Results of falling-head tests Nos. 12 and 13.

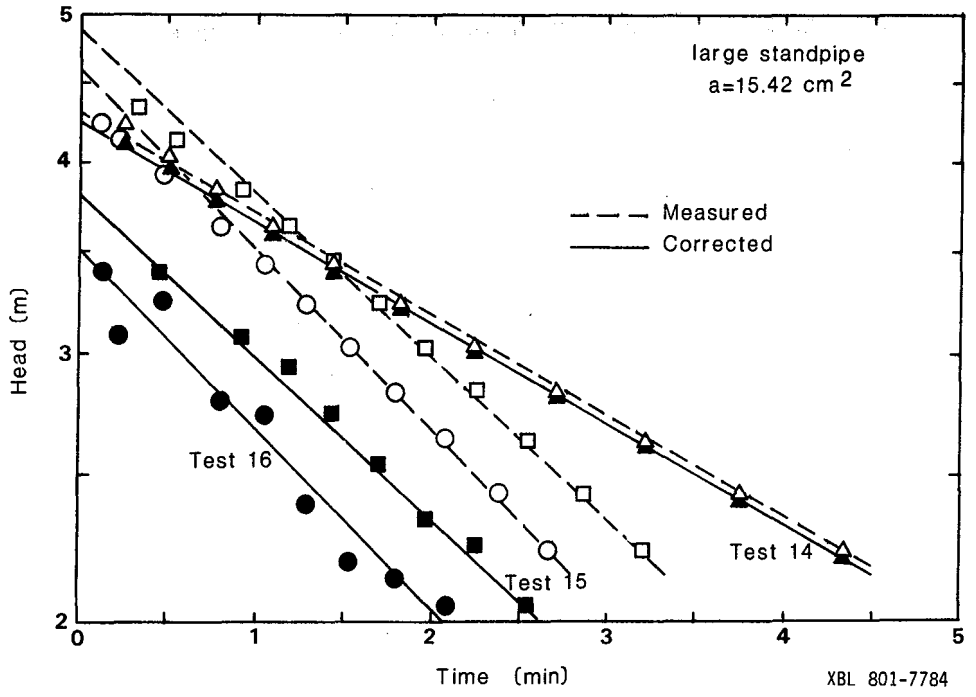

Fig. A5.8 Results of falling-head tests Nos. 14, 15 and 16.

head loss (in this case equal to the pressure in the interval), A is the cross-sectional area of flow and L is the length of the flowpath. Because of the geometric complexity of the fracture system in the large Stripa core, results were expressed in the normalized form $Q/\Delta h$, the flow-per-unit-head. This avoids determination of A and L. The flow rate Q is found from the volume change in the standpipe per time interval:

$$Q = (\Delta h/\Delta t)\ a_s, \tag{A5.3}$$

where h and time, t, are measured during the test, and a_s is the area of the standpipe. The linear portion of the curves shown in the figures can be represented by

$$h_m = a_m\ b_m^t \quad . \tag{A5.4}$$

The coefficient a_m is equal to the extrapolated initial head h_o in meters and b_m is given by

$$b_m = (h_m/h_o)^{1/t_m} \quad , \tag{A5.5}$$

where t_m is the time in seconds since t=0, and h_m is the corresponding head in meters. Both values are chosen arbitrarily from the curve representing the measured data. The head in the injection interval must be calculated by

$$h_c = h_m - h_l \quad , \tag{A5.6}$$

where h_c is the corrected head, h_m is the measured head, and h_l is the head loss according to Eq. (A5.1). For many of these tests, the head losses were less than a centimeter, so $h_c \approx h_m$. For flow rates greater than 0.1 liters/min, losses were more significant. For these cases corrected data are shown on Figs. A5.2 through A5.8. Since the corrected head data are also linear on the semilog graph, they too can be represented in the form of

(A5.4). Since (A5.4) is continuous, Eq. (A5.3) can be written:

$$Q = a_s\ (dh_m/dt) = a_s\ (a_m\ b_m^{\ t}\ \log_e b_m) \quad . \tag{A5.7}$$

Substituting into (A5.2) gives:

$$Q/\Delta h = \frac{a_s\ a_m\ b_m^t\ \log_e b_m}{a_c\ b_c^t} \quad . \tag{A5.8}$$

The figures show the measured and corrected curves to be parallel, so $b_m = b_c$. (Nonparallel curves would indicate unsteady flow conditions). Converting to base 10 logarithms, and substituting for a_m, a_c, and b_m, we get:

$$Q/\Delta h = 2.3\ a_s\ (h_{om}/h_{oc}) \left[\frac{\log_{10}(h_{om}/h_m)}{t_m}\right] \tag{A5.9}$$

where h_{om} and h_{oc} are extrapolated heads at t=0 for the measured and corrected curves, and (t_m, h_m) is an arbitrary point on the curve fitted to the measured data.

Values of $Q/\Delta h$ computed using Eq. (A5.9) are listed in Table A5.1 and were presented graphically in Fig. 4.2. Interpretations of flowpaths inferred during the falling head-tests were given in Table 4.1 and Fig. 4.3.

A5.4 INTERPRETATION

A5.4.1 Primary Flowpaths

The preceding analysis clearly indicates the dominance of fracture B as a flowpath through the sample. Its flow resistance was less than that of the falling-head apparatus; hence its $Q/\Delta h$ value in Table A5.1 (Test No. 2) is probably an underestimate. Fracture B was accidentally disturbed during sample preparation. The analysis of the falling-head test results assumes that the fracture aperture remained constant as the water pressure in the

Table A5.1. Flow parameters computed from falling-head test results.

Test no.	Standpipe area ($10^{-4}m^2$)	Borehole interval (m)	Measured heads (m) h_{om}	Measured heads (m) h_m	Measured time, t_m (min)	Corrected head, h_{oc} (m)	$Q/\Delta h$ (m^2/s)	Flowrate for head of 1 m (l/min)
1	2.95	0.114-0.286	4.65	4.6	520	4.65	$1.2x10^{-10}$	$7.2x10^{-6}$
2	15.42	0.904-1.076	5.09	3.5	0.62	1.1	$7.2x10^{-5}$	4.3
3	0.283	1.390-1.562	4.43	4.0	87	4.43	$5.5x10^{-10}$	$3.3x10^{-5}$
4	15.42	1.278-1.450	4.65	4.0	3	4.5	$1.3x10^{-6}$	0.078
5	0.283	1.124-1.300	4.29	4.1	1190	4.29	$1.8x10^{-11}$	$1.1x10^{-6}$
6	0.283	1.010-1.186	4.32	4.25	220	4.32	$3.5x10^{-11}$	$2.1x10^{-6}$
7	2.95	0.800-0.976	4.66	4.5	72	4.66	$2.4x10^{-9}$	$1.4x10^{-4}$
8	15.42	0.624-0.800	4.67	2.5	2.67	3.65	$7.7x10^{-6}$	0.46
9	15.42	0.470-0.646	4.75	2.5	2.47	3.55	$8.9x10^{-6}$	0.53
10	0.283	0.360-0.536	4.49	2.5	224	4.49	$1.2x10^{-9}$	$7.2x10^{-5}$
11	0.283	0.214-0.390	1.62	1.0	205	1.62	$1.1x10^{-9}$	$6.6x10^{-5}$
12	15.42	0.229-0.581	4.92	2.5	3.82	4.15	$5.4x10^{-6}$	0.32
13	15.42	1.304-1.656	4.65	2.5	6.25	4.4	$2.7x10^{-6}$	0.16
14	15.42	1.043-1.395	4.30	2.5	15.8	4.25	$8.9x10^{-7}$	0.53
15	15.42	0.590-0.942	4.93	2.5	2.74	3.75	$8.4x10^{-6}$	0.50
16	15.42	0.492-0.844	4.54	2.5	2.25	3.50	$8.8x10^{-6}$	0.53

borehole changed. Witherspoon et al.(1977) have shown that fracture conductivity is sensitive to small changes in stress. Changes in effective stress as the water level in the standpipe fell were of relatively small magnitude but are a potential source of error, affecting the absolute values of $Q/\Delta h$ given in Table A5.1.

A5.4.2 Overall Flow

To estimate the macroscopic flow characteristics of the core, an upper bound for $Q/\Delta h$ was found using Eq. (A5.1) and the sum of the flow rates computed for the major flowpaths. Representing the total flow for 1 m head by tests 2,13, and 16, we have:

$$Q/\Delta h_{total} = (4.3 + 0.16 + 0.53 \text{ liters/min})\ (1 \text{ m}) = 0.8\ \text{cm}^2/\text{sec}$$

This approach probably overestimates the conductivity, due to duplication of flowpaths. As evident from Table 4.1, virtually all the tests involve fractures intersecting fracture B, hence proper treatment of the problem would require three-dimensional modeling of the flow network.

A5.4.3 Matrix Permeability

The use of $Q/\Delta h$ to compare the hydraulic characteristics of different sections of the core avoids the difficulty of defining discrete flowpaths and boundary conditions. However, it is usually preferable to estimate the coefficient of permeability directly. This was possible for tests 1, 3, 5, 6, 7, 10, and 11, in which no major fractures intersected the injection interval. We can assume that flow immediately adjacent to the borehole was essentially through the rock matrix itself. The matrix permeability, k_m, can be estimated by Bouwer's (1978) slug-test procedure for partially penetrating wells in unconfined aquifers. Applied to our test configuration,

$$k_m = \left[\frac{r^2 \log_e (R_e/r)}{2\,L}\right] \frac{\log_e(h_o/h_t)}{t} \quad , \tag{A5.10}$$

where r = borehole radius = 0.038 m, L = interval length, h_o = initial head in standpipe, h_t = head at time t in standpipe, t = elapsed time since h_o, and R_e = effective radial distance while the head difference is dissipated. When the injection interval is small compared to the size of the aquifer, the empirical relation between R_e and the geometry and boundary conditions of the system reduces to

$$\log_e (R_e/r) = \frac{L/r}{(A + 6B)} \quad . \tag{A5.11}$$

For L/r less than about 5, A and B are approximately 1.7 and 0.2, respectively. For the short-interval tests (numbers 1 through 11), L = 172 mm and r = 38 mm, which by (A5.11) gives R_e = 190 cm. This is about the same as the distance to major fractures from the low-flow intervals; therefore, for practical purposes the shape of the actual flow regime should be similar to that of the homogeneous matrix model assumed here. Table A5.2 summarizes the matrix permeabilities computed with R_e = 20 cm. Because of the uncertainty in this parameter, k_m is estimated to range from 10^{-5} to 10^{-7} cm/sec.

Table A5.2. Approximate matrix permeabilities.

Test no.	Borehole interval	h_o (m)	h_t (m)	t (min)	k_m (cm/s)
1	0.114-0.286	4.65	4.6	520	9.1×10^{-7}
3	1.390-1.562	4.43	4.0	87	5.3×10^{-5}
5	1.124-1.300	4.29	4.1	1190	1.7×10^{-6}
6	1.010-1.186	4.32	4.25	220	3.3×10^{-6}
7	0.800-0.976	4.66	4.5	72	2.2×10^{-5}
10	0.360-0.536	4.49	2.5	224	1.1×10^{-4}
11	0.214-0.390	1.62	1.0	205	1.0×10^{-4}

APPENDIX VI

CONTROL, INSTRUMENTATION, AND DATA ACQUISITION EQUIPMENT

The purpose and general design of the instrumentation, load control, fluid pressure control and data acquisition systems used to test the ultra-large Stripa core were described in Section 5. A system schematic was shown in Fig. 5.4 and the instrumented core was shown in Figs. 5.5 and 5.6. This appendix provides additional details of the equipment used and its performance during the test program.

A6.1 INVENTORY OF PRINCIPAL EQUIPMENT

The principal equipment used for the tests is inventoried in Table A6.1 by manufacturer and, where appropriate, by model and serial number.

A6.2 AXIAL LOAD CONTROL

Axial loading was controlled by electrical feedback servo-control of the triaxial machine's hydraulic actuator. Feedback was from a load cell mounted in the end of the loading piston (Hsu and Watkins, 1979). The load cell is equipped with four full-bridge and four half-bridge strain gauges. One full bridge was used for servo-control of axial load and was balanced for maximum control resolution. A second full bridge provided an independent measure of absolute axial load. The half bridges checked the eccentricity of the load across two orthogonal diameters of the loading piston.

A6.3 FLUID PRESSURE AND FLOW CONTROL

The operation of the fluid pressure and flow control system was described in Section 5.3. Difficulty was experienced in maintaining steady control of pressures and flows at the high flow rates and low differential

Table A6.1. Principal instrumentation and control equipment.

Item	Manufacturer	Model	Serial No.
Accumulator	Greer Hydraulics	30A-1WS	--
Bridge Excitation (Load Cell)	Power Designs	Power Supply 2050	F405055
Bridge Excitation (Strain Gauges)	Baldwin-Lima-Hamilton	Custom	--
Controller (Back Pressure)	Terra Tek	2013	--
Controller (Diff. Pressure)	Terra Tek	2013	--
Servo Controller (Actuator)	Terra Tek	2050	--
Signal Conditioner (Load-Actuator Servo)	Terra Tek	2085	--
Cable (Instrumentation Signal)	Baldwin-Lima-Hamilton	103998-1	--
Cable (Trunk Signal)	Columbia Wire	C6046 C6044	-- --
Date Logger	Fluke	2240A	069017
Flow Meter	Flow Technology	OmniFlow FTM-N20-LJS	8503075
Flow Totalizer	Flow Technology	7010AA3	AA79010004
Function Generator (Actuator Servo)	Exact	340	19303
Load Cell	Baldwin-Lima-Hamilton	Custom	--
LVDT(DC)	Schaevitz Engineering	HPD125(±0.16cm) HPD150(±0.31cm)	3 digits* 4 digits*
Power Supplies(LVDT)	Micro Power	9040	--
Power Supply & Signal Cond. (Flowmeter)	Flow Technology	PRI-102AA2	1E7901-0004
Power Supply & Signal Cond. (Abs. Press. Trans.)	Baldwin-Lima-Hamilton	Custom	--
Power Supply & Signal Cond.(Abs.Press.Trans.)	Terra Tek	2013	--

(continued next page)

Table A6.1 (continued)

Item	Manufacturer	Model	Serial No.
Power Supply & Signal Cond.(Diff.Press.Trans.)	Validyne	CD-23-1181	50836
Pump	S.C. Hydraulic Engineering	1.50	14510
Back Pressure Regulator	Terra Tek	--	--
Diff. Pressure Regulator	Terra Tek	(modified)	--
Absolute Pressure Trans.	Baldwin-Lima-Hamilton	GP-CG	20934
Absolute Pressure Trans.	Dynisco	PT310JA-1M	113917
Diff. Pressure Trans.	Validyne	DP215TL	37693
Signal Cond. & Digital Output(Thermocouple)	Analog Devices	AD2036/J1121	7908
Printer Terminal	Teletype	43 Basic KSR	848 039896
Tape Cassette	TechTran	8400	10498
Strain Gauges(on sample)			
Thermocouple	Terra Tek	--	--
XYY Recorders	Hewlett-Packard	7046A	1914A05816 1739A03877
Strip Chart Recorder	Soltec	1330/46/3415	792375

* See Table A6.3.

pressures called for in the test program. The pressure pulses generated by the air-activated recipocating pumps could not easily be attenuated. This tended to produce undesirable pulsing feedback from the pressure transducers to the pressure controllers. The problem was partially eliminated by placing the pressure transducers at the maximum possible distance downstream of the pumps, although a large phase-lag between the input pressure signal to the controller and the actual pressure at the control point resulted. It was thus not an entirely satisfactory solution. The pressure controllers were themselves a source of uncontrolled oscillation. They were of the upper-and-lower-set-point type. When the pressure in the vessel fell below set point they caused the back pressure regulator to close suddenly, causing a disruption of flow, which was immediately followed by a rise in vessel pressure, and reopening of the back pressure regulator. This process was further complicated by elastic expansion and contraction of the triaxial vessel in response to the pressure changes. The oscillatory pattern of flow that resulted could be kept to an acceptably small amplitude only through a tedious and time-consuming series of fine adjustments to the control equipment. It is recommended that in future designs of such equipment, use of non-reciprocating pumps and fully continuous servo-control of pressure regulators be considered.

A6.4 INSTRUMENTS MOUNTED ON THE CORE

A6.4.1 Strain Gauges

The type of strain gauge used for the tests and the procedures used to mount them on the core are given in Table A6.2.

Table A6.2. Strain gauge mounting procedure.

Strain Gauge	Type CEA-09-500UW-120 by Micro-Measurement, Inc. (M-M) Raleigh, N.C. (Encapsulated, epoxy, advanced temperature compensated to 9×10^{-6} in./°F, 0.5 in length, 120 Ohm)
Calibration	1 mV/V = 2000 Microstrain for Gauge Factor = 2.00
Gauge Factor	2.015
Preparation	1. Grind flat and sand rock surface
	2. Clean with 190-proof ethyl alcohol
	3. Clean with M-M neutralizer
	4. Dry with heat lamp
	5. Apply 3 coats M-M type AE-10 cement. Cure, sand lightly and clean between coats
	6. Position gauge and conductor tabs on Teflon tape, position tape mounted gauges and tabs on rock, lift one end of tape to allow coating of gauge and rock with M-M type AE-10 cement, then replace tape on rock.
	7. Press gauge against rock by tensioning length of glass fiber tape wrapped several times around rock. Gauge protected by silicon rubber pad
	8. Wire gauges to tabs using M-M Soldereze
	9. Wire shieded conductor to tabs
	10. Coat gauge, tabs and Soldereze wire with M-M Coat D vinyl coating and allow to cure
	11. Coat wire with M-M Coat B nitrile rubber and allow to cure
	12. Coat entire area around gauge and tabs with M-M Coat G flexible polysulphide base epoxy

A6.4.2 LVDTs

A6.4.2.1 LVDTs Across Fractures

The DC-LVDT's were mounted in a system of clamps (see Fig. A6.1) that acted as a universal joint for precise alignment of the LVDT core in the body. Deformation was measured between pairs of 1.27 cm diameter stainless steel or aluminum anchors set with epoxy into holes drilled about 5 cm into the rock. To prevent leaks through the electrical cables, brass mechanical seals constructed from standard Swageloc tubing unions were used to form the cable to LVDT coupling. To prevent jamming of the LVDT core in the body and to minimize alignment errors from the motion of fractures normal to the LVDT axis, the cores were connected to the anchors through a short section of brass wire, soft soldered to the core extension rods. Each core was then centered in the LVDT body by a Teflon guide that also served to prevent debris falling into the body. This arrangement is shown in Figs. A6.2 and A6.3.

The locations of the LVDTs on the core were given in Fig. 5.5. Their orientations relative to the fractures at these points are given in Fig. A6.4 and in Table A6.3.

A6.4.2.2. Total Axial Deformations

Overall axial deformation was measured by LVDTs mounted on aluminum bars approximately 1.3 m long and anchored near the top and bottom of the core in a manner similar to that for LVDTs measuring fracture deformation. The arrangment is shown in Fig. A6.5.

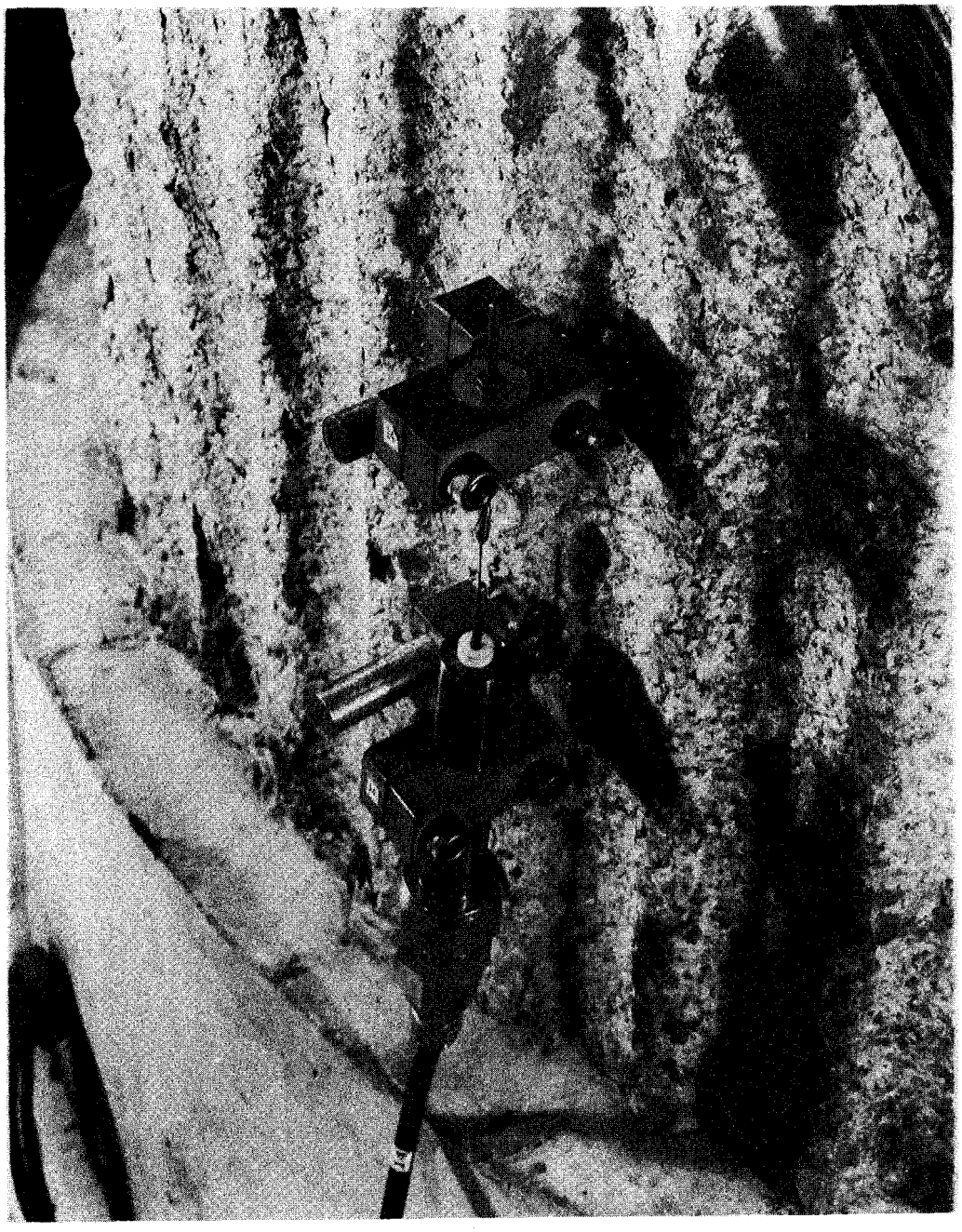

CBB 803-3607

Fig. A6.1 Mounted LVDT.

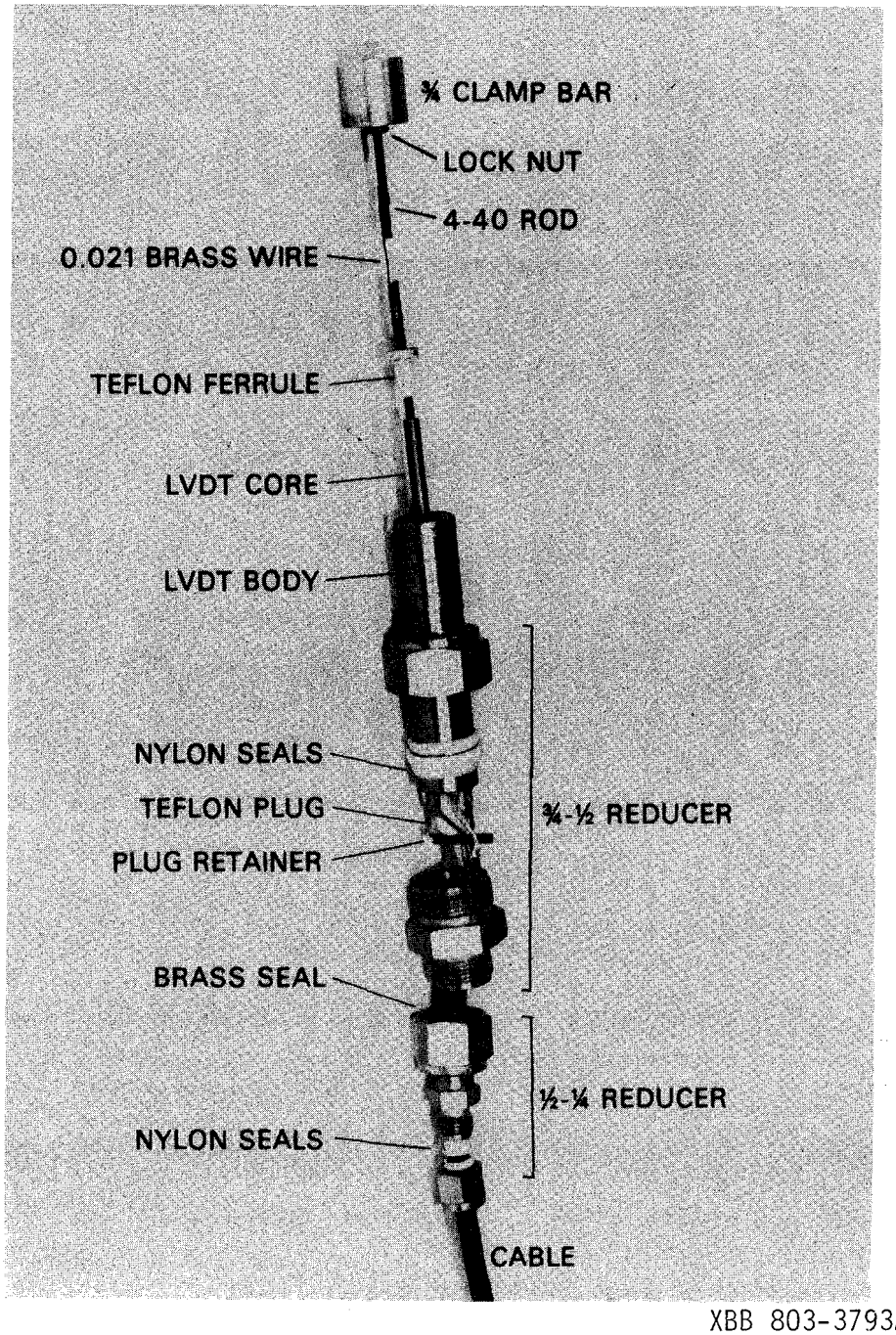

XBB 803-3793A

Fig. A6.2 Exploded view of LVDT unit.

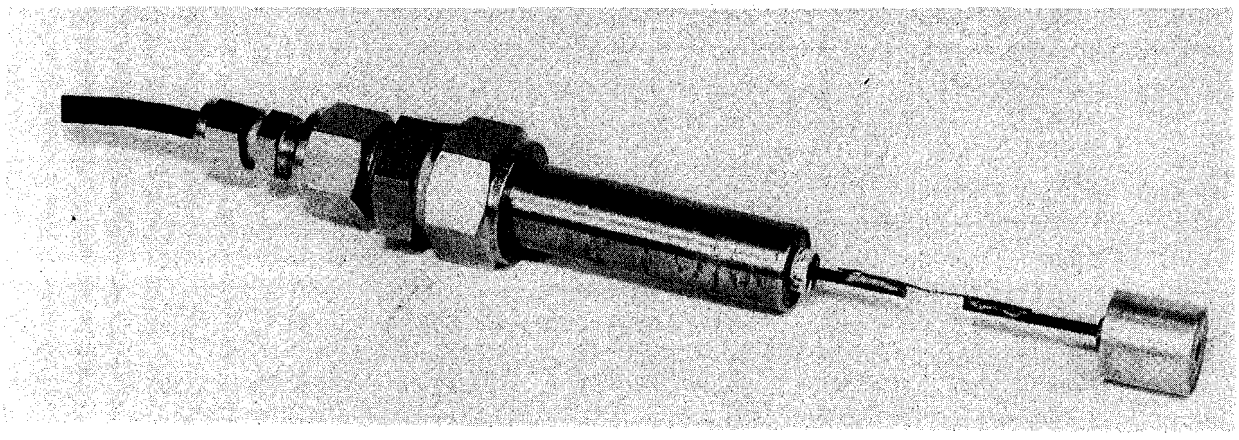

CBB 803-3791

Fig. A6.3 Assembled LVDT unit.

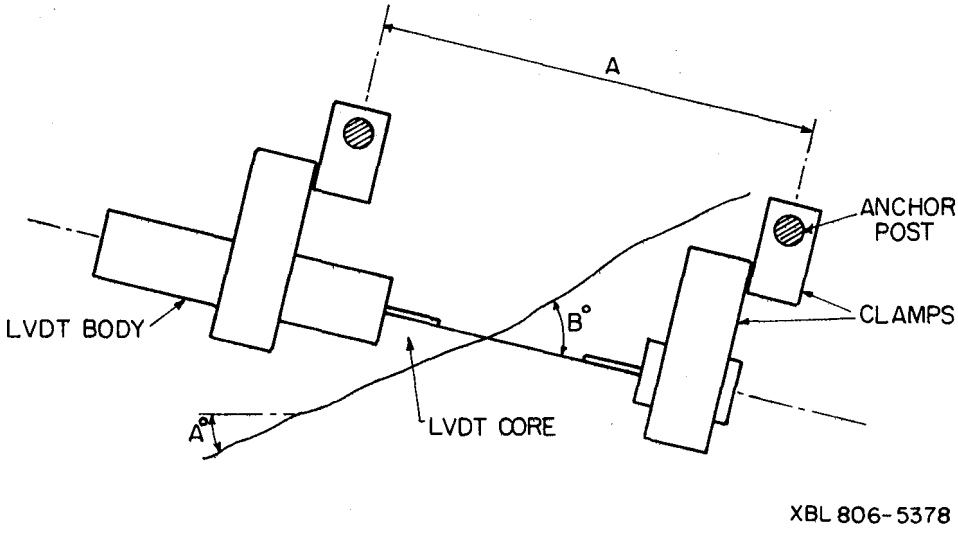

Fig. A6.4 LVDT orientation references.

Table A6.3. LVDT locations and orientations.

LVDT No.	Serial No.	Location (Fracture)	Orientation	A (cm)	Fracture Dip Angle A*	LVDT-Fracture Angle B*
1	300	A	vert.	10.8	6°	75°
2	297	C	vert.	9.8	6°	85°
3	141	D	vert.	14.9	57°	35°
5	126	A	vert.	9.6	10°	83°
6	1422	B	horiz.	14.9	17°	20°
7	301	D	vert.	14.3	60°	25°
8	299	D	horiz.	10.2	60°	65°
9	145	E	vert.	15.1	60°	30°
10	337	A	vert.	10.8	5°	85°
11	1501	B	vert.	8.5	6°	85°
12	298	E	horiz.	10.4	60°	55°
13	1419	B	vert.	10.3	17°	10°
14	1423	C	vert.	9.6	7°	82°
16	1496	C	vert.	10.3	3°	85°
17	1420	B	vert.	10.4	10°	80°
18	1427	Girth Gauge		Girth - 3.3 meters		
19	1494	Total Axial Disp.		1305.0	--	--
20	1421	Total Axial Disp.		1304.0	--	--
21	1495	Total Axial Disp.		1300.0	--	--
22	912	F	vert.	10.4	63°	62°

* See Fig. A6.4 for illustration of angles A and B.

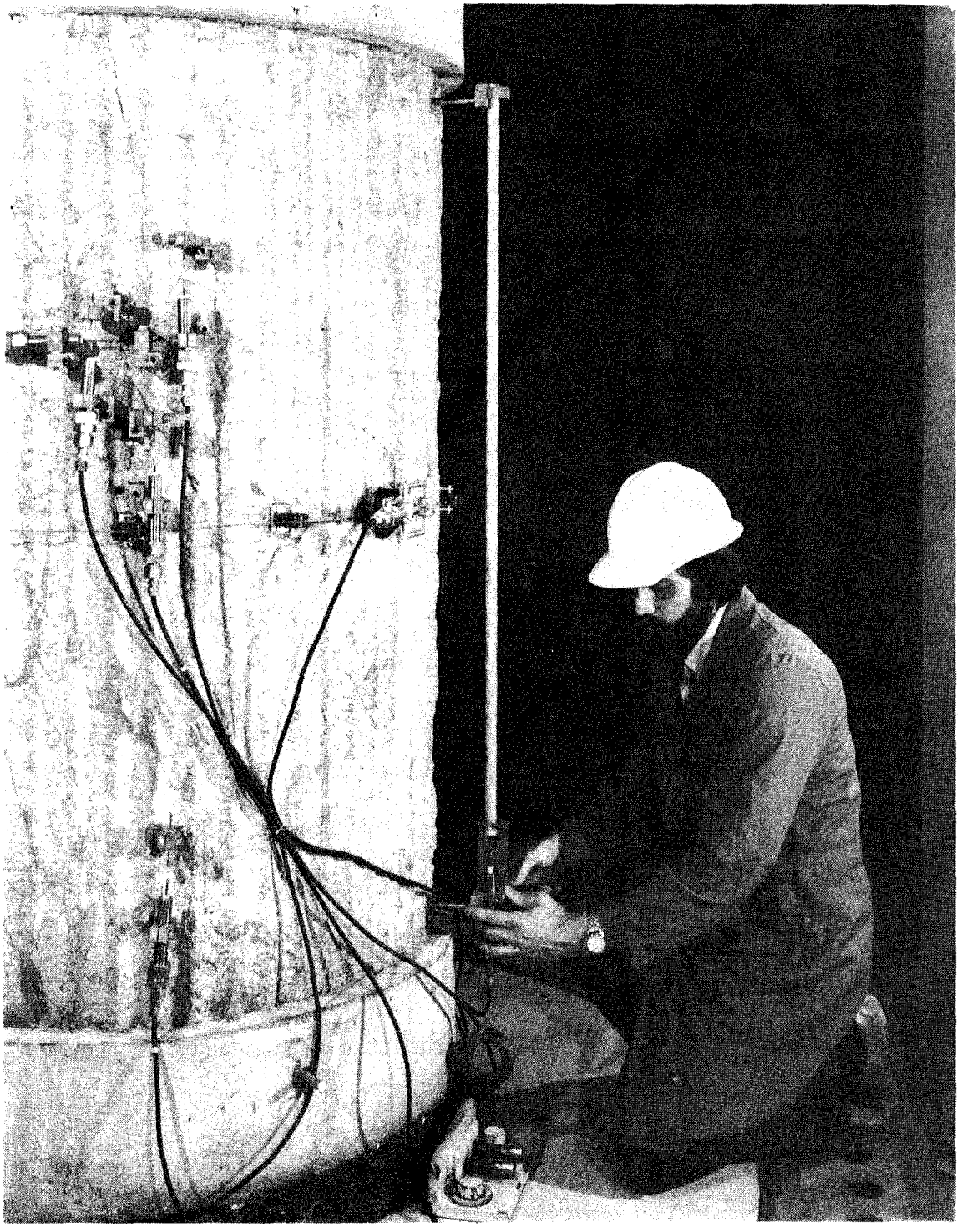

CBB 802-2036

Fig. A6.5 LVDT for measuring axial deformation.

A6.4.2.3 Girth Gauge

Radial deformation was measured by an LVDT mounted between the ends of a spring-tensioned cable. As shown in Fig. A6.6, the cable was stretched over a series of grooved low-friction pulleys mounted at 25 cm centers around the circumference of the core. The pulleys were mounted on curved aluminum base plates epoxyed onto the fluted surface of the core.

A6.4.2.4 LVDT Performance

Difficulty was encountered during the test program due to failure of the LVDT seals. LVDT's designed for complete immersion in pressurized fluids are not available from manufacturers. Water pressures in the triaxial vessel ranged between 1350 and 2050 kPa (200-300 psi). The seal system shown in Fig. A6.2 was basically similar to those used successfully in previous work with a small number of units. In the present application, the total number of units required was much greater, and the reliability of the LVDT system as a whole was poor. With maximum care in assembly, it was possible to seal most of the units. Failures were generally associated with the nylon seals around the LVDT body. These occurred because: 1) the positive pressure imbalance on the seal was of opposite sense to that for which the seal was designed, and 2) tightening the retaining nut sufficiently to form a reliable seal bent the body of the LVDT and resulted in damage to its internal components.

Leaks into the LVDT signal cable resulted in grounding of the power supply and signal conductors. Large leaks also allowed water to penetrate into the cable and flow into the pressure feed-through junction box. This resulted in generalized short-circuiting of the instrumentation system.

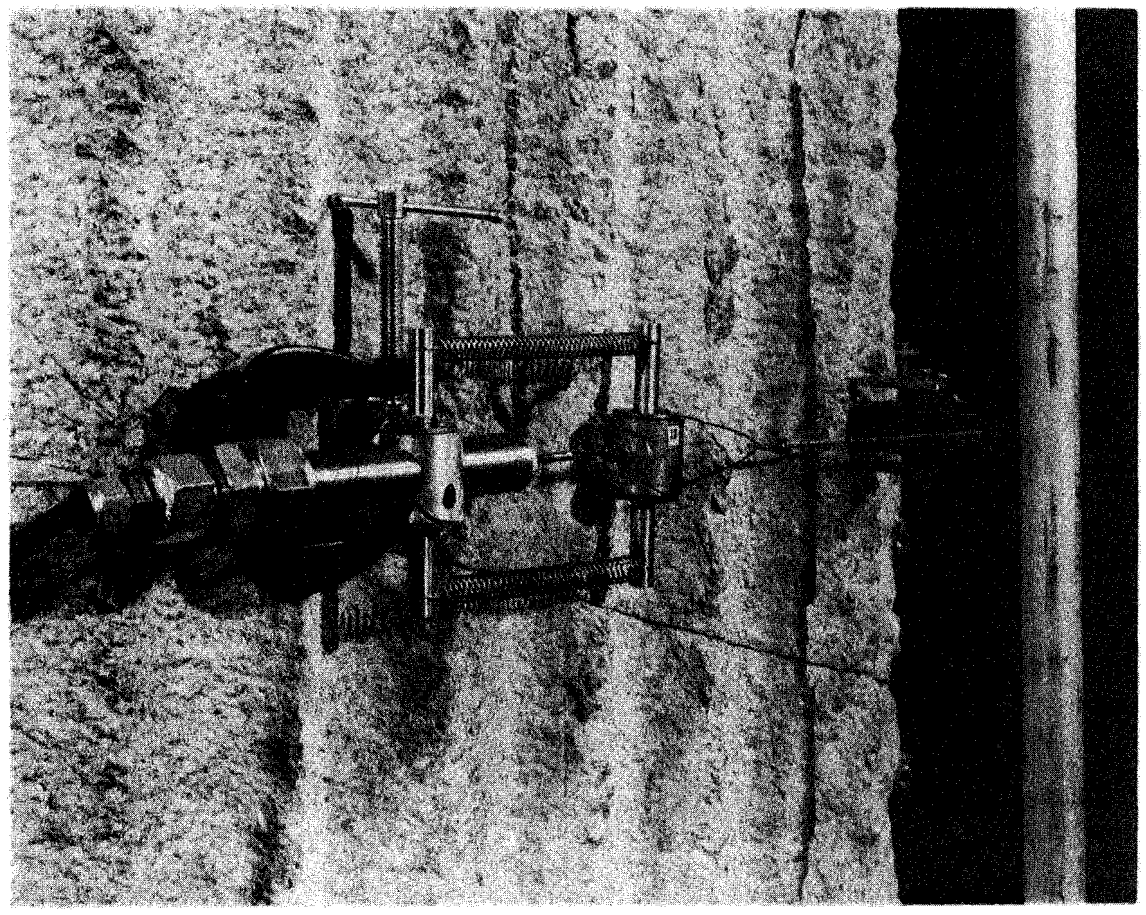

CBB 802-8022

Fig. A6.6 Girth gauge.

Tracing the source of leaks to individual LVDT's was difficult and time consuming, for it required complete depressurization and disassembly of the triaxial vessel. Also, due to the congested nature of the electrical junction box and the delicacy of the electronic components, repair of leaks frequently involved extensive secondary damage to the system. In some cases leaks through the seals were insufficient to produce a detectable flow through the cable to the exterior of the triaxial vessel. In other cases repeated re-sealing of the LVDT units caused damage to the conductor insulation. Either of these conditions could result in a short of the power supply to the body of the LVDT. On completion of the test program the LVDT units were inspected and some were found to have been damaged by electrolytic corrosion resulting from short circuits. Most of these exhibited only minor etching of metal surfaces and no significant malfunction resulted. In others, notably LVDT No. 14, the brass connection wire was completely dissolved and the instrument was encrusted with galvanic products. The appearance of this LVDT is shown in Fig. A6.7. Analyses of the deposits by energy-dispersive x-ray and x-ray diffraction techniques showed them to be aluminum hydroxide, copper, copper oxide, zinc hydroxide carbonate, calcium carbonate and minor amounts of other compounds compatible with corrosion of the brass and aluminium in a tap water environment (Anamet Laboratories, 1980). A fully engineered, custom-built LVDT sealing system is currently being developed to eliminate these problems in future test programs.

A6.5 DATA ACQUISITION

The data acquisition system has been described in Section 5.5 and Fig. 5.4. The data channel assignments used for recording instrument outputs, together with the instrument ranges and calibrations are given in Table A6.4.

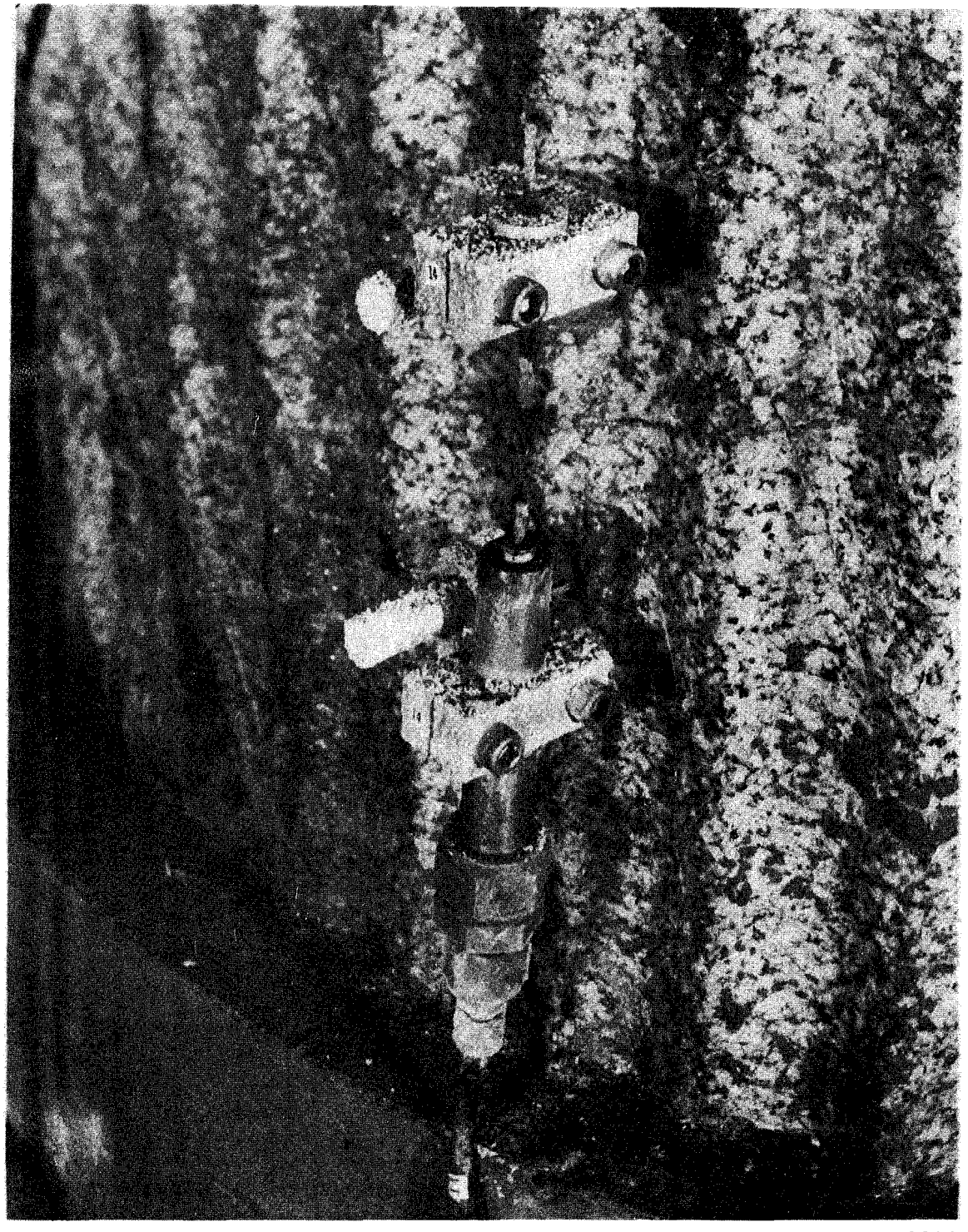

CBB 802-2026

Fig. A6.7 LVDT Damaged by corrosion.

Table A6.4. Data channel assignments.

Channel No.	Transducer	Range	Calibration
0	Flowmeter(Omniflow)	0.7-7.5 l/m	2 liters/min/volt
1	LVDT#1(Schaevitz)	±0.16 cm.	-0.3375 mm/V
2	LVDT#2(Schaevitz)	"	-0.3149 mm/V
3	LVDT#3(Schaevitz)	"	-0.3056 mm/V
4	Not Used	--	--
5	LVDT#5(Schaevitz)	±0.16cm	-0.3110 mm/V
6	LVDT#6(Scahevitz)	±0.31 cm	-0.6195 mm/V
7	LVDT#7(Schaevitz)	±0.16 cm	-0.3411 mm/V
8	LVDT#8(Schaevitz)	"	-0.3092 mm/V
9	LVDT#9(Schaevitz)	"	-0.3137 mm/V
10	LVDT#10(Schaevitz)	"	-0.3240 mm/V
11	LVDT#11(Schaevitz)	±0.31 cm	-0.6303 mm/V
12	LVDT"12(Schaevitz)	±0.16 cm	-0.3097 mm/V
13	LVDT#13(Schaevitz)	±0.31 cm	-0.6408 mm/V
14	LVDT#14(Schaevitz)	"	-0.6237 mm/V
15	Not Used	--	--
16	LVDT#16(Schaevitz)	±0.31 cm	-0.6379 mm/V
17	LVDT#17(Schaevitz)	"	-0.5876 mm/V
18	LVDT#18(Schaevitz)	"	-0.5953 mm/V
19	LVDT#19(Schaevitz)	"	-0.6161 mm/V
20	LVDT#20(Schaevitz)	"	-0.6122 mm/V
21	LVDT#21(Schaevitz)	"	-0.6284 mm/V
22	LVDT#22(Schaevitz)	±0.16 cm	-0.3104 mm/V
23	Load Cell(Bridge #1)	*	*
24	Strain Gauge #24	2%	674.45 micro-strain/mV
25	Strain Gauge #25	"	"
26	Strain Gauge #26	"	"
27	Strain Gauge #27	"	"
28	Abs. Pres. (Dynesco)	0-6900 kPa	6.9 kPa/mV
29	Diff. Pres. (Validyne)	±552 kPa	†
30	Abs. Pres. (BLH)	0-3450 kPa	92.8 kPa/mV
31	Load Cell (1/2 Bridge A)	*	*
32	Load Cell (1/2 Bridge B)	*	*
33	Load Cell (1/2 Bridge C)	*	*
34	Load Cell (1/2 Bridge D)	*	*
35	Thermocouple	-60°-760°C	0.5605 °C/μV

* See Hsu and Watkins (1979).

† Δp = [34.886 (output in V) - 0.6977] kPa.

APPENDIX VII

TEST DATA IN ENGINEERING UNITS

The raw-voltage outputs gathered from the instrumentation during testing were recorded in digital form on magnetic tape. The raw data was reduced to the form of engineering units with the aid of a Tektronix 4051 computer. The following pages document the complete test record in Standard International (SI) units. The record is organized chronologically by successive data-logger scans. The same data has been recorded on magnetic tape using a Tektronix 4051 computer. The tape record has been organized in an array format suitable for direct input in computer-aided analysis.

STRENGTH AND PERMEABILITY TESTS ON ULTRA-LARGE STRIPA GRANITE CORE (Engineering Units Data)

This appendix contains instrumentation output gathered from a laboratory test program performed on a 1.89 meter high by 1.04 meter diameter cylindrical sample of quartz-monzonite rock recovered from the iron-ore mine at Stripa Sweden. The data is presented in engineering units.

The purpose of the test was to obtain the strength (unconfined compressive) and deformation (stress-strain) characteristics of the sample and to study the permeability of the core at different states of axial stress.

The core was placed in the triaxial vessel on 22 February 1980. After several attempts the vessel was sealed against leaks at a pressure of 1380 kPa and the core was tested on 20 March 1980. Axial load was applied to the sample at a rate of 11203 Newtons/minute but the loading ramp was interupted at four stages when the load was held constant while withdrawal and injection permeability tests were performed. The following summarizes the test program:

Time hr:min:sec	Duration hr:min:sec	Action
11:28:19-11:46:19	00:18:00	Initiate data gathering; zero load; vessel pressurizing
11:49:57-12:32:42	00:42:45	Zero load injection test
12:42:20-13:41:26	00:59:06	Lower piston; apply seating load
13:42:10-13:54:10	00:12:00	Loading to 0.85 MPa
14:03:16-14:53:22	00:50:06	Permeability testing at 0.85 MPa axial stress
14:58:20-15:26:16	00:27:56	Loading from 0.85 to 2.89 MPa
15:31:27-17:03:33	01:32:06	Permeability testing at 2.89 MPa axial stress
17:13:03-18:19:02	01:05:59	Loading from 2.89 to 5.55 MPa
18:22:35-19:58:47	01:36:12	Permeability testing at 5.55 MPa axial stress
20:18:36-20:55:05	00:36:29	Loading from 5.55 MPa to failure at 7.5 MPa peak axial stress
21:08:49-21:12:49	00:04:00	Permeability test on failed sample
21:19:50-21:42:31	00:22:41	Sample unloading
21:47:04-23:07:36	01:20:32	No load; vessel draining
		End of data gathering

Each instrument can be identified by its respective index number as shown below:

Index	Instrument	Units
	Time Base	day:hr:min:sec
1	Flow Meter	liters/min
2	LVDT # 1 (deformation)	mm
3	LVDT # 2 (deformation)	mm
4	LVDT # 3 (deformation)	mm
5	LVDT # 5 (deformation)	mm
6	LVDT # 6 (deformation)	mm
7	LVDT # 7 (deformation)	mm
8	LVDT # 8 (deformation)	mm
9	LVDT # 9 (deformation)	mm
10	LVDT #10 (deformation)	mm
11	LVDT #11 (deformation)	mm
12	LVDT #12 (deformation)	mm
13	LVDT #13 (deformation)	mm
14	LVDT #14 (deformation)	mm
15	LVDT #16 (deformation)	mm
16	LVDT #17 (deformation)	mm
17	LVDT #18 (deformation)	mm
18	LVDT #19 (deformation)	mm
19	LVDT #20 (deformation)	mm
20	LVDT #21 (deformation)	mm
21	LVDT #22 (deformation)	mm
22	Load Cell (axial stress)	MPa
23	Strain Gage #24	microstrain
24	Strain Gage #25	microstrain
25	Strain Gage #26	microstrain
26	Strain Gage #27	microstrain
27	Press. Trans (Abs. Vessel)	KPa
28	Press. Trans (Differential)	KPa
29	Press. Trans (Abs. Borehole)	KPa
30	Load Cells (Eccentricity)	cm
31	Thermocouple	degrees C

```
**STRENGTH AND PERMEABILITY TESTS ON ULTRA-LARGE
**STRIPA GRANITE CORE (Engineering Units Data)
**11:28:19 - 11:46:19
**Initiate data gathering; zero load; vessel pressurizing
**Notes:  1. LVDT's 13 & 14 have failed.  Fracture C now has only
**           one active LVDT.  Fracture B now has two vertical
**           and one horizontal LVDT.
**        2. LVDT 7 has erratic response but passes electrical
**           check.  Assume O.K.
**        3. Vessel pressure locked in at 202 psi at 18:30 on
**           3/19/80.  Rose to 207 psi by 8:00 on 3/20/80.
**Probably due to temperature response of triaxial
**vessel.
Scan #  1
20:11:28:19
    1      0 lpm    2      0  mm    3      0  mm    4      0  mm    5      0  mm    6      0  mm    7      0  mm
    8      0  mm    9      0  mm   10      0  mm   11      0  mm   12      0  mm   13      0  mm   14      0  mm
   15      0  mm   16      0  mm   17      0  mm   18      0  mm   19      0  mm   20      0  mm   21      0  mm
   22      0 MPa   23      0  ms   24      0  ms   25      0  ms   26      0  ms   27    974 KPa   28 -1.814 KPa
   29    949 KPa   30      0  cm   31   17.8  dC
Scan #  2
20:11:30:19
    1      0 lpm    2      0  mm    3-4.0E-4  mm    4      0  mm    5      0  mm    6-7.0E-4  mm    7-4.0E-4  mm
    8-4.0E-4  mm    9-4.0E-4  mm   10      0  mm   11      0  mm   12-1.0E-3  mm   13 0.0877  mm   14 0.0149  mm
   15-7.0E-4  mm   16      0  mm   17      0  mm   18      0  mm   19-7.0E-4  mm   20-7.0E-4  mm   21-4.0E-4  mm
   22      0 MPa   23      0  ms   24      0  ms   25      0  ms   26    5.8  ms   27    975 KPa   28 -1.814 KPa
   29    950 KPa   30      0  cm   31   17.7  dC
Scan #  3
20:11:32:19
    1      0 lpm    2      0  mm    3-4.0E-4  mm    4 3.0E-4  mm    5      0  mm    6-7.0E-4  mm    7-4.0E-4  mm
    8-4.0E-4  mm    9-4.0E-4  mm   10      0  mm   11      0  mm   12-1.0E-3  mm   13 0.0557  mm   14 0.0018  mm
   15-7.0E-4  mm   16      0  mm   17-6.0E-4  mm   18      0  mm   19-7.0E-4  mm   20-7.0E-4  mm   21-4.0E-4  mm
   22      0 MPa   23      0  ms   24      0  ms   25      0  ms   26    6.7  ms   27    975 KPa   28 -1.814 KPa
   29    950 KPa   30      0  cm   31   17.6  dC
Scan #  4
20:11:34:19
    1      0 lpm    2-4.0E-4  mm    3-1.0E-3  mm    4 6.0E-4  mm    5 3.0E-4  mm    6      0  mm    7-0.0011  mm
    8-1.0E-3  mm    9-0.0013  mm   10      0  mm   11-7.0E-4  mm   12-0.0031  mm   13-0.1609  mm   14 0.0193  mm
   15-7.0E-4  mm   16      0  mm   17      0  mm   18-7.0E-4  mm   19-0.0013  mm   20-7.0E-4  mm   21-4.0E-4  mm
   22      0 MPa   23      0  ms   24      0  ms   25      0  ms   26    0.9  ms   27   1323 KPa   28  -1.43 KPa
   29   1287 KPa   30      0  cm   31     20  dC
Scan #  5
20:11:36:19
    1      0 lpm    2-4.0E-4  mm    3 0.0018  mm    4 3.0E-4  mm    5 3.0E-4  mm    6-7.0E-4  mm    7      0  mm
    8-0.0013  mm    9-0.0013  mm   10      0  mm   11      0  mm   12-0.0019  mm   13-0.1878  mm   14 0.0424  mm
   15      0  mm   16      0  mm   17      0  mm   18-0.0013  mm   19-0.0013  mm   20      0  mm   21-4.0E-4  mm
   22      0 MPa   23      0  ms   24     -6  ms   25      0  ms   26      0  ms   27   1380 KPa   28 -1.744 KPa
   29   1341 KPa   30      0  cm   31   20.2  dC
Scan #  6
20:11:38:19
    1      0 lpm    2-4.0E-4  mm    3 0.0021  mm    4 6.0E-4  mm    5 3.0E-4  mm    6      0  mm    7      0  mm
    8-0.0013  mm    9-0.0013  mm   10      0  mm   11      0  mm   12-0.0022  mm   13-0.1647  mm   14 0.1004  mm
   15      0  mm   16      0  mm   17      0  mm   18-0.0013  mm   19-0.0013  mm   20      0  mm   21-4.0E-4  mm
   22      0 MPa   23      0  ms   24   -6.8  ms   25      0  ms   26      0  ms   27   1360 KPa   28 -1.709 KPa
   29   1323 KPa   30      0  cm   31   21.4  dC
```

```
Scan #  7
20:11:40:19
    1       0 lpm    2-4.0E-4  mm    3 0.0021  mm    4 3.0E-4  mm    5 3.0E-4  mm    6       0  mm    7 3.0E-4  mm
    8-0.0013  mm     9-0.0013  mm   10       0  mm   11       0  mm   12-0.0022  mm   13-0.1878  mm   14 0.2812  mm
   15       0  mm   16-6.0E-4  mm   17       0  mm   18-0.0013  mm   19-0.0013  mm   20       0  mm   21-4.0E-4  mm
   22       0 MPa    23       0  ms   24   -6.8  ms   25       0  ms   26       0  ms   27    1374 KPa   28 -1.779 KPa
   29    1335 KPa    30       0  cm   31   21.8  dC
Scan #  8
20:11:42:19
    1       0 lpm    2-4.0E-4  mm    3 0.0025  mm    4 3.0E-4  mm    5 3.0E-4  mm    6       0  mm    7 3.0E-4  mm
    8-1.0E-3  mm     9-0.0016  mm   10       0  mm   11-7.0E-4  mm   12-0.0019  mm   13-0.1878  mm   14 0.3311  mm
   15       0  mm   16       0  mm   17-6.0E-4  mm   18-0.0019  mm   19-0.0013  mm   20       0  mm   21-4.0E-4  mm
   22       0 MPa    23       0  ms   24   -6.8  ms   25       0  ms   26       0  ms   27    1365 KPa   28 -1.779 KPa
   29    1326 KPa    30       0  cm   31   21.9  dC
Scan #  9
20:11:44:19
    1       0 lpm    2-4.0E-4  mm    3 0.0025  mm    4 3.0E-4  mm    5 3.0E-4  mm    6-7.0E-4  mm    7 6.0E-4  mm
    8-1.0E-3  mm     9-0.0013  mm   10       0  mm   11       0  mm   12-0.0013  mm   13-0.1833  mm   14 0.2818  mm
   15       0  mm   16       0  mm   17       0  mm   18-0.0013  mm   19-0.0013  mm   20       0  mm   21-7.0E-4  mm
   22       0 MPa    23       0  ms   24   -6.8  ms   25       0  ms   26       0  ms   27    1372 KPa   28 -1.814 KPa
   29    1333 KPa    30       0  cm   31   21.7  dC
Scan # 10
20:11:46:19
    1       0 lpm    2-4.0E-4  mm    3 0.0025  mm    4 3.0E-4  mm    5       0  mm    6       0  mm    7 6.0E-4  mm
    8-1.0E-3  mm     9-0.0016  mm   10       0  mm   11       0  mm   12-0.0019  mm   13-0.1948  mm   14 0.3723  mm
   15       0  mm   16       0  mm   17       0  mm   18-0.0019  mm   19-0.0013  mm   20       0  mm   21-4.0E-4  mm
   22       0 MPa    23       0  ms   24   -6.8  ms   25       0  ms   26       0  ms   27    1371 KPa   28 -1.814 KPa
   29    1332 KPa    30       0  cm   31   21.7  dC

**STRENGTH AND PERMEABILITY TESTS ON ULTRA-LARGE
**STRIPA GRANITE CORE (Engineering Units Data)
**11:49:57 - 12:30:42
**Zero-load injection test
Scan # 11
**First reading before flow testing:
20:11:49:57
    1  0.006 lpm    2-4.0E-4  mm    3 0.0025  mm    4 3.0E-4  mm    5 3.0E-4  mm    6       0  mm    7 0.0023  mm
    8-0.0013  mm     9-0.0016  mm   10       0  mm   11       0  mm   12-0.0025  mm   13-0.1692  mm   14 0.3286  mm
   15 6.0E-4  mm    16       0  mm   17       0  mm   18-0.0019  mm   19-0.0013  mm   20       0  mm   21-4.0E-4  mm
   22       0 MPa    23       0  ms   24   -6.8  ms   25       0  ms   26       0  ms   27    1365 KPa   28 -1.988 KPa
   29    1326 KPa    30       0  cm   31   21.4  dC
Scan # 12
**Approximate steady flow at 0.5 psi (3.4 KPa) injection:
20:12:13:33
    1  2.492 lpm    2-7.0E-4  mm    3 0.0034  mm    4       0  mm    5-4.0E-4  mm    6 0.0012  mm    7  0.002  mm
    8-1.0E-3  mm     9-0.0022  mm   10       0  mm   11 6.0E-4  mm   12  0.004  mm   13-0.2326  mm   14 1.9233  mm
   15 0.0012  mm    16 0.0017  mm   17       0  mm   18-0.0031  mm   19-0.0013  mm   20-7.0E-4  mm   21-7.0E-4  mm
   22       0 MPa    23       0  ms   24   -6.8  ms   25   -6.6  ms   26       0  ms   27    1372 KPa   28  0.977 KPa
   29    1344 KPa    30       0  cm   31   19.7  dC
Scan # 13
20:12:14: 3
    1  2.544 lpm    2-7.0E-4  mm    3 0.0034  mm    4       0  mm    5-4.0E-4  mm    6 0.0012  mm    7  0.003  mm
    8-1.0E-3  mm     9-0.0022  mm   10       0  mm   11 6.0E-4  mm   12 0.0046  mm   13-0.2333  mm   14 1.9239  mm
   15 0.0012  mm    16 0.0017  mm   17-6.0E-4  mm   18-0.0031  mm   19-0.0013  mm   20       0  mm   21-7.0E-4  mm
   22       0 MPa    23       0  ms   24   -3.3  ms   25   -6.7  ms   26       0  ms   27    1353 KPa   28  0.698 KPa
   29    1326 KPa    30       0  cm   31   19.6  dC
```

Scan # 14
20:12:14:33

1	2.525	lpm	2	-7.0E-4	mm	3	0.0034	mm	4	3.0E-4	mm	5	-4.0E-4	mm	6	0.0012	mm	7	0.0027	mm			
8	-1.0E-3	mm	9	-0.0022	mm	10	0	mm	11	0.0018	mm	12	0.0046	mm	13	-0.2339	mm	14	1.9127	mm			
15	0.0012	mm	16	0.0017	mm	17	0	mm	18	-0.0037	mm	19	-0.0013	mm	20	0	mm	21	-7.0E-4	mm			
22	0	MPa	23	0	ms	24	0	ms	25	-6.7	ms	26	0	ms	27	1353	KPa	28	1.081	KPa			
29	1316	KPa	30	0	cm	31	19.6	dC															

Scan # 15
20:12:15: 3

1	2.334	lpm	2	-7.0E-4	mm	3	0.0034	mm	4	3.0E-4	mm	5	-4.0E-4	mm	6	0.0012	mm	7	0.0027	mm			
8	-1.0E-3	mm	9	-0.0022	mm	10	0	mm	11	0.0018	mm	12	0.0049	mm	13	-0.2339	mm	14	1.9177	mm			
15	0.0012	mm	16	0.0017	mm	17	0	mm	18	-0.0031	mm	19	-0.0013	mm	20	-7.0E-4	mm	21	-7.0E-4	mm			
22	0	MPa	23	0	ms	24	-3.5	ms	25	-6.7	ms	26	0	ms	27	1354	KPa	28	0.942	KPa			
29	1314	KPa	30	0	cm	31	19.8	dC															

Scan # 16
20:12:15:33

1	2.049	lpm	2	-7.0E-4	mm	3	0.0034	mm	4	0	mm	5	-4.0E-4	mm	6	0.0012	mm	7	0.0027	mm			
8	-0.0013	mm	9	-0.0022	mm	10	0	mm	11	0.0018	mm	12	0.0061	mm	13	-0.2346	mm	14	1.8896	mm			
15	0.0012	mm	16	0.0017	mm	17	0	mm	18	-0.0037	mm	19	-0.0013	mm	20	0	mm	21	-7.0E-4	mm			
22	0	MPa	23	0	ms	24	-6.8	ms	25	-6.7	ms	26	0	ms	27	1364	KPa	28	0.768	KPa			
29	1323	KPa	30	0	cm	31	19.6	dC															

Scan # 17
20:12:16: 3

1	2.659	lpm	2	-7.0E-4	mm	3	0.0034	mm	4	0	mm	5	-4.0E-4	mm	6	0.0012	mm	7	0.003	mm			
8	-1.0E-3	mm	9	-0.0022	mm	10	0	mm	11	0.0025	mm	12	0.0061	mm	13	-0.2346	mm	14	1.8934	mm			
15	0.0012	mm	16	0.0017	mm	17	0	mm	18	-0.0037	mm	19	-0.0013	mm	20	0	mm	21	-7.0E-4	mm			
22	0	MPa	23	0	ms	24	-6.8	ms	25	-6.7	ms	26	0	ms	27	1367	KPa	28	0.837	KPa			
29	1327	KPa	30	0	cm	31	19.7	dC															

Scan # 18
20:12:16:33

1	2.854	lpm	2	-7.0E-4	mm	3	0.0034	mm	4	0	mm	5	-4.0E-4	mm	6	0.0012	mm	7	0.0023	mm			
8	-0.0013	mm	9	-0.0022	mm	10	0	mm	11	0.0025	mm	12	0.0058	mm	13	-0.2339	mm	14	1.884	mm			
15	0.0012	mm	16	0.0017	mm	17	0	mm	18	-0.0031	mm	19	-0.0013	mm	20	0	mm	21	-7.0E-4	mm			
22	0	MPa	23	0	ms	24	-6.8	ms	25	-6.7	ms	26	0	ms	27	1374	KPa	28	0.698	KPa			
29	1332	KPa	30	0	cm	31	19.6	dC															

Scan # 19
20:12:17: 3

1	2.848	lpm	2	-7.0E-4	mm	3	0.0034	mm	4	0	mm	5	-4.0E-4	mm	6	0.0012	mm	7	0.002	mm			
8	-1.0E-3	mm	9	-0.0022	mm	10	0	mm	11	0.0018	mm	12	0.0055	mm	13	-0.2352	mm	14	1.9426	mm			
15	0.0012	mm	16	0.0023	mm	17	0	mm	18	-0.0031	mm	19	-0.0013	mm	20	0	mm	21	-7.0E-4	mm			
22	0	MPa	23	0	ms	24	-6.8	ms	25	-6.7	ms	26	0	ms	27	1380	KPa	28	1.326	KPa			
29	1342	KPa	30	0	cm	31	19.7	dC															

Scan # 20
20:12:17:33

1	2.415	lpm	2	-7.0E-4	mm	3	0.0034	mm	4	0	mm	5	-4.0E-4	mm	6	0.0012	mm	7	0.002	mm			
8	-1.0E-3	mm	9	-0.0026	mm	10	0	mm	11	0.0025	mm	12	0.0052	mm	13	-0.2346	mm	14	2.0262	mm			
15	0.0012	mm	16	0.0017	mm	17	0	mm	18	-0.0037	mm	19	-0.0013	mm	20	0	mm	21	-7.0E-4	mm			
22	0	MPa	23	0	ms	24	-3.3	ms	25	-6.7	ms	26	0	ms	27	1366	KPa	28	0.907	KPa			
29	1338	KPa	30	0	cm	31	19.6	dC															

Scan # 21
20:12:18: 3

1	2.392	lpm	2	-7.0E-4	mm	3	0.0034	mm	4	0	mm	5	-4.0E-4	mm	6	0.0012	mm	7	0.002	mm			
8	-0.0013	mm	9	-0.0022	mm	10	0	mm	11	0.0025	mm	12	0.0049	mm	13	-0.2307	mm	14	2.02	mm			
15	0.0012	mm	16	0.0023	mm	17	0	mm	18	-0.0031	mm	19	-0.0013	mm	20	0	mm	21	-7.0E-4	mm			
22	0	MPa	23	0	ms	24	-3.5	ms	25	-6.7	ms	26	0	ms	27	1351	KPa	28	0.942	KPa			
29	1325	KPa	30	0	cm	31	19.7	dC															

```
Scan # 22
20:12:18:33
   1  2.469 lpm    2-7.0E-4  mm    3 0.0034  mm    4       0  mm    5-4.0E-4  mm    6 0.0012  mm    7  0.003  mm
   8-0.0013  mm    9-0.0026  mm   10       0  mm   11 0.0018  mm   12 0.0046  mm   13-0.2307  mm   14 2.0343  mm
  15 0.0012  mm   16 0.0023  mm   17       0  mm   18-0.0037  mm   19-0.0013  mm   20       0  mm   21-7.0E-4  mm
  22       0 MPa  23       0  ms   24    -6.8  ms   25    -6.7  ms   26       0  ms   27    1351 KPa  28  1.047 KPa
  29    1316 KPa  30       0  cm   31    19.6  dC
Scan # 23
20:12:19: 3
   1  2.186 lpm    2-7.0E-4  mm    3 0.0034  mm    4       0  mm    5-4.0E-4  mm    6 0.0012  mm    7 0.0027  mm
   8-1.0E-3  mm    9-0.0026  mm   10       0  mm   11 0.0025  mm   12 0.0043  mm   13-0.2326  mm   14 2.0225  mm
  15 0.0012  mm   16 0.0023  mm   17-6.0E-4  mm   18-0.0037  mm   19-7.0E-4  mm   20       0  mm   21-7.0E-4  mm
  22       0 MPa  23       0  ms   24    -3.3  ms   25    -6.7  ms   26       0  ms   27    1362 KPa  28  0.907 KPa
  29    1322 KPa  30       0  cm   31    19.7  dC
Scan # 24
20:12:19:33
   1  2.109 lpm    2-7.0E-4  mm    3 0.0034  mm    4       0  mm    5-4.0E-4  mm    6 0.0012  mm    7 0.0027  mm
   8-1.0E-3  mm    9-0.0022  mm   10       0  mm   11 0.0025  mm   12 0.0043  mm   13-0.2346  mm   14 2.0094  mm
  15 0.0012  mm   16 0.0023  mm   17       0  mm   18-0.0037  mm   19-7.0E-4  mm   20       0  mm   21-7.0E-4  mm
  22       0 MPa  23       0  ms   24       0  ms   25    -6.7  ms   26       0  ms   27    1366 KPa  28  0.837 KPa
  29    1325 KPa  30       0  cm   31    19.6  dC
Scan # 25
20:12:20: 3
   1  2.791 lpm    2-7.0E-4  mm    3 0.0034  mm    4       0  mm    5-4.0E-4  mm    6 0.0012  mm    7  0.003  mm
   8-1.0E-3  mm    9-0.0026  mm   10 3.0E-4  mm   11 0.0025  mm   12 0.0043  mm   13-0.2333  mm   14 2.0019  mm
  15 0.0012  mm   16 0.0023  mm   17       0  mm   18-0.0037  mm   19-0.0013  mm   20       0  mm   21-7.0E-4  mm
  22       0 MPa  23       0  ms   24    -3.5  ms   25    -6.7  ms   26       0  ms   27    1382 KPa  28  0.837 KPa
  29    1340 KPa  30       0  cm   31    19.7  dC
Scan # 26
20:12:20:33
   1  2.452 lpm    2-7.0E-4  mm    3 0.0034  mm    4       0  mm    5-4.0E-4  mm    6 0.0018  mm    7 0.0023  mm
   8-1.0E-3  mm    9-0.0022  mm   10       0  mm   11 0.0025  mm   12 0.0034  mm   13-0.2326  mm   14 1.9439  mm
  15 0.0012  mm   16 0.0023  mm   17       0  mm   18-0.0037  mm   19-0.0013  mm   20       0  mm   21-7.0E-4  mm
  22       0 MPa  23       0  ms   24    -3.3  ms   25    -6.7  ms   26       0  ms   27    1358 KPa  28     1.5 KPa
  29    1332 KPa  30       0  cm   31    19.6  dC
Scan # 27
20:12:21: 3
   1   1.96 lpm    2-7.0E-4  mm    3 0.0034  mm    4       0  mm    5-4.0E-4  mm    6 0.0012  mm    7  0.002  mm
   8-1.0E-3  mm    9-0.0026  mm   10       0  mm   11 0.0025  mm   12 0.0034  mm   13-0.2333  mm   14 1.9358  mm
  15 0.0012  mm   16 0.0023  mm   17       0  mm   18-0.0037  mm   19-0.0013  mm   20       0  mm   21-7.0E-4  mm
  22       0 MPa  23       0  ms   24    -3.5  ms   25    -6.7  ms   26       0  ms   27    1355 KPa  28  0.907 KPa
  29    1315 KPa  30       0  cm   31    19.6  dC
Scan # 28
20:12:21:33
   1    2.09 lpm    2-7.0E-4  mm    3 0.0034  mm    4 3.0E-4  mm    5-4.0E-4  mm    6 0.0018  mm    7  0.002  mm
   8-1.0E-3  mm    9-0.0026  mm   10 3.0E-4  mm   11 0.0031  mm   12 0.0037  mm   13-0.2314  mm   14 1.9445  mm
  15 0.0012  mm   16 0.0023  mm   17       0  mm   18-0.0037  mm   19-0.0013  mm   20       0  mm   21-7.0E-4  mm
  22       0 MPa  23       0  ms   24    -3.3  ms   25    -6.7  ms   26       0  ms   27    1371 KPa  28  0.942 KPa
  29    1330 KPa  30       0  cm   31    19.6  dC
Scan # 29
20:12:22: 3
   1  2.676 lpm    2-7.0E-4  mm    3 0.0034  mm    4 3.0E-4  mm    5-4.0E-4  mm    6 0.0018  mm    7  0.002  mm
   8-1.0E-3  mm    9-0.0026  mm   10       0  mm   11 0.0025  mm   12  0.004  mm   13-0.2314  mm   14 1.9108  mm
  15 0.0012  mm   16 0.0023  mm   17       0  mm   18-0.0037  mm   19-0.0013  mm   20       0  mm   21-7.0E-4  mm
  22       0 MPa  23       0  ms   24    -3.5  ms   25    -6.7  ms   26       0  ms   27    1381 KPa  28  1.186 KPa
  29    1340 KPa  30       0  cm   31    19.6  dC
```

```
Scan # 30
**Coincedence point on Soltec Record:
20:12:24:42
    1  2.461 lpm    2-7.0E-4  mm    3 0.0034  mm    4       0  mm    5-4.0E-4  mm    6 0.0018  mm    7  0.002  mm
    8-1.0E-3  mm    9-0.0026  mm   10       0  mm   11 0.0025  mm   12  0.004  mm   13 -0.232  mm   14 1.8154  mm
   15 0.0012  mm   16 0.0023  mm   17       0  mm   18-0.0037  mm   19-7.0E-4  mm   20-7.0E-4  mm   21-7.0E-4  mm
   22       0 MPa  23       0  ms   24    -6.8  ms   25    -6.7  ms   26       0  ms   27   1372 KPa   28  0.977 KPa
   29    1345 KPa  30       0  cm   31    19.6  dC
Scan # 31
20:12:26:42
    1  2.628 lpm    2-7.0E-4  mm    3 0.0034  mm    4 3.0E-4  mm    5-4.0E-4  mm    6 0.0018  mm    7  0.003  mm
    8-1.0E-3  mm    9-0.0026  mm   10       0  mm   11 0.0031  mm   12 0.0037  mm   13-0.2333  mm   14 1.7387  mm
   15 0.0012  mm   16 0.0023  mm   17       0  mm   18-0.0037  mm   19-0.0013  mm   20       0  mm   21-7.0E-4  mm
   22       0 MPa  23       0  ms   24    -0.8  ms   25    -6.7  ms   26       0  ms   27   1375 KPa   28  1.081 KPa
   29    1334 KPa  30       0  cm   31    19.6  dC
Scan # 32
20:12:28:42
    1  2.486 lpm    2-7.0E-4  mm    3 0.0034  mm    4       0  mm    5-4.0E-4  mm    6 0.0018  mm    7 0.0027  mm
    8-1.0E-3  mm    9-0.0026  mm   10 3.0E-4  mm   11 0.0031  mm   12 0.0043  mm   13-0.2397  mm   14 1.6651  mm
   15 0.0012  mm   16 0.0023  mm   17-6.0E-4  mm   18-0.0037  mm   19-0.0013  mm   20       0  mm   21-7.0E-4  mm
   22       0 MPa  23     5.9  ms   24       0  ms   25    -6.7  ms   26       0  ms   27   1362 KPa   28  1.186 KPa
   29    1321 KPa  30       0  cm   31    19.6  dC
Scan # 33
20:12:30:42
    1  2.254 lpm    2-7.0E-4  mm    3 0.0031  mm    4       0  mm    5-4.0E-4  mm    6 0.0018  mm    7 0.0027  mm
    8-1.0E-3  mm    9-0.0026  mm   10       0  mm   11 0.0031  mm   12 0.0046  mm   13 -0.239  mm   14 1.6832  mm
   15 0.0012  mm   16 0.0029  mm   17-6.0E-4  mm   18-0.0037  mm   19-0.0013  mm   20       0  mm   21-7.0E-4  mm
   22       0 MPa  23     0.8  ms   24       0  ms   25    -6.7  ms   26       0  ms   27   1361 KPa   28  0.942 KPa
   29    1320 KPa  30       0  cm   31    19.6  dC
Scan # 34
**End of flow test at 0.5 psi.
20:12:32:42
    1  2.014 lpm    2-7.0E-4  mm    3 0.0034  mm    4       0  mm    5-4.0E-4  mm    6 0.0018  mm    7 0.0027  mm
    8-1.0E-3  mm    9-0.0026  mm   10       0  mm   11 0.0031  mm   12 0.0052  mm   13-0.2371  mm   14 1.7231  mm
   15 0.0012  mm   16 0.0029  mm   17       0  mm   18-0.0037  mm   19-0.0013  mm   20       0  mm   21-1.0E-3  mm
   22       0 MPa  23       0  ms   24       0  ms   25    -6.7  ms   26       0  ms   27   1363 KPa   28  1.047 KPa
   29    1322 KPa  30       0  cm   31    19.7  dC

**STRENGTH AND PERMEABILITY TESTING ON ULTRA-LARGE
**STRIPA GRANITE CORE (Engineering Units Data)
**12:42:20 - 13:41:26
**Lower piston; apply seating load
Scan # 35
**Zero-load scan.
20:12:42:20
    1       0 lpm    2-7.0E-4  mm    3 0.0031  mm    4       0  mm    5-4.0E-4  mm    6 0.0018  mm    7  0.003  mm
    8-1.0E-3  mm    9-0.0022  mm   10       0  mm   11 0.0031  mm   12 0.0027  mm   13 -0.239  mm   14 1.9826  mm
   15 6.0E-4  mm   16 0.0029  mm   17       0  mm   18 -0.005  mm   19-0.0013  mm   20-7.0E-4  mm   21-7.0E-4  mm
   22       0 MPa  23     6.5  ms   24       0  ms   25    -0.2  ms   26     6.5  ms   27   1327 KPa   28   -1.5 KPa
   29    1290 KPa  30       0  cm   31    19.7  dC
Scan # 36
20:12:44:20
    1       0 lpm    2-7.0E-4  mm    3 0.0031  mm    4       0  mm    5-4.0E-4  mm    6 0.0018  mm    7 0.0034  mm
    8-7.0E-4  mm    9-0.0022  mm   10       0  mm   11 0.0031  mm   12 0.0012  mm   13 -0.241  mm   14 1.9214  mm
   15 6.0E-4  mm   16 0.0029  mm   17       0  mm   18-0.0056  mm   19-0.0013  mm   20-7.0E-4  mm   21-7.0E-4  mm
   22       0 MPa  23     6.7  ms   24     5.9  ms   25       0  ms   26     6.7  ms   27   1327 KPa   28   -1.5 KPa
   29    1290 KPa  30       0  cm   31    19.7  dC
```

Scan # 37
20:12:46:20

1	0	lpm	2	-7.0E-4	mm	3	0.0031	mm	4	0	mm	5	-4.0E-4	mm	6	0.0018	mm	7	0.0034	mm
8	-7.0E-4	mm	9	-0.0022	mm	10	0	mm	11	0.0031	mm	12	9.0E-4	mm	13	-0.2397	mm	14	1.8572	mm
15	6.0E-4	mm	16	0.0029	mm	17	-6.0E-4	mm	18	-0.0056	mm	19	-0.0013	mm	20	-7.0E-4	mm	21	-7.0E-4	mm
22	0	MPa	23	6.7	ms	24	0.8	ms	25	0	ms	26	6.7	ms	27	1327	KPa	28	-1.5	KPa
29	1290	KPa	30	0	cm	31	19.8	dC												

Scan # 38
20:12:48:20

1	0	lpm	2	-7.0E-4	mm	3	0.0031	mm	4	0	mm	5	-4.0E-4	mm	6	0.0012	mm	7	0.0034	mm
8	-1.0E-3	mm	9	-0.0026	mm	10	0	mm	11	0.0031	mm	12	0.0034	mm	13	-0.2397	mm	14	1.8684	mm
15	0.0012	mm	16	0.0029	mm	17	0	mm	18	-0.005	mm	19	-0.0013	mm	20	-7.0E-4	mm	21	-7.0E-4	mm
22	0	MPa	23	6.7	ms	24	0	ms	25	0	ms	26	6.7	ms	27	1327	KPa	28	-1.5	KPa
29	1290	KPa	30	0	cm	31	19.9	dC												

Scan # 39
20:12:50:20

1	0	lpm	2	-7.0E-4	mm	3	0.0031	mm	4	0	mm	5	-4.0E-4	mm	6	0.0018	mm	7	0.0034	mm
8	-7.0E-4	mm	9	-0.0026	mm	10	0	mm	11	0.0031	mm	12	0.004	mm	13	-0.2422	mm	14	1.8684	mm
15	6.0E-4	mm	16	0.0029	mm	17	0	mm	18	-0.005	mm	19	-0.0013	mm	20	-0.0013	mm	21	-7.0E-4	mm
22	0	MPa	23	6.7	ms	24	5.9	ms	25	0	ms	26	6.7	ms	27	1327	KPa	28	-1.5	KPa
29	1290	KPa	30	0	cm	31	19.8	dC												

Scan # 40
20:12:52:20

1	0	lpm	2	-7.0E-4	mm	3	0.0031	mm	4	0	mm	5	-4.0E-4	mm	6	0.0012	mm	7	0.0037	mm
8	-7.0E-4	mm	9	-0.0022	mm	10	0	mm	11	0.0025	mm	12	0.0024	mm	13	-0.248	mm	14	1.8622	mm
15	0.0012	mm	16	0.0023	mm	17	0	mm	18	-0.005	mm	19	-0.0013	mm	20	-7.0E-4	mm	21	-7.0E-4	mm
22	0	MPa	23	6.7	ms	24	6.7	ms	25	6	ms	26	6.7	ms	27	1326	KPa	28	-1.5	KPa
29	1290	KPa	30	0	cm	31	19.7	dC												

Scan # 41
20:12:54:20

1	0	lpm	2	-7.0E-4	mm	3	0.0031	mm	4	0	mm	5	-4.0E-4	mm	6	0.0018	mm	7	0.0037	mm
8	-7.0E-4	mm	9	-0.0026	mm	10	0	mm	11	0.0031	mm	12	0.0027	mm	13	-0.2487	mm	14	1.8036	mm
15	6.0E-4	mm	16	0.0029	mm	17	-6.0E-4	mm	18	-0.0056	mm	19	-0.0013	mm	20	-7.0E-4	mm	21	-7.0E-4	mm
22	0	MPa	23	6.7	ms	24	6.7	ms	25	6.8	ms	26	6.7	ms	27	1326	KPa	28	-1.5	KPa
29	1289	KPa	30	0	cm	31	19.8	dC												

Scan # 42
20:12:56:20

1	0	lpm	2	-7.0E-4	mm	3	0.0031	mm	4	0	mm	5	-4.0E-4	mm	6	0.0018	mm	7	0.0037	mm
8	-1.0E-3	mm	9	-0.0022	mm	10	0	mm	11	0.0025	mm	12	0.0027	mm	13	-0.2467	mm	14	1.8784	mm
15	0.0012	mm	16	0.0029	mm	17	-6.0E-4	mm	18	-0.005	mm	19	-0.0013	mm	20	-7.0E-4	mm	21	-7.0E-4	mm
22	0	MPa	23	6.7	ms	24	6.7	ms	25	0.8	ms	26	6.7	ms	27	1326	KPa	28	-1.5	KPa
29	1289	KPa	30	0	cm	31	19.7	dC												

Scan # 43
20:12:58:20

1	0	lpm	2	-7.0E-4	mm	3	0.0031	mm	4	0	mm	5	-4.0E-4	mm	6	0.0012	mm	7	0.0037	mm
8	-1.0E-3	mm	9	-0.0022	mm	10	0	mm	11	0.0025	mm	12	0.0027	mm	13	-0.2531	mm	14	1.9663	mm
15	6.0E-4	mm	16	0.0023	mm	17	0	mm	18	-0.005	mm	19	-0.0013	mm	20	-7.0E-4	mm	21	-7.0E-4	mm
22	0	MPa	23	6.7	ms	24	6.7	ms	25	0	ms	26	6.7	ms	27	1326	KPa	28	-1.5	KPa
29	1289	KPa	30	0	cm	31	19.6	dC												

Scan # 44
20:13: 0:20

1	0	lpm	2	-7.0E-4	mm	3	0.0031	mm	4	0	mm	5	-4.0E-4	mm	6	0.0018	mm	7	0.0037	mm
8	-7.0E-4	mm	9	-0.0022	mm	10	0	mm	11	0.0025	mm	12	0.0037	mm	13	-0.2448	mm	14	1.8928	mm
15	0.0012	mm	16	0.0023	mm	17	-6.0E-4	mm	18	-0.005	mm	19	-0.0013	mm	20	-7.0E-4	mm	21	-7.0E-4	mm
22	0	MPa	23	12.7	ms	24	6.7	ms	25	6	ms	26	6.7	ms	27	1326	KPa	28	-1.5	KPa
29	1289	KPa	30	0	cm	31	19.8	dC												

```
Scan # 45
20:13: 2:20
    1       0 lpm    2-7.0E-4  mm    3 0.0031  mm    4       0  mm    5-4.0E-4  mm    6 0.0012  mm    7  0.004  mm
    8-7.0E-4  mm     9-0.0022  mm   10       0  mm   11 0.0025  mm   12 0.0018  mm   13-0.2544  mm   14 1.8067  mm
   15 0.0012  mm    16 0.0023  mm   17       0  mm   18-0.0056  mm   19-0.0013  mm   20-7.0E-4  mm   21-7.0E-4  mm
   22       0 MPa   23   13.5  ms   24     6.7  ms   25     6.8  ms   26     6.7  ms   27   1325 KPa   28   -1.5 KPa
   29    1289 KPa   30       0  cm   31    19.8  dC
Scan # 46
20:13: 4:20
    1       0 lpm    2-7.0E-4  mm    3 0.0031  mm    4       0  mm    5-4.0E-4  mm    6 0.0012  mm    7 0.0037  mm
    8-7.0E-4  mm     9-0.0022  mm   10       0  mm   11 0.0025  mm   12  0.003  mm   13-0.2519  mm   14 1.8242  mm
   15 0.0012  mm    16 0.0023  mm   17       0  mm   18 -0.005  mm   19-0.0013  mm   20-7.0E-4  mm   21-7.0E-4  mm
   22       0 MPa   23    7.5  ms   24     6.7  ms   25     6.8  ms   26    12.6  ms   27   1325 KPa   28   -1.5 KPa
   29    1288 KPa   30       0  cm   31    19.6  dC
Scan # 47
20:13: 6:20
    1       0 lpm    2-7.0E-4  mm    3 0.0031  mm    4       0  mm    5-4.0E-4  mm    6 0.0012  mm    7 0.0037  mm
    8-7.0E-4  mm     9-0.0022  mm   10       0  mm   11 0.0025  mm   12 0.0027  mm   13-0.2557  mm   14 1.7543  mm
   15 6.0E-4  mm    16 0.0023  mm   17       0  mm   18 -0.005  mm   19-0.0013  mm   20-7.0E-4  mm   21-7.0E-4  mm
   22       0 MPa   23     6.7  ms   24     6.7  ms   25     6.8  ms   26    13.5  ms   27   1325 KPa   28   -1.5 KPa
   29    1288 KPa   30       0  cm   31    19.7  dC
Scan # 48
20:13: 8:20
    1       0 lpm    2-7.0E-4  mm    3 0.0031  mm    4       0  mm    5       0  mm    6 0.0012  mm    7 0.0044  mm
    8-7.0E-4  mm     9-0.0022  mm   10       0  mm   11 0.0018  mm   12  0.004  mm   13-0.2544  mm   14 1.7942  mm
   15 0.0012  mm    16 0.0023  mm   17       0  mm   18 -0.005  mm   19-0.0013  mm   20-7.0E-4  mm   21-7.0E-4  mm
   22       0 MPa   23    12.7  ms   24     6.7  ms   25     6.8  ms   26    13.5  ms   27   1324 KPa   28   -1.5 KPa
   29    1288 KPa   30       0  cm   31    19.6  dC
Scan # 49
20:13:10:20
    1       0 lpm    2-7.0E-4  mm    3 0.0031  mm    4 3.0E-4  mm    5-4.0E-4  mm    6 0.0012  mm    7  0.004  mm
    8-1.0E-3  mm     9-0.0026  mm   10       0  mm   11 0.0025  mm   12 0.0052  mm   13-0.2595  mm   14 1.9221  mm
   15 0.0012  mm    16 0.0023  mm   17-6.0E-4  mm   18 -0.005  mm   19-0.0013  mm   20-7.0E-4  mm   21-7.0E-4  mm
   22       0 MPa   23   13.5  ms   24     6.7  ms   25     6.8  ms   26     7.6  ms   27   1324 KPa   28   -1.5 KPa
   29    1288 KPa   30       0  cm   31    19.7  dC
Scan # 50
**Begin dropping load piston into vessel:
20:13:15:26
    1       0 lpm    2-7.0E-4  mm    3 0.0031  mm    4       0  mm    5       0  mm    6 0.0012  mm    7 0.0037  mm
    8-1.0E-3  mm     9-0.0026  mm   10       0  mm   11 0.0018  mm   12 0.0058  mm   13-0.2602  mm   14 1.8878  mm
   15 0.0012  mm    16 0.0023  mm   17-6.0E-4  mm   18 -0.005  mm   19-0.0013  mm   20-7.0E-4  mm   21-7.0E-4  mm
   22       0 MPa   23   13.5  ms   24     6.7  ms   25     6.8  ms   26    13.2  ms   27   1348 KPa   28 -1.535 KPa
   29    1311 KPa   30       0  cm   31    19.6  dC
Scan # 51
20:13:17:26
    1       0 lpm    2-7.0E-4  mm    3 0.0028  mm    4       0  mm    5       0  mm    6 0.0012  mm    7  0.004  mm
    8-1.0E-3  mm     9-0.0022  mm   10       0  mm   11 0.0018  mm   12 0.0049  mm   13-0.2595  mm   14 1.9009  mm
   15 0.0012  mm    16 0.0023  mm   17-6.0E-4  mm   18-0.0056  mm   19-0.0013  mm   20-0.0013  mm   21-7.0E-4  mm
   22       0 MPa   23   13.5  ms   24     6.7  ms   25     6.8  ms   26    13.5  ms   27   1363 KPa   28 -1.361 KPa
   29    1318 KPa   30       0  cm   31    19.7  dC
Scan # 52
20:13:19:26
    1       0 lpm    2-7.0E-4  mm    3 0.0031  mm    4 3.0E-4  mm    5       0  mm    6 0.0012  mm    7 0.0037  mm
    8-1.0E-3  mm     9-0.0026  mm   10       0  mm   11 0.0018  mm   12 0.0043  mm   13-0.2583  mm   14  1.846  mm
   15 0.0012  mm    16 0.0023  mm   17       0  mm   18 -0.005  mm   19-0.0013  mm   20-7.0E-4  mm   21-7.0E-4  mm
   22       0 MPa   23     7.5  ms   24     6.7  ms   25     6.8  ms   26    13.5  ms   27   1366 KPa   28 -1.395 KPa
   29    1327 KPa   30       0  cm   31    19.5  dC
```

```
Scan # 53
20:13:21:26
    1      0 lpm    2-0.0085  mm    3 0.0021  mm    4-0.0092  mm    5-7.0E-4  mm    6 0.0105  mm    7-0.0058  mm
    8-0.0028  mm    9-0.0044  mm   10-4.0E-4  mm   11-0.0057  mm   12 0.0037  mm   13-0.2608  mm   14 1.8404  mm
   15-0.0083  mm   16-0.0394  mm   17 5.0E-4  mm   18-0.0081  mm   19-0.0356  mm   20-0.0685  mm   21-0.0016  mm
   22      0 MPa   23   12.7  ms   24    6.7  ms   25    0.8  ms   26   13.5  ms   27   1309 KPa   28   -1.5 KPa
   29   1274 KPa   30      0  cm   31   19.6  dC
Scan # 54
20:13:23:26
    1      0 lpm    2-0.0085  mm    3 0.0021  mm    4-0.0092  mm    5-7.0E-4  mm    6 0.0111  mm    7-0.0062  mm
    8-0.0031  mm    9-0.0048  mm   10-4.0E-4  mm   11-0.0057  mm   12 0.0058  mm   13-0.2634  mm   14 1.7768  mm
   15 -0.009  mm   16-0.0435  mm   17 5.0E-4  mm   18-0.0093  mm   19-0.0392  mm   20-0.0761  mm   21-0.0016  mm
   22      0 MPa   23   13.5  ms   24    6.7  ms   25      0  ms   26   13.5  ms   27   1310 KPa   28   -1.5 KPa
   29   1274 KPa   30      0  cm   31   19.7  dC
Scan # 55
**Seating load applied.
20:13:25:26
    1      0 lpm    2-0.0102  mm    3 0.0015  mm    4-0.0199  mm    5-1.0E-3  mm    6 0.0099  mm    7-0.0133  mm
    8-0.0041  mm    9-0.0066  mm   10-4.0E-4  mm   11-0.0076  mm   12 0.0058  mm   13-0.2679  mm   14 1.7138  mm
   15-0.0173  mm   16-0.0764  mm   17 5.0E-4  mm   18 -0.021  mm   19-0.0729  mm   20 -0.127  mm   21-0.0031  mm
   22   0.04 MPa   23   13.5  ms   24    6.7  ms   25  -11.8  ms   26   13.5  ms   27   1322 KPa   28   -1.5 KPa
   29   1285 KPa   30      0  cm   31   19.6  dC
Scan # 56
**Begin load record:
20:13:27:26
    1      0 lpm    2-0.0108  mm    3 0.0012  mm    4-0.0217  mm    5-0.0013  mm    6 0.0099  mm    7-0.0154  mm
    8-0.0041  mm    9-0.0069  mm   10-7.0E-4  mm   11-0.0076  mm   12 0.0043  mm   13-0.2724  mm   14 1.6763  mm
   15-0.0185  mm   16-0.0823  mm   17 5.0E-4  mm   18-0.0259  mm   19-0.0796  mm   20-0.1364  mm   21-0.0038  mm
   22   0.04 MPa   23   13.5  ms   24    6.7  ms   25  -13.5  ms   26   13.5  ms   27   1321 KPa   28   -1.5 KPa
   29   1285 KPa   30      0  cm   31   19.6  dC
Scan # 57
20:13:29:26
    1      0 lpm    2-0.0108  mm    3 0.0012  mm    4-0.0217  mm    5-0.0013  mm    6 0.0099  mm    7-0.0154  mm
    8-0.0041  mm    9-0.0069  mm   10-7.0E-4  mm   11-0.0076  mm   12 0.0046  mm   13 -0.273  mm   14 1.6146  mm
   15-0.0185  mm   16-0.0817  mm   17 5.0E-4  mm   18-0.0265  mm   19-0.0802  mm   20 -0.137  mm   21-0.0038  mm
   22   0.04 MPa   23   13.5  ms   24    6.7  ms   25  -13.5  ms   26   13.5  ms   27   1322 KPa   28   -1.5 KPa
   29   1285 KPa   30      0  cm   31   19.7  dC
Scan # 58
20:13:31:26
    1      0 lpm    2-0.0108  mm    3 0.0012  mm    4-0.0217  mm    5-0.0013  mm    6 0.0099  mm    7-0.0154  mm
    8-0.0041  mm    9-0.0069  mm   10-7.0E-4  mm   11-0.0076  mm   12  0.004  mm   13 -0.273  mm   14 1.6265  mm
   15-0.0185  mm   16-0.0823  mm   17 5.0E-4  mm   18-0.0265  mm   19-0.0802  mm   20 -0.137  mm   21-0.0038  mm
   22   0.04 MPa   23   13.5  ms   24    6.7  ms   25  -13.5  ms   26   13.5  ms   27   1322 KPa   28   -1.5 KPa
   29   1286 KPa   30      0  cm   31   19.5  dC
Scan # 59
20:13:33:26
    1      0 lpm    2-0.0112  mm    3 0.0012  mm    4-0.0217  mm    5-0.0013  mm    6 0.0099  mm    7-0.0154  mm
    8-0.0041  mm    9-0.0073  mm   10-4.0E-4  mm   11-0.0076  mm   12 0.0046  mm   13-0.2672  mm   14  1.594  mm
   15-0.0185  mm   16-0.0823  mm   17 5.0E-4  mm   18-0.0265  mm   19-0.0809  mm   20 -0.137  mm   21-0.0038  mm
   22   0.04 MPa   23   13.5  ms   24    6.7  ms   25  -13.5  ms   26   13.5  ms   27   1323 KPa   28   -1.5 KPa
   29   1286 KPa   30      0  cm   31   19.7  dC
Scan # 60
20:13:35:26
    1      0 lpm    2-0.0108  mm    3 0.0012  mm    4-0.0217  mm    5-0.0013  mm    6 0.0099  mm    7-0.0154  mm
    8-0.0041  mm    9-0.0069  mm   10-7.0E-4  mm   11-0.0076  mm   12 0.0049  mm   13-0.2743  mm   14 1.5878  mm
   15-0.0185  mm   16-0.0823  mm   17 5.0E-4  mm   18-0.0272  mm   19-0.0802  mm   20-0.1364  mm   21-0.0038  mm
   22   0.04 MPa   23   13.5  ms   24    6.7  ms   25  -13.5  ms   26   13.5  ms   27   1323 KPa   28   -1.5 KPa
   29   1286 KPa   30      0  cm   31   19.4  dC
```

```
Scan # 61
20:13:37:26
    1       0 lpm    2-0.0108  mm    3 0.0012  mm    4-0.0217  mm    5-0.0013  mm    6 0.0092  mm    7-0.0154  mm
    8-0.0041  mm     9-0.0069  mm   10-7.0E-4  mm   11-0.0076  mm   12  0.004  mm   13-0.2724  mm   14 1.5672  mm
   15-0.0185  mm    16-0.0823  mm   17 5.0E-4  mm   18-0.0272  mm   19-0.0802  mm   20 -0.137  mm   21-0.0038  mm
   22    0.04 MPa   23    13.5  ms   24     6.7  ms   25  -19.4  ms   26    13.5  ms   27    1323 KPa   28    -1.5 KPa
   29    1286 KPa   30       0  cm   31    19.5  dC
Scan # 62
20:13:39:26
    1       0 lpm    2-0.0108  mm    3 9.0E-4  mm    4-0.0217  mm    5-0.0013  mm    6 0.0092  mm    7-0.0154  mm
    8-0.0041  mm     9-0.0073  mm   10-7.0E-4  mm   11-0.0076  mm   12 0.0037  mm   13-0.2743  mm   14 1.7094  mm
   15-0.0185  mm    16-0.0823  mm   17 5.0E-4  mm   18-0.0272  mm   19-0.0809  mm   20 -0.137  mm   21-0.0038  mm
   22    0.04 MPa   23    19.4  ms   24     6.7  ms   25  -14.3  ms   26    13.5  ms   27    1323 KPa   28    -1.5 KPa
   29    1286 KPa   30       0  cm   31    19.5  dC
Scan # 63
20:13:41:26
    1       0 lpm    2-0.0112  mm    3 9.0E-4  mm    4 -0.022  mm    5-0.0013  mm    6 0.0092  mm    7-0.0154  mm
    8-0.0041  mm     9-0.0073  mm   10-7.0E-4  mm   11-0.0076  mm   12 0.0037  mm   13-0.2749  mm   14 1.6701  mm
   15-0.0185  mm    16-0.0823  mm   17 5.0E-4  mm   18-0.0278  mm   19-0.0809  mm   20 -0.137  mm   21-0.0041  mm
   22    0.04 MPa   23    20.2  ms   24    12.7  ms   25  -13.5  ms   26    13.5  ms   27    1323 KPa   28    -1.5 KPa
   29    1287 KPa   30       0  cm   31    19.6  dC

**STRENGTH AND PERMEABILITY TESTING ON ULTRA-LARGE
**STRIPA GRANITE CORE (Engineering Units Data)
**13:42:10 - 13:54:10
**Loading to 0.85 MPa
Scan # 64
**Start loading:
20:13:42:10
    1       0 lpm    2-0.0112  mm    3 9.0E-4  mm    4 -0.022  mm    5-0.0013  mm    6 0.0092  mm    7-0.0154  mm
    8-0.0041  mm     9-0.0073  mm   10-7.0E-4  mm   11-0.0076  mm   12 0.0027  mm   13-0.2756  mm   14 1.6676  mm
   15-0.0185  mm    16-0.0823  mm   17 5.0E-4  mm   18-0.0284  mm   19-0.0809  mm   20 -0.137  mm   21-0.0041  mm
   22    0.04 MPa   23    20.2  ms   24    13.5  ms   25  -13.5  ms   26    13.5  ms   27    1323 KPa   28    -1.5 KPa
   29    1287 KPa   30       0  cm   31    19.6  dC
Scan # 65
20:13:42:40
    1       0 lpm    2-0.0112  mm    3 9.0E-4  mm    4 -0.022  mm    5-0.0013  mm    6 0.0099  mm    7-0.0154  mm
    8-0.0044  mm     9-0.0069  mm   10-7.0E-4  mm   11-0.0076  mm   12 0.0024  mm   13-0.2762  mm   14 1.6664  mm
   15-0.0185  mm    16-0.0823  mm   17 5.0E-4  mm   18-0.0284  mm   19-0.0802  mm   20-0.1364  mm   21-0.0038  mm
   22    0.02 MPa   23    20.2  ms   24    13.5  ms   25  -10.1  ms   26    13.5  ms   27    1321 KPa   28 -1.535 KPa
   29    1285 KPa   30       0  cm   31    19.6  dC
Scan # 66
20:13:43:10
    1       0 lpm    2-0.0105  mm    3 0.0012  mm    4-0.0181  mm    5-1.0E-3  mm    6 0.0105  mm    7-0.0133  mm
    8 -0.005  mm     9-0.0066  mm   10-7.0E-4  mm   11-0.0076  mm   12 0.0021  mm   13-0.2717  mm   14 1.6626  mm
   15-0.0179  mm    16-0.0747  mm   17 5.0E-4  mm   18-0.0247  mm   19-0.0729  mm   20-0.1245  mm   21-0.0031  mm
   22    0.02 MPa   23    20.2  ms   24    13.5  ms   25    -3.4  ms   26    16.7  ms   27    1318 KPa   28    -1.5 KPa
   29    1282 KPa   30       0  cm   31    19.6  dC
Scan # 67
20:13:43:40
    1       0 lpm    2-0.0102  mm    3 0.0018  mm    4-0.0144  mm    5-7.0E-4  mm    6 0.0105  mm    7-0.0116  mm
    8-0.0053  mm     9-0.0063  mm   10-7.0E-4  mm   11 -0.007  mm   12 0.0021  mm   13-0.2724  mm   14 1.6745  mm
   15-0.0166  mm    16-0.0653  mm   17 5.0E-4  mm   18-0.0204  mm   19-0.0643  mm   20-0.1087  mm   21-0.0028  mm
   22       0 MPa   23    20.2  ms   24    13.5  ms   25       0  ms   26    20.2  ms   27    1316 KPa   28    -1.5 KPa
   29    1280 KPa   30       0  cm   31    19.6  dC
```

Scan # 68
20:13:44:10

1 0 lpm	2-0.0098 mm	3 0.0015 mm	4-0.0129 mm	5-7.0E-4 mm	6 0.0105 mm	7-0.0103 mm	
8-0.0053 mm	9 -0.006 mm	10-7.0E-4 mm	11 -0.007 mm	12 0.0034 mm	13 -0.273 mm	14 1.6957 mm	
15-0.0154 mm	16-0.0612 mm	17 5.0E-4 mm	18-0.0185 mm	19-0.0594 mm	20-0.1006 mm	21-0.0025 mm	
22 0 MPa	23 20.2 ms	24 13.5 ms	25 0 ms	26 20.2 ms	27 1316 KPa	28 -1.5 KPa	
29 1280 KPa	30 0 cm	31 19.4 dC					

Scan # 69
20:13:44:40

1 0 lpm	2-0.0105 mm	3 0.0012 mm	4-0.0199 mm	5-1.0E-3 mm	6 0.0099 mm	7-0.0147 mm	
8-0.0053 mm	9-0.0069 mm	10-7.0E-4 mm	11-0.0076 mm	12 0.0037 mm	13-0.2711 mm	14 1.7007 mm	
15-0.0192 mm	16-0.0888 mm	17 5.0E-4 mm	18 -0.037 mm	19-0.0876 mm	20-0.1477 mm	21-0.0041 mm	
22 0.1 MPa	23 23.9 ms	24 13.5 ms	25 -13.5 ms	26 17 ms	27 1329 KPa	28 -1.43 KPa	
29 1293 KPa	30 0 cm	31 19.6 dC					

Scan # 70
20:13:45:10

1 0 lpm	2-0.0304 mm	3-0.0117 mm	4-0.0642 mm	5-0.0184 mm	6 0.0099 mm	7-0.0556 mm	
8 9.0E-4 mm	9-0.0129 mm	10-0.0033 mm	11 -0.007 mm	12 0.004 mm	13 -0.273 mm	14 1.682 mm	
15-0.0275 mm	16-0.1599 mm	17 5.0E-4 mm	18-0.1097 mm	19-0.1659 mm	20-0.2621 mm	21-0.0078 mm	
22 0.3 MPa	23 30.6 ms	24 17 ms	25 -43.8 ms	26 10.2 ms	27 1339 KPa	28 -1.43 KPa	
29 1302 KPa	30 3 cm	31 19.6 dC					

Scan # 71
20:13:45:40

1 0 lpm	2 -0.049 mm	3-0.0318 mm	4-0.0963 mm	5-0.0336 mm	6 0.0136 mm	7-0.0959 mm	
8 0.0074 mm	9-0.0179 mm	10-0.0062 mm	11-0.0045 mm	12 0.0046 mm	13-0.2717 mm	14 1.6738 mm	
15-0.0339 mm	16 -0.221 mm	17 0 mm	18-0.1904 mm	19-0.2418 mm	20-0.3613 mm	21-0.0115 mm	
22 0.6 MPa	23 33.7 ms	24 20.2 ms	25 -67.5 ms	26 3.5 ms	27 1343 KPa	28 -1.535 KPa	
29 1306 KPa	30 2.4 cm	31 19.5 dC					

Scan # 72
20:13:46:10

1 0 lpm	2-0.0544 mm	3-0.0381 mm	4-0.1058 mm	5-0.0383 mm	6 0.0154 mm	7-0.1089 mm	
8 0.0092 mm	9-0.0195 mm	10-0.0075 mm	11-0.0026 mm	12 0.0043 mm	13-0.2743 mm	14 1.6807 mm	
15-0.0364 mm	16-0.2427 mm	17 5.0E-4 mm	18-0.2249 mm	19-0.2725 mm	20-0.3984 mm	21-0.0131 mm	
22 0.76 MPa	23 33.7 ms	24 20.2 ms	25 -77.6 ms	26 -3.3 ms	27 1344 KPa	28 -1.535 KPa	
29 1306 KPa	30 2.4 cm	31 19.6 dC					

Scan # 73
20:13:46:40

1 0 lpm	2-0.0568 mm	3-0.0404 mm	4-0.1097 mm	5-0.0402 mm	6 0.0154 mm	7-0.1143 mm	
8 0.0105 mm	9-0.0204 mm	10-0.0081 mm	11-0.0019 mm	12 0.003 mm	13-0.2762 mm	14 1.6888 mm	
15-0.0377 mm	16 -0.248 mm	17 5.0E-4 mm	18-0.2366 mm	19-0.2829 mm	20-0.4097 mm	21-0.0137 mm	
22 0.81 MPa	23 33.7 ms	24 20.2 ms	25 -80.9 ms	26 -6.8 ms	27 1345 KPa	28 -1.535 KPa	
29 1307 KPa	30 2.5 cm	31 19.5 dC					

Scan # 74
20:13:47:10

1 0 lpm	2-0.0584 mm	3-0.0422 mm	4-0.1113 mm	5-0.0411 mm	6 0.0161 mm	7 -0.117 mm	
8 0.0111 mm	9-0.0207 mm	10-0.0081 mm	11-0.0013 mm	12 0.0034 mm	13-0.2743 mm	14 1.7038 mm	
15-0.0383 mm	16-0.2515 mm	17 5.0E-4 mm	18-0.2428 mm	19-0.2884 mm	20 -0.416 mm	21 -0.014 mm	
22 0.81 MPa	23 33.7 ms	24 20.2 ms	25 -80.9 ms	26 -6.8 ms	27 1345 KPa	28 -1.535 KPa	
29 1307 KPa	30 2.6 cm	31 19.5 dC					

Scan # 75
20:[illegible]

1 0 lpm	2-0.0588 mm	3-0.0426 mm	4-0.1119 mm	5-0.0414 mm	6 0.0161 mm	7-0.1177 mm	
8 0.0111 mm	9-0.0207 mm	10-0.0081 mm	11-0.0013 mm	12 0.0034 mm	13-0.2743 mm	14 1.7231 mm	
15-0.0383 mm	16-0.2527 mm	17 5.0E-4 mm	18-0.2446 mm	19-0.2902 mm	20-0.4179 mm	21 -0.014 mm	
22 0.79 MPa	23 33.7 ms	24 20.2 ms	25 -80.9 ms	26 -6.8 ms	27 1345 KPa	28 -1.535 KPa	
29 1307 KPa	30 2.5 cm	31 19.6 dC					

Scan # 76
20:13:48:10

1 0 lpm	2-0.0591 mm	3-0.0429 mm	4-0.1122 mm	5-0.0414 mm	6 0.0161 mm	7-0.1181 mm
8 0.0111 mm	9-0.0211 mm	10-0.0081 mm	11-0.0019 mm	12 0.0034 mm	13-0.2749 mm	14 1.7125 mm
15 -0.039 mm	16-0.2533 mm	17 0.0011 mm	18-0.2453 mm	19-0.2908 mm	20-0.4185 mm	21-0.0143 mm
22 0.79 MPa	23 33.7 ms	24 20.2 ms	25 -80.9 ms	26 -6.8 ms	27 1345 KPa	28 -1.535 KPa
29 1307 KPa	30 2.5 cm	31 19.5 dC				

Scan # 77
20:13:48:40

1 0 lpm	2-0.0591 mm	3-0.0429 mm	4-0.1122 mm	5-0.0414 mm	6 0.0161 mm	7-0.1181 mm
8 0.0111 mm	9-0.0207 mm	10-0.0081 mm	11-0.0013 mm	12 0.003 mm	13-0.2756 mm	14 1.7057 mm
15 -0.039 mm	16-0.2533 mm	17 0.0011 mm	18-0.2453 mm	19-0.2908 mm	20-0.4185 mm	21-0.0143 mm
22 0.79 MPa	23 33.7 ms	24 20.2 ms	25 -80.9 ms	26 -6.8 ms	27 1345 KPa	28 -1.535 KPa
29 1308 KPa	30 2.3 cm	31 19.4 dC				

Scan # 78
20:13:49:10

1 0 lpm	2-0.0588 mm	3-0.0429 mm	4-0.1122 mm	5-0.0414 mm	6 0.0161 mm	7-0.1181 mm
8 0.0111 mm	9-0.0211 mm	10-0.0081 mm	11-0.0013 mm	12 0.003 mm	13-0.2756 mm	14 1.7169 mm
15-0.0383 mm	16-0.2539 mm	17 5.0E-4 mm	18-0.2453 mm	19-0.2914 mm	20-0.4185 mm	21-0.0143 mm
22 0.79 MPa	23 33.7 ms	24 20.2 ms	25 -80.9 ms	26 -6.8 ms	27 1345 KPa	28 -1.535 KPa
29 1308 KPa	30 2.4 cm	31 19.5 dC				

Scan # 79
20:13:49:40

1 0 lpm	2-0.0591 mm	3-0.0429 mm	4-0.1122 mm	5-0.0414 mm	6 0.0161 mm	7-0.1184 mm
8 0.0111 mm	9-0.0211 mm	10-0.0081 mm	11-0.0013 mm	12 0.003 mm	13-0.2781 mm	14 1.7163 mm
15 -0.039 mm	16-0.2539 mm	17 5.0E-4 mm	18-0.2459 mm	19-0.2908 mm	20-0.4185 mm	21-0.0143 mm
22 0.77 MPa	23 33.7 ms	24 20.2 ms	25 -80.9 ms	26 -6.8 ms	27 1345 KPa	28 -1.535 KPa
29 1308 KPa	30 2.5 cm	31 19.6 dC				

Scan # 80
20:13:50:10

1 0 lpm	2-0.0591 mm	3-0.0432 mm	4-0.1122 mm	5-0.0414 mm	6 0.0161 mm	7-0.1184 mm
8 0.0111 mm	9-0.0211 mm	10-0.0081 mm	11-0.0013 mm	12 0.0034 mm	13-0.2768 mm	14 1.7262 mm
15-0.0383 mm	16-0.2539 mm	17 5.0E-4 mm	18-0.2453 mm	19-0.2914 mm	20-0.4185 mm	21-0.0143 mm
22 0.77 MPa	23 33.7 ms	24 20.2 ms	25 -84.3 ms	26 -6.8 ms	27 1345 KPa	28 -1.535 KPa
29 1308 KPa	30 2.5 cm	31 19.4 dC				

Scan # 81
20:13:50:40

1 0 lpm	2-0.0591 mm	3-0.0429 mm	4-0.1122 mm	5-0.0414 mm	6 0.0161 mm	7-0.1184 mm
8 0.0111 mm	9-0.0211 mm	10-0.0081 mm	11-0.0013 mm	12 0.0034 mm	13-0.2743 mm	14 1.7294 mm
15-0.0383 mm	16-0.2539 mm	17 5.0E-4 mm	18-0.2453 mm	19-0.2914 mm	20-0.4185 mm	21-0.0143 mm
22 0.77 MPa	23 30.1 ms	24 20.2 ms	25 -84.3 ms	26 -6.8 ms	27 1345 KPa	28 -1.535 KPa
29 1308 KPa	30 2.3 cm	31 19.5 dC				

Scan # 82
20:13:51:10

1 0 lpm	2-0.0595 mm	3-0.0432 mm	4-0.1125 mm	5-0.0414 mm	6 0.0161 mm	7-0.1184 mm
8 0.0111 mm	9-0.0211 mm	10-0.0081 mm	11-0.0019 mm	12 0.0034 mm	13-0.2749 mm	14 1.7449 mm
15-0.0383 mm	16-0.2539 mm	17 5.0E-4 mm	18-0.2459 mm	19 -0.292 mm	20-0.4185 mm	21-0.0143 mm
22 0.79 MPa	23 27 ms	24 20.2 ms	25 -84.3 ms	26 -6.8 ms	27 1345 KPa	28 -1.535 KPa
29 1308 KPa	30 2.4 cm	31 19.4 dC				

Scan # 83
20:13:51:40

1 0 lpm	2-0.0595 mm	3-0.0432 mm	4-0.1125 mm	5-0.0414 mm	6 0.0161 mm	7-0.1187 mm
8 0.0111 mm	9-0.0211 mm	10-0.0081 mm	11-0.0019 mm	12 0.0034 mm	13-0.2756 mm	14 1.7655 mm
15 -0.039 mm	16-0.2539 mm	17 5.0E-4 mm	18-0.2465 mm	19 -0.292 mm	20-0.4192 mm	21-0.0143 mm
22 0.79 MPa	23 27 ms	24 20.2 ms	25 -84.3 ms	26 -6.8 ms	27 1345 KPa	28 -1.535 KPa
29 1308 KPa	30 2.3 cm	31 19.6 dC				

```
Scan # 84
20:13:52:10
    1       0 lpm    2-0.0595  mm    3-0.0432  mm    4-0.1125  mm    5-0.0414  mm    6 0.0161  mm    7-0.1187  mm
    8 0.0111  mm     9-0.0211  mm   10-0.0081  mm   11-0.0013  mm   12  0.003  mm   13-0.2794  mm   14 1.7481  mm
   15 -0.039  mm    16-0.2539  mm   17 5.0E-4  mm   18-0.2465  mm   19-0.2927  mm   20-0.4192  mm   21-0.0143  mm
   22   0.79 MPa   23      27  ms   24    16.7  ms   25  -80.9  ms   26    -6.8  ms   27    1345 KPa   28 -1.535 KPa
   29   1308 KPa   30     2.1  cm   31    19.4  dC
Scan # 85
20:13:52:40
    1       0 lpm    2-0.0598  mm    3-0.0432  mm    4-0.1128  mm    5-0.0414  mm    6 0.0161  mm    7-0.1187  mm
    8 0.0114  mm     9-0.0211  mm   10-0.0081  mm   11-0.0013  mm   12 0.0034  mm   13-0.2801  mm   14 1.7425  mm
   15 -0.039  mm    16-0.2545  mm   17 5.0E-4  mm   18-0.2465  mm   19-0.2927  mm   20-0.4192  mm   21-0.0143  mm
   22   0.79 MPa   23      27  ms   24      17  ms   25  -80.9  ms   26    -6.8  ms   27    1346 KPa   28 -1.535 KPa
   29   1308 KPa   30     2.1  cm   31    19.6  dC
Scan # 86
20:13:53:10
    1       0 lpm    2-0.0598  mm    3-0.0435  mm    4-0.1128  mm    5-0.0414  mm    6 0.0161  mm    7-0.1187  mm
    8 0.0111  mm     9-0.0211  mm   10-0.0081  mm   11-0.0013  mm   12 0.0037  mm   13-0.2794  mm   14 1.7312  mm
   15 -0.039  mm    16-0.2545  mm   17 5.0E-4  mm   18-0.2471  mm   19-0.2927  mm   20-0.4198  mm   21-0.0143  mm
   22   0.79 MPa   23      27  ms   24    16.7  ms   25  -84.3  ms   26    -6.8  ms   27    1346 KPa   28 -1.535 KPa
   29   1308 KPa   30     2.1  cm   31    19.4  dC
Scan # 87
20:13:53:40
    1       0 lpm    2-0.0598  mm    3-0.0435  mm    4-0.1128  mm    5-0.0414  mm    6 0.0161  mm    7-0.1187  mm
    8 0.0114  mm     9-0.0211  mm   10-0.0081  mm   11-0.0013  mm   12 0.0037  mm   13-0.2813  mm   14 1.7275  mm
   15 -0.039  mm    16-0.2545  mm   17 5.0E-4  mm   18-0.2477  mm   19-0.2933  mm   20-0.4198  mm   21-0.0143  mm
   22   0.79 MPa   23      27  ms   24    13.5  ms   25  -87.6  ms   26     -10  ms   27    1346 KPa   28 -1.535 KPa
   29   1308 KPa   30       2  cm   31    19.6  dC
Scan # 88
20:13:54:10
    1       0 lpm    2-0.0598  mm    3-0.0438  mm    4-0.1131  mm    5-0.0414  mm    6 0.0161  mm    7-0.1191  mm
    8 0.0117  mm     9-0.0214  mm   10-0.0085  mm   11-0.0013  mm   12 0.0037  mm   13-0.2826  mm   14 1.7231  mm
   15 -0.039  mm    16-0.2545  mm   17 5.0E-4  mm   18-0.2483  mm   19-0.2939  mm   20-0.4204  mm   21-0.0143  mm
   22   0.81 MPa   23      27  ms   24      17  ms   25  -87.6  ms   26   -13.5  ms   27    1325 KPa   28 -1.535 KPa
   29   1288 KPa   30     2.2  cm   31    19.6  dC

**STRENGTH AND PERMEABILITY TESTING ON ULTRA-LARGE
**STRIPA GRANITE CORE (Engineering Units Data)
**14:03:16 - 14:53:22
**Permeability testing at 0.85 MPa axial stress
Scan # 89
**Approximate steady flow at 10.3 KPa (1.5 psi) injection:
20:14: 3:16
    1  2.619 lpm    2-0.0625  mm    3-0.0457  mm    4-0.1165  mm    5-0.0433  mm    6 0.0179  mm    7-0.1235  mm
    8 0.0148  mm     9-0.0226  mm   10-0.0088  mm   11 6.0E-4  mm   12  0.008  mm   13-0.2865  mm   14 1.7281  mm
   15-0.0402  mm    16-0.2556  mm   17 0.0017  mm   18-0.2582  mm   19-0.3031  mm   20-0.4292  mm   21-0.0153  mm
   22   0.85 MPa   23      27  ms   24    13.7  ms   25  -94.2  ms   26   -13.5  ms   27    1354 KPa   28 10.257 KPa
   29   1336 KPa   30     1.9  cm   31    19.9  dC
Scan # 90
20:14: 4:16
    1  2.626 lpm    2-0.0628  mm    3-0.0457  mm    4-0.1168  mm    5-0.0433  mm    6 0.0179  mm    7-0.1235  mm
    8 0.0151  mm     9-0.0226  mm   10-0.0085  mm   11       0  mm   12 0.0083  mm   13-0.2884  mm   14 1.7437  mm
   15-0.0402  mm    16-0.2556  mm   17 0.0017  mm   18-0.2588  mm   19-0.3037  mm   20-0.4292  mm   21-0.0153  mm
   22   0.85 MPa   23      27  ms   24    13.5  ms   25  -94.4  ms   26   -13.5  ms   27    1366 KPa   28  8.896 KPa
   29   1335 KPa   30     2.3  cm   31    19.8  dC
```

Scan # 91
20:14: 5:16

1 2.726 lpm	2-0.0628 mm	3-0.0457 mm	4-0.1168 mm	5-0.0436 mm	6 0.0179 mm	7-0.1239 mm	
8 0.0151 mm	9-0.0226 mm	10-0.0085 mm	11 6.0E-4 mm	12 0.0092 mm	13-0.2871 mm	14 1.725 mm	
15-0.0402 mm	16-0.2556 mm	17 0.0017 mm	18-0.2594 mm	19-0.3037 mm	20-0.4298 mm	21-0.0153 mm	
22 0.85 MPa	23 27 ms	24 13.5 ms	25 -94.4 ms	26 -13.5 ms	27 1381 KPa	28 9.21 KPa	
29 1349 KPa	30 2.1 cm	31 20 dC					

Scan # 92
20:14: 6:16

1 2.856 lpm	2-0.0628 mm	3 -0.046 mm	4-0.1171 mm	5-0.0436 mm	6 0.0185 mm	7-0.1239 mm	
8 0.0154 mm	9-0.0226 mm	10-0.0085 mm	11 6.0E-4 mm	12 0.0092 mm	13-0.2941 mm	14 1.7443 mm	
15-0.0402 mm	16-0.2562 mm	17 0.0017 mm	18 -0.26 mm	19-0.3043 mm	20-0.4298 mm	21-0.0153 mm	
22 0.87 MPa	23 27 ms	24 13.5 ms	25 -94.4 ms	26 -13.5 ms	27 1352 KPa	28 9.559 KPa	
29 1332 KPa	30 2.4 cm	31 19.8 dC					

Scan # 93
20:14: 7:16

1 2.726 lpm	2-0.0632 mm	3 -0.046 mm	4-0.1171 mm	5-0.0436 mm	6 0.0179 mm	7-0.1239 mm	
8 0.0157 mm	9-0.0226 mm	10-0.0085 mm	11 0.0012 mm	12 0.0083 mm	13-0.2941 mm	14 1.7075 mm	
15-0.0402 mm	16-0.2562 mm	17 0.0017 mm	18 -0.26 mm	19-0.3043 mm	20-0.4298 mm	21-0.0153 mm	
22 0.85 MPa	23 27 ms	24 13.5 ms	25 -94.4 ms	26 -18.5 ms	27 1366 KPa	28 9.733 KPa	
29 1334 KPa	30 2.2 cm	31 19.9 dC					

Scan # 94
20:14: 8:16

1 2.844 lpm	2-0.0632 mm	3 -0.046 mm	4-0.1174 mm	5-0.0439 mm	6 0.0185 mm	7-0.1239 mm	
8 0.0157 mm	9-0.0229 mm	10-0.0088 mm	11 6.0E-4 mm	12 0.0071 mm	13 -0.298 mm	14 1.7131 mm	
15-0.0402 mm	16-0.2562 mm	17 0.0023 mm	18 -0.26 mm	19-0.3043 mm	20-0.4305 mm	21-0.0153 mm	
22 0.85 MPa	23 27 ms	24 13.5 ms	25 -94.4 ms	26 -20.3 ms	27 1378 KPa	28 8.582 KPa	
29 1346 KPa	30 1.7 cm	31 20 dC					

Scan # 95
20:14: 9:16

1 2.653 lpm	2-0.0635 mm	3-0.0463 mm	4-0.1174 mm	5-0.0439 mm	6 0.0185 mm	7-0.1239 mm	
8 0.016 mm	9-0.0229 mm	10-0.0088 mm	11 0.0012 mm	12 0.0064 mm	13-0.2999 mm	14 1.7368 mm	
15-0.0402 mm	16-0.2562 mm	17 0.0023 mm	18-0.2607 mm	19-0.3043 mm	20-0.4305 mm	21-0.0153 mm	
22 0.87 MPa	23 27 ms	24 13.5 ms	25 -94.4 ms	26 -15.3 ms	27 1365 KPa	28 8.896 KPa	
29 1348 KPa	30 2 cm	31 19.9 dC					

Scan # 96
20:14:10:16

1 2.731 lpm	2-0.0635 mm	3-0.0463 mm	4-0.1174 mm	5-0.0439 mm	6 0.0185 mm	7-0.1239 mm	
8 0.016 mm	9-0.0229 mm	10-0.0088 mm	11 0.0012 mm	12 0.0055 mm	13-0.3018 mm	14 1.7387 mm	
15-0.0402 mm	16-0.2562 mm	17 0.0023 mm	18-0.2613 mm	19-0.3049 mm	20-0.4305 mm	21-0.0153 mm	
22 0.85 MPa	23 27 ms	24 13.5 ms	25 -94.4 ms	26 -18.5 ms	27 1355 KPa	28 8.791 KPa	
29 1325 KPa	30 1.7 cm	31 20 dC					

Scan # 97
20:14:11:16

1 2.672 lpm	2-0.0635 mm	3-0.0463 mm	4-0.1177 mm	5-0.0439 mm	6 0.0185 mm	7-0.1239 mm	
8 0.016 mm	9-0.0229 mm	10-0.0088 mm	11 0.0012 mm	12 0.0058 mm	13-0.3018 mm	14 1.7736 mm	
15-0.0402 mm	16-0.2562 mm	17 0.0023 mm	18-0.2613 mm	19-0.3049 mm	20-0.4305 mm	21-0.0153 mm	
22 0.85 MPa	23 27 ms	24 13.5 ms	25 -94.4 ms	26 -15.3 ms	27 1370 KPa	28 8.966 KPa	
29 1338 KPa	30 2.1 cm	31 20 dC					

Scan # 98
20:14:12:16

1 2.622 lpm	2-0.0638 mm	3-0.0463 mm	4-0.1177 mm	5-0.0439 mm	6 0.0185 mm	7-0.1239 mm	
8 0.0163 mm	9-0.0229 mm	10-0.0088 mm	11 0.0012 mm	12 0.0064 mm	13-0.3031 mm	14 1.7044 mm	
15-0.0402 mm	16-0.2556 mm	17 0.0023 mm	18-0.2619 mm	19-0.3049 mm	20-0.4311 mm	21-0.0153 mm	
22 0.87 MPa	23 27 ms	24 13.5 ms	25 -94.4 ms	26 -18.5 ms	27 1380 KPa	28 9.175 KPa	
29 1351 KPa	30 2.2 cm	31 20 dC					

```
Scan # 99
**Stop flow:
20:14:15:25
    1  0.006 lpm    2-0.0638  mm    3 -0.047  mm    4 -0.118  mm    5-0.0442  mm    6 0.0185  mm    7-0.1242  mm
    8 0.0166  mm    9-0.0226  mm   10-0.0088  mm   11 0.0018  mm   12 0.0034  mm   13 -0.305  mm   14 1.7593  mm
   15-0.0409  mm   16-0.2562  mm   17 0.0035  mm   18-0.2631  mm   19-0.3061  mm   20-0.4317  mm   21-0.0153  mm
   22   0.85 MPa   23     27  ms   24   13.5  ms   25  -94.4  ms   26  -20.3  ms   27   1330 KPa   28   0.07 KPa
   29   1294 KPa   30    1.9  cm   31   20.5  dC
Scan #100
20:14:26:36
    1  3.715 lpm    2-0.0645  mm    3-0.0473  mm    4-0.1192  mm    5-0.0445  mm    6 0.0185  mm    7-0.1239  mm
    8 0.0151  mm    9 -0.022  mm   10-0.0094  mm   11       0  mm   12 0.0055  mm   13-0.2589  mm   14 2.0194  mm
   15-0.0409  mm   16-0.2615  mm   17 0.0035  mm   18-0.2681  mm   19-0.3098  mm   20-0.4355  mm   21-0.0153  mm
   22   0.85 MPa   23   33.6  ms   24   13.5  ms   25  -87.8  ms   26  -13.7  ms   27   1294 KPa   28 17.199 KPa
   29   1241 KPa   30    1.7  cm   31   20.4  dC
Scan #101
**Approximate steady flow at 17.2 KPa (2.5 psi) withdrawal:
20:14:34: 4
    1  3.953 lpm    2-0.0645  mm    3-0.0492  mm    4-0.1195  mm    5-0.0445  mm    6 0.0185  mm    7-0.1249  mm
    8 0.0151  mm    9 -0.022  mm   10-0.0091  mm   11       0  mm   12 0.0068  mm   13 -0.289  mm   14 2.0063  mm
   15-0.0409  mm   16-0.2621  mm   17 0.0029  mm   18-0.2693  mm   19-0.3122  mm   20-0.4367  mm   21-0.0153  mm
   22   0.85 MPa   23   33.7  ms   24   13.5  ms   25  -94.2  ms   26  -13.5  ms   27   1302 KPa   28 17.094 KPa
   29   1249 KPa   30    1.8  cm   31     20  dC
Scan #102
20:14:35: 4
    1  3.732 lpm    2-0.0645  mm    3-0.0492  mm    4-0.1195  mm    5-0.0445  mm    6 0.0185  mm    7-0.1249  mm
    8 0.0148  mm    9 -0.022  mm   10-0.0094  mm   11       0  mm   12 0.0068  mm   13-0.2916  mm   14 2.0181  mm
   15-0.0409  mm   16-0.2627  mm   17 0.0035  mm   18-0.2699  mm   19-0.3129  mm   20-0.4374  mm   21-0.0153  mm
   22   0.85 MPa   23   28.6  ms   24   13.5  ms   25  -94.4  ms   26  -13.5  ms   27   1294 KPa   28  16.92 KPa
   29   1242 KPa   30    2.2  cm   31   20.5  dC
Scan #103
20:14:36: 4
    1  3.622 lpm    2-0.0649  mm    3-0.0492  mm    4-0.1198  mm    5-0.0445  mm    6 0.0185  mm    7-0.1252  mm
    8 0.0148  mm    9 -0.022  mm   10-0.0094  mm   11       0  mm   12 0.0064  mm   13-0.2967  mm   14 1.9932  mm
   15-0.0409  mm   16-0.2627  mm   17 0.0035  mm   18-0.2705  mm   19-0.3135  mm   20-0.4374  mm   21-0.0153  mm
   22   0.85 MPa   23   32.1  ms   24   13.5  ms   25  -94.4  ms   26  -13.5  ms   27   1292 KPa   28  16.92 KPa
   29   1240 KPa   30      2  cm   31   20.5  dC
Scan #104
20:14:37: 4
    1  3.762 lpm    2-0.0649  mm    3-0.0495  mm    4-0.1198  mm    5-0.0445  mm    6 0.0185  mm    7-0.1252  mm
    8 0.0151  mm    9 -0.022  mm   10-0.0094  mm   11       0  mm   12 0.0058  mm   13 -0.298  mm   14 2.0325  mm
   15-0.0409  mm   16-0.2627  mm   17 0.0035  mm   18-0.2705  mm   19-0.3135  mm   20-0.4374  mm   21-0.0153  mm
   22   0.85 MPa   23   28.6  ms   24   13.5  ms   25  -94.4  ms   26  -13.5  ms   27   1291 KPa   28 16.885 KPa
   29   1240 KPa   30      2  cm   31     20  dC
Scan #105
20:14:38: 4
    1  3.692 lpm    2-0.0649  mm    3-0.0495  mm    4-0.1198  mm    5-0.0445  mm    6 0.0185  mm    7-0.1256  mm
    8 0.0148  mm    9 -0.022  mm   10-0.0094  mm   11       0  mm   12 0.0074  mm   13-0.2954  mm   14 3.2692  mm
   15-0.0409  mm   16-0.2627  mm   17 0.0035  mm   18-0.2711  mm   19-0.3141  mm   20-0.4374  mm   21-0.0153  mm
   22   0.85 MPa   23     27  ms   24   13.5  ms   25  -94.4  ms   26  -13.5  ms   27   1289 KPa   28 17.129 KPa
   29   1237 KPa   30    2.3  cm   31   20.4  dC
Scan #106
20:14:39: 4
    1   3.97 lpm    2-0.0649  mm    3-0.0498  mm    4-0.1201  mm    5-0.0445  mm    6 0.0185  mm    7-0.1256  mm
    8 0.0151  mm    9 -0.022  mm   10-0.0094  mm   11       0  mm   12 0.0074  mm   13-0.2929  mm   14 3.4045  mm
   15-0.0409  mm   16-0.2627  mm   17 0.0035  mm   18-0.2711  mm   19-0.3141  mm   20-0.4374  mm   21-0.0153  mm
   22   0.85 MPa   23     27  ms   24   13.5  ms   25  -89.3  ms   26  -13.5  ms   27   1294 KPa   28 17.164 KPa
   29   1241 KPa   30      2  cm   31   19.7  dC
```

```
Scan #107
20:14:53:22
    1  0.006 lpm    2-0.0672  mm    3-0.0489  mm    4-0.1229  mm    5-0.0461  mm    6 0.0185  mm    7-0.1327  mm
    8 0.0173  mm    9-0.0229  mm   10-0.0101  mm   11       0  mm   12 0.0068  mm   13-0.3352  mm   14  3.644  mm
   15-0.0441  mm   16-0.2662  mm   17 0.0065  mm   18-0.2779  mm   19-0.3227  mm   20-0.4437  mm   21-0.0153  mm
   22    0.85 MPa  23      27  ms   24   13.5  ms   25  -87.6  ms   26  -13.5  ms   27   1343 KPa   28   -1.5 KPa
   29   1306 KPa   30     2.2  cm   31   22.6  dC

**STRENGTH AND PERMEABILITY TESTS ON ULTRA-LARGE
**STRIPA GRANITE CORE (Engineering Units Data)
**14:58:20 - 15:26:16
**Loading from 0.85 MPa to 2.89 MPa
Scan #108
**Initial readings:
20:14:58:20
    1       0 lpm    2-0.0672  mm    3-0.0489  mm    4-0.1229  mm    5-0.0461  mm    6 0.0185  mm    7-0.1324  mm
    8  0.017  mm    9-0.0229  mm   10-0.0101  mm   11       0  mm   12 0.0068  mm   13-0.3454  mm   14 3.6471  mm
   15-0.0447  mm   16-0.2662  mm   17 0.0065  mm   18-0.2779  mm   19-0.3227  mm   20-0.4437  mm   21-0.0156  mm
   22    0.85 MPa  23      27  ms   24   13.5  ms   25  -87.6  ms   26  -13.5  ms   27   1342 KPa   28 -1.535 KPa
   29   1305 KPa   30     2.2  cm   31   21.9  dC
Scan #109
**Resume loading:
20:15: 0:28
    1       0 lpm    2-0.0672  mm    3-0.0492  mm    4-0.1229  mm    5-0.0461  mm    6 0.0185  mm    7-0.1324  mm
    8  0.017  mm    9-0.0229  mm   10-0.0098  mm   11       0  mm   12 0.0055  mm   13-0.6203  mm   14 3.7219  mm
   15-0.0441  mm   16-0.2662  mm   17 0.0065  mm   18-0.2779  mm   19-0.3227  mm   20-0.4437  mm   21-0.0156  mm
   22    0.85 MPa  23      33  ms   24   13.5  ms   25  -87.6  ms   26  -13.5  ms   27   1342 KPa   28   -1.5 KPa
   29   1306 KPa   30     7.4  cm   31   21.8  dC
Scan #110
20:15: 0:58
    1       0 lpm    2-0.0672  mm    3-0.0492  mm    4-0.1229  mm    5-0.0461  mm    6 0.0185  mm    7-0.1324  mm
    8  0.017  mm    9-0.0229  mm   10-0.0101  mm   11-7.0E-4  mm   12 0.0058  mm   13-0.4306  mm   14 3.7831  mm
   15-0.0441  mm   16-0.2662  mm   17 0.0065  mm   18-0.2785  mm   19-0.3227  mm   20-0.4443  mm   21-0.0156  mm
   22    0.93 MPa  23    33.7  ms   24   13.5  ms   25  -87.6  ms   26  -13.5  ms   27   1342 KPa   28   -1.5 KPa
   29   1306 KPa   30     2.2  cm   31   21.7  dC
Scan #111
20:15: 1:28
    1       0 lpm    2-0.0699  mm    3 -0.052  mm    4-0.1281  mm    5-0.0486  mm    6 0.0204  mm    7-0.1399  mm
    8 0.0179  mm    9-0.0236  mm   10-0.0107  mm   11 6.0E-4  mm   12 0.0058  mm   13 -0.348  mm   14 3.6945  mm
   15-0.0447  mm   16-0.2727  mm   17 0.0065  mm   18 -0.297  mm   19 -0.338  mm   20  -0.46  mm   21-0.0162  mm
   22     1.1 MPa  23    33.7  ms   24     17  ms   25  -94.4  ms   26    -20  ms   27   1344 KPa   28 -1.465 KPa
   29   1307 KPa   30     1.6  cm   31   21.7  dC
Scan #112
20:15: 1:58
    1       0 lpm    2-0.0773  mm    3-0.0596  mm    4-0.1388  mm    5-0.0538  mm    6 0.0241  mm    7-0.1559  mm
    8 0.0219  mm    9-0.0251  mm   10 -0.012  mm   11 0.0018  mm   12 0.0061  mm   13-0.3473  mm   14 3.6615  mm
   15 -0.046  mm   16-0.2868  mm   17  0.016  mm   18-0.3303  mm   19 -0.368  mm   20-0.4927  mm   21-0.0171  mm
   22    1.36 MPa  23    33.7  ms   24   20.2  ms   25 -104.5  ms   26  -30.2  ms   27   1345 KPa   28   -1.5 KPa
   29   1309 KPa   30     1.8  cm   31   21.7  dC
Scan #113
20:15: 2:28
    1       0 lpm    2-0.0841  mm    3-0.0662  mm    4-0.1486  mm    5-0.0576  mm    6 0.0278  mm    7-0.1713  mm
    8 0.0275  mm    9-0.0267  mm   10-0.0137  mm   11 0.0025  mm   12 0.0068  mm   13-0.3499  mm   14 3.6883  mm
   15-0.0479  mm   16-0.3009  mm   17 0.0321  mm   18-0.3623  mm   19-0.3986  mm   20-0.5247  mm   21-0.0184  mm
   22     1.6 MPa  23    37.3  ms   24   23.7  ms   25 -114.7  ms   26  -40.2  ms   27   1346 KPa   28   -1.5 KPa
   29   1310 KPa   30     1.9  cm   31   21.6  dC
```

Scan #114
20:15: 2:58

1 0 lpm	2-0.0895 mm	3-0.0715 mm	4-0.1562 mm	5-0.0607 mm	6 0.0315 mm	7-0.1846 mm	
8 0.033 mm	9 -0.028 mm	10-0.0153 mm	11 0.0031 mm	12 0.0064 mm	13-0.3499 mm	14 3.7525 mm	
15-0.0504 mm	16 -0.312 mm	17 0.0476 mm	18-0.3894 mm	19-0.4255 mm	20-0.5492 mm	21-0.0196 mm	
22 1.84 MPa	23 40.4 ms	24 26.9 ms	25 -124.8 ms	26 -50.5 ms	27 1347 KPa	28 -1.5 KPa	
29 1311 KPa	30 1.8 cm	31 21.5 dC					

Scan #115
20:15: 3:28

1 0 lpm	2-0.0946 mm	3-0.0766 mm	4-0.1632 mm	5-0.0632 mm	6 0.034 mm	7-0.1969 mm	
8 0.0405 mm	9-0.0289 mm	10-0.0166 mm	11 0.0037 mm	12 0.0061 mm	13-0.3473 mm	14 3.7987 mm	
15-0.0523 mm	16-0.3214 mm	17 0.0625 mm	18-0.4128 mm	19-0.4494 mm	20 -0.57 mm	21-0.0208 mm	
22 2.07 MPa	23 40.4 ms	24 26.9 ms	25 -131.5 ms	26 -57.2 ms	27 1347 KPa	28 -1.5 KPa	
29 1311 KPa	30 1.8 cm	31 21.6 dC					

Scan #116
20:15: 3:58

1 0 lpm	2-0.0989 mm	3-0.0807 mm	4-0.1693 mm	5-0.0647 mm	6 0.0371 mm	7-0.2098 mm	
8 0.0479 mm	9-0.0302 mm	10-0.0179 mm	11 0.0044 mm	12 0.0061 mm	13-0.3505 mm	14 3.7338 mm	
15-0.0536 mm	16-0.3297 mm	17 0.0785 mm	18-0.4332 mm	19-0.4708 mm	20-0.5894 mm	21-0.0215 mm	
22 2.29 MPa	23 40.4 ms	24 26.9 ms	25 -138.3 ms	26 -64 ms	27 1348 KPa	28 -1.5 KPa	
29 1312 KPa	30 1.5 cm	31 21.5 dC					

Scan #117
20:15: 4:28

1 0 lpm	2 -0.103 mm	3-0.0844 mm	4-0.1754 mm	5-0.0666 mm	6 0.0396 mm	7-0.2224 mm	
8 0.0562 mm	9-0.0311 mm	10-0.0188 mm	11 0.0044 mm	12 0.0064 mm	13-0.3518 mm	14 3.6958 mm	
15-0.0555 mm	16-0.3379 mm	17 0.097 mm	18-0.4529 mm	19-0.4916 mm	20-0.6077 mm	21-0.0224 mm	
22 2.53 MPa	23 40.4 ms	24 30.4 ms	25 -145 ms	26 -74 ms	27 1349 KPa	28 -1.535 KPa	
29 1312 KPa	30 1.4 cm	31 21.6 dC					

Scan #118
20:15: 4:58

1 0 lpm	2 -0.107 mm	3-0.0879 mm	4-0.1806 mm	5-0.0678 mm	6 0.0421 mm	7-0.2344 mm	
8 0.0643 mm	9 -0.032 mm	10-0.0201 mm	11 0.005 mm	12 0.0064 mm	13-0.3512 mm	14 3.6827 mm	
15-0.0568 mm	16-0.3443 mm	17 0.1136 mm	18-0.4714 mm	19-0.5124 mm	20-0.6234 mm	21 -0.023 mm	
22 2.76 MPa	23 40.4 ms	24 33.7 ms	25 -151.7 ms	26 -84.2 ms	27 1349 KPa	28 -1.5 KPa	
29 1313 KPa	30 1.4 cm	31 21.5 dC					

Scan #119
20:15: 5:28

1 0 lpm	2-0.1094 mm	3-0.0901 mm	4-0.1843 mm	5-0.0688 mm	6 0.0439 mm	7-0.2422 mm	
8 0.0704 mm	9-0.0327 mm	10-0.0208 mm	11 0.005 mm	12 0.0064 mm	13 -0.355 mm	14 3.6558 mm	
15-0.0568 mm	16-0.3485 mm	17 0.1244 mm	18-0.4819 mm	19-0.5241 mm	20-0.6322 mm	21-0.0236 mm	
22 2.89 MPa	23 44.1 ms	24 33.7 ms	25 -155.1 ms	26 -87.7 ms	27 1350 KPa	28 -1.535 KPa	
29 1314 KPa	30 1.4 cm	31 21.5 dC					

Scan #120
20:15: 5:58

1 0 lpm	2-0.1101 mm	3 -0.091 mm	4-0.1855 mm	5-0.0691 mm	6 0.0433 mm	7-0.2446 mm	
8 0.0732 mm	9 -0.033 mm	10-0.0208 mm	11 0.005 mm	12 0.0068 mm	13-0.3589 mm	14 3.6265 mm	
15-0.0568 mm	16-0.3496 mm	17 0.1273 mm	18-0.4862 mm	19-0.5277 mm	20-0.6347 mm	21-0.0236 mm	
22 2.89 MPa	23 43.5 ms	24 33.7 ms	25 -155.1 ms	26 -90.9 ms	27 1350 KPa	28 -1.535 KPa	
29 1314 KPa	30 1.2 cm	31 21.4 dC					

Scan #121
20:15: 6:28

1 0 lpm	2-0.1104 mm	3-0.0914 mm	4-0.1861 mm	5-0.0691 mm	6 0.0439 mm	7-0.2456 mm	
8 0.0742 mm	9 -0.033 mm	10-0.0208 mm	11 0.005 mm	12 0.0068 mm	13-0.3601 mm	14 3.6272 mm	
15-0.0568 mm	16-0.3502 mm	17 0.1285 mm	18 -0.488 mm	19 -0.529 mm	20-0.6353 mm	21-0.[illegible]	
22 2.89 MPa	23 40.4 ms	24 33.7 ms	25 -155.1 ms	26 -94.4 ms	27 1351 KPa	28 -1.535 KPa	
29 1315 KPa	30 1 cm	31 21.4 dC					

Scan #122
**Monitor at 2.89 MPa stress.
20:15: 8:16

1	0	lpm	2	-0.1111	mm	3	-0.0917	mm	4	-0.1871	mm	5	-0.0694	mm	6	0.0439	mm	7	-0.2473	mm			
8	0.076	mm	9	-0.033	mm	10	-0.0208	mm	11	0.0056	mm	12	0.0071	mm	13	-0.3672	mm	14	3.5336	mm			
15	-0.0568	mm	16	-0.3514	mm	17	0.1297	mm	18	-0.4899	mm	19	-0.5308	mm	20	-0.6359	mm	21	-0.0239	mm			
22	2.89	MPa	23	40.4	ms	24	33.7	ms	25	-155.1	ms	26	-94.4	ms	27	1351	KPa	28	-1.535	KPa			
29	1315	KPa	30	1.2	cm	31	21.3	dC															

Scan #123
20:15:10:16

1	0	lpm	2	-0.1118	mm	3	-0.092	mm	4	-0.188	mm	5	-0.0694	mm	6	0.0439	mm	7	-0.248	mm			
8	0.0769	mm	9	-0.033	mm	10	-0.0205	mm	11	0.005	mm	12	0.0074	mm	13	-0.364	mm	14	3.387	mm			
15	-0.0568	mm	16	-0.3514	mm	17	0.1303	mm	18	-0.4905	mm	19	-0.532	mm	20	-0.6372	mm	21	-0.0239	mm			
22	2.89	MPa	23	40.4	ms	24	33.7	ms	25	-155.1	ms	26	-94.4	ms	27	1352	KPa	28	-1.535	KPa			
29	1316	KPa	30	1.3	cm	31	21.2	dC															

Scan #124
20:15:12:16

1	0	lpm	2	-0.1121	mm	3	-0.092	mm	4	-0.1886	mm	5	-0.0694	mm	6	0.0439	mm	7	-0.249	mm			
8	0.0782	mm	9	-0.033	mm	10	-0.0208	mm	11	0.0056	mm	12	0.0068	mm	13	-0.3691	mm	14	2.1248	mm			
15	-0.0568	mm	16	-0.352	mm	17	0.1315	mm	18	-0.4911	mm	19	-0.5332	mm	20	-0.6384	mm	21	-0.0243	mm			
22	2.89	MPa	23	40.4	ms	24	33.7	ms	25	-155.1	ms	26	-94.4	ms	27	1352	KPa	28	-1.535	KPa			
29	1316	KPa	30	1.3	cm	31	21.1	dC															

Scan #125
20:15:14:16

1	0	lpm	2	-0.1124	mm	3	-0.092	mm	4	-0.1889	mm	5	-0.0694	mm	6	0.0433	mm	7	-0.2494	mm			
8	0.0788	mm	9	-0.033	mm	10	-0.0208	mm	11	0.005	mm	12	0.0064	mm	13	-0.3736	mm	14	2.0181	mm			
15	-0.0568	mm	16	-0.3526	mm	17	0.1315	mm	18	-0.4911	mm	19	-0.5338	mm	20	-0.6391	mm	21	-0.0243	mm			
22	2.89	MPa	23	40.4	ms	24	33.7	ms	25	-155.1	ms	26	-94.4	ms	27	1352	KPa	28	-1.535	KPa			
29	1316	KPa	30	1.3	cm	31	21	dC															

Scan #126
20:15:16:16

1	0	lpm	2	-0.1124	mm	3	-0.092	mm	4	-0.1895	mm	5	-0.0694	mm	6	0.0433	mm	7	-0.2497	mm			
8	0.0794	mm	9	-0.0333	mm	10	-0.0208	mm	11	0.005	mm	12	0.0064	mm	13	-0.3749	mm	14	1.8684	mm			
15	-0.0568	mm	16	-0.3526	mm	17	0.1315	mm	18	-0.4911	mm	19	-0.5345	mm	20	-0.6397	mm	21	-0.0243	mm			
22	2.89	MPa	23	40.4	ms	24	33.7	ms	25	-155.1	ms	26	-94.4	ms	27	1353	KPa	28	-1.535	KPa			
29	1317	KPa	30	1.3	cm	31	20.9	dC															

Scan #127
20:15:18:16

1	0	lpm	2	-0.1128	mm	3	-0.092	mm	4	-0.1898	mm	5	-0.0694	mm	6	0.0433	mm	7	-0.2501	mm			
8	0.0797	mm	9	-0.0333	mm	10	-0.0208	mm	11	0.0056	mm	12	0.0058	mm	13	-0.3736	mm	14	1.8734	mm			
15	-0.0568	mm	16	-0.3532	mm	17	0.1321	mm	18	-0.4911	mm	19	-0.5351	mm	20	-0.6403	mm	21	-0.0243	mm			
22	2.89	MPa	23	40.4	ms	24	27.7	ms	25	-155.1	ms	26	-94.4	ms	27	1353	KPa	28	-1.535	KPa			
29	1317	KPa	30	1.2	cm	31	20.7	dC															

Scan #128
20:15:20:16

1	0	lpm	2	-0.1128	mm	3	-0.092	mm	4	-0.1901	mm	5	-0.0694	mm	6	0.0433	mm	7	-0.2504	mm			
8	0.08	mm	9	-0.0333	mm	10	-0.0208	mm	11	0.005	mm	12	0.0055	mm	13	-0.3781	mm	14	1.7574	mm			
15	-0.0568	mm	16	-0.3532	mm	17	0.1327	mm	18	-0.4917	mm	19	-0.5357	mm	20	-0.6416	mm	21	-0.0243	mm			
22	2.9	MPa	23	40.4	ms	24	26.9	ms	25	-155.1	ms	26	-94.4	ms	27	1353	KPa	28	-1.535	KPa			
29	1317	KPa	30	1.5	cm	31	20.7	dC															

Scan #129
20:15:22:16

1	0	lpm	2	-0.1131	mm	3	-0.092	mm	4	-0.1904	mm	5	-0.0694	mm	6	0.0433	mm	7	-0.2504	mm			
8	0.0807	mm	9	-0.0333	mm	10	-0.0208	mm	11	0.005	mm	12	0.0049	mm	13	-0.3819	mm	14	1.7387	mm			
15	-0.0568	mm	16	-0.3538	mm	17	0.1351	mm	18	-0.4917	mm	19	-0.5357	mm	20	-0.6428	mm	21	-0.0243	mm			
22	2.89	MPa	23	40.4	ms	24	32.9	ms	25	-155.1	ms	26	-94.4	ms	27	1354	KPa	28	-1.535	KPa			
29	1318	KPa	30	1.5	cm	31	20.6	dC															

```
Scan #130
20:15:24:16
    1       0 lpm    2-0.1135  mm    3 -0.092  mm    4-0.1907  mm    5-0.0694  mm    6 0.0439  mm    7-0.2504  mm
    8  0.081  mm    9-0.0333  mm   10-0.0208  mm   11 0.0056  mm   12 0.0058  mm   13  -0.38  mm   14 1.5516  mm
   15-0.0568  mm   16-0.3538  mm   17 0.1351  mm   18-0.4917  mm   19-0.5357  mm   20-0.6435  mm   21-0.0239  mm
   22     2.9 MPa   23    40.4  ms   24    27.7  ms   25 -155.1  ms   26  -94.4  ms   27    1354 KPa   28  -1.57 KPa
   29   1318 KPa   30     1.5  cm   31    20.6  dC
Scan #131
20:15:26:16
    1       0 lpm    2-0.1165  mm    3 -0.092  mm    4 -0.191  mm    5-0.0694  mm    6 0.0433  mm    7-0.2508  mm
    8  0.081  mm    9 -0.033  mm   10-0.0208  mm   11 0.0056  mm   12-0.2286  mm   13-0.4524  mm   14 0.8781  mm
   15-0.0568  mm   16-0.3538  mm   17 0.1351  mm   18-0.4923  mm   19-0.5277  mm   20-0.6441  mm   21-0.0277  mm
   22     2.9 MPa   23    46.4  ms   24    32.9  ms   25 -143.3  ms   26  -88.6  ms   27    1354 KPa   28  -1.57 KPa
   29   1318 KPa   30     1.7  cm   31    20.5  dC

**STRENGTH AND PERMEABILITY TESTS ON ULTRA-LARGE
**STRIPA GRANITE CORE (Engineering Units Data)
**15:31:27 - 17:03:33
**Permeability testing at 2.89 MPa axial stress
Scan #132
**Initial readings:
20:15:31:27
    1  0.006 lpm    2-0.1172  mm    3 -0.092  mm    4-0.1916  mm    5-0.0694  mm    6 0.0433  mm    7-0.2511  mm
    8 0.0819  mm    9-0.0333  mm   10-0.0208  mm   11  0.005  mm   12-0.2624  mm   13  -0.48  mm   14 0.6654  mm
   15-0.0568  mm   16-0.3543  mm   17 0.1351  mm   18-0.4917  mm   19-0.5302  mm   20-0.6454  mm   21 -0.028  mm
   22    2.89 MPa   23    47.2  ms   24    33.7  ms   25 -141.6  ms   26  -87.7  ms   27    1393 KPa   28  26.06 KPa
   29   1376 KPa   30     1.5  cm   31    20.4  dC
Scan #133
**Approximate steady flow at 15.9 KPa (23 psi) injection:
20:15:43: 4
    1  1.873 lpm    2-0.1182  mm    3 -0.092  mm    4-0.1923  mm    5-0.0697  mm    6 0.0433  mm    7-0.2511  mm
    8 0.0868  mm    9-0.0346  mm   10-0.0208  mm   11 0.0056  mm   12-0.2682  mm   13 -0.503  mm   14 0.3099  mm
   15-0.0568  mm   16-0.3543  mm   17  0.144  mm   18-0.4917  mm   19-0.5375  mm   20 -0.646  mm   21 -0.028  mm
   22     2.9 MPa   23    47.2  ms   24    33.7  ms   25 -141.6  ms   26  -87.7  ms   27    1373 KPa   28 15.629 KPa
   29   1358 KPa   30     1.6  cm   31    20.5  dC
Scan #134
20:15:44: 4
    1  1.836 lpm    2-0.1185  mm    3 -0.092  mm    4-0.1926  mm    5-0.0694  mm    6 0.0433  mm    7-0.2508  mm
    8 0.0871  mm    9-0.0342  mm   10-0.0208  mm   11 0.0056  mm   12-0.2689  mm   13-0.5037  mm   14 0.4165  mm
   15-0.0568  mm   16-0.3543  mm   17  0.144  mm   18-0.4917  mm   19-0.5375  mm   20 -0.646  mm   21 -0.028  mm
   22     2.9 MPa   23    47.2  ms   24    33.7  ms   25 -141.6  ms   26  -87.7  ms   27    1346 KPa   28 15.489 KPa
   29   1331 KPa   30     1.6  cm   31    20.5  dC
Scan #135
20:15:45: 4
    1  1.834 lpm    2-0.1185  mm    3 -0.092  mm    4-0.1923  mm    5-0.0694  mm    6 0.0433  mm    7-0.2508  mm
    8 0.0875  mm    9-0.0342  mm   10-0.0208  mm   11 0.0056  mm   12-0.2723  mm   13 -0.505  mm   14 0.4446  mm
   15-0.0568  mm   16-0.3543  mm   17 0.1446  mm   18-0.4917  mm   19-0.5381  mm   20 -0.646  mm   21 -0.028  mm
   22    2.89 MPa   23    47.2  ms   24    33.7  ms   25 -141.6  ms   26  -87.7  ms   27    1373 KPa   28 16.048 KPa
   29   1345 KPa   30     1.6  cm   31    20.5  dC
Scan #136
20:15:46: 4
    1  1.817 lpm    2-0.1185  mm    3 -0.092  mm    4-0.1926  mm    5-0.0694  mm    6 0.0433  mm    7-0.2508  mm
    8 0.0875  mm    9-0.0342  mm   10-0.0208  mm   11 0.0056  mm   12-0.2713  mm   13-0.5069  mm   14 0.3592  mm
   15-0.0568  mm   16-0.3543  mm   17  0.147  mm   18-0.4917  mm   19-0.5381  mm   20 -0.646  mm   21 -0.028  mm
   22     2.9 MPa   23    47.2  ms   24    33.7  ms   25 -141.6  ms   26  -87.7  ms   27    1368 KPa   28 15.245 KPa
   29   1353 KPa   30     1.7  cm   31    20.5  dC
```

```
Scan #137
20:15:47: 4
    1  1.828 lpm    2-0.1185  mm    3 -0.092  mm    4-0.1926  mm    5-0.0697  mm    6 0.0433  mm    7-0.2508  mm
    8 0.0878  mm    9-0.0342  mm   10-0.0208  mm   11 0.0062  mm   12-0.2747  mm   13-0.5075  mm   14 0.4452  mm
   15-0.0568  mm   16-0.3543  mm   17 0.1476  mm   18-0.4923  mm   19-0.5375  mm   20 -0.646  mm   21 -0.028  mm
   22    2.89 MPa  23    47.2  ms   24    33.7  ms   25 -141.6  ms   26  -87.7  ms   27    1359 KPa   28 15.734 KPa
   29    1332 KPa  30     1.6  cm   31    20.5  dC
Scan #138
20:15:48: 4
    1  1.815 lpm    2-0.1185  mm    3 -0.092  mm    4-0.1926  mm    5-0.0694  mm    6 0.0433  mm    7-0.2508  mm
    8 0.0881  mm    9-0.0342  mm   10-0.0208  mm   11 0.0056  mm   12-0.2754  mm   13-0.5075  mm   14 0.2806  mm
   15-0.0568  mm   16-0.3543  mm   17 0.1476  mm   18-0.4917  mm   19-0.5387  mm   20-0.6454  mm   21 -0.028  mm
   22     2.9 MPa  23    47.2  ms   24    33.7  ms   25 -141.6  ms   26  -87.7  ms   27    1367 KPa   28 15.594 KPa
   29    1353 KPa  30     1.7  cm   31    20.5  dC
Scan #139
20:15:49: 4
    1  1.861 lpm    2-0.1185  mm    3 -0.092  mm    4-0.1926  mm    5-0.0694  mm    6 0.0433  mm    7-0.2508  mm
    8 0.0881  mm    9-0.0346  mm   10-0.0208  mm   11 0.0062  mm   12-0.2661  mm   13-0.5082  mm   14 0.1783  mm
   15-0.0568  mm   16-0.3543  mm   17 0.1482  mm   18-0.4917  mm   19-0.5406  mm   20 -0.646  mm   21-0.0283  mm
   22    2.89 MPa  23    47.2  ms   24    33.7  ms   25 -141.6  ms   26  -87.7  ms   27    1364 KPa   28 15.524 KPa
   29    1336 KPa  30     1.5  cm   31    20.6  dC
Scan #140
**Approximate steady flow at 27.5 KPa (4 psi) injection:
20:15:55:39
    1  2.789 lpm    2-0.1189  mm    3 -0.092  mm    4-0.1929  mm    5-0.0697  mm    6 0.0433  mm    7-0.2501  mm
    8 0.0899  mm    9-0.0346  mm   10-0.0208  mm   11 0.0069  mm   12-0.2593  mm   13-0.5139  mm   14 0.0548  mm
   15-0.0568  mm   16-0.3543  mm   17 0.1505  mm   18-0.4917  mm   19-0.5436  mm   20 -0.646  mm   21 -0.028  mm
   22     2.9 MPa  23    47.2  ms   24    33.7  ms   25 -141.6  ms   26  -94.1  ms   27    1360 KPa   28 24.839 KPa
   29    1345 KPa  30     1.6  cm   31    20.6  dC
Scan #141
20:15:56:39
    1  2.781 lpm    2-0.1189  mm    3 -0.092  mm    4-0.1929  mm    5-0.0697  mm    6 0.0433  mm    7-0.2501  mm
    8 0.0899  mm    9-0.0346  mm   10-0.0208  mm   11 0.0069  mm   12-0.2617  mm   13-0.5146  mm   14-0.1092  mm
   15-0.0568  mm   16-0.3543  mm   17 0.1505  mm   18-0.4917  mm   19-0.5424  mm   20 -0.646  mm   21-0.0283  mm
   22    2.89 MPa  23    47.2  ms   24    33.7  ms   25 -141.6  ms   26  -89.4  ms   27    1389 KPa   28 26.548 KPa
   29    1375 KPa  30     1.6  cm   31    20.6  dC
Scan #142
20:15:57:39
    1  2.517 lpm    2-0.1192  mm    3-0.0923  mm    4-0.1929  mm    5-0.0697  mm    6 0.0439  mm    7-0.2501  mm
    8 0.0902  mm    9-0.0346  mm   10-0.0208  mm   11 0.0069  mm   12-0.2543  mm   13-0.5152  mm   14-0.2127  mm
   15-0.0568  mm   16-0.3543  mm   17 0.1505  mm   18-0.4917  mm   19-0.5412  mm   20 -0.646  mm   21 -0.028  mm
   22    2.89 MPa  23    47.2  ms   24    33.7  ms   25 -141.6  ms   26  -87.7  ms   27    1365 KPa   28  24.35 KPa
   29    1349 KPa  30     1.6  cm   31    20.6  dC
Scan #143
20:15:58:39
    1  2.798 lpm    2-0.1192  mm    3 -0.092  mm    4-0.1929  mm    5-0.0697  mm    6 0.0439  mm    7-0.2501  mm
    8 0.0905  mm    9-0.0349  mm   10-0.0208  mm   11 0.0069  mm   12 -0.262  mm   13-0.5152  mm   14-0.2277  mm
   15-0.0568  mm   16-0.3543  mm   17 0.1511  mm   18-0.4917  mm   19-0.5424  mm   20 -0.646  mm   21 -0.028  mm
   22     2.9 MPa  23    47.2  ms   24    33.7  ms   25 -141.6  ms   26  -87.7  ms   27    1354 KPa   28 26.339 KPa
   29    1355 KPa  30     1.6  cm   31    20.6  dC
```

```
Scan #144
20:15:59:39
    1   2.81 lpm    2-0.1192  mm    3 -0.092  mm    4-0.1932  mm    5-0.0697  mm    6 0.0439  mm    7-0.2501  mm
    8 0.0905  mm    9-0.0349  mm   10-0.0208  mm   11 0.0069  mm   12-0.2679  mm   13-0.5165  mm   14-0.2377  mm
   15-0.0568  mm   16-0.3543  mm   17 0.1511  mm   18-0.4917  mm   19-0.5424  mm   20 -0.646  mm   21-0.0283  mm
   22     2.9 MPa  23   47.2  ms   24   33.7  ms   25 -136.6  ms   26  -87.7  ms   27   1386 KPa   28 27.106 KPa
   29   1381 KPa  30    1.6  cm   31   20.6  dC
Scan #145
20:16: 0:39
    1   2.77 lpm    2-0.1192  mm    3 -0.092  mm    4-0.1932  mm    5-0.0697  mm    6 0.0439  mm    7-0.2501  mm
    8 0.0905  mm    9-0.0346  mm   10-0.0208  mm   11 0.0069  mm   12-0.2673  mm   13-0.5178  mm   14-0.2738  mm
   15-0.0568  mm   16-0.3543  mm   17 0.1511  mm   18-0.4917  mm   19-0.5418  mm   20 -0.646  mm   21-0.0283  mm
   22   2.89 MPa  23   47.2  ms   24   33.7  ms   25 -139.9  ms   26  -87.7  ms   27   1380 KPa   28 24.978 KPa
   29   1364 KPa  30    1.6  cm   31   20.6  dC
Scan #146
20:16: 1:39
    1  2.796 lpm    2-0.1192  mm    3 -0.092  mm    4-0.1932  mm    5-0.0697  mm    6 0.0439  mm    7-0.2501  mm
    8 0.0909  mm    9-0.0346  mm   10-0.0208  mm   11 0.0075  mm   12-0.2648  mm   13-0.5184  mm   14-0.3387  mm
   15-0.0568  mm   16-0.3543  mm   17 0.1517  mm   18-0.4917  mm   19-0.5412  mm   20 -0.646  mm   21-0.0283  mm
   22   2.89 MPa  23   47.2  ms   24   33.7  ms   25 -141.6  ms   26  -87.7  ms   27   1367 KPa   28 26.513 KPa
   29   1353 KPa  30    1.7  cm   31   20.6  dC
Scan #147
**Approximate steady flow at 15.9 KPa (2.3 psi) injection:
20:16: 4:25
    1  1.607 lpm    2-0.1192  mm    3-0.0923  mm    4-0.1932  mm    5  -0.07  mm    6 0.0439  mm    7-0.2501  mm
    8 0.0909  mm    9-0.0346  mm   10-0.0208  mm   11 0.0075  mm   12-0.2676  mm   13-0.5197  mm   14-0.3774  mm
   15-0.0575  mm   16-0.3543  mm   17 0.1523  mm   18-0.4917  mm   19-0.5424  mm   20-0.6466  mm   21 -0.028  mm
   22     2.9 MPa  23   47.2  ms   24   33.7  ms   25 -135.5  ms   26  -87.7  ms   27   1348 KPa   28  15.28 KPa
   29   1334 KPa  30    1.7  cm   31   20.7  dC
Scan #148
20:16: 5:25
    1  1.747 lpm    2-0.1192  mm    3-0.0923  mm    4-0.1935  mm    5  -0.07  mm    6 0.0439  mm    7-0.2504  mm
    8 0.0909  mm    9-0.0346  mm   10-0.0208  mm   11 0.0075  mm   12-0.2689  mm   13-0.5203  mm   14-0.3524  mm
   15-0.0568  mm   16-0.3543  mm   17 0.1523  mm   18-0.4923  mm   19 -0.543  mm   20-0.6466  mm   21 -0.028  mm
   22   2.89 MPa  23   52.3  ms   24   33.7  ms   25 -134.9  ms   26  -87.7  ms   27   1351 KPa   28  15.42 KPa
   29   1328 KPa  30    1.6  cm   31   20.7  dC
Scan #149
20:16: 6:25
    1  1.716 lpm    2-0.1192  mm    3-0.0923  mm    4-0.1935  mm    5-0.0697  mm    6 0.0439  mm    7-0.2504  mm
    8 0.0909  mm    9-0.0346  mm   10-0.0208  mm   11 0.0075  mm   12-0.2599  mm   13-0.5216  mm   14-0.3343  mm
   15-0.0568  mm   16-0.3543  mm   17 0.1529  mm   18-0.4923  mm   19-0.5443  mm   20-0.6466  mm   21 -0.028  mm
   22   2.89 MPa  23   53.9  ms   24   33.7  ms   25 -134.9  ms   26  -87.7  ms   27   1358 KPa   28 15.071 KPa
   29   1330 KPa  30    1.7  cm   31   20.7  dC
Scan #150
20:16: 7:25
    1  1.724 lpm    2-0.1195  mm    3-0.0923  mm    4-0.1935  mm    5-0.0697  mm    6 0.0439  mm    7-0.2501  mm
    8 0.0912  mm    9-0.0346  mm   10-0.0208  mm   11 0.0075  mm   12-0.2624  mm   13-0.5223  mm   14-0.3337  mm
   15-0.0575  mm   16-0.3543  mm   17 0.1529  mm   18-0.4923  mm   19-0.5449  mm   20 -0.646  mm   21-0.0283  mm
   22   2.89 MPa  23   48.8  ms   24   33.7  ms   25 -134.9  ms   26  -87.7  ms   27   1368 KPa   28 14.268 KPa
   29   1338 KPa  30    1.6  cm   31   20.6  dC
Scan #151
20:16: 8:25
    1  1.572 lpm    2-0.1195  mm    3-0.0923  mm    4-0.1935  mm    5-0.0697  mm    6 0.0439  mm    7-0.2504  mm
    8 0.0912  mm    9-0.0346  mm   10-0.0208  mm   11 0.0075  mm   12-0.2577  mm   13-0.5223  mm   14-0.3025  mm
   15-0.0575  mm   16-0.3543  mm   17 0.1529  mm   18-0.4917  mm   19-0.5455  mm   20-0.6466  mm   21-0.0283  mm
   22   2.89 MPa  23   47.2  ms   24   33.7  ms   25 -134.9  ms   26  -87.7  ms   27   1376 KPa   28  15.42 KPa
   29   1348 KPa  30    1.7  cm   31   20.6  dC
```

```
Scan #152
20:16: 9:25
    1  1.774 lpm    2-0.1195  mm    3 -0.092  mm    4-0.1935  mm    5  -0.07  mm    6 0.0439  mm    7-0.2504  mm
    8 0.0912  mm    9-0.0349  mm   10-0.0208  mm   11 0.0075  mm   12-0.2614  mm   13-0.5235  mm   14-0.3094  mm
   15-0.0575  mm   16-0.3543  mm   17 0.1529  mm   18-0.4923  mm   19-0.5443  mm   20-0.6466  mm   21 -0.028  mm
   22    2.89 MPa  23    52.3  ms   24    33.7  ms   25 -134.9  ms   26  -87.7  ms   27    1386 KPa   28 15.629 KPa
   29    1360 KPa  30     1.7  cm   31    20.7  dC
Scan #153
20:16:13: 2
    1  0.006 lpm    2-0.1195  mm    3-0.0923  mm    4-0.1935  mm    5  -0.07  mm    6 0.0439  mm    7-0.2508  mm
    8 0.0912  mm    9-0.0346  mm   10-0.0208  mm   11 0.0075  mm   12-0.2862  mm   13-0.5274  mm   14-0.3368  mm
   15-0.0575  mm   16-0.3543  mm   17 0.1529  mm   18-0.4929  mm   19-0.5467  mm   20-0.6466  mm   21 -0.028  mm
   22     2.9 MPa  23    53.9  ms   24    33.7  ms   25 -134.9  ms   26  -87.7  ms   27    1351 KPa   28  0.174 KPa
   29    1319 KPa  30     1.6  cm   31    20.7  dC
Scan #154
**Approximate steady flow at 10.3 KPa (1.5 psi) withdrawal:
20:16:56:10
    1  0.873 lpm    2-0.1205  mm    3-0.0958  mm    4-0.1959  mm    5  -0.07  mm    6 0.0439  mm    7-0.2555  mm
    8 0.0881  mm    9-0.0342  mm   10-0.0211  mm   11  0.005  mm   12-0.2822  mm   13-0.5485  mm   14-0.4248  mm
   15-0.0581  mm   16-0.3579  mm   17 0.1571  mm   18-0.4979  mm   19-0.5589  mm   20-0.6523  mm   21 -0.028  mm
   22    2.89 MPa  23    53.9  ms   24    40.4  ms   25 -134.9  ms   26  -87.7  ms   27    1245 KPa   28  5.791 KPa
   29    1217 KPa  30     1.7  cm   31    19.8  dC
Scan #155
**Stop flow:
20:16:58:33
    1  0.006 lpm    2-0.1205  mm    3-0.0958  mm    4-0.1959  mm    5  -0.07  mm    6 0.0433  mm    7-0.2559  mm
    8 0.0881  mm    9-0.0346  mm   10-0.0211  mm   11 0.0056  mm   12-0.2812  mm   13-0.5492  mm   14-0.3574  mm
   15-0.0575  mm   16-0.3579  mm   17 0.1571  mm   18-0.4985  mm   19-0.5577  mm   20-0.6523  mm   21 -0.028  mm
   22     2.9 MPa  23    53.9  ms   24    40.4  ms   25 -140.9  ms   26  -87.7  ms   27    1341 KPa   28  -1.57 KPa
   29    1306 KPa  30     1.6  cm   31    19.8  dC
Scan #156
20:16:59:33
    1  0.006 lpm    2-0.1205  mm    3-0.0958  mm    4-0.1959  mm    5  -0.07  mm    6 0.0433  mm    7-0.2559  mm
    8 0.0881  mm    9-0.0342  mm   10-0.0211  mm   11 0.0056  mm   12-0.2843  mm   13-0.5498  mm   14-0.4135  mm
   15-0.0575  mm   16-0.3579  mm   17 0.1571  mm   18-0.4985  mm   19-0.5571  mm   20-0.6523  mm   21 -0.028  mm
   22     2.9 MPa  23    53.9  ms   24    40.4  ms   25 -141.6  ms   26  -87.7  ms   27    1341 KPa   28 -1.535 KPa
   29    1306 KPa  30     1.6  cm   31    19.8  dC
Scan #157
20:17: 0:33
    1  0.003 lpm    2-0.1205  mm    3-0.0958  mm    4-0.1959  mm    5  -0.07  mm    6 0.0433  mm    7-0.2562  mm
    8 0.0881  mm    9-0.0342  mm   10-0.0211  mm   11  0.005  mm   12-0.2887  mm   13-0.5504  mm   14-0.3942  mm
   15-0.0575  mm   16-0.3579  mm   17 0.1571  mm   18-0.4979  mm   19-0.5583  mm   20-0.6523  mm   21 -0.028  mm
   22     2.9 MPa  23    53.9  ms   24    40.4  ms   25 -136.6  ms   26  -87.7  ms   27    1341 KPa   28 -1.535 KPa
   29    1307 KPa  30     1.6  cm   31    19.8  dC
Scan #158
20:17: 1:33
    1  0.003 lpm    2-0.1205  mm    3-0.0958  mm    4-0.1959  mm    5  -0.07  mm    6 0.0433  mm    7-0.2562  mm
    8 0.0881  mm    9-0.0342  mm   10-0.0211  mm   11  0.005  mm   12-0.2862  mm   13-0.5504  mm   14-0.4198  mm
   15-0.0581  mm   16-0.3579  mm   17 0.1571  mm   18-0.4985  mm   19-0.5602  mm   20-0.6523  mm   21 -0.028  mm
   22     2.9 MPa  23    53.9  ms   24    40.4  ms   25 -134.9  ms   26  -87.7  ms   27    1341 KPa   28  -1.57 KPa
   29    1306 KPa  30     1.6  cm   31    19.8  dC
Scan #159
20:17: 2:33
    1  0.006 lpm    2-0.1205  mm    3-0.0955  mm    4-0.1959  mm    5  -0.07  mm    6 0.0433  mm    7-0.2562  mm
    8 0.0878  mm    9-0.0346  mm   10-0.0211  mm   11 0.0056  mm   12-0.2905  mm   13-0.5511  mm   14-0.4304  mm
   15-0.0581  mm   16-0.3579  mm   17 0.1571  mm   18-0.4979  mm   19 -0.562  mm   20-0.6523  mm   21 -0.028  mm
   22    2.89 MPa  23    53.9  ms   24    40.4  ms   25 -134.9  ms   26  -82.7  ms   27    1341 KPa   28  -1.57 KPa
   29    1306 KPa  30     1.6  cm   31    19.8  dC
```

```
Scan #160
20:17: 3:33
    1  0.003 lpm    2-0.1205  mm    3-0.0955  mm    4-0.1959  mm    5  -0.07  mm    6 0.0433  mm    7-0.2562  mm
    8 0.0881  mm    9-0.0346  mm   10-0.0211  mm   11 0.0056  mm   12-0.2967  mm   13-0.5517  mm   14-0.4572  mm
   15-0.0575  mm   16-0.3579  mm   17 0.1571  mm   18-0.4985  mm   19-0.5608  mm   20-0.6523  mm   21 -0.028  mm
   22     2.9 MPa  23    53.9  ms   24    40.4  ms   25 -134.9  ms   26     -86  ms   27    1341 KPa   28 -1.605 KPa
   29    1307 KPa  30     1.6  cm   31    19.8  dC

**STRENGTH AND PERMEABILITY TESTING ON ULTRA-LARGE
**STRIPA GRANITE CORE (Engineering Units Data)
**17:13:03 - 18:19:02
**Loading from 2.89 MPa to 5.55 MPa
Scan #161
**Initial conditions:
20:17:13: 3
    1       0 lpm    2-0.1205  mm    3-0.0955  mm    4-0.1962  mm    5  -0.07  mm    6 0.0439  mm    7-0.2562  mm
    8 0.0881  mm    9-0.0346  mm   10-0.0211  mm   11 0.0056  mm   12-0.2843  mm   13-0.5575  mm   14-0.4871  mm
   15-0.0581  mm   16-0.3579  mm   17 0.1571  mm   18-0.4985  mm   19 -0.562  mm   20-0.6523  mm   21 -0.028  mm
   22     2.9 MPa  23    53.9  ms   24    40.4  ms   25 -134.9  ms   26  -87.7  ms   27    1343 KPa   28  -1.57 KPa
   29    1308 KPa  30     1.5  cm   31    19.8  dC
Scan #162
**Resume loading:
20:17:14:12
    1       0 lpm    2-0.1209  mm    3-0.0955  mm    4-0.1962  mm    5  -0.07  mm    6 0.0433  mm    7-0.2559  mm
    8 0.0878  mm    9-0.0346  mm   10-0.0211  mm   11 0.0056  mm   12  -0.28  mm   13-0.5575  mm   14-0.4753  mm
   15-0.0581  mm   16-0.3579  mm   17 0.1571  mm   18-0.4985  mm   19-0.5608  mm   20-0.6523  mm   21 -0.028  mm
   22    2.89 MPa  23    59.3  ms   24    40.4  ms   25 -134.9  ms   26  -82.5  ms   27    1343 KPa   28 -1.605 KPa
   29    1309 KPa  30     1.6  cm   31    19.8  dC
Scan #163
20:17:14:42
    1       0 lpm    2-0.1209  mm    3-0.0955  mm    4-0.1962  mm    5  -0.07  mm    6 0.0439  mm    7-0.2559  mm
    8 0.0881  mm    9-0.0346  mm   10-0.0211  mm   11 0.0056  mm   12-0.2781  mm   13-0.5575  mm   14-0.4859  mm
   15-0.0581  mm   16-0.3579  mm   17 0.1571  mm   18-0.4985  mm   19-0.5608  mm   20-0.6523  mm   21 -0.028  mm
   22    2.92 MPa  23      57  ms   24    43.9  ms   25 -134.9  ms   26     -81  ms   27    1344 KPa   28 -1.605 KPa
   29    1309 KPa  30     1.6  cm   31    19.8  dC
Scan #164
20:17:15:12
    1       0 lpm    2-0.1216  mm    3-0.0961  mm    4-0.1971  mm    5-0.0703  mm    6 0.0439  mm    7-0.2583  mm
    8 0.0893  mm    9-0.0346  mm   10-0.0214  mm   11 0.0056  mm   12-0.2785  mm   13-0.5575  mm   14-0.4828  mm
   15-0.0581  mm   16-0.3585  mm   17 0.1571  mm   18-0.5034  mm   19-0.5663  mm   20-0.6567  mm   21-0.0283  mm
   22    3.05 MPa  23    57.6  ms   24    43.7  ms   25 -138.3  ms   26  -84.2  ms   27    1343 KPa   28  -1.57 KPa
   29    1308 KPa  30     1.5  cm   31    19.8  dC
Scan #165
20:17:15:42
    1       0 lpm    2-0.1236  mm    3-0.0977  mm    4-0.1996  mm    5-0.0706  mm    6 0.0452  mm    7-0.2654  mm
    8  0.094  mm    9-0.0352  mm   10-0.0218  mm   11  0.005  mm   12-0.2769  mm   13-0.5575  mm   14-0.5008  mm
   15-0.0581  mm   16-0.3602  mm   17 0.1648  mm   18-0.5139  mm   19-0.5773  mm   20-0.6655  mm   21-0.0286  mm
   22    3.27 MPa  23    60.7  ms   24    43.9  ms   25 -141.6  ms   26  -90.9  ms   27    1342 KPa   28  -1.57 KPa
   29    1308 KPa  30     1.4  cm   31    19.8  dC
Scan #166
20:17:16:12
    1       0 lpm    2-0.1266  mm    3-0.0999  mm    4 -0.203  mm    5-0.0713  mm    6  0.047  mm    7-0.2753  mm
    8 0.1011  mm    9-0.0358  mm   10-0.0224  mm   11  0.005  mm   12-0.2822  mm   13-0.5581  mm   14-0.5008  mm
   15-0.0581  mm   16-0.3637  mm   17 0.1773  mm   18-0.5268  mm   19-0.5938  mm   20-0.6768  mm   21-0.0289  mm
   22    3.51 MPa  23    60.7  ms   24    47.2  ms   25    -145  ms   26  -97.7  ms   27    1342 KPa   28 -1.535 KPa
   29    1307 KPa  30     1.4  cm   31    19.8  dC
```

Scan #167
20:17:16:42

1 0 lpm	2-0.1297 mm	3 -0.103 mm	4-0.2072 mm	5-0.0722 mm	6 0.0489 mm	7-0.2876 mm	
8 0.11 mm	9-0.0364 mm	10-0.0234 mm	11 0.0056 mm	12-0.2868 mm	13-0.5581 mm	14-0.5065 mm	
15-0.0587 mm	16-0.3679 mm	17 0.1958 mm	18-0.5422 mm	19-0.6128 mm	20 -0.69 mm	21-0.0292 mm	
22 3.76 MPa	23 60.7 ms	24 50.7 ms	25 -151.7 ms	26 -107.7 ms	27 1341 KPa	28 -1.535 KPa	
29 1307 KPa	30 1.4 cm	31 19.8 dC					

Scan #168
20:17:17:12

1 0 lpm	2 -0.133 mm	3-0.1058 mm	4-0.2121 mm	5-0.0731 mm	6 0.0514 mm	7-0.3012 mm	
8 0.1221 mm	9-0.0374 mm	10 -0.024 mm	11 0.0056 mm	12-0.2868 mm	13-0.5581 mm	14-0.5027 mm	
15-0.0587 mm	16 -0.372 mm	17 0.2178 mm	18-0.5576 mm	19 -0.633 mm	20-0.7044 mm	21-0.0298 mm	
22 4.01 MPa	23 64.3 ms	24 53.9 ms	25 -158.5 ms	26 -121.2 ms	27 1341 KPa	28 -1.57 KPa	
29 1306 KPa	30 1.4 cm	31 19.9 dC					

Scan #169
20:17:17:42

1 0 lpm	2-0.1357 mm	3 -0.109 mm	4 -0.217 mm	5-0.0741 mm	6 0.0532 mm	7-0.3156 mm	
8 0.1351 mm	9-0.0383 mm	10 -0.025 mm	11 0.0062 mm	12-0.2877 mm	13-0.5594 mm	14-0.5127 mm	
15-0.0587 mm	16-0.3773 mm	17 0.241 mm	18-0.5737 mm	19-0.6557 mm	20-0.7176 mm	21-0.0308 mm	
22 4.26 MPa	23 67.4 ms	24 53.9 ms	25 -165.2 ms	26 -131.4 ms	27 1340 KPa	28 -1.57 KPa	
29 1306 KPa	30 1.4 cm	31 19.8 dC					

Scan #170
20:17:18:12

1 0 lpm	2-0.1384 mm	3-0.1115 mm	4-0.2222 mm	5-0.0747 mm	6 0.0557 mm	7-0.3306 mm	
8 0.1496 mm	9-0.0393 mm	10-0.0256 mm	11 0.0069 mm	12-0.2881 mm	13-0.5601 mm	14-0.5264 mm	
15-0.0587 mm	16 -0.382 mm	17 0.2678 mm	18-0.5897 mm	19-0.6795 mm	20-0.7308 mm	21-0.0314 mm	
22 4.52 MPa	23 67.4 ms	24 57.4 ms	25 -172 ms	26 -138.2 ms	27 1340 KPa	28 -1.57 KPa	
29 1305 KPa	30 1.3 cm	31 19.8 dC					

Scan #171
20:17:18:42

1 0 lpm	2-0.1415 mm	3-0.1147 mm	4-0.2277 mm	5-0.0753 mm	6 0.0582 mm	7-0.3493 mm	
8 0.1663 mm	9-0.0405 mm	10-0.0263 mm	11 0.0075 mm	12-0.2887 mm	13-0.5601 mm	14 -0.527 mm	
15-0.0587 mm	16-0.3872 mm	17 0.2946 mm	18-0.6051 mm	19-0.7046 mm	20 -0.744 mm	21 -0.032 mm	
22 4.77 MPa	23 67.4 ms	24 60.7 ms	25 -178.7 ms	26 -144.9 ms	27 1339 KPa	28 -1.605 KPa	
29 1305 KPa	30 1.3 cm	31 19.8 dC					

Scan #172
20:17:19:12

1 0 lpm	2-0.1435 mm	3-0.1175 mm	4-0.2329 mm	5-0.0762 mm	6 0.0607 mm	7-0.3664 mm	
8 0.1815 mm	9-0.0418 mm	10-0.0269 mm	11 0.0088 mm	12-0.2847 mm	13-0.5607 mm	14-0.5302 mm	
15-0.0587 mm	16-0.3919 mm	17 0.3267 mm	18-0.6199 mm	19-0.7291 mm	20-0.7566 mm	21 -0.033 mm	
22 5.03 MPa	23 67.4 ms	24 60.7 ms	25 -182.1 ms	26 -154.9 ms	27 1338 KPa	28 -1.57 KPa	
29 1304 KPa	30 1.3 cm	31 19.8 dC					

Scan #173
20:17:19:42

1 0 lpm	2-0.1455 mm	3 -0.12 mm	4-0.2372 mm	5-0.0765 mm	6 0.0625 mm	7-0.3838 mm	
8 0.1963 mm	9-0.0427 mm	10-0.0269 mm	11 0.0094 mm	12-0.2877 mm	13-0.5613 mm	14-0.5308 mm	
15-0.0581 mm	16-0.3961 mm	17 0.3583 mm	18-0.6346 mm	19-0.7548 mm	20-0.7685 mm	21-0.0336 mm	
22 5.29 MPa	23 67.4 ms	24 64.2 ms	25 -185.5 ms	26 -165.1 ms	27 1338 KPa	28 -1.57 KPa	
29 1303 KPa	30 1.2 cm	31 19.8 dC					

Scan #174
20:17:20:12

1 0 lpm	2-0.1475 mm	3-0.1225 mm	4-0.2415 mm	5-0.0775 mm	6 0.0644 mm	7-0.4022 mm	
8 0.2121 mm	9-0.0433 mm	10-0.0273 mm	11 0.0107 mm	12-0.2834 mm	13-0.5613 mm	14 -0.522 mm	
15-0.0575 mm	16-0.3996 mm	17 0.3922 mm	18 -0.647 mm	19-0.7799 mm	20-0.7779 mm	21-0.0342 mm	
22 5.55 MPa	23 67.4 ms	24 67.4 ms	25 -188.8 ms	26 -175.1 ms	27 1338 KPa	28 -1.64 KPa	
29 1303 KPa	30 1.2 cm	31 19.9 dC					

```
Scan #175
20:17:20:42
   1      0 lpm    2-0.1489  mm    3-0.1235  mm    4-0.2436  mm    5-0.0775  mm    6  0.065  mm    7-0.4111  mm
   8 0.2207  mm    9-0.0433  mm   10-0.0273  mm   11 0.0113  mm   12-0.2865  mm   13-0.5613  mm   14-0.5158  mm
  15-0.0575  mm   16-0.4019  mm   17 0.4125  mm   18-0.6531  mm   19-0.7952  mm   20-0.7817  mm   21-0.0342  mm
  22    5.55 MPa  23    67.4  ms   24    67.4  ms   25 -188.8  ms   26 -182.1  ms   27    1338 KPa   28  -1.64 KPa
  29    1304 KPa  30     1.2  cm   31    19.8  dC
Scan #176
20:17:21:12
   1      0 lpm    2-0.1496  mm    3-0.1238  mm    4-0.2451  mm    5-0.0778  mm    6 0.0656  mm    7-0.4148  mm
   8 0.2251  mm    9-0.0433  mm   10-0.0273  mm   11 0.0113  mm   12-0.2893  mm   13 -0.562  mm   14-0.5196  mm
  15-0.0575  mm   16-0.4031  mm   17 0.4202  mm   18-0.6544  mm   19-0.7995  mm   20 -0.783  mm   21-0.0345  mm
  22    5.55 MPa  23    67.4  ms   24    67.4  ms   25 -188.8  ms   26 -182.1  ms   27    1339 KPa   28 -1.605 KPa
  29    1304 KPa  30     1.2  cm   31    19.8  dC
Scan #177
20:17:21:42
   1      0 lpm    2-0.1499  mm    3-0.1241  mm    4-0.2457  mm    5-0.0778  mm    6 0.0656  mm    7-0.4179  mm
   8 0.2275  mm    9-0.0433  mm   10-0.0273  mm   11 0.0107  mm   12-0.2908  mm   13 -0.562  mm   14-0.5164  mm
  15-0.0568  mm   16-0.4037  mm   17 0.4256  mm   18-0.6556  mm   19-0.8008  mm   20-0.7842  mm   21-0.0345  mm
  22    5.55 MPa  23    67.4  ms   24    67.4  ms   25 -188.8  ms   26 -182.1  ms   27    1339 KPa   28 -1.605 KPa
  29    1305 KPa  30     1.2  cm   31    19.8  dC
Scan #178
**Monitor at 5.55 MPa.
20:17:23: 2
   1      0 lpm    2-0.1506  mm    3-0.1244  mm    4 -0.247  mm    5-0.0778  mm    6 0.0656  mm    7-0.4223  mm
   8 0.2322  mm    9-0.0436  mm   10-0.0273  mm   11 0.0126  mm   12  -0.28  mm   13 -0.562  mm   14-0.5183  mm
  15-0.0568  mm   16-0.4043  mm   17 0.4387  mm   18-0.6568  mm   19-0.8075  mm   20-0.7855  mm   21-0.0345  mm
  22    5.55 MPa  23    67.4  ms   24    67.4  ms   25 -188.8  ms   26 -182.1  ms   27    1340 KPa   28 -1.605 KPa
  29    1306 KPa  30     1.2  cm   31    19.9  dC
Scan #179
20:17:25: 2
   1      0 lpm    2-0.1519  mm    3-0.1247  mm    4-0.2482  mm    5-0.0778  mm    6 0.0656  mm    7-0.4271  mm
   8 0.2365  mm    9-0.0436  mm   10-0.0273  mm   11 0.0126  mm   12-0.2766  mm   13-0.5626  mm   14-0.5433  mm
  15-0.0562  mm   16-0.4049  mm   17 0.4541  mm   18-0.6587  mm   19-0.8136  mm   20-0.7867  mm   21-0.0345  mm
  22    5.55 MPa  23    67.4  ms   24    61.5  ms   25 -188.8  ms   26 -182.1  ms   27    1341 KPa   28 -1.605 KPa
  29    1307 KPa  30     1.2  cm   31    19.8  dC
Scan #180
20:17:27: 2
   1      0 lpm    2-0.1529  mm    3-0.1251  mm    4-0.2491  mm    5-0.0781  mm    6 0.0656  mm    7-0.4305  mm
   8 0.2399  mm    9-0.0436  mm   10-0.0273  mm   11 0.0126  mm   12 -0.267  mm   13 -0.562  mm   14-0.5308  mm
  15-0.0568  mm   16-0.4049  mm   17 0.4631  mm   18-0.6599  mm   19-0.8136  mm   20 -0.788  mm   21-0.0345  mm
  22    5.55 MPa  23    67.4  ms   24    60.7  ms   25 -188.8  ms   26    -188  ms   27    1342 KPa   28 -1.605 KPa
  29    1307 KPa  30     1.2  cm   31    19.8  dC
Scan #181
20:17:29: 2
   1      0 lpm    2 -0.154  mm    3-0.1254  mm    4-0.2494  mm    5-0.0781  mm    6 0.0656  mm    7-0.4329  mm
   8 0.2421  mm    9-0.0433  mm   10-0.0273  mm   11 0.0126  mm   12-0.2707  mm   13-0.5633  mm   14-0.5433  mm
  15-0.0562  mm   16-0.4055  mm   17 0.4672  mm   18-0.6605  mm   19-0.8161  mm   20-0.7893  mm   21-0.0345  mm
  22    5.55 MPa  23    67.4  ms   24    60.7  ms   25 -188.8  ms   26    -183  ms   27    1343 KPa   28 -1.605 KPa
  29    1308 KPa  30     1.2  cm   31    19.8  dC
Scan #182
20:17:31: 2
   1      0 lpm    2-0.1546  mm    3-0.1257  mm    4-0.2503  mm    5-0.0781  mm    6 0.0656  mm    7-0.4346  mm
   8 0.2439  mm    9-0.0436  mm   10-0.0273  mm   11 0.0132  mm   12-0.2763  mm   13-0.5645  mm   14-0.5408  mm
  15-0.0562  mm   16-0.4055  mm   17  0.472  mm   18-0.6618  mm   19-0.8179  mm   20-0.7899  mm   21-0.0345  mm
  22    5.55 MPa  23    67.4  ms   24    60.7  ms   25 -188.8  ms   26    -188  ms   27    1343 KPa   28  -1.57 KPa
  29    1309 KPa  30     1.2  cm   31    19.9  dC
```

Scan #183
20:17:33: 2

1 0 lpm	2-0.1553 mm	3-0.1257 mm	4-0.2509 mm	5-0.0781 mm	6 0.0656 mm	7-0.4363 mm	
8 0.2455 mm	9-0.0436 mm	10-0.0273 mm	11 0.0132 mm	12-0.2794 mm	13-0.5645 mm	14-0.5395 mm	
15-0.0562 mm	16 -0.406 mm	17 0.4756 mm	18 -0.663 mm	19-0.8191 mm	20-0.7899 mm	21-0.0345 mm	
22 5.55 MPa	23 67.4 ms	24 60.7 ms	25 -188.8 ms	26 -188.9 ms	27 1344 KPa	28 -1.605 KPa	
29 1310 KPa	30 1.2 cm	31 19.9 dC					

Scan #184
20:17:35: 2

1 0 lpm	2 -0.156 mm	3-0.1257 mm	4-0.2512 mm	5-0.0781 mm	6 0.0656 mm	7-0.4377 mm	
8 0.2464 mm	9-0.0436 mm	10-0.0273 mm	11 0.0126 mm	12-0.2862 mm	13-0.5658 mm	14-0.5351 mm	
15-0.0562 mm	16 -0.406 mm	17 0.4791 mm	18 -0.663 mm	19-0.8228 mm	20-0.7905 mm	21-0.0348 mm	
22 5.55 MPa	23 67.4 ms	24 60.7 ms	25 -188.8 ms	26 -188.9 ms	27 1345 KPa	28 -1.605 KPa	
29 1311 KPa	30 1.1 cm	31 19.8 dC					

Scan #185
20:17:37: 2

1 0 lpm	2-0.1563 mm	3 -0.126 mm	4-0.2518 mm	5-0.0784 mm	6 0.0656 mm	7-0.4387 mm	
8 0.2476 mm	9-0.0436 mm	10-0.0273 mm	11 0.0126 mm	12-0.2874 mm	13-0.5665 mm	14-0.5351 mm	
15-0.0555 mm	16-0.4066 mm	17 0.4821 mm	18-0.6642 mm	19-0.8277 mm	20-0.7905 mm	21-0.0348 mm	
22 5.55 MPa	23 67.4 ms	24 60.7 ms	25 -188.8 ms	26 -188.9 ms	27 1346 KPa	28 -1.605 KPa	
29 1311 KPa	30 1.1 cm	31 19.8 dC					

Scan #186
20:17:39: 2

1 0 lpm	2 -0.157 mm	3 -0.126 mm	4-0.2521 mm	5-0.0784 mm	6 0.0656 mm	7-0.4397 mm	
8 0.2486 mm	9-0.0436 mm	10-0.0273 mm	11 0.0132 mm	12-0.2921 mm	13-0.5671 mm	14-0.5065 mm	
15-0.0555 mm	16-0.4066 mm	17 0.4851 mm	18-0.6642 mm	19-0.8301 mm	20-0.7911 mm	21-0.0348 mm	
22 5.57 MPa	23 67.4 ms	24 60.7 ms	25 -188.8 ms	26 -188.9 ms	27 1346 KPa	28 -1.57 KPa	
29 1312 KPa	30 1.1 cm	31 19.8 dC					

Scan #187
20:17:41: 2

1 0 lpm	2-0.1577 mm	3 -0.126 mm	4-0.2528 mm	5-0.0784 mm	6 0.0656 mm	7-0.4407 mm	
8 0.2492 mm	9-0.0436 mm	10-0.0273 mm	11 0.0132 mm	12-0.2949 mm	13-0.5677 mm	14-0.5482 mm	
15-0.0562 mm	16-0.4072 mm	17 0.4869 mm	18-0.6648 mm	19-0.8307 mm	20-0.7911 mm	21-0.0348 mm	
22 5.55 MPa	23 67.4 ms	24 60.7 ms	25 -188.8 ms	26 -188.9 ms	27 1347 KPa	28 -1.605 KPa	
29 1312 KPa	30 1.1 cm	31 19.9 dC					

Scan #188
20:17:43: 2

1 0 lpm	2 -0.158 mm	3-0.1263 mm	4-0.2531 mm	5-0.0784 mm	6 0.0656 mm	7-0.4414 mm	
8 0.2498 mm	9-0.0436 mm	10-0.0273 mm	11 0.0132 mm	12-0.2884 mm	13-0.5677 mm	14-0.5719 mm	
15-0.0555 mm	16-0.4066 mm	17 0.4881 mm	18-0.6655 mm	19-0.8314 mm	20-0.7911 mm	21-0.0348 mm	
22 5.55 MPa	23 67.4 ms	24 60.7 ms	25 -188.8 ms	26 -188.9 ms	27 1348 KPa	28 -1.605 KPa	
29 1313 KPa	30 1.1 cm	31 19.8 dC					

Scan #189
20:17:45: 2

1 0 lpm	2-0.1583 mm	3-0.1263 mm	4-0.2534 mm	5-0.0784 mm	6 0.0656 mm	7-0.4425 mm	
8 0.2504 mm	9-0.0436 mm	10-0.0273 mm	11 0.0132 mm	12 -0.285 mm	13-0.5684 mm	14-0.5183 mm	
15-0.0555 mm	16-0.4072 mm	17 0.4898 mm	18-0.6655 mm	19-0.8326 mm	20-0.7918 mm	21-0.0348 mm	
22 5.55 MPa	23 67.4 ms	24 60.7 ms	25 -188.8 ms	26 -188.9 ms	27 1348 KPa	28 -1.605 KPa	
29 1314 KPa	30 1.2 cm	31 19.8 dC					

Scan #190
20:17:47: 2

1 0 lpm	2-0.1587 mm	3-0.1263 mm	4-0.2537 mm	5-0.0784 mm	6 0.0662 mm	7-0.4431 mm	
8 0.251 mm	9-0.0436 mm	10-0.0273 mm	11 0.0126 mm	12-0.2862 mm	13 -0.569 mm	14-0.4959 mm	
15-0.0555 mm	16-0.4072 mm	17 0.491 mm	18-0.6661 mm	19-0.8344 mm	20-0.7918 mm	21-0.0345 mm	
22 5.55 MPa	23 67.4 ms	24 60.7 ms	25 -188.8 ms	26 -194.7 ms	27 1349 KPa	28 -1.57 KPa	
29 1314 KPa	30 1.1 cm	31 20 dC					

Scan #191
20:17:49: 2

1	0	lpm	2	-0.159	mm	3	-0.126	mm	4	-0.254	mm	5	-0.0784	mm	6	0.0656	mm	7	-0.4435 mm
8	0.2517	mm	9	-0.0436	mm	10	-0.0273	mm	11	0.0132	mm	12	-0.2874	mm	13	-0.569	mm	14	-0.5027 mm
15	-0.0555	mm	16	-0.4072	mm	17	0.4922	mm	18	-0.6661	mm	19	-0.8332	mm	20	-0.7918	mm	21	-0.0348 mm
22	5.55	MPa	23	67.4	ms	24	60.7	ms	25	-188.8	ms	26	-189.8	ms	27	1349	KPa	28	-1.605 KPa
29	1315	KPa	30	1.1	cm	31	20	dC											

Scan #192
20:17:51: 2

1	0	lpm	2	-0.1594	mm	3	-0.1263	mm	4	-0.254	mm	5	-0.0787	mm	6	0.0656	mm	7	-0.4442 mm
8	0.252	mm	9	-0.0436	mm	10	-0.0273	mm	11	0.0132	mm	12	-0.2859	mm	13	-0.5697	mm	14	-0.5152 mm
15	-0.0555	mm	16	-0.4072	mm	17	0.4928	mm	18	-0.6667	mm	19	-0.835	mm	20	-0.7918	mm	21	-0.0348 mm
22	5.55	MPa	23	67.4	ms	24	60.7	ms	25	-188.8	ms	26	-188.9	ms	27	1350	KPa	28	-1.57 KPa
29	1315	KPa	30	1.1	cm	31	20	dC											

Scan #193
20:17:53: 2

1	0	lpm	2	-0.1597	mm	3	-0.1263	mm	4	-0.2543	mm	5	-0.0787	mm	6	0.0662	mm	7	-0.4445 mm
8	0.2523	mm	9	-0.0436	mm	10	-0.0273	mm	11	0.0132	mm	12	-0.285	mm	13	-0.5697	mm	14	-0.527 mm
15	-0.0562	mm	16	-0.4078	mm	17	0.494	mm	18	-0.6667	mm	19	-0.8338	mm	20	-0.7918	mm	21	-0.0348 mm
22	5.57	MPa	23	67.4	ms	24	60.7	ms	25	-188.8	ms	26	-188.9	ms	27	1351	KPa	28	-1.605 KPa
29	1316	KPa	30	1.1	cm	31	20	dC											

Scan #194
20:17:55: 2

1	0	lpm	2	-0.1597	mm	3	-0.1263	mm	4	-0.2546	mm	5	-0.0784	mm	6	0.0656	mm	7	-0.4452 mm
8	0.2529	mm	9	-0.0436	mm	10	-0.0273	mm	11	0.0126	mm	12	-0.2912	mm	13	-0.5703	mm	14	-0.5638 mm
15	-0.0555	mm	16	-0.4078	mm	17	0.4952	mm	18	-0.6667	mm	19	-0.8338	mm	20	-0.7924	mm	21	-0.0348 mm
22	5.55	MPa	23	67.4	ms	24	60.7	ms	25	-188.8	ms	26	-188.9	ms	27	1351	KPa	28	-1.57 KPa
29	1316	KPa	30	1.1	cm	31	20	dC											

Scan #195
20:17:57: 2

1	0	lpm	2	-0.16	mm	3	-0.1263	mm	4	-0.2549	mm	5	-0.0787	mm	6	0.0656	mm	7	-0.4455 mm
8	0.2532	mm	9	-0.0436	mm	10	-0.0273	mm	11	0.0126	mm	12	-0.297	mm	13	-0.571	mm	14	-0.5426 mm
15	-0.0555	mm	16	-0.4078	mm	17	0.4958	mm	18	-0.6667	mm	19	-0.835	mm	20	-0.7924	mm	21	-0.0348 mm
22	5.55	MPa	23	67.4	ms	24	60.7	ms	25	-188.8	ms	26	-188.9	ms	27	1351	KPa	28	-1.605 KPa
29	1317	KPa	30	1.1	cm	31	20	dC											

Scan #196
20:17:59: 2

1	0	lpm	2	-0.1604	mm	3	-0.1263	mm	4	-0.2552	mm	5	-0.0787	mm	6	0.0656	mm	7	-0.4462 mm
8	0.2535	mm	9	-0.0436	mm	10	-0.0273	mm	11	0.0132	mm	12	-0.3088	mm	13	-0.5716	mm	14	-0.5457 mm
15	-0.0555	mm	16	-0.4078	mm	17	0.4964	mm	18	-0.6673	mm	19	-0.8381	mm	20	-0.793	mm	21	-0.0348 mm
22	5.57	MPa	23	67.4	ms	24	60.7	ms	25	-188.8	ms	26	-194.7	ms	27	1352	KPa	28	-1.605 KPa
29	1317	KPa	30	1.1	cm	31	20	dC											

Scan #197
20:18: 1: 2

1	0	lpm	2	-0.1607	mm	3	-0.1263	mm	4	-0.2552	mm	5	-0.0787	mm	6	0.0662	mm	7	-0.4465 mm
8	0.2538	mm	9	-0.0436	mm	10	-0.0273	mm	11	0.0126	mm	12	-0.3029	mm	13	-0.5716	mm	14	-0.5638 mm
15	-0.0555	mm	16	-0.4078	mm	17	0.4976	mm	18	-0.6673	mm	19	-0.8399	mm	20	-0.793	mm	21	-0.0348 mm
22	5.57	MPa	23	67.4	ms	24	60.7	ms	25	-188.8	ms	26	-189.8	ms	27	1352	KPa	28	-1.605 KPa
29	1318	KPa	30	1.2	cm	31	20	dC											

Scan #198
20:18: 3: 2

1	0	lpm	2	-0.1607	mm	3	-0.1263	mm	4	-0.2555	mm	5	-0.0787	mm	6	0.0662	mm	7	-0.4472 mm
8	0.2544	mm	9	-0.0436	mm	10	-0.0273	mm	11	0.0132	mm	12	-0.302	mm	13	-0.5722	mm	14	-0.5663 mm
15	-0.0555	mm	16	-0.4078	mm	17	0.4988	mm	18	-0.6679	mm	19	-0.8399	mm	20	-0.793	mm	21	-0.0348 mm
22	5.57	MPa	23	67.4	ms	24	60.7	ms	25	-188.8	ms	26	-188.9	ms	27	1353	KPa	28	-1.605 KPa
29	1318	KPa	30	1.1	cm	31	19.9	dC											

Scan #199
20:18: 5: 2

1 0 lpm	2 -0.161 mm	3-0.1263 mm	4-0.2555 mm	5-0.0787 mm	6 0.0662 mm	7-0.4479 mm
8 0.2548 mm	9-0.0436 mm	10-0.0273 mm	11 0.0126 mm	12-0.3023 mm	13-0.5729 mm	14-0.5875 mm
15-0.0555 mm	16-0.4084 mm	17 0.5 mm	18-0.6679 mm	19-0.8418 mm	20-0.7937 mm	21-0.0348 mm
22 5.55 MPa	23 67.4 ms	24 60.7 ms	25 -188.8 ms	26 -188.9 ms	27 1353 KPa	28 -1.605 KPa
29 1319 KPa	30 1.1 cm	31 20 dC				

Scan #200
20:18: 7: 2

1 0 lpm	2-0.1614 mm	3-0.1263 mm	4-0.2555 mm	5-0.0787 mm	6 0.0662 mm	7-0.4483 mm
8 0.2554 mm	9-0.0436 mm	10-0.0273 mm	11 0.0132 mm	12-0.2921 mm	13-0.5735 mm	14-0.5663 mm
15-0.0555 mm	16-0.4084 mm	17 0.5006 mm	18-0.6679 mm	19-0.8405 mm	20 -0.793 mm	21-0.0348 mm
22 5.55 MPa	23 67.4 ms	24 60.7 ms	25 -188.8 ms	26 -188.9 ms	27 1354 KPa	28 -1.605 KPa
29 1319 KPa	30 1.2 cm	31 19.9 dC				

Scan #201
20:18: 9: 2

1 0 lpm	2-0.1614 mm	3-0.1263 mm	4-0.2558 mm	5-0.0787 mm	6 0.0662 mm	7-0.4489 mm
8 0.2557 mm	9-0.0436 mm	10-0.0273 mm	11 0.0132 mm	12-0.2973 mm	13-0.5742 mm	14-0.5788 mm
15-0.0555 mm	16-0.4084 mm	17 0.5023 mm	18-0.6685 mm	19-0.8424 mm	20 -0.793 mm	21-0.0348 mm
22 5.57 MPa	23 67.4 ms	24 60.7 ms	25 -188.8 ms	26 -194.7 ms	27 1354 KPa	28 -1.57 KPa
29 1319 KPa	30 1.2 cm	31 19.9 dC				

Scan #202
20:18:11: 2

1 0 lpm	2-0.1617 mm	3-0.1263 mm	4-0.2558 mm	5-0.0787 mm	6 0.0662 mm	7-0.4493 mm
8 0.2563 mm	9-0.0436 mm	10-0.0269 mm	11 0.0126 mm	12-0.2859 mm	13-0.5735 mm	14-0.5551 mm
15-0.0555 mm	16-0.4084 mm	17 0.5029 mm	18-0.6685 mm	19-0.8405 mm	20-0.7937 mm	21-0.0348 mm
22 5.57 MPa	23 67.4 ms	24 60.7 ms	25 -188.8 ms	26 -195.6 ms	27 1355 KPa	28 -1.57 KPa
29 1320 KPa	30 1.1 cm	31 19.9 dC				

Scan #203
20:18:13: 2

1 0 lpm	2-0.1617 mm	3-0.1263 mm	4-0.2561 mm	5-0.0787 mm	6 0.0662 mm	7 -0.45 mm
8 0.2566 mm	9-0.0436 mm	10-0.0273 mm	11 0.0119 mm	12-0.2887 mm	13-0.5748 mm	14-0.5651 mm
15-0.0555 mm	16-0.4084 mm	17 0.5035 mm	18-0.6685 mm	19-0.8405 mm	20-0.7937 mm	21-0.0348 mm
22 5.57 MPa	23 67.4 ms	24 54.7 ms	25 -188.8 ms	26 -195.6 ms	27 1355 KPa	28 -1.605 KPa
29 1320 KPa	30 1.1 cm	31 19.9 dC				

Scan #204
20:18:15: 2

1 0 lpm	2-0.1621 mm	3-0.1266 mm	4-0.2561 mm	5-0.0787 mm	6 0.0662 mm	7-0.4503 mm
8 0.2569 mm	9-0.0436 mm	10-0.0273 mm	11-1.1642 mm	12-0.2899 mm	13-0.5748 mm	14-0.5626 mm
15-0.0555 mm	16-0.4084 mm	17 0.5047 mm	18-0.6692 mm	19-0.8418 mm	20-0.7937 mm	21-0.0348 mm
22 5.55 MPa	23 67.4 ms	24 59.9 ms	25 -188.8 ms	26 -189.8 ms	27 1356 KPa	28 -1.605 KPa
29 1321 KPa	30 1.2 cm	31 19.8 dC				

Scan #205
20:18:17: 2

1 0 lpm	2-0.1621 mm	3-0.1263 mm	4-0.2561 mm	5-0.0787 mm	6 0.0662 mm	7-0.4506 mm
8 0.2572 mm	9-0.0436 mm	10-0.0273 mm	11-1.2405 mm	12-0.2788 mm	13-0.5748 mm	14-0.5501 mm
15-0.0555 mm	16-0.4084 mm	17 0.5059 mm	18-0.6692 mm	19-0.8405 mm	20-0.7943 mm	21-0.0348 mm
22 5.55 MPa	23 67.4 ms	24 54.7 ms	25 -188.8 ms	26 -188.9 ms	27 1356 KPa	28 -1.57 KPa
29 1321 KPa	30 1.1 cm	31 19.8 dC				

Scan #206
20:18:19: 2

1 0 lpm	2-0.1624 mm	3-0.1263 mm	4-0.2564 mm	5-0.0787 mm	6 0.0662 mm	7 -0.451 mm
8 0.2575 mm	9-0.0436 mm	10-0.0269 mm	11-1.2663 mm	12-0.2871 mm	13-0.5748 mm	14 -0.547 mm
15-0.0555 mm	16 -0.409 mm	17 0.5065 mm	18-0.6692 mm	19-0.8436 mm	20-0.7943 mm	21-0.0348 mm
22 5.57 MPa	23 67.4 ms	24 59.9 ms	25 -188.8 ms	26 -194.7 ms	27 1357 KPa	28 -1.605 KPa
29 1321 KPa	30 1.1 cm	31 19.8 dC				

```
**STRENGTH AND PREMEABILITY TESTS ON ULTRA-LARGE
**STRIPA GRANITE CORE (Engineering Units Data)
**18:22:35 - 19:58:47
**Permeability testing at 5.55 MPa axial stress
Scan #207
**Initial conditions:
20:18:22:35
    1  0.941 lpm    2-0.1627  mm    3-0.1263  mm    4-0.2567  mm    5-0.0787  mm    6 0.0662  mm    7 -0.452  mm
    8 0.2588  mm    9 -0.044  mm   10-0.0269  mm   11-1.2631  mm   12-0.2608  mm   13-0.5767  mm   14 -0.567  mm
   15-0.0555  mm   16 -0.409  mm   17 0.5107  mm   18-0.6698  mm   19-0.8454  mm   20-0.7943  mm   21-0.0348  mm
   22    5.57 MPa  23   61.1  ms   24   54.4  ms   25 -188.8  ms   26 -195.6  ms   27   1370 KPa   28  9.315 KPa
   29   1349 KPa   30    1.2  cm   31   19.8  dC
Scan #208
20:18:24:35
    1    3.29 lpm    2-0.1631  mm    3-0.1263  mm    4-0.2567  mm    5-0.0787  mm    6 0.0662  mm    7 -0.452  mm
    8 0.2603  mm    9 -0.044  mm   10-0.0269  mm   11-1.2682  mm   12-0.2577  mm   13-0.5767  mm   14-0.5763  mm
   15-0.0555  mm   16 -0.409  mm   17 0.5131  mm   18-0.6698  mm   19-0.8454  mm   20-0.7943  mm   21-0.0348  mm
   22    5.57 MPa  23   66.6  ms   24   59.9  ms   25 -188.8  ms   26 -195.6  ms   27   1352 KPa   28 57.562 KPa
   29   1364 KPa   30    1.2  cm   31   19.9  dC
Scan #209
**Unsteady flow.
20:18:26:35
    1  4.262 lpm    2-0.1631  mm    3-0.1263  mm    4-0.2567  mm    5-0.0787  mm    6 0.0662  mm    7 -0.452  mm
    8 0.2622  mm    9 -0.044  mm   10-0.0273  mm   11-1.2833  mm   12-0.2503  mm   13-0.5774  mm   14-0.5726  mm
   15-0.0555  mm   16 -0.409  mm   17 0.5148  mm   18-0.6698  mm   19-0.8454  mm   20-0.7943  mm   21-0.0348  mm
   22    5.55 MPa  23   67.4  ms   24   54.7  ms   25 -188.8  ms   26 -195.6  ms   27   1407 KPa   28 59.376 KPa
   29   1428 KPa   30    1.1  cm   31     20  dC
Scan #210
20:18:28:35
    1  3.429 lpm    2-0.1634  mm    3 -0.126  mm    4-0.2567  mm    5-0.0787  mm    6 0.0662  mm    7-0.4513  mm
    8 0.2637  mm    9-0.0443  mm   10-0.0273  mm   11-1.2934  mm   12-0.2583  mm   13-0.5774  mm   14-0.5757  mm
   15-0.0549  mm   16 -0.409  mm   17 0.5172  mm   18-0.6698  mm   19-0.8442  mm   20-0.7943  mm   21-0.0348  mm
   22    5.57 MPa  23   67.4  ms   24   59.9  ms   25 -188.8  ms   26 -195.6  ms   27   1381 KPa   28 40.398 KPa
   29   1384 KPa   30    1.2  cm   31   20.1  dC
Scan #211
**Unsteady flow.
20:18:30:35
    1  3.341 lpm    2-0.1637  mm    3 -0.126  mm    4 -0.257  mm    5-0.0787  mm    6 0.0662  mm    7 -0.451  mm
    8 0.2646  mm    9-0.0443  mm   10-0.0273  mm   11-1.3035  mm   12-0.2698  mm   13-0.5786  mm   14-0.5738  mm
   15-0.0549  mm   16 -0.409  mm   17  0.519  mm   18-0.6698  mm   19 -0.843  mm   20-0.7943  mm   21-0.0348  mm
   22    5.57 MPa  23   61.5  ms   24   54.7  ms   25 -188.8  ms   26 -195.6  ms   27   1361 KPa   28 40.956 KPa
   29   1366 KPa   30    1.2  cm   31   20.2  dC
Scan #212
20:18:32:35
    1  3.315 lpm    2-0.1637  mm    3 -0.126  mm    4 -0.257  mm    5-0.0787  mm    6 0.0668  mm    7 -0.451  mm
    8 0.2656  mm    9-0.0443  mm   10-0.0273  mm   11-1.3066  mm   12-0.2624  mm   13 -0.578  mm   14  -0.58  mm
   15-0.0549  mm   16 -0.409  mm   17 0.5214  mm   18-0.6698  mm   19-0.8436  mm   20-0.7943  mm   21-0.0348  mm
   22    5.55 MPa  23   66.6  ms   24   53.9  ms   25 -188.8  ms   26 -195.6  ms   27   1372 KPa   28 42.421 KPa
   29   1375 KPa   30    1.2  cm   31   20.2  dC
Scan #213
**Approximate steady flow at 41.4 KPa (6 psi) injection:
20:18:33:45
    1    3.32 lpm    2-0.1641  mm    3 -0.126  mm    4 -0.257  mm    5-0.0787  mm    6 0.0668  mm    7-0.4506  mm
    8 0.2659  mm    9-0.0443  mm   10-0.0269  mm   11 -1.306  mm   12-0.2614  mm   13-0.5786  mm   14-0.5532  mm
   15-0.0549  mm   16 -0.409  mm   17  0.522  mm   18-0.6704  mm   19-0.8442  mm   20-0.7943  mm   21-0.0348  mm
   22    5.55 MPa  23     62  ms   24   53.9  ms   25 -188.8  ms   26 -195.6  ms   27   1372 KPa   28 42.247 KPa
   29   1376 KPa   30    1.2  cm   31   20.2  dC
```

Scan #214
20:18:35:45

1 3.355 lpm	2-0.1641 mm	3 -0.126 mm	4 -0.257 mm	5-0.0787 mm	6 0.0668 mm	7 -0.451 mm
8 0.2665 mm	9-0.0446 mm	10-0.0269 mm	11-1.3054 mm	12-0.2636 mm	13-0.5786 mm	14-0.5663 mm
15-0.0549 mm	16 -0.409 mm	17 0.5232 mm	18-0.6698 mm	19-0.8436 mm	20-0.7943 mm	21-0.0348 mm
22 5.57 MPa	23 60.7 ms	24 53.9 ms	25 -194.8 ms	26 -195.6 ms	27 1360 KPa	28 42.735 KPa
29 1380 KPa	30 1.2 cm	31 20.3 dC				

Scan #215
20:18:37:45

1 3.309 lpm	2-0.1648 mm	3-0.1263 mm	4 -0.257 mm	5-0.0787 mm	6 0.0668 mm	7 -0.451 mm
8 0.2671 mm	9-0.0443 mm	10-0.0269 mm	11-1.3066 mm	12-0.2651 mm	13-0.5793 mm	14 -0.58 mm
15-0.0549 mm	16 -0.409 mm	17 0.5244 mm	18-0.6698 mm	19-0.8454 mm	20-0.7943 mm	21-0.0348 mm
22 5.55 MPa	23 60.7 ms	24 53.9 ms	25 -195.6 ms	26 -195.6 ms	27 1365 KPa	28 42.491 KPa
29 1369 KPa	30 1.1 cm	31 20.3 dC				

Scan #216
20:18:39:45

1 3.396 lpm	2-0.1658 mm	3 -0.126 mm	4 -0.257 mm	5-0.0787 mm	6 0.0668 mm	7-0.4513 mm
8 0.2674 mm	9-0.0443 mm	10-0.0269 mm	11 -1.306 mm	12-0.2679 mm	13-0.5793 mm	14-0.5825 mm
15-0.0549 mm	16 -0.409 mm	17 0.5256 mm	18-0.6704 mm	19-0.8461 mm	20-0.7943 mm	21-0.0348 mm
22 5.57 MPa	23 60.7 ms	24 53.9 ms	25 -195.6 ms	26 -201.5 ms	27 1367 KPa	28 20.339 KPa
29 1359 KPa	30 1.2 cm	31 20.4 dC				

Scan #217
**Approximate steady flow at 20.7 KPa (3 psi) injection:
20:18:41: 4

1 1.832 lpm	2-0.1661 mm	3 -0.126 mm	4 -0.257 mm	5 -0.079 mm	6 0.0668 mm	7 -0.451 mm
8 0.2674 mm	9-0.0443 mm	10-0.0269 mm	11-1.3029 mm	12-0.2732 mm	13-0.5799 mm	14-0.5888 mm
15-0.0549 mm	16 -0.409 mm	17 0.5256 mm	18 -0.671 mm	19-0.8461 mm	20-0.7943 mm	21-0.0348 mm
22 5.55 MPa	23 66.2 ms	24 53.9 ms	25 -195.6 ms	26 -196.9 ms	27 1346 KPa	28 21.141 KPa
29 1338 KPa	30 1.2 cm	31 20.4 dC				

Scan #218
20:18:43: 4

1 1.852 lpm	2-0.1668 mm	3-0.1263 mm	4 -0.257 mm	5-0.0787 mm	6 0.0668 mm	7-0.4513 mm
8 0.2674 mm	9-0.0443 mm	10-0.0269 mm	11 -1.306 mm	12 -0.272 mm	13-0.5799 mm	14 -0.605 mm
15-0.0549 mm	16 -0.409 mm	17 0.5262 mm	18-0.6704 mm	19-0.8461 mm	20-0.7943 mm	21-0.0348 mm
22 5.55 MPa	23 61.5 ms	24 53.9 ms	25 -195.6 ms	26 -195.6 ms	27 1356 KPa	28 21.56 KPa
29 1335 KPa	30 1.2 cm	31 20.4 dC				

Scan #219
20:18:45: 4

1 1.854 lpm	2-0.1671 mm	3-0.1263 mm	4 -0.257 mm	5 -0.079 mm	6 0.0668 mm	7-0.4513 mm
8 0.2674 mm	9-0.0446 mm	10-0.0269 mm	11-1.3123 mm	12-0.2695 mm	13-0.5806 mm	14-0.6013 mm
15-0.0555 mm	16 -0.409 mm	17 0.5268 mm	18 -0.671 mm	19-0.8448 mm	20-0.7943 mm	21-0.0351 mm
22 5.55 MPa	23 60.7 ms	24 53.9 ms	25 -195.6 ms	26 -201.5 ms	27 1356 KPa	28 20.827 KPa
29 1334 KPa	30 1.1 cm	31 20.5 dC				

Scan #220
**Change to withdrawal; unsteady flow.
20:18:54:23

1 1.114 lpm	2-0.1685 mm	3-0.1266 mm	4 -0.257 mm	5 -0.079 mm	6 0.0668 mm	7 -0.454 mm
8 0.2671 mm	9-0.0443 mm	10-0.0266 mm	11-1.3167 mm	12-0.2884 mm	13-0.5806 mm	14-0.6162 mm
15-0.0555 mm	16 -0.409 mm	17 0.5279 mm	18-0.6728 mm	19-0.8497 mm	20-0.7943 mm	21-0.0351 mm
22 5.55 MPa	23 60.7 ms	24 53.9 ms	25 -195.6 ms	26 -202.4 ms	27 1374 KPa	28 51.562 KPa
29 1272 KPa	30 1.1 cm	31 20.4 dC				

Scan #221
20:18:56:23

1 1.178 lpm	2-0.1688 mm	3-0.1266 mm	4 -0.257 mm	5 -0.079 mm	6 0.0675 mm	7-0.4551 mm
8 0.2668 mm	9-0.0443 mm	10-0.0269 mm	11-1.3148 mm	12-0.2936 mm	13-0.5812 mm	14-0.6168 mm
15-0.0549 mm	16 -0.409 mm	17 0.5279 mm	18-0.6728 mm	19-0.8522 mm	20-0.7943 mm	21-0.0351 mm
22 5.55 MPa	23 60.7 ms	24 53.9 ms	25 -195.6 ms	26 -202.4 ms	27 1367 KPa	28 0.314 KPa
29 1335 KPa	30 1.2 cm	31 20.3 dC				

```
Scan #222
**Unsteady flow:
20:18:58:23
    1  1.164 lpm    2-0.1691  mm    3-0.1266  mm    4-0.2573  mm    5 -0.079  mm    6 0.0668  mm    7-0.4554  mm
    8 0.2668  mm    9-0.0446  mm   10-0.0266  mm   11-1.3117  mm   12-0.2958  mm   13-0.5812  mm   14-0.6243  mm
   15-0.0549  mm   16 -0.409  mm   17 0.5279  mm   18-0.6735  mm   19-0.8528  mm   20-0.7943  mm   21-0.0351  mm
   22    5.57 MPa  23    60.7  ms   24    53.9  ms   25 -195.6  ms   26 -202.4  ms   27    1333 KPa   28  0.593 KPa
   29    1301 KPa  30     1.2  cm   31    20.3  dC
Scan #223
20:19: 0:23
    1  1.189 lpm    2-0.1695  mm    3-0.1266  mm    4-0.2573  mm    5 -0.079  mm    6 0.0668  mm    7-0.4561  mm
    8 0.2662  mm    9-0.0446  mm   10-0.0269  mm   11-1.3155  mm   12-0.2955  mm   13-0.5825  mm   14-0.6187  mm
   15-0.0549  mm   16-0.4096  mm   17 0.5279  mm   18-0.6735  mm   19-0.8528  mm   20-0.7943  mm   21-0.0351  mm
   22    5.58 MPa  23    60.7  ms   24    53.9  ms   25 -195.6  ms   26 -202.4  ms   27    1353 KPa   28 60.248 KPa
   29    1250 KPa  30     1.1  cm   31    20.3  dC
Scan #224
**Unsteady flow:
20:19: 2:23
    1   1.11 lpm    2-0.1695  mm    3-0.1273  mm    4-0.2576  mm    5 -0.079  mm    6 0.0675  mm    7-0.4564  mm
    8 0.2665  mm    9-0.0443  mm   10-0.0269  mm   11-1.3148  mm   12-0.3017  mm   13-0.5825  mm   14-0.6218  mm
   15-0.0549  mm   16-0.4096  mm   17 0.5333  mm   18-0.6741  mm   19 -0.854  mm   20-0.7943  mm   21-0.0351  mm
   22    5.55 MPa  23    60.7  ms   24    53.9  ms   25 -195.6  ms   26 -202.4  ms   27    1338 KPa   28  1.954 KPa
   29    1304 KPa  30     1.1  cm   31    20.2  dC
Scan #225
20:19: 4:23
    1  1.377 lpm    2-0.1698  mm    3-0.1279  mm    4 -0.258  mm    5 -0.079  mm    6 0.0668  mm    7-0.4571  mm
    8 0.2665  mm    9-0.0443  mm   10-0.0266  mm   11-1.3129  mm   12-0.3011  mm   13-0.5825  mm   14 -0.625  mm
   15-0.0549  mm   16-0.4096  mm   17 0.5357  mm   18-0.6741  mm   19-0.8534  mm   20-0.7949  mm   21-0.0351  mm
   22    5.55 MPa  23    66.6  ms   24    53.9  ms   25 -195.6  ms   26 -202.4  ms   27    1335 KPa   28  4.989 KPa
   29    1300 KPa  30     1.1  cm   31    20.2  dC
Scan #226
**Unsteady flow:
20:19: 6:23
    1  1.539 lpm    2-0.1702  mm    3-0.1273  mm    4 -0.258  mm    5-0.0793  mm    6 0.0668  mm    7-0.4575  mm
    8 0.2665  mm    9-0.0446  mm   10-0.0269  mm   11-1.3085  mm   12-0.3237  mm   13-0.5825  mm   14-0.6299  mm
   15-0.0549  mm   16-0.4096  mm   17 0.5357  mm   18-0.6741  mm   19 -0.854  mm   20-0.7943  mm   21-0.0351  mm
   22    5.55 MPa  23    61.5  ms   24    53.9  ms   25 -195.6  ms   26 -202.4  ms   27    1415 KPa   28 17.722 KPa
   29    1361 KPa  30     1.1  cm   31    20.2  dC
Scan #227
20:19: 8:23
    1  1.786 lpm    2-0.1702  mm    3-0.1269  mm    4 -0.258  mm    5-0.0793  mm    6 0.0675  mm    7-0.4575  mm
    8 0.2662  mm    9-0.0446  mm   10-0.0269  mm   11 -1.306  mm   12  -0.32  mm   13-0.5818  mm   14-0.6287  mm
   15-0.0549  mm   16-0.4102  mm   17 0.5357  mm   18-0.6747  mm   19 -0.854  mm   20-0.7943  mm   21-0.0348  mm
   22    5.55 MPa  23    60.7  ms   24    53.9  ms   25 -195.6  ms   26 -202.4  ms   27    1431 KPa   28 19.536 KPa
   29    1374 KPa  30     1.1  cm   31    20.1  dC
Scan #228
**Unsteady flow:
20:19:10:23
    1  1.805 lpm    2-0.1702  mm    3-0.1269  mm    4 -0.258  mm    5 -0.079  mm    6 0.0668  mm    7-0.4575  mm
    8 0.2659  mm    9-0.0446  mm   10-0.0266  mm   11-1.3035  mm   12-0.3054  mm   13-0.5818  mm   14-0.6231  mm
   15-0.0549  mm   16-0.4102  mm   17 0.5357  mm   18-0.6747  mm   19-0.8552  mm   20-0.7949  mm   21-0.0348  mm
   22    5.57 MPa  23    66.6  ms   24    53.9  ms   25 -195.6  ms   26 -202.4  ms   27    1420 KPa   28  19.99 KPa
   29    1362 KPa  30     1.1  cm   31    20.1  dC
Scan #229
20:19:12:23
    1  1.164 lpm    2-0.1705  mm    3-0.1269  mm    4 -0.258  mm    5-0.0793  mm    6 0.0675  mm    7-0.4575  mm
    8 0.2662  mm    9-0.0446  mm   10-0.0269  mm   11-1.3003  mm   12 -0.297  mm   13-0.5825  mm   14-0.6231  mm
   15-0.0549  mm   16-0.4102  mm   17 0.5357  mm   18-0.6747  mm   19-0.8571  mm   20-0.7943  mm   21-0.0348  mm
   22    5.57 MPa  23    67.4  ms   24    53.9  ms   25 -195.6  ms   26 -202.4  ms   27    1402 KPa   28  19.85 KPa
   29    1344 KPa  30     1.1  cm   31    20.1  dC
```

Scan #230
**Approximate steady flow at 20.7 KPa (3 psi) withdrawal:
20:19:15: 2

1 1.273 lpm	2-0.1705 mm	3-0.1269 mm	4-0.2583 mm	5-0.0793 mm	6 0.0675 mm	7-0.4578 mm
8 0.2662 mm	9-0.0443 mm	10-0.0269 mm	11-1.2984 mm	12-0.2936 mm	13-0.5825 mm	14-0.6237 mm
15-0.0549 mm	16-0.4102 mm	17 0.5357 mm	18-0.6747 mm	19-0.8583 mm	20-0.7949 mm	21-0.0351 mm
22 5.57 MPa	23 61.3 ms	24 53.9 ms	25 -195.6 ms	26 -202.4 ms	27 1382 KPa	28 18.629 KPa
29 1328 KPa	30 1.1 cm	31 20 dC				

Scan #231
20:19:17: 2

1 1.442 lpm	2-0.1705 mm	3-0.1269 mm	4-0.2583 mm	5 -0.079 mm	6 0.0668 mm	7-0.4578 mm
8 0.2662 mm	9-0.0443 mm	10-0.0269 mm	11-1.2991 mm	12-0.2939 mm	13-0.5831 mm	14-0.6181 mm
15-0.0549 mm	16-0.4102 mm	17 0.5357 mm	18-0.6747 mm	19-0.8583 mm	20-0.7949 mm	21-0.0348 mm
22 5.55 MPa	23 60.7 ms	24 53.9 ms	25 -195.6 ms	26 -202.4 ms	27 1384 KPa	28 18.734 KPa
29 1331 KPa	30 1.1 cm	31 20 dC				

Scan #232
20:19:19: 2

1 1.807 lpm	2-0.1705 mm	3-0.1269 mm	4-0.2583 mm	5 -0.079 mm	6 0.0668 mm	7-0.4578 mm
8 0.2662 mm	9-0.0443 mm	10-0.0269 mm	11-1.2984 mm	12-0.2936 mm	13-0.5831 mm	14-0.6162 mm
15-0.0549 mm	16-0.4107 mm	17 0.5357 mm	18-0.6747 mm	19-0.8589 mm	20-0.7949 mm	21-0.0351 mm
22 5.55 MPa	23 60.7 ms	24 53.9 ms	25 -195.6 ms	26 -202.4 ms	27 1409 KPa	28 20.059 KPa
29 1351 KPa	30 1.1 cm	31 19.9 dC				

Scan #233
20:19:21: 2

1 1.164 lpm	2-0.1708 mm	3-0.1269 mm	4-0.2583 mm	5-0.0793 mm	6 0.0668 mm	7-0.4581 mm
8 0.2662 mm	9-0.0446 mm	10-0.0269 mm	11 -1.301 mm	12 -0.293 mm	13-0.5831 mm	14-0.6087 mm
15-0.0549 mm	16-0.4107 mm	17 0.5357 mm	18-0.6747 mm	19-0.8595 mm	20-0.7949 mm	21-0.0351 mm
22 5.57 MPa	23 60.7 ms	24 53.9 ms	25 -195.6 ms	26 -202.4 ms	27 1390 KPa	28 19.92 KPa
29 1332 KPa	30 1.1 cm	31 19.9 dC				

Scan #234
20:19:23: 2

1 1.148 lpm	2-0.1708 mm	3-0.1269 mm	4-0.2583 mm	5 -0.079 mm	6 0.0675 mm	7-0.4581 mm
8 0.2662 mm	9-0.0443 mm	10-0.0269 mm	11-1.2984 mm	12-0.2961 mm	13-0.5838 mm	14-0.6119 mm
15-0.0549 mm	16-0.4107 mm	17 0.5357 mm	18-0.6753 mm	19-0.8595 mm	20-0.7949 mm	21-0.0351 mm
22 5.57 MPa	23 66.6 ms	24 53.9 ms	25 -195.6 ms	26 -202.4 ms	27 1376 KPa	28 19.78 KPa
29 1319 KPa	30 1.1 cm	31 19.8 dC				

Scan #235
20:19:25: 2

1 1.18 lpm	2-0.1712 mm	3-0.1273 mm	4-0.2586 mm	5-0.0793 mm	6 0.0675 mm	7-0.4585 mm
8 0.2662 mm	9-0.0443 mm	10-0.0266 mm	11-1.2984 mm	12-0.2964 mm	13-0.5838 mm	14-0.6087 mm
15-0.0549 mm	16-0.4107 mm	17 0.5357 mm	18-0.6753 mm	19-0.8601 mm	20-0.7949 mm	21-0.0348 mm
22 5.57 MPa	23 61.5 ms	24 53.9 ms	25 -201.5 ms	26 -202.4 ms	27 1361 KPa	28 19.327 KPa
29 1306 KPa	30 1.1 cm	31 19.8 dC				

Scan #236
20:19:45:31

1 1.117 lpm	2-0.1729 mm	3-0.1266 mm	4-0.2601 mm	5-0.0797 mm	6 0.0681 mm	7-0.4605 mm
8 0.2671 mm	9-0.0446 mm	10-0.0269 mm	11-1.2713 mm	12-0.3104 mm	13 -0.587 mm	14-0.6193 mm
15-0.0543 mm	16-0.4119 mm	17 0.55 mm	18-0.6784 mm	19-0.8614 mm	20-0.7974 mm	21-0.0351 mm
22 5.55 MPa	23 60.7 ms	24 47.3 ms	25 -195.7 ms	26 -202.4 ms	27 1314 KPa	28 13.78 KPa
29 1267 KPa	30 1.1 cm	31 19.6 dC				

Scan #237
20:19:48:43

1 1.275 lpm	2-0.1729 mm	3-0.1266 mm	4-0.2604 mm	5-0.0797 mm	6 0.0681 mm	7-0.4609 mm
8 0.2668 mm	9-0.0449 mm	10-0.0269 mm	11-1.2739 mm	12-0.2992 mm	13 -0.587 mm	14 -0.625 mm
15-0.0543 mm	16-0.4119 mm	17 0.5506 mm	18 -0.679 mm	19-0.8614 mm	20-0.7974 mm	21-0.0351 mm
22 5.55 MPa	23 60.7 ms	24 47.2 ms	25 -201.8 ms	26 -202.4 ms	27 1469 KPa	28 17.897 KPa
29 1423 KPa	30 1.1 cm	31 19.6 dC				

Scan #238
**Approximate steady flow at 41.4 KPa (6 psi) withdrawal:
20:19:56:47

1	2.754	lpm	2-0.1732	mm	3-0.1273	mm	4-0.2604	mm	5-0.0797	mm	6	0.0681	mm	7-0.4612	mm
8	0.2674	mm	9-0.0449	mm	10-0.0266	mm	11-1.2808	mm	12-0.2939	mm	13-0.5883		mm	14-0.5532	mm
15-0.0543		mm	16-0.4119	mm	17	0.5506	mm	[illegible]	-0.079	mm	19-0.8632		mm	20 -0.798	mm
21-0.0351		mm	22	5.55	MPa	23	60.7	ms	24	47.2	ms	25 -202.3	ms	26 -202.4	ms
27	1341	KPa	28	40.398	KPa	29	1266	KPa	30	1.1	cm	31	19.5	dC	

Scan #239
20:19:58:47

1	2.745	lpm	2-0.1735	mm	3-0.1276	mm	4-0.2604	mm	5-0.0797	mm	6	0.0675	mm	7-0.4612	mm
8	0.2671	mm	9-0.0449	mm	10-0.0269	mm	11-1.2707	mm	12 -0.298	mm	13-0.5883		mm	14 -0.537	mm
15-0.0543		mm	16-0.4125	mm	17	0.5506	mm	18-0.6796	mm	19-0.8638	mm	20-0.7974		mm	21-0.0351	mm
22	5.55	MPa	23	60.7	ms	24	47.2	ms	25 -202.3	ms	26 -202.4	ms	27	1341	KPa
28	40.572	KPa	29	1266	KPa	30	1.1	cm	31	19.5	dC				

**STRENGTH AND PERMEABILITY TESTS ON ULTRA-LARGE
**STRIPA GRANITE CORE (Engineering Units Data)
**20:18:36 - 20:55:05
**Loading from 5.55 MPa to failure at 7.5 MPa peak axial stress
Scan #240
**Initial conditions:
20:20:18:36

1	0	lpm	2-0.1742	mm	3-0.1276	mm	4-0.2607	mm	5-0.0793	mm	6	0.0675	mm	7-0.4626	mm
8	0.2677	mm	9-0.0449	mm	10-0.0266	mm	11-1.2877	mm	12-0.2973	mm	13-0.5927		mm	14-0.5408	mm
15-0.0543		mm	16-0.4125	mm	17	0.55	mm	18-0.6796	mm	19-0.8644	mm	20 -0.798		mm	21-0.0351	mm
22	5.55	MPa	23	60.7	ms	24	47.2	ms	25 -202.3	ms	26 -202.4	ms	27	1338	KPa
28	-1.535	KPa	29	1304	KPa	30	1.1	cm	31	21.9	dC				

Scan #241
**Resume loading:
20:20:19:24

1	0	lpm	2-0.1742	mm	3-0.1276	mm	4-0.2607	mm	5-0.0797	mm	6	0.0681	mm	7-0.4626	mm
8	0.268	mm	9-0.0449	mm	10-0.0266	mm	11-1.2821	mm	12 -0.298	mm	13-0.5927		mm	14-0.5308	mm
15-0.0543		mm	16-0.4119	mm	17	0.55	mm	18-0.6796	mm	19-0.8644	mm	20 -0.798		mm	21-0.0351	mm
22	5.55	MPa	23	60.7	ms	24	47.2	ms	25 -202.3	ms	26 -206.9	ms	27	1338	KPa
28	-1.5	KPa	29	1304	KPa	30	1.1	cm	31	21.8	dC				

Scan #242
20:20:19:54

1	0	lpm	2-0.1742	mm	3-0.1279	mm	4 -0.261	mm	5-0.0797	mm	6	0.0681	mm	7-0.4643	mm
8	0.2687	mm	9-0.0452	mm	10-0.0269	mm	11-1.2846	mm	12-0.2258	mm	13-0.5883		mm	14 -0.504	mm
15-0.0549		mm	16-0.4125	mm	17	0.5506	mm	18-0.6827	mm	19-0.8571	mm	20-0.8006		mm	21-0.0351	mm
22	5.67	MPa	23	60.7	ms	24	50.7	ms	25 -202.3	ms	26 -209.1	ms	27	1338	KPa
28	-1.5	KPa	29	1303	KPa	30	1.1	cm	31	21.7	dC				

Scan #243
20:20:20:24

1	0	lpm	2-0.1769	mm	3-0.1295	mm	4-0.2622	mm	5-0.0797	mm	6	0.0687	mm	7-0.4704	mm
8	0.2733	mm	9-0.0455	mm	10-0.0269	mm	11-1.2858	mm	12-0.2865	mm	13-0.5915		mm	14 -0.509	mm
15-0.0543		mm	16-0.4131	mm	17	0.5631	mm	18-0.6901	mm	19-0.8754	mm	20-0.8062		mm	21-0.0354	mm
22	5.91	MPa	23	64.3	ms	24	53.9	ms	25 -205.7	ms	26 -212.3	ms	27	1337	KPa
28	-1.5	KPa	29	1302	KPa	30	1	cm	31	21.7	dC				

Scan #244
20:20:20:54

1	0	lpm	2-0.1806	mm	3 -0.131	mm	4-0.2644	mm	5 -0.08	mm	6	0.0699	mm	7 -0.482	mm
8	0.2817	mm	9-0.0462	mm	10-0.0269	mm	11-1.2739	mm	12-0.3113	mm	13-0.5934		mm	14-0.5258	mm
15-0.0543		mm	16-0.4143	mm	17	0.5839	mm	18 -0.7	mm	19 -0.903	mm	20-0.8144		mm	21-0.0361	mm
22	6.16	MPa	23	63.8	ms	24	57.4	ms	25 -212.4	ms	26 -222.3	ms	27	1336	KPa
28	-1.5	KPa	29	1301	KPa	30	1	cm	31	21.6	dC				

Scan #245
20:20:21:24

1 0 lpm	2-0.1853 mm	3-0.1326 mm	4-0.2668 mm	5-0.0803 mm	6 0.0718 mm	7-0.4981 mm	
8 0.2937 mm	9-0.0468 mm	10-0.0273 mm	11-1.2676 mm	12-0.3113 mm	13 -0.594 mm	14-0.5389 mm	
15-0.0543 mm	16-0.4166 mm	17 0.6119 mm	18-0.7104 mm	19 -0.925 mm	20-0.8219 mm	21-0.0364 mm	
22 6.42 MPa	23 64.3 ms	24 60.7 ms	25 -215.8 ms	26 -232.6 ms	27 1335 KPa	28 -1.5 KPa	
29 1300 KPa	30 1 cm	31 21.6 dC					

Scan #246
20:20:21:54

1 0 lpm	2-0.1911 mm	3-0.1348 mm	4-0.2693 mm	5-0.0806 mm	6 0.073 mm	7-0.5165 mm	
8 0.3076 mm	9-0.0471 mm	10-0.0273 mm	11-1.2701 mm	12-0.3159 mm	13 -0.594 mm	14 -0.532 mm	
15-0.0536 mm	16-0.4196 mm	17 0.6488 mm	18-0.7221 mm	19-0.9507 mm	20-0.8295 mm	21-0.0367 mm	
22 6.68 MPa	23 67.4 ms	24 60.7 ms	25 -219.2 ms	26 -239.3 ms	27 1334 KPa	28 -1.535 KPa	
29 1299 KPa	30 1 cm	31 21.6 dC					

Scan #247
20:20:22:24

1 0 lpm	2-0.2022 mm	3-0.1373 mm	4-0.2708 mm	5-0.0806 mm	6 0.0749 mm	7-0.5407 mm	
8 0.3283 mm	9-0.0474 mm	10-0.0273 mm	11-1.2726 mm	12-0.3131 mm	13 -0.594 mm	14-0.5121 mm	
15 -0.053 mm	16-0.4231 mm	17 0.7024 mm	18-0.7345 mm	19-0.9832 mm	20-0.8351 mm	21 -0.037 mm	
22 6.93 MPa	23 63.8 ms	24 64.2 ms	25 -222.5 ms	26 -249.3 ms	27 1333 KPa	28 -1.64 KPa	
29 1298 KPa	30 1 cm	31 21.5 dC					

Scan #248
20:20:22:54

1 0 lpm	2-0.2836 mm	3-0.1449 mm	4-0.2045 mm	5-0.0809 mm	6 0.0805 mm	7-0.6372 mm	
8 0.4322 mm	9-0.0468 mm	10-0.0256 mm	11-1.2694 mm	12-0.3135 mm	13 -0.594 mm	14-0.5233 mm	
15-0.0409 mm	16-0.4348 mm	17 0.9726 mm	18-0.7579 mm	19-1.0707 mm	20-0.8295 mm	21-0.0379 mm	
22 7.18 MPa	23 60.7 ms	24 70.9 ms	25 -215.8 ms	26 -272.5 ms	27 1335 KPa	28 -1.605 KPa	
29 1300 KPa	30 1.2 cm	31 21.2 dC					

Scan #249
20:20:23:24

1 0 lpm	2-0.3494 mm	3-0.1496 mm	4-0.1819 mm	5-0.0809 mm	6 0.0842 mm	7-0.7126 mm	
8 0.5105 mm	9-0.0465 mm	10 -0.024 mm	11-1.2638 mm	12-0.3063 mm	13 -0.594 mm	14-0.5451 mm	
15-0.0243 mm	16-0.4454 mm	17 1.2345 mm	18-0.7745 mm	19-1.1552 mm	20-0.8131 mm	21-0.0382 mm	
22 7.39 MPa	23 60.7 ms	24 74.2 ms	25 -209 ms	26 -293.3 ms	27 1336 KPa	28 -1.57 KPa	
29 1301 KPa	30 1.2 cm	31 21.2 dC					

Scan #250
20:20:23:54

1 0 lpm	2 -0.369 mm	3-0.1512 mm	4-0.1706 mm	5-0.0806 mm	6 0.0854 mm	7-0.7508 mm	
8 0.5748 mm	9-0.0462 mm	10-0.0231 mm	11-1.2657 mm	12-0.3147 mm	13 -0.594 mm	14-0.5582 mm	
15-0.0103 mm	16-0.4507 mm	17 1.3786 mm	18-0.7782 mm	19-1.1956 mm	20-0.7987 mm	21-0.0382 mm	
22 7.4 MPa	23 60.7 ms	24 74.2 ms	25 -209 ms	26 -300 ms	27 1337 KPa	28 -1.535 KPa	
29 1302 KPa	30 1.2 cm	31 21.2 dC					

Scan #251
20:20:24:24

1 0 lpm	2-0.3771 mm	3-0.1518 mm	4-0.1648 mm	5-0.0809 mm	6 0.086 mm	7-0.7723 mm	
8 0.5748 mm	9-0.0462 mm	10-0.0221 mm	11-1.2688 mm	12 -0.315 mm	13-0.5947 mm	14-0.5489 mm	
15 6.0E-4 mm	16-0.4536 mm	17 1.4619 mm	18-0.7794 mm	19-1.2176 mm	20-0.7886 mm	21-0.0382 mm	
22 7.39 MPa	23 60.7 ms	24 74.2 ms	25 -209 ms	26 -303.5 ms	27 1337 KPa	28 -1.535 KPa	
29 1302 KPa	30 1.2 cm	31 21.1 dC					

Scan #252
20:20:24:54

1 0 lpm	2-0.3815 mm	3-0.1525 mm	4-0.1617 mm	5-0.0806 mm	6 0.0854 mm	7-0.7863 mm	
8 0.5906 mm	9-0.0462 mm	10-0.0218 mm	11-1.2669 mm	12 -0.284 mm	13-0.5927 mm	14-0.5227 mm	
15 0.0089 mm	16 -0.456 mm	17 1.5179 mm	18-0.7801 mm	19-1.2299 mm	20-0.7823 mm	21-0.0379 mm	
22 7.39 MPa	23 57 ms	24 74.2 ms	25 -209 ms	26 -303.5 ms	27 1338 KPa	28 -1.535 KPa	
29 1303 KPa	30 1.3 cm	31 21.1 dC					

Scan #253
20:20:25:24

1	0	lpm	2	-0.3845	mm	3	-0.1528	mm	4	-0.1596	mm	5	-0.0806	mm	6	0.086	mm	7	-0.7979	mm			
8	0.6042	mm	9	-0.0458	mm	10	-0.0214	mm	11	-1.2739	mm	12	-0.2992	mm	13	-0.5934	mm	14	-0.527	mm			
15	0.0159	mm	16	-0.4572	mm	17	1.5625	mm	18	-0.7801	mm	19	-1.2397	mm	20	-0.7779	mm	21	-0.0379	mm			
22	7.39	MPa	23	57.6	ms	24	74.2	ms	25	-209	ms	26	-303.5	ms	27	1338	KPa	28	-1.5	KPa			
29	1303	KPa	30	1.3	cm	31	21	dC															

Scan #254
20:20:25:54

1	0	lpm	2	-0.3869	mm	3	-0.1531	mm	4	-0.1577	mm	5	-0.0806	mm	6	0.086	mm	7	-0.8074	mm			
8	0.6147	mm	9	-0.0458	mm	10	-0.0211	mm	11	-1.2745	mm	12	-0.3107	mm	13	-0.594	mm	14	-0.5588	mm			
15	0.021	mm	16	-0.4583	mm	17	1.5994	mm	18	-0.7801	mm	19	-1.2495	mm	20	-0.7742	mm	21	-0.0379	mm			
22	7.39	MPa	23	60.7	ms	24	70.7	ms	25	-209	ms	26	-303.5	ms	27	1338	KPa	28	-1.5	KPa			
29	1304	KPa	30	1.3	cm	31	21	dC															

Scan #255
20:20:26:24

1	0	lpm	2	-0.3889	mm	3	-0.1531	mm	4	-0.1562	mm	5	-0.0806	mm	6	0.086	mm	7	-0.8149	mm			
8	0.6234	mm	9	-0.0455	mm	10	-0.0208	mm	11	-1.2707	mm	12	-0.32	mm	13	-0.5947	mm	14	-0.5688	mm			
15	0.0261	mm	16	-0.4595	mm	17	1.625	mm	18	-0.7801	mm	19	-1.2574	mm	20	-0.7717	mm	21	-0.0379	mm			
22	7.39	MPa	23	57	ms	24	67.4	ms	25	-209	ms	26	-303.5	ms	27	1338	KPa	28	-1.535	KPa			
29	1304	KPa	30	1.3	cm	31	21	dC															

Scan #256
20:20:27:19

1	0	lpm	2	-0.3916	mm	3	-0.1534	mm	4	-0.1538	mm	5	-0.0806	mm	6	0.086	mm	7	-0.8258	mm			
8	0.636	mm	9	-0.0455	mm	10	-0.0208	mm	11	-1.2701	mm	12	-0.3085	mm	13	-0.594	mm	14	-0.557	mm			
15	0.0318	mm	16	-0.4607	mm	17	1.6685	mm	18	-0.7801	mm	19	-1.2666	mm	20	-0.7679	mm	21	-0.0379	mm			
22	7.39	MPa	23	59	ms	24	67.4	ms	25	-209	ms	26	-303.5	ms	27	1339	KPa	28	-1.535	KPa			
29	1304	KPa	30	1.3	cm	31	20.9	dC															

Scan #257
20:20:28:19

1	0	lpm	2	-0.3939	mm	3	-0.1537	mm	4	-0.1516	mm	5	-0.0806	mm	6	0.086	mm	7	-0.8368	mm			
8	0.6487	mm	9	-0.0455	mm	10	-0.0205	mm	11	-1.2631	mm	12	-0.3162	mm	13	-0.5947	mm	14	-0.5395	mm			
15	0.0382	mm	16	-0.4342	mm	17	1.7119	mm	18	-0.7801	mm	19	-1.277	mm	20	-0.7629	mm	21	-0.0376	mm			
22	7.4	MPa	23	60.7	ms	24	67.4	ms	25	-209	ms	26	-308.5	ms	27	1340	KPa	28	-1.535	KPa			
29	1305	KPa	30	1.3	cm	31	20.9	dC															

Scan #258
20:20:29:19

1	0	lpm	2	-0.3987	mm	3	-0.154	mm	4	-0.1486	mm	5	-0.0803	mm	6	0.086	mm	7	-0.8521	mm			
8	0.6673	mm	9	-0.0455	mm	10	-0.0201	mm	11	-1.2587	mm	12	-0.3196	mm	13	-0.594	mm	14	-0.5258	mm			
15	0.0522	mm	16	-0.4254	mm	17	1.7774	mm	18	-0.7801	mm	19	-1.2935	mm	20	-0.756	mm	21	-0.0376	mm			
22	7.39	MPa	23	55.5	ms	24	67.4	ms	25	-209	ms	26	-305.3	ms	27	1340	KPa	28	-1.5	KPa			
29	1305	KPa	30	1.3	cm	31	20.8	dC															

Scan #259
20:20:30:19

1	0	lpm	2	-0.4034	mm	3	-0.154	mm	4	-0.1449	mm	5	-0.08	mm	6	0.086	mm	7	-0.8743	mm			
8	0.696	mm	9	-0.0449	mm	10	-0.0198	mm	11	-1.2518	mm	12	-0.3175	mm	13	-0.5947	mm	14	-0.5383	mm			
15	0.0727	mm	16	-0.4231	mm	17	1.8548	mm	18	-0.7794	mm	19	-1.3131	mm	20	-0.7484	mm	21	-0.0376	mm			
22	7.39	MPa	23	53.9	ms	24	67.4	ms	25	-209	ms	26	-303.5	ms	27	1340	KPa	28	-1.535	KPa			
29	1305	KPa	30	1.3	cm	31	20.8	dC															

Scan #260
20:20:31:19

1	0	lpm	2	-0.3825	mm	3	-0.154	mm	4	-0.1406	mm	5	-0.0797	mm	6	0.086	mm	7	-0.9016	mm			
8	0.7322	mm	9	-0.044	mm	10	-0.0192	mm	11	-1.2594	mm	12	-0.3097	mm	13	-0.5947	mm	14	-0.5358	mm			
15	0.0988	mm	16	-0.4225	mm	17	1.9566	mm	18	-0.7776	mm	19	-1.3352	mm	20	-0.739	mm	21	-0.037	mm			
22	7.4	MPa	23	53.9	ms	24	67.4	ms	25	-209	ms	26	-303.5	ms	27	1341	KPa	28	-1.535	KPa			
29	1306	KPa	30	1.4	cm	31	20.7	dC															

```
Scan #261
20:20:32:19
    1       0 lpm    2-0.3757  mm    3-0.1543  mm    4-0.1366  mm    5-0.0793  mm    6  0.086  mm    7-0.9244  mm
    8 0.7625  mm     9-0.0433  mm   10-0.0188  mm   11-1.2524  mm   12-0.3169  mm   13-0.5947  mm   14-0.5283  mm
   15 0.1211  mm    16-0.4225  mm   17 2.0524  mm   18-0.7751  mm   19-1.3554  mm   20-0.7308  mm   21-0.0367  mm
   22    7.39 MPa   23    53.9  ms   24    67.4  ms   25    -209  ms   26 -303.5  ms   27    1341 KPa   28 -1.535 KPa
   29    1306 KPa   30     1.4  cm   31    20.7  dC
Scan #262
20:20:33:19
    1       0 lpm    2 -0.373  mm    3-0.1543  mm    4 -0.133  mm    5 -0.079  mm    6 0.0854  mm    7-0.9463  mm
    8 0.7922  mm     9-0.0424  mm   10-0.0185  mm   11-1.2531  mm   12-0.3162  mm   13-0.5947  mm   14-0.5364  mm
   15 0.1415  mm    16-0.4219  mm   17 2.1405  mm   18-0.7727  mm   19-1.3762  mm   20-0.7233  mm   21-0.0367  mm
   22     7.4 MPa   23    53.9  ms   24    62.3  ms   25    -209  ms   26 -303.5  ms   27    1341 KPa   28 -1.535 KPa
   29    1306 KPa   30     1.4  cm   31    20.6  dC
Scan #263
20:20:34:19
    1       0 lpm    2-0.3713  mm    3-0.1543  mm    4 -0.129  mm    5-0.0787  mm    6  0.086  mm    7-0.9626  mm
    8 0.8154  mm     9-0.0418  mm   10-0.0182  mm   11  -1.26  mm   12 -0.315  mm   13-0.5947  mm   14-0.5252  mm
   15   0.16  mm    16-0.4219  mm   17 2.2191  mm   18-0.7696  mm   19-1.3927  mm   20-0.7157  mm   21-0.0361  mm
   22     7.4 MPa   23    53.9  ms   24    60.7  ms   25    -209  ms   26 -303.5  ms   27    1341 KPa   28 -1.535 KPa
   29    1306 KPa   30     1.4  cm   31    20.5  dC
Scan #264
20:20:35:19
    1       0 lpm    2 -0.369  mm    3-0.1547  mm    4-0.1259  mm    5-0.0787  mm    6 0.0854  mm    7-0.9763  mm
    8 0.8342  mm     9-0.0415  mm   10-0.0182  mm   11-1.2575  mm   12-0.3135  mm   13-0.5947  mm   14-0.5245  mm
   15  0.176  mm    16-0.4219  mm   17 2.2976  mm   18-0.7677  mm   19-1.4056  mm   20-0.7107  mm   21-0.0361  mm
   22     7.4 MPa   23    53.9  ms   24    60.7  ms   25    -209  ms   26 -303.5  ms   27    1341 KPa   28 -1.535 KPa
   29    1306 KPa   30     1.5  cm   31    20.5  dC
Scan #265
20:20:36:19
    1       0 lpm    2 -0.368  mm    3-0.1547  mm    4-0.1232  mm    5-0.0784  mm    6 0.0854  mm    7-0.9882  mm
    8 0.8513  mm     9-0.0411  mm   10-0.0179  mm   11-1.2613  mm   12-0.2893  mm   13 -0.594  mm   14-0.5395  mm
   15 0.1907  mm    16-0.4219  mm   17 2.3673  mm   18-0.7646  mm   19 -1.416  mm   20-0.7063  mm   21-0.0357  mm
   22    7.39 MPa   23    53.9  ms   24    60.7  ms   25    -209  ms   26 -303.5  ms   27    1340 KPa   28 -1.535 KPa
   29    1305 KPa   30     1.4  cm   31    20.5  dC
Scan #266
**Monitor at 7.4 MPa axial stress:
20:20:45: 5
    1       0 lpm    2-0.3615  mm    3-0.1553  mm    4-0.0865  mm    5-0.0753  mm    6 0.0848  mm    7-1.1199  mm
    8 1.0708  mm     9 -0.038  mm   10 -0.015  mm   11 -1.272  mm   12 -0.302  mm   13-0.5959  mm   14-0.5744  mm
   15 0.4388  mm    16-0.4196  mm   17 3.4923  mm   18-0.7283  mm   19  -1.58  mm   20-0.3676  mm   21-0.0342  mm
   22    7.39 MPa   23    53.9  ms   24    54.1  ms   25 -215.6  ms   26    -297  ms   27    1322 KPa   28    -1.5 KPa
   29    1288 KPa   30     1.5  cm   31    20.1  dC
Scan #267
20:20:47: 5
    1       0 lpm    2-0.3619  mm    3 -0.155  mm    4-0.0813  mm    5-0.0747  mm    6 0.0848  mm    7-1.1359  mm
    8 1.1104  mm     9 -0.038  mm   10-0.0146  mm   11-1.2808  mm   12 -0.311  mm   13-0.5966  mm   14 -0.595  mm
   15 0.4726  mm    16 -0.419  mm   17 3.6602  mm   18-0.7215  mm   19-1.6002  mm   20-0.3312  mm   21-0.0342  mm
   22     7.4 MPa   23    53.9  ms   24    53.9  ms   25 -215.8  ms   26 -290.9  ms   27    1323 KPa   28    -1.5 KPa
   29    1288 KPa   30     1.5  cm   31    20.1  dC
Scan #268
20:20:49: 5
    1       0 lpm    2-0.3619  mm    3 -0.155  mm    4-0.0783  mm    5-0.0744  mm    6 0.0848  mm    7-1.1461  mm
    8 1.1339  mm     9 -0.038  mm   10-0.0146  mm   11-1.2808  mm   12-0.3172  mm   13-0.5966  mm   14-0.5869  mm
   15 0.4936  mm    16 -0.419  mm   17 3.7531  mm   18-0.7172  mm   19-1.6125  mm   20-0.3123  mm   21-0.0342  mm
   22     7.4 MPa   23      48  ms   24    53.9  ms   25 -215.8  ms   26    -290  ms   27    1323 KPa   28    -1.5 KPa
   29    1288 KPa   30     1.5  cm   31    20.1  dC
```

```
Scan #269
20:20:51: 5
    1      0 lpm    2-0.3622  mm    3 -0.155  mm    4-0.0761  mm    5-0.0741  mm    6 0.0848  mm    7 -1.154  mm
    8 1.1528  mm    9 -0.038  mm   10-0.0143  mm   11-1.2713  mm   12-0.3125  mm   13-0.5966  mm   14-0.5988  mm
   15 0.5096  mm   16 -0.419  mm   17 3.8304  mm   18-0.7135  mm   19-1.6223  mm   20-0.3017  mm   21-0.0339  mm
   22    7.4 MPa   23   47.2  ms   24   53.9  ms   25 -215.8  ms   26   -290  ms   27   1323 KPa   28   -1.5 KPa
   29   1289 KPa   30    1.5  cm   31   20.1  dC
Scan #270
20:20:53: 5
    1      0 lpm    2-0.3622  mm    3-0.1547  mm    4 -0.074  mm    5-0.0737  mm    6 0.0848  mm    7-1.1608  mm
    8 1.1695  mm    9 -0.038  mm   10-0.0143  mm   11-1.2802  mm   12-0.3268  mm   13-0.5972  mm   14-0.5713  mm
   15  0.523  mm   16 -0.419  mm   17 3.9043  mm   18-0.7098  mm   19-1.6308  mm   20-0.2954  mm   21-0.0339  mm
   22    7.4 MPa   23   47.2  ms   24   53.9  ms   25 -215.8  ms   26   -290  ms   27   1324 KPa   28   -1.5 KPa
   29   1289 KPa   30    1.5  cm   31     20  dC
Scan #271
20:20:55: 5
    1      0 lpm    2-0.3622  mm    3-0.1547  mm    4-0.0712  mm    5-0.0734  mm    6 0.0842  mm    7-1.1697  mm
    8  1.193  mm    9 -0.038  mm   10-0.0143  mm   11-1.2764  mm   12-0.3172  mm   13-0.5966  mm   14-0.5919  mm
   15 0.5396  mm   16 -0.419  mm   17 3.9793  mm   18-0.7055  mm   19  -1.64  mm   20-0.2941  mm   21-0.0336  mm
   22    7.4 MPa   23   47.2  ms   24   53.9  ms   25 -215.8  ms   26   -290  ms   27   1324 KPa   28   -1.5 KPa
   29   1289 KPa   30    1.5  cm   31     20  dC

**STRENGTH AND PERMEABILITY TESTS ON ULTRA-LARGE
**STRIPA GRANITE CORE (Engineering Units Data)
**21:08:49 - 21:12:49
**Permeability testing on failed sample
Scan #272
**Approximate steady flow at 10.3 KPa (1.5 psi) injection:
20:21: 8:49
    1  3.364 lpm    2-0.3649  mm    3-0.1525  mm    4-0.0599  mm    5-0.0722  mm    6 0.0842  mm    7-1.2034  mm
    8 1.2879  mm    9-0.0389  mm   10 -0.014  mm   11-1.2827  mm   12-0.3283  mm   13-0.5985  mm   14-0.5713  mm
   15 0.6065  mm   16-0.4184  mm   17 4.3203  mm   18 -0.679  mm   19-1.6816  mm   20-0.2797  mm   21-0.0333  mm
   22    7.4 MPa   23   47.2  ms   24   47.3  ms   25 -215.8  ms   26   -290  ms   27   1377 KPa   28  0.419 KPa
   29   1341 KPa   30    1.6  cm   31   20.1  dC
Scan #273
20:21:10:49
    1  3.313 lpm    2-0.3646  mm    3-0.1525  mm    4-0.0584  mm    5-0.0719  mm    6 0.0842  mm    7-1.2065  mm
    8 1.2953  mm    9-0.0393  mm   10 -0.014  mm   11-1.2884  mm   12-0.3354  mm   13-0.5991  mm   14-0.6081  mm
   15 0.6123  mm   16-0.4184  mm   17 4.3507  mm   18-0.6765  mm   19-1.6853  mm   20-0.2797  mm   21 -0.033  mm
   22    7.4 MPa   23   47.2  ms   24   47.2  ms   25 -209.9  ms   26   -290  ms   27   1365 KPa   28  0.349 KPa
   29   1330 KPa   30    1.6  cm   31   20.1  dC
Scan #274
20:21:12:49
    1  0.009 lpm    2-0.3646  mm    3-0.1525  mm    4-0.0575  mm    5-0.0719  mm    6 0.0842  mm    7-1.2106  mm
    8 1.3027  mm    9-0.0393  mm   10 -0.014  mm   11-1.2758  mm   12-0.3234  mm   13-0.5985  mm   14-0.5994  mm
   15  0.618  mm   16-0.4178  mm   17 4.3817  mm   18-0.6747  mm   19-1.6902  mm   20 -0.279  mm   21 -0.033  mm
   22   7.42 MPa   23   47.2  ms   24   47.2  ms   25   -215  ms   26   -290  ms   27   1326 KPa   28 -1.151 KPa
   29   1292 KPa   30    1.6  cm   31   20.1  dC

**STRENGTH AND PERMEABILITY TESTS ON ULTRA-LARGE
**STRIPA GRANITE CORE (Engineering Units Data)
**12:19:50 - 21:42:31
**Sample unloading
```

Scan #275
**Monitor at 7.4 MPa axial load:
20:21:19:50

1 0 lpm	2-0.3646 mm	3-0.1525 mm	4-0.0538 mm	5-0.0716 mm	6 0.0842 mm	7-1.2219 mm
8 1.3259 mm	9-0.0396 mm	10 -0.014 mm	11-1.2625 mm	12-0.3069 mm	13-0.5908 mm	1411.0768 mm
15 0.6359 mm	16-0.4178 mm	17 4.4733 mm	18-0.6692 mm	19-1.7031 mm	20-0.2778 mm	21 -0.033 mm
22 7.4 MPa	23 47.2 ms	24 47.2 ms	25 -209.2 ms	26 -283.5 ms	27 1330 KPa	28 -1.395 KPa
29 1295 KPa	30 1.6 cm	31 20.1 dC				

Scan #276
20:21:20:20

1 0 lpm	2-0.3639 mm	3-0.1525 mm	4-0.0535 mm	5-0.0716 mm	6 0.0842 mm	7-1.2225 mm
8 1.3275 mm	9-0.0396 mm	10 -0.014 mm	11 -1.26 mm	12-0.3073 mm	13-0.5902 mm	1411.5339 mm
15 0.6372 mm	16-0.4178 mm	17 4.4775 mm	18-0.6685 mm	19-1.7043 mm	20-0.2778 mm	21-0.0326 mm
22 7.4 MPa	23 47.2 ms	24 47.2 ms	25 -209 ms	26 -283.3 ms	27 1330 KPa	28 -1.361 KPa
29 1295 KPa	30 1.6 cm	31 20.1 dC				

Scan #277
20:21:20:50

1 0 lpm	2-0.3639 mm	3-0.1525 mm	4-0.0532 mm	5-0.0716 mm	6 0.0842 mm	7-1.2236 mm
8 1.3287 mm	9-0.0396 mm	10 -0.014 mm	11-1.2581 mm	12-0.3122 mm	13-0.5902 mm	1411.6094 mm
15 0.6384 mm	16-0.4178 mm	17 4.4817 mm	18-0.6679 mm	19-1.7049 mm	20-0.2778 mm	21 -0.033 mm
22 7.4 MPa	23 47.2 ms	24 47.2 ms	25 -209 ms	26 -283.3 ms	27 1330 KPa	28 -1.395 KPa
29 1295 KPa	30 1.6 cm	31 20.1 dC				

Scan #278
20:21:21:20

1 0 lpm	2-0.3639 mm	3-0.1525 mm	4-0.0529 mm	5-0.0716 mm	6 0.0842 mm	7-1.2239 mm
8 1.3303 mm	9-0.0396 mm	10-0.0137 mm	11-1.2531 mm	12-0.3104 mm	13-0.5908 mm	1411.6593 mm
15 0.6397 mm	16-0.4184 mm	17 4.4846 mm	18-0.6679 mm	19-1.7055 mm	20-0.2778 mm	21-0.0326 mm
22 7.4 MPa	23 47.2 ms	24 47.2 ms	25 -209 ms	26 -283.3 ms	27 1330 KPa	28 -1.361 KPa
29 1295 KPa	30 1.6 cm	31 20.1 dC				

Scan #279
20:21:21:50

1 0 lpm	2-0.3639 mm	3-0.1528 mm	4-0.0529 mm	5-0.0716 mm	6 0.0842 mm	7-1.2253 mm
8 1.3318 mm	9-0.0396 mm	10-0.0137 mm	11-1.2543 mm	12-0.3066 mm	13-0.5908 mm	1411.7466 mm
15 0.641 mm	16-0.4184 mm	17 4.4906 mm	18-0.6673 mm	19-1.7086 mm	20-0.2778 mm	21-0.0326 mm
22 7.49 MPa	23 47.2 ms	24 47.2 ms	25 -212.4 ms	26 -283.3 ms	27 1330 KPa	28 -1.326 KPa
29 1295 KPa	30 1.6 cm	31 20.1 dC				

Scan #280
**Peak axial stress of 7.5 MPa:
20:21:22:20

1 0 lpm	2-0.3656 mm	3-0.1531 mm	4-0.0523 mm	5-0.0713 mm	6 0.0842 mm	7-1.2294 mm
8 1.3355 mm	9-0.0396 mm	10 -0.014 mm	11-1.2537 mm	12-0.3069 mm	13-0.5908 mm	1411.7029 mm
15 0.6435 mm	16-0.4178 mm	17 4.5025 mm	18-0.6673 mm	19-1.7123 mm	20-0.2778 mm	21-0.0326 mm
22 7.5 MPa	23 47.2 ms	24 47.2 ms	25 -212.4 ms	26 -286.5 ms	27 1330 KPa	28 -1.361 KPa
29 1295 KPa	30 1.6 cm	31 20.1 dC				

Scan #281
20:21:22:50

1 0 lpm	2-0.3663 mm	3-0.1531 mm	4 -0.052 mm	5-0.0716 mm	6 0.0842 mm	7-1.2314 mm
8 1.3383 mm	9-0.0399 mm	10-0.0137 mm	11-1.2568 mm	12-0.3042 mm	13-0.5902 mm	1411.6717 mm
15 0.6454 mm	16-0.4178 mm	17 4.5132 mm	18-0.6679 mm	19-1.7147 mm	20-0.2778 mm	21-0.0326 mm
22 7.5 MPa	23 47.2 ms	24 47.2 ms	25 -209 ms	26 -290 ms	27 1330 KPa	28 -1.395 KPa
29 1295 KPa	30 1.6 cm	31 20.1 dC				

Scan #282
**Begin unloading:
20:21:25: 1

1 0 lpm	2-0.3666 mm	3-0.1531 mm	4-0.0508 mm	5-0.0713 mm	6 0.0842 mm	7-1.2355 mm
8 1.346 mm	9-0.0399 mm	10-0.0137 mm	11-1.2631 mm	12-0.2946 mm	13-0.5908 mm	1411.7347 mm
15 0.6525 mm	16-0.4178 mm	17 4.5406 mm	18-0.6648 mm	19-1.7196 mm	20-0.2746 mm	21-0.0326 mm
22 7.37 MPa	23 47.2 ms	24 47.2 ms	25 -209 ms	26 -284.1 ms	27 1327 KPa	28 -1.047 KPa
29 1293 KPa	30 1.6 cm	31 20.1 dC				

Scan #283
20:21:25:31

1	0	lpm	2	-0.3649	mm	3	-0.1515	mm	4	-0.0502	mm	5	-0.0713	mm	6	0.0842	mm	7	-1.2277	mm
8	1.3457	mm	9	-0.0399	mm	10	-0.0133	mm	11	-1.2594	mm	12	-0.2933	mm	13	-0.5908	mm	14	11.6705	mm
15	0.6525	mm	16	-0.4172	mm	17	4.543	mm	18	-0.6599	mm	19	-1.7147	mm	20	-0.2709	mm	21	-0.0323	mm
22	7.22	MPa	23	47.2	ms	24	43.7	ms	25	-205.7	ms	26	-280	ms	27	1328	KPa	28	-1.186	KPa
29	1293	KPa	30	1.7	cm	31	20.1	dC												

Scan #284
20:21:26: 1

1	0	lpm	2	-0.3619	mm	3	-0.1506	mm	4	-0.0[illegible]	mm	5	-0.0709	mm	6	0.0836	mm	7	-1.2181	mm
8	1.3451	mm	9	-0.0393	mm	10	-0.013	mm	11	-1.2556	mm	12	-0.2874	mm	13	-0.5908	mm	14	11.6112	mm
15	0.6525	mm	16	-0.416	mm	17	4.543	mm	18	-0.6519	mm	19	-1.7043	mm	20	-0.2652	mm	21	-0.0295	mm
22	6.95	MPa	23	43.5	ms	24	40.4	ms	25	-205.7	ms	26	-273.3	ms	27	1329	KPa	28	-1.361	KPa
29	1294	KPa	30	1.7	cm	31	20.1	dC												

Scan #285
20:21:26:31

1	0	lpm	2	-0.3551	mm	3	-0.149	mm	4	-0.0483	mm	5	-0.0706	mm	6	0.083	mm	7	-1.2079	mm
8	1.3435	mm	9	-0.0389	mm	10	-0.0127	mm	11	-1.2524	mm	12	-0.1032	mm	13	-0.562	mm	14	11.6867	mm
15	0.6531	mm	16	-0.4149	mm	17	4.543	mm	18	-0.6439	mm	19	-1.6872	mm	20	-0.2589	mm	21	-0.0274	mm
22	6.7	MPa	23	40.4	ms	24	40.4	ms	25	-209	ms	26	-266.6	ms	27	1330	KPa	28	-1.395	KPa
29	1295	KPa	30	1.8	cm	31	20	dC												

Scan #286
20:21:27: 1

1	0	lpm	2	-0.3497	mm	3	-0.1477	mm	4	-0.0474	mm	5	-0.0703	mm	6	0.0823	mm	7	-1.1973	mm
8	1.3414	mm	9	-0.0383	mm	10	-0.012	mm	11	-1.2505	mm	12	-0.0353	mm	13	-0.5511	mm	14	11.711	mm
15	0.6525	mm	16	-0.4137	mm	17	4.543	mm	18	-0.6359	mm	19	-1.6706	mm	20	-0.2526	mm	21	-0.0267	mm
22	6.44	MPa	23	36.8	ms	24	36.9	ms	25	-205.7	ms	26	-259.8	ms	27	1331	KPa	28	-1.43	KPa
29	1297	KPa	30	1.8	cm	31	20	dC												

Scan #287
20:21:27:31

1	0	lpm	2	-0.3443	mm	3	-0.1465	mm	4	-0.0468	mm	5	-0.07	mm	6	0.0823	mm	7	-1.1864	mm
8	1.3389	mm	9	-0.0377	mm	10	-0.0114	mm	11	-1.2575	mm	12	-0.0329	mm	13	-0.5517	mm	14	11.7746	mm
15	0.6525	mm	16	-0.4125	mm	17	4.543	mm	18	-0.6285	mm	19	-1.6572	mm	20	-0.2464	mm	21	-0.0264	mm
22	6.18	MPa	23	33.7	ms	24	33.7	ms	25	-199	ms	26	-253.1	ms	27	1333	KPa	28	-1.43	KPa
29	1298	KPa	30	1.9	cm	31	20	dC												

Scan #288
20:21:28: 1

1	0	lpm	2	-0.3386	mm	3	-0.1449	mm	4	-0.0456	mm	5	-0.0697	mm	6	0.0817	mm	7	-1.1748	mm
8	1.3358	mm	9	-0.0371	mm	10	-0.0107	mm	11	-1.2619	mm	12	-0.0307	mm	13	-0.5511	mm	14	11.7965	mm
15	0.6525	mm	16	-0.4113	mm	17	4.5424	mm	18	-0.6199	mm	19	-1.6437	mm	20	-0.2407	mm	21	-0.0261	mm
22	5.92	MPa	23	33.7	ms	24	33.7	ms	25	-192.2	ms	26	-246.3	ms	27	1334	KPa	28	-1.43	KPa
29	1299	KPa	30	2	cm	31	20	dC												

Scan #289
20:21:28:31

1	0	lpm	2	-0.3322	mm	3	-0.1436	mm	4	-0.045	mm	5	-0.0697	mm	6	0.0811	mm	7	-1.1625	mm
8	1.3327	mm	9	-0.0364	mm	10	-0.0104	mm	11	-1.2606	mm	12	-0.0298	mm	13	-0.5504	mm	14	11.8476	mm
15	0.6525	mm	16	-0.4096	mm	17	4.54	mm	18	-0.6112	mm	19	-1.6296	mm	20	-0.2338	mm	21	-0.0255	mm
22	5.66	MPa	23	33.7	ms	24	33.7	ms	25	-185.5	ms	26	-236.3	ms	27	1336	KPa	28	-1.43	KPa
29	1301	KPa	30	2	cm	31	20	dC												

Scan #290
20:21:29: 1

1	0	lpm	2	-0.3258	mm	3	-0.1421	mm	4	-0.0444	mm	5	-0.0694	mm	6	0.0805	mm	7	-1.1499	mm
8	1.329	mm	9	-0.0358	mm	10	-0.0098	mm	11	-1.2613	mm	12	-0.0292	mm	13	-0.5498	mm	14	11.7319	mm
15	0.6525	mm	16	-0.4078	mm	17	4.5352	mm	18	-0.6026	mm	19	-1.6149	mm	20	-0.2275	mm	21	-0.0252	mm
22	5.41	MPa	23	33.7	ms	24	33.7	ms	25	-178.7	ms	26	-226.1	ms	27	1337	KPa	28	-1.43	KPa
29	1302	KPa	30	2.1	cm	31	20	dC												

Scan #291
20:21:29:31

1 0 lpm	2-0.3187 mm	3-0.1405 mm	4-0.0434 mm	5-0.0691 mm	6 0.0799 mm	7-1.1369 mm	
8 1.325 mm	9-0.0349 mm	10-0.0091 mm	11-1.2568 mm	12-0.0285 mm	13-0.5485 mm	1410.0827 mm	
15 0.6518 mm	16-0.4066 mm	17 4.5287 mm	18 -0.594 mm	19-1.5996 mm	20-0.2212 mm	21-0.0246 mm	
22 5.16 MPa	23 33.7 ms	24 30.2 ms	25 -172 ms	26 -219.3 ms	27 1339 KPa	28 -1.43 KPa	
29 1304 KPa	30 2.1 cm	31 20 dC					

Scan #292
20:21:30: 1

1 0 lpm	2-0.3106 mm	3-0.1389 mm	4-0.0428 mm	5-0.0691 mm	6 0.0792 mm	7-1.1233 mm	
8 1.321 mm	9-0.0342 mm	10-0.0085 mm	11-1.2568 mm	12-0.0273 mm	13-0.5479 mm	14 9.9592 mm	
15 0.6518 mm	16-0.4049 mm	17 4.5198 mm	18-0.5854 mm	19-1.5843 mm	20-0.2143 mm	21-0.0243 mm	
22 4.9 MPa	23 33.7 ms	24 26.9 ms	25 -165.2 ms	26 -212.6 ms	27 1340 KPa	28 -1.43 KPa	
29 1305 KPa	30 2.2 cm	31 20 dC					

Scan #293
20:21:30:31

1 0 lpm	2-0.3021 mm	3-0.1373 mm	4-0.0422 mm	5-0.0685 mm	6 0.078 mm	7 -1.109 mm	
8 1.317 mm	9-0.0336 mm	10-0.0081 mm	11-1.2499 mm	12-0.0257 mm	13-0.5472 mm	14 9.9305 mm	
15 0.6512 mm	16-0.4031 mm	17 4.5067 mm	18-0.5761 mm	19-1.5672 mm	20-0.2074 mm	21-0.0239 mm	
22 4.64 MPa	23 33.7 ms	24 26.9 ms	25 -158.5 ms	26 -202.6 ms	27 1342 KPa	28 -1.465 KPa	
29 1307 KPa	30 2.3 cm	31 20 dC					

Scan #294
20:21:31: 1

1 0 lpm	2-0.2927 mm	3-0.1358 mm	4-0.0416 mm	5-0.0685 mm	6 0.0774 mm	7-1.0936 mm	
8 1.3129 mm	9-0.0327 mm	10-0.0075 mm	11-1.2505 mm	12-0.0245 mm	13-0.5466 mm	14 9.9068 mm	
15 0.6499 mm	16-0.4008 mm	17 4.4888 mm	18-0.5669 mm	19-1.5494 mm	20-0.1999 mm	21-0.0233 mm	
22 4.39 MPa	23 33.7 ms	24 26.9 ms	25 -151.7 ms	26 -192.4 ms	27 1344 KPa	28 -1.465 KPa	
29 1308 KPa	30 2.3 cm	31 20 dC					

Scan #295
20:21:31:31

1 0 lpm	2-0.2826 mm	3-0.1339 mm	4-0.0413 mm	5-0.0681 mm	6 0.0761 mm	7-1.0776 mm	
8 1.308 mm	9-0.0317 mm	10-0.0068 mm	11-1.2499 mm	12-0.0242 mm	13 -0.546 mm	14 9.9087 mm	
15 0.6493 mm	16 -0.399 mm	17 4.4721 mm	18 -0.557 mm	19-1.5311 mm	20-0.1929 mm	21 -0.023 mm	
22 4.13 MPa	23 33.7 ms	24 23.4 ms	25 -145 ms	26 -185.6 ms	27 1345 KPa	28 -1.465 KPa	
29 1310 KPa	30 2.4 cm	31 20 dC					

Scan #296
20:21:32: 1

1 0 lpm	2-0.2714 mm	3 -0.132 mm	4 -0.041 mm	5-0.0681 mm	6 0.0749 mm	7-1.0605 mm	
8 1.3027 mm	9-0.0311 mm	10-0.0065 mm	11-1.2562 mm	12-0.0242 mm	13-0.5453 mm	14 9.9168 mm	
15 0.648 mm	16-0.3966 mm	17 4.4525 mm	18-0.5459 mm	19-1.5115 mm	20-0.1854 mm	21-0.0224 mm	
22 3.87 MPa	23 33.7 ms	24 20.2 ms	25 -138.3 ms	26 -175.6 ms	27 1347 KPa	28 -1.43 KPa	
29 1311 KPa	30 2.5 cm	31 20 dC					

Scan #297
20:21:32:31

1 0 lpm	2-0.2603 mm	3-0.1301 mm	4-0.0407 mm	5-0.0678 mm	6 0.0743 mm	7-1.0421 mm	
8 1.2969 mm	9-0.0302 mm	10-0.0059 mm	11-1.2537 mm	12 -0.023 mm	13-0.5447 mm	14 9.8862 mm	
15 0.6454 mm	16-0.3943 mm	17 4.4328 mm	18-0.5348 mm	19-1.4894 mm	20-0.1791 mm	21-0.0221 mm	
22 3.62 MPa	23 33.7 ms	24 20.2 ms	25 -131.5 ms	26 -165.4 ms	27 1348 KPa	28 -1.395 KPa	
29 1313 KPa	30 2.6 cm	31 20 dC					

Scan #298
20:21:33: 1

1 0 lpm	2-0.2481 mm	3-0.1279 mm	4-0.0404 mm	5-0.0678 mm	6 0.073 mm	7-1.0233 mm	
8 1.2907 mm	9-0.0292 mm	10-0.0052 mm	11 -1.255 mm	12-0.0227 mm	13-0.5447 mm	14 9.8706 mm	
15 0.6416 mm	16-0.3914 mm	17 4.4096 mm	18-0.5237 mm	19-1.4674 mm	20-0.1735 mm	21-0.0218 mm	
22 3.38 MPa	23 33.7 ms	24 20.2 ms	25 -124.8 ms	26 -158.6 ms	27 1349 KPa	28 -1.43 KPa	
29 1314 KPa	30 2.7 cm	31 20 dC					

Scan #299
20:21:33:31

1 0 lpm	2-0.2367 mm	3 -0.126 mm	4-0.0404 mm	5-0.0675 mm	6 0.0718 mm	7-1.0053 mm	
8 1.2839 mm	9-0.0283 mm	10-0.0046 mm	11-1.2531 mm	12-0.0214 mm	13 -0.544 mm	14 9.8026 mm	
15 0.6378 mm	16 -0.389 mm	17 4.3846 mm	18-0.5127 mm	19 -1.446 mm	20-0.1678 mm	21-0.0212 mm	
22 3.15 MPa	23 30.1 ms	24 16.7 ms	25 -118 ms	26 -148.6 ms	27 1350 KPa	28 -1.43 KPa	
29 1315 KPa	30 2.8 cm	31 20 dC					

Scan #300
20:21:34: 1

1 0 lpm	2-0.2245 mm	3-0.1238 mm	4-0.0401 mm	5-0.0672 mm	6 0.0706 mm	7-0.9862 mm	
8 1.2768 mm	9-0.0277 mm	10-0.0039 mm	11-1.2518 mm	12-0.0211 mm	13-0.5434 mm	14 9.7534 mm	
15 0.6327 mm	16-0.3861 mm	17 4.3596 mm	18 -0.501 mm	19-1.4233 mm	20-0.1622 mm	21-0.0208 mm	
22 2.92 MPa	23 27 ms	24 13.5 ms	25 -111.3 ms	26 -138.4 ms	27 1351 KPa	28 -1.43 KPa	
29 1316 KPa	30 2.9 cm	31 20 dC					

Scan #301
20:21:34:31

1 0 lpm	2 -0.212 mm	3-0.1219 mm	4-0.0401 mm	5-0.0669 mm	6 0.0693 mm	7-0.9654 mm	
8 1.269 mm	9 -0.027 mm	10-0.0033 mm	11-1.2486 mm	12-0.0223 mm	13 -0.544 mm	14 8.4923 mm	
15 0.6263 mm	16-0.3831 mm	17 4.3281 mm	18-0.4886 mm	19-1.3976 mm	20-0.1578 mm	21-0.0205 mm	
22 2.69 MPa	23 30.6 ms	24 13.5 ms	25 -104.5 ms	26 -128.4 ms	27 1352 KPa	28 -1.43 KPa	
29 1316 KPa	30 3 cm	31 20 dC					

Scan #302
20:21:35: 1

1 0 lpm	2-0.1989 mm	3-0.1194 mm	4-0.0398 mm	5-0.0663 mm	6 0.0681 mm	7-0.9432 mm	
8 1.2594 mm	9-0.0264 mm	10-0.0026 mm	11-1.2461 mm	12-0.0223 mm	13 -0.544 mm	14 7.8493 mm	
15 0.6187 mm	16-0.3796 mm	17 4.2906 mm	18-0.4757 mm	19-1.3701 mm	20-0.1534 mm	21-0.0199 mm	
22 2.46 MPa	23 30.1 ms	24 13.5 ms	25 -97.7 ms	26 -118.2 ms	27 1353 KPa	28 -1.43 KPa	
29 1317 KPa	30 3.2 cm	31 20 dC					

Scan #303
20:21:35:31

1 0 lpm	2 -0.185 mm	3-0.1169 mm	4-0.0395 mm	5-0.0657 mm	6 0.0662 mm	7 -0.919 mm	
8 1.2468 mm	9-0.0258 mm	10 -0.002 mm	11-1.2442 mm	12-0.0214 mm	13-0.5434 mm	14 7.7683 mm	
15 0.6091 mm	16-0.3755 mm	17 4.2513 mm	18-0.4609 mm	19-1.3388 mm	20-0.1496 mm	21-0.0196 mm	
22 2.23 MPa	23 27 ms	24 13.5 ms	25 -91 ms	26 -108.2 ms	27 1353 KPa	28 -1.43 KPa	
29 1317 KPa	30 3.3 cm	31 19.9 dC					

Scan #304
20:21:36: 1

1 0 lpm	2-0.1712 mm	3 -0.114 mm	4-0.0395 mm	5-0.0647 mm	6 0.0644 mm	7 -0.892 mm	
8 1.2301 mm	9-0.0251 mm	10-0.0017 mm	11-1.2455 mm	12-0.0205 mm	13-0.5428 mm	14 7.7539 mm	
15 0.597 mm	16-0.3714 mm	17 4.2007 mm	18-0.4455 mm	19-1.3046 mm	20-0.1477 mm	21-0.0193 mm	
22 2 MPa	23 27 ms	24 10 ms	25 -84.3 ms	26 -94.7 ms	27 1353 KPa	28 -1.43 KPa	
29 1317 KPa	30 3.4 cm	31 20 dC					

Scan #305
20:21:36:31

1 0 lpm	2-0.1567 mm	3-0.1106 mm	4-0.0389 mm	5-0.0638 mm	6 0.0625 mm	7-0.8613 mm	
8 1.2069 mm	9-0.0245 mm	10-1.0E-3 mm	11-1.2524 mm	12-0.0192 mm	13-0.5421 mm	14 7.7695 mm	
15 0.5829 mm	16-0.3667 mm	17 4.1346 mm	18-0.4282 mm	19-1.2648 mm	20-0.1471 mm	21-0.0187 mm	
22 1.78 MPa	23 27 ms	24 10.2 ms	25 -77.6 ms	26 -84.5 ms	27 1353 KPa	28 -1.395 KPa	
29 1317 KPa	30 3.6 cm	31 20 dC					

Scan #306
20:21:37: 1

1 0 lpm	2-0.1432 mm	3-0.1065 mm	4-0.0385 mm	5-0.0616 mm	6 0.06 mm	7-0.8272 mm	
8 1.1784 mm	9-0.0239 mm	10-4.0E-4 mm	11-1.2562 mm	12-0.0189 mm	13-0.5421 mm	14 7.7976 mm	
15 0.5644 mm	16-0.3608 mm	17 4.0513 mm	18-0.4079 mm	19-1.2195 mm	20-0.1471 mm	21-0.0181 mm	
22 1.55 MPa	23 27 ms	24 10 ms	25 -70.8 ms	26 -74.5 ms	27 1352 KPa	28 -1.326 KPa	
29 1317 KPa	30 3.7 cm	31 20 dC					

```
Scan #307
20:21:37:31
    1       0 lpm    2 -0.131  mm    3-0.1018  mm    4-0.0376  mm    5-0.0585  mm    6 0.0569  mm    7-0.7883  mm
    8 1.1438  mm    9-0.0233  mm   10 3.0E-4  mm   11-1.2556  mm   12-0.0177  mm   13-0.5415  mm   14 7.8188  mm
   15 0.5434  mm   16-0.3532  mm   17 3.9584  mm   18-0.3839  mm   19-1.1656  mm   20-0.1477  mm   21-0.0171  mm
   22    1.32 MPa   23      27  ms   24    10.2  ms   25  -64.1  ms   26     -61  ms   27    1351 KPa   28 -1.151 KPa
   29    1316 KPa   30     3.9  cm   31    19.9  dC
Scan #308
20:21:38: 1
    1       0 lpm    2-0.1195  mm    3-0.0955  mm    4-0.0364  mm    5-0.0542  mm    6 0.0532  mm    7-0.7419  mm
    8 1.1011  mm    9-0.0229  mm   10 9.0E-4  mm   11 -1.255  mm   12 -0.018  mm   13-0.5415  mm   14 7.8231  mm
   15 0.5192  mm   16-0.3426  mm   17 3.8477  mm   18-0.3531  mm   19-1.1019  mm   20 -0.149  mm   21-0.0162  mm
   22    1.06 MPa   23      27  ms   24    13.5  ms   25  -57.3  ms   26   -50.7  ms   27    1350 KPa   28 -1.116 KPa
   29    1314 KPa   30     4.1  cm   31    19.9  dC
Scan #309
20:21:38:31
    1       0 lpm    2-0.1104  mm    3-0.0863  mm    4-0.0346  mm    5-0.0461  mm    6 0.0495  mm    7-0.6826  mm
    8  1.047  mm    9 -0.022  mm   10 0.0016  mm   11-1.2518  mm   12-0.0171  mm   13-0.5408  mm   14 7.8188  mm
   15 0.4911  mm   16 -0.325  mm   17  3.706  mm   18-0.3075  mm   19-1.0211  mm   20-0.1508  mm   21-0.0149  mm
   22    0.77 MPa   23      27  ms   24     10  ms   25  -47.2  ms   26   -40.7  ms   27    1346 KPa   28 -1.047 KPa
   29    1311 KPa   30     4.8  cm   31     20  dC
Scan #310
20:21:39: 1
    1       0 lpm    2-0.1037  mm    3-0.0722  mm    4  -0.03  mm    5-0.0296  mm    6  0.047  mm    7-0.6065  mm
    8 0.9814  mm    9-0.0198  mm   10 0.0022  mm   11-1.2505  mm   12-0.0155  mm   13-0.5402  mm   14 7.8287  mm
   15 0.4586  mm   16-0.2968  mm   17 3.5471  mm   18-0.2373  mm   19-0.9146  mm   20-0.1502  mm   21-0.0125  mm
   22    0.47 MPa   23      27  ms   24     6.7  ms   25  -37.1  ms   26   -27.2  ms   27    1340 KPa   28 -1.012 KPa
   29    1305 KPa   30     5.9  cm   31    19.9  dC
Scan #311
20:21:39:31
    1       0 lpm    2-0.0949  mm    3-0.0545  mm    4-0.0193  mm    5 0.0087  mm    6 0.0483  mm    7-0.5107  mm
    8 0.9029  mm    9-0.0164  mm   10 0.0029  mm   11-1.2499  mm   12-0.0149  mm   13-0.5402  mm   14 7.8431  mm
   15 0.4273  mm   16-0.2451  mm   17 3.3763  mm   18-0.1227  mm   19-0.7714  mm   20-0.1119  mm   21 -0.009  mm
   22    0.21 MPa   23    23.3  ms   24     6.7  ms   25  -23.6  ms   26   -13.8  ms   27    1326 KPa   28 -0.977 KPa
   29    1291 KPa   30     9.8  cm   31    19.9  dC
Scan #312
**End load record.
20:21:40: 1
    1       0 lpm    2-0.0834  mm    3-0.0451  mm    4-0.0065  mm    5 0.0279  mm    6 0.0718  mm    7-0.3957  mm
    8 0.8871  mm    9 -0.012  mm   10 0.0038  mm   11-1.2512  mm   12-0.0146  mm   13-0.5396  mm   14 7.8512  mm
   15  0.419  mm   16-0.1311  mm   17 3.2965  mm   18 0.0073  mm   19-0.6079  mm   20-0.0107  mm   21 -0.005  mm
   22    0.02 MPa   23    20.2  ms   24    10.2  ms   25   -6.8  ms   26    -6.8  ms   27    1311 KPa   28 -1.047 KPa
   29    1276 KPa   30       0  cm   31      20  dC
Scan #313
20:21:40:31
    1       0 lpm    2 -0.078  mm    3-0.0429  mm    4-1.0E-3  mm    5  0.031  mm    6 0.0966  mm    7-0.3272  mm
    8 0.9054  mm    9-0.0098  mm   10 0.0042  mm   11-1.2486  mm   12-0.0146  mm   13-0.5389  mm   14 7.8618  mm
   15 0.4254  mm   16-0.0441  mm   17 3.2929  mm   18 0.0991  mm   19-0.4953  mm   20  0.064  mm   21-0.0022  mm
   22       0 MPa   23    20.2  ms   24    13.5  ms   25    6.7  ms   26    -6.8  ms   27    1300 KPa   28 -1.047 KPa
   29    1267 KPa   30       0  cm   31    19.9  dC
Scan #314
20:21:41: 1
    1       0 lpm    2 -0.073  mm    3  -0.04  mm    4 0.0061  mm    5 0.0335  mm    6 0.1102  mm    7-0.3125  mm
    8 0.9134  mm    9-0.0095  mm   10 0.0045  mm   11-1.2512  mm   12-0.0158  mm   13-0.5389  mm   14 7.8687  mm
   15 0.4273  mm   16-0.0288  mm   17 3.3019  mm   18 0.1355  mm   19-0.4788  mm   20 0.0923  mm   21-0.0019  mm
   22       0 MPa   23    20.2  ms   24    13.5  ms   25   10.2  ms   26    -6.8  ms   27    1291 KPa   28 -1.047 KPa
   29    1257 KPa   30       0  cm   31    19.9  dC
```

```
Scan #315
20:21:41:31
    1       0 lpm    2-0.0716  mm    3  -0.04  mm    4 0.0088  mm    5 0.0348  mm    6 0.1121  mm    7-0.3087  mm
    8 0.9156  mm    9-0.0095  mm   10 0.0045  mm   11-1.2537  mm   12-0.0143  mm   13-0.5383  mm   14 7.8712  mm
   15 0.4267  mm   16-0.0294  mm   17 3.3054  mm   18 0.1417  mm   19-0.4879  mm   20 0.1036  mm   21-0.0019  mm
   22       0 MPa   23   20.2  ms   24   13.5  ms   25    6.8  ms   26   -6.8  ms   27    1282 KPa   28 -1.047 KPa
   29    1249 KPa   30      0  cm   31   19.9  dC
Scan #316
20:21:42: 1
    1       0 lpm    2-0.0709  mm    3-0.0397  mm    4   0.01  mm    5 0.0354  mm    6 0.1121  mm    7-0.3053  mm
    8 0.9162  mm    9-0.0095  mm   10 0.0045  mm   11 -1.255  mm   12-0.0149  mm   13-0.5376  mm   14 7.8755  mm
   15 0.4267  mm   16-0.0277  mm   17 3.3066  mm   18 0.1417  mm   19-0.4879  mm   20  0.108  mm   21-0.0019  mm
   22       0 MPa   23   20.2  ms   24   13.5  ms   25    6.8  ms   26   -3.5  ms   27    1274 KPa   28 -1.012 KPa
   29    1241 KPa   30      0  cm   31   19.8  dC
Scan #317
20:21:42:31
    1       0 lpm    2-0.0706  mm    3  -0.04  mm    4 0.0109  mm    5 0.0357  mm    6 0.1127  mm    7-0.3029  mm
    8 0.9165  mm    9-0.0095  mm   10 0.0045  mm   11-1.2518  mm   12-0.0149  mm   13-0.5376  mm   14 7.8712  mm
   15  0.426  mm   16-0.0259  mm   17 3.3078  mm   18 0.1423  mm   19-0.4873  mm   20 0.1105  mm   21-0.0019  mm
   22       0 MPa   23   20.2  ms   24   13.5  ms   25    6.8  ms   26       0  ms   27    1266 KPa   28 -1.012 KPa
   29    1233 KPa   30      0  cm   31   19.9  dC

**STRENGTH AND PERMEABILITY TESTS ON ULTRA-LARGE
**STRIPA GRANITE CORE (Engineering Units Data)
**21:47:04 - 23:07:06
**No load; vessel draining
Scan #318
20:21:47: 4
    1       0 lpm    2-0.0686  mm    3  -0.04  mm    4 0.0146  mm    5 0.0382  mm    6 0.1133  mm    7-0.2924  mm
    8 0.9162  mm    9-0.0091  mm   10 0.0051  mm   11-1.2253  mm   12-0.0131  mm   13-0.5357  mm   14 7.9129  mm
   15 0.4254  mm   16-0.0177  mm   17 3.3102  mm   18 0.1429  mm   19-0.4806  mm   20 0.1187  mm   21-0.0016  mm
   22       0 MPa   23   26.7  ms   24   19.8  ms   25    6.8  ms   26       0  ms   27    1244 KPa   28   -1.5 KPa
   29    1206 KPa   30      0  cm   31   19.7  dC
Scan #319
20:21:47:34
    1       0 lpm    2-0.0682  mm    3  -0.04  mm    4 0.0158  mm    5 0.0382  mm    6 0.1133  mm    7 -0.291  mm
    8 0.9165  mm    9-0.0088  mm   10 0.0051  mm   11-1.2297  mm   12-0.0127  mm   13-0.5351  mm   14 7.9073  mm
   15 0.4248  mm   16-0.0177  mm   17 3.3126  mm   18 0.1435  mm   19-0.4794  mm   20   0.12  mm   21-0.0013  mm
   22       0 MPa   23      27  ms   24   20.2  ms   25    6.8  ms   26    3.2  ms   27    1071 KPa   28 -1.291 KPa
   29    1040 KPa   30      0  cm   31   19.7  dC
Scan #320
20:21:47:59
    1       0 lpm    2-0.0679  mm    3 -0.041  mm    4 0.0168  mm    5 0.0385  mm    6 0.1139  mm    7 -0.291  mm
    8 0.9171  mm    9-0.0082  mm   10 0.0055  mm   11-1.2253  mm   12-0.0115  mm   13-0.5351  mm   14 7.9055  mm
   15 0.4241  mm   16-0.0171  mm   17 3.3155  mm   18 0.1441  mm   19-0.4781  mm   20 0.1212  mm   21-0.0013  mm
   22       0 MPa   23      27  ms   24   20.2  ms   25    6.8  ms   26    6.7  ms   27     917 KPa   28 -1.151 KPa
   29     893 KPa   30      0  cm   31   19.7  dC
Scan #321
20:21:49:59
    1       0 lpm    2-0.0676  mm    3-0.0378  mm    4 0.0223  mm    5 0.0388  mm    6  0.117  mm    7-0.2937  mm
    8 0.9267  mm    9-0.0076  mm   10 0.0061  mm   11-1.2159  mm   12-0.0115  mm   13 0.5568  mm   14 7.9254  mm
   15  0.419  mm   16-0.0159  mm   17 3.3334  mm   18 0.1466  mm   19-0.4745  mm   20 0.1262  mm   21-1.0E-3  mm
   22       0 MPa   23      27  ms   24   26.1  ms   25    6.8  ms   26   12.6  ms   27     580 KPa   28 -0.802 KPa
   29     579 KPa   30      0  cm   31   19.8  dC
```

Scan #322
20:22: 1:43

1	0	lpm	2	-0.0659	mm	3	-0.0388	mm	4	0.0223	mm	5	0.0407	mm	6	0.1158	mm	7	-0.2804 mm
8	0.9156	mm	9	-0.0082	mm	10	0.0058	mm	11	-1.2241	mm	12	-0.0124	mm	13	-0.4249	mm	14	7.9603 mm
15	0.4177	mm	16	-0.01	mm	17	3.3352	mm	18	0.1472	mm	19	-0.4714	mm	20	0.1288	mm	21	-0.0013 mm
22	0	MPa	23	20.3	ms	24	13.8	ms	25	6.8	ms	26	6.9	ms	27	1366	KPa	28	-1.64 KPa
29	1329	KPa	30	0	cm	31	21.1	dC											

Scan #323
**Piston suspended; vessel draining:
20:22:22:36

1	0	lpm	2	-0.0638	mm	3	-0.0246	mm	4	0.0366	mm	5	0.0413	mm	6	0.1245	mm	7	-0.2924 mm
8	0.9357	mm	9	-0.0051	mm	10	0.0067	mm	11	-1.2398	mm	12	-0.0165	mm	13	0.6183	mm	14	7.8587 mm
15	0.4005	mm	16	-0.0059	mm	17	3.381	mm	18	0.1521	mm	19	-0.4641	mm	20	0.1457	mm	21	6.0E-4 mm
22	0	MPa	23	20.2	ms	24	26.7	ms	25	0.1	ms	26	20	ms	27	-1	KPa	28	-0.733 KPa
29	3713	KPa	30	0	cm	31	-0.8	dC											

Scan #324
20:22:27:36

1	0	lpm	2	-0.0638	mm	3	-0.0246	mm	4	0.0366	mm	5	0.0413	mm	6	0.1201	mm	7	-0.3006 mm
8	0.9304	mm	9	-0.0051	mm	10	0.0067	mm	11	-1.2367	mm	12	-0.0161	mm	13	0.6144	mm	14	7.8568 mm
15	0.3967	mm	16	-0.0147	mm	17	3.3816	mm	18	0.1429	mm	19	-0.4788	mm	20	0.1413	mm	21	3.0E-4 mm
22	0	MPa	23	26.7	ms	24	33.4	ms	25	0	ms	26	20.2	ms	27	19	KPa	28	-0.837 KPa
29	3713	KPa	30	0	cm	31	-0.1	dC											

Scan #325
20:22:32:36

1	0	lpm	2	-0.0638	mm	3	-0.0249	mm	4	0.0375	mm	5	0.0419	mm	6	0.1201	mm	7	-0.3057 mm
8	0.9283	mm	9	-0.0054	mm	10	0.0064	mm	11	-1.2581	mm	12	-0.0075	mm	13	0.6029	mm	14	7.8699 mm
15	0.3929	mm	16	-0.0235	mm	17	3.3769	mm	18	0.1312	mm	19	-0.4977	mm	20	0.1319	mm	21	3.0E-4 mm
22	0	MPa	23	20.5	ms	24	33.7	ms	25	-6.4	ms	26	13.8	ms	27	-20	KPa	28	-0.837 KPa
29	3560	KPa	30	0	cm	31	0.2	dC											

Scan #326
20:22:37:36

1	0	lpm	2	-0.0638	mm	3	-0.0249	mm	4	0.0388	mm	5	0.0425	mm	6	0.1108	mm	7	-0.306 mm
8	0.9286	mm	9	-0.0054	mm	10	0.0071	mm	11	-1.2499	mm	12	0.0012	mm	13	0.6048	mm	14	7.9055 mm
15	0.3916	mm	16	-0.0241	mm	17	3.3769	mm	18	0.1269	mm	19	-0.5032	mm	20	0.1256	mm	21	-0.0019 mm
22	0	MPa	23	20.2	ms	24	27.2	ms	25	-6.7	ms	26	13.5	ms	27	-2	KPa	28	-0.802 KPa
29	3713	KPa	30	0	cm	31	-0.4	dC											

Scan #327
20:22:42:36

1	0	lpm	2	-0.0591	mm	3	-0.023	mm	4	0.0458	mm	5	0.0475	mm	6	0.1059	mm	7	-0.2988 mm
8	0.9369	mm	9	0.0043	mm	10	0.0103	mm	11	-1.2316	mm	12	0.0114	mm	13	0.6048	mm	14	7.8955 mm
15	0.3897	mm	16	-0.0235	mm	17	3.6602	mm	18	0.178	mm	19	-0.4371	mm	20	0.1677	mm	21	0.0034 mm
22	0	MPa	23	0.9	ms	24	20.5	ms	25	38.1	ms	26	0.7	ms	27	-1	KPa	28	-0.802 KPa
29	3713	KPa	30	0	cm	31	-0.3	dC											

Scan #328
20:22:47:36

1	0	lpm	2	-0.0601	mm	3	-0.0284	mm	4	0.0452	mm	5	0.0466	mm	6	0.1053	mm	7	-0.305 mm
8	0.936	mm	9	-7.0E-4	mm	10	0.01	mm	11	-1.226	mm	12	0.008	mm	13	0.6003	mm	14	7.9048 mm
15	0.3865	mm	16	-0.0235	mm	17	3.415	mm	18	0.1854	mm	19	-0.4341	mm	20	0.1771	mm	21	3.0E-4 mm
22	0	MPa	23	12.9	ms	24	26.6	ms	25	40.5	ms	26	6.4	ms	27	-2	KPa	28	-0.767 KPa
29	3713	KPa	30	0	cm	31	-0.2	dC											

Scan #329
20:22:52:36

1	0	lpm	2	-0.0601	mm	3	-0.0256	mm	4	0.0464	mm	5	0.0469	mm	6	0.1028	mm	7	-0.3057 mm
8	0.9351	mm	9	-0.0013	mm	10	0.01	mm	11	-1.2253	mm	12	0.0071	mm	13	0.5978	mm	14	7.9092 mm
15	0.3865	mm	16	-0.0247	mm	17	3.4322	mm	18	0.1799	mm	19	-0.4432	mm	20	0.1715	mm	21	6.0E-4 mm
22	0	MPa	23	13.5	ms	24	26.9	ms	25	40.5	ms	26	13.1	ms	27	-2	KPa	28	-0.802 KPa
29	3713	KPa	30	0	cm	31	-0.2	dC											

1

Scan #330

20:22:57:36

1	0	lpm	2	-0.0598	mm	3	-0.0476	mm	4	0.0485	mm	5	0.0481	mm	6	0.1034	mm	7	-0.305	mm
8	0.9335	mm	9	-4.0E-4	mm	10	0.0103	mm	11	-1.2165	mm	12	0.0086	mm	13	0.5958	mm	14	7.9042	mm
15	0.3839	mm	16	-0.0247	mm	17	3.4405	mm	18	0.1823	mm	19	-0.4279	mm	20	0.169	mm	21	0.0015	mm
22	0	MPa	23	13.5	ms	24	26.9	ms	25	34.1	ms	26	7.1	ms	27	12	KPa	28	-0.837	KPa
29	3713	KPa	30	0	cm	31	-0.4	dC												

Scan #331

20:23: 2:36

1	0	lpm	2	-0.0598	mm	3	-0.0577	mm	4	0.0491	mm	5	0.0481	mm	6	0.1028	mm	7	-0.3053	mm
8	0.9326	mm	9	-4.0E-4	mm	10	0.0103	mm	11	-1.214	mm	12	0.0086	mm	13	0.5958	mm	14	7.9142	mm
15	0.3839	mm	16	-0.0247	mm	17	3.5102	mm	18	0.1774	mm	19	-0.4243	mm	20	0.1583	mm	21	0.0015	mm
22	0	MPa	23	13.5	ms	24	26.9	ms	25	155.5	ms	26	19.5	ms	27	-6	KPa	28	-0.837	KPa
29	3713	KPa	30	0	cm	31	-0.2	dC												

Scan #332

**Last scan!

20:23: 7:36

1	0	lpm	2	-0.0598	mm	3	-0.0605	mm	4	0.0494	mm	5	0.0478	mm	6	0.0978	mm	7	-0.306	mm
8	0.8411	mm	9	-4.0[illegible]	mm	10	0.01	mm	11	-1.2178	mm	12	0.0086	mm	13	0.5952	mm	14	7.9404	mm
15	0.3839	mm	16	-0.0241	mm	17	3.5102	mm	18	0.1743	mm	19	-0.4206	mm	20	0.1558	mm	21	0.0015	mm
22	0	MPa	23	58.5	ms	24	39.8	ms	25	1366.5	ms	26	65	ms	27	0	KPa	28	-0.837	KPa
29	3713	KPa	30	0	cm	31	-0.1	dC												